Finite Element Models for Multiscale Theory of Porous Media

by

Bruna Campos

A thesis
presented to the University Of Waterloo
in fulfillment of the
thesis requirement for the degree of
Doctor of Philosophy
in
Civil Engineering

Waterloo, Ontario, Canada, 2024

© Bruna Campos 2024

Examining Committee Membership

The following served on the Examining Committee for this thesis. The decision of the Examining Committee is by majority vote.

External Examiner:	Dr. Richard Wan Professor, Dept. of Civil Engineering University of Calgary
Supervisor:	Dr. Robert Gracie Associate Professor, Dept. of Civil and Environmental Engineering University of Waterloo
Internal Member:	Dr. Dipanjan Basu Professor, Dept. of Civil and Environmental Engineering University of Waterloo
Internal Member:	Dr. Giovanni Cascante Professor, Dept. of Civil and Environmental Engineering University of Waterloo
Internal-External Member:	Dr. Maurice B. Dusseault Professor, Dept. of Earth and Environmental Sciences University of Waterloo

Author's Declaration

This thesis consists of material all of which I authored or co-authored: see Statement of Contributions included in the thesis. This is a true copy of the thesis, including any required final revisions, as accepted by my examiners.

I understand that my thesis may be made electronically available to the public.

Statement of Contributions

This thesis consists of four manuscripts written for publication. Exceptions to sole authorship of material are as follows:

Chapter 3 is based on the following journal article:

B. Campos and R. Gracie, "A FEM for three-field u–p–η poroelasticity with nonreciprocal interactions", *International Journal for Numerical and Analytical Methods in Geomechanics*, vol. 48 (1), p. 332–355, 2024.

In this journal article, I was the primary author and was responsible for writing the article. Dr. Robert Gracie was responsible for editing the paper and conceptualization of the idea. I developed the mathematical formulation, implemented the computer code, and ran the simulations.

Chapter 4 is based on the following journal article:

B. Campos and R. Gracie, "A dynamic three-field finite element model for wave propagation in linear elastic porous media". Submitted to *International Journal for Numerical and Analytical Methods in Geomechanics*, May 2024.

In this journal article, I was the primary author and was responsible for writing the article. Dr. Robert Gracie was responsible for editing the paper and conceptualization of the idea. I developed the mathematical formulation, implemented the computer code, and ran the simulations.

Chapter 5 is based on the following journal article:

B. Campos and R. Gracie, "Wave velocity and attenuation in generalized Biot porous media model", Submitted for publication, September 2024.

In this journal article, I was the primary author and was responsible for writing the article. Dr. Robert Gracie was responsible for editing the paper and conceptualization of the idea. I developed the methodology, conceptualized and ran the wave analysis.

Chapter 6 is based on the following journal article:

B. Campos and R. Gracie, "Fluid velocity finite element formulation for layered porous media domain", Manuscript under preparation, September 2024.

In this journal article, I was the primary author and was responsible for writing the article. Dr. Robert Gracie was responsible for editing the paper and conceptualization of the idea. I developed the mathematical formulation, implemented the computer code, and ran the simulations.

Abstract

Theories to describe porous media aim to represent a combination of a solid matrix and a connected pore space, which may be occupied by fluids. Porous media applications are found in structural materials, geomechanics, biological tissues, and chemical filtration processes, amongst others. Early developments are attributed to Biot who, based on experimental data, derived a set of governing equations for consolidation problems. Concomitantly, other theories were based on mixture theory and volume averaging concept, establishing a clear connection between micro and macro scales.

The work presented by de la Cruz and Spanos (dCS) is an example of a volume-averaging theory. The Biot (BT) theory can be seen as a simplified version of the dCS formulation, since the former assumes a unique energy potential, restrains solid-fluid deformations to reciprocal interactions, and does not account for fluid viscous dissipation terms on the fluid stress definition. Due to the complexity of the dCS theory governing equations, correspondent numerical models have been scarce in literature. To fill this gap, this research focuses on the development of novel finite element (FE) models for the dCS theory. The main applications are consolidation and wave propagation problems in water-saturated rock formations. Results are compared to the BT formulation, and the circumstances which can lead to discrepancies between these theories are studied.

First, a novel FE method is developed for quasi-static solid deformations and transient pore fluid flow, where dynamic effects are neglected. The governing equations are written in terms of solid displacement, fluid pressure, and porosity. Fully implicit time integration and a mixed-element formulation are employed to ensure stability. The convergence rate of the dCS FE model is shown to be optimal in a one-dimensional consolidation problem, considering that rates are dependent on how significant the solid-fluid coupling terms are compared to the uncoupled terms. Two-dimensional examples further attest the robustness of the implementation and are shown to reproduce BT model results as a special case. Non-reciprocal solid-fluid interactions, inherent to the dCS theory, lead to significant differences depending on the properties of the porous media (e.g., permeability) and problem specific constraints.

Extending the transient formulation to include inertia (acceleration) terms, a three-field dCS FE model for dynamic porous media is presented, now formulated in terms of solid displacement, fluid pressure, and fluid displacement. Due to fluid viscous dissipation terms, wave propagation in the dCS theory yields an additional rotational wave compared to BT theory. Besides the introduction of non-reciprocal solid fluid interactions, the dCS model further accounts for a dimensionless parameter related to the macroscopic shear

modulus. Space and time convergence rates are demonstrated in a one-dimensional case. A dimensionless analysis performed in the dCS framework led to negligible differences between BT and dCS models except when assuming high fluid viscosity. Domains with small characteristic lengths resulted in BT and dCS damping terms in the same order of magnitude. One- and two-dimensional examples showed that the dCS non-reciprocal interactions and the macroscopic shear modulus parameter are responsible for modifying wave patterns. A two-dimensional injection well simulation with water and slickwater showed higher wave attenuation for the latter.

Following the derivation of the dCS dynamic formulation, wave propagation phenomena in porous media is analyzed. The dCS slow S wave is studied, essential in the representation of fluid vorticity and shear motion at high frequencies. Differences between dCS and BT results appear at high frequency range. Solid-fluid non-reciprocal interactions and changes in the macroscopic solid shear modulus lead to distinct P wave patterns. The influence of permeability, porosity, and dynamic viscosity is evaluated, showing that wave patterns are generally most affected at the ultrasonic frequency range. At low frequencies, BT and dCS yield the same results for saturated rocks, except when the slow P wave is non-dissipative. While BT theory incorporates a correction factor to reproduce fluid behavior at high frequency, the dCS model naturally accounts for this effect due to the complete fluid stress tensor. High-frequency results from both theories, nonetheless, are discrepant.

Since the dCS equations can be written in terms of different main variables, they can be chosen according to the problem setup. In this sense, a three-field dCS formulation is written in terms of solid displacement, fluid pressure, and relative fluid velocity. The verification study is in agreement with BT results, highlighting how the addition of fluid viscous dissipation terms does not influence load bearing. However, it is essential in the representation of fluid vorticity motion at high frequencies and in wave reflection/transmission problems. Optimal convergence rates for a one-dimensional example are obtained for same-order linear elements. Two-dimensional examples with sandstone and shale layers show how waves are transmitted and reflected at the domain interface at the low- and high-frequency regimes.

The research development and findings reported in this thesis consist in novel FE models to represent the dCS porous media theory. The results show how the dCS formulation is able not only to recover BT results but further circumvent gaps in the BT theory. The dCS FE framework herein presented is also a foundation for future studies in the area. Examples are the expansion of wave propagation studies with a reduced number of assumptions, the combination of a inertial fracture flow model with a porous media representation of fractured rocks, the simulation of nonlinear solid matrix behavior, and the development of a dCS FE model for inertia-driven flow in porous media.

Acknowledgements

I am extremely grateful to have arrived at this stage of my academic journey and to have so many people supporting me through it. I wish to express my deepest gratitude to Prof. Robert Gracie for giving me the opportunity to join his research group. I have grown immensely with your advice and guidance. I extend my thanks to the committee members for taking the time to read my work and provide valuable feedback.

I would like to thank my previous supervisors and mentors during all my years in academia, especially Prof. Jesiel Cunha, Prof. Maria Cristina Vidigal, Prof. Samuel Penna, and Prof. Felício Barros, who gave me immeasurable advice and who supported my most ambitious dreams. A special thanks to the friends I have made in the research groups; you gave me the motivation and inspiration when I needed the most.

To the friendships I have made along the years, my biggest appreciation. You kept me sane, happy, and taught me that there is more in life than your professional career. Time took us apart since we keep following different paths but, no matter the distance, I am honoured to have your company.

To my family, I do not have enough words to express my appreciation and love. Júlia, Oscar, and Simone, you indeed were always with me. I would have never thought that I could live so distant from you for so long. Thank you for keeping me grounded, for supporting my dreams, and for your unconditional love. My heartfelt thanks to all my relatives for the words of admiration and encouragement.

Lastly, I would like to thank God for the opportunities I have had and for giving me the tools to conquer my goals. I am truly grateful for all the moments that led me to this point.

Table of Contents

Examining Committee ii

Author's Declaration iii

Statement of Contributions iv

Abstract v

Acknowledgements vii

List of Figures xiii

List of Tables xix

1 Introduction 1

1.1 Porous Media: Definition and Applications 1

1.2 Poroelasticity Theories 3

1.2.1 Biot theory 4

1.2.2 De la Cruz and Spanos theory 7

1.3 Porous Media Numerical Models 10

1.4 Research Gaps 12

1.5 Goals and Objectives 12

1.5.1 Objective 1: Derive and implement a numerical model for the dCS theory in the quasi-steady case . . . 13
1.5.2 Objective 2: Expand the dCS numerical model for dynamic simulations 13
1.5.3 Objective 3: Study wave velocity and attenuation patterns in dCS theory . . . 14
1.5.4 Objective 4: Derive a three-field dCS numerical model based on fluid velocity . . . 14

2 Numerical Framework of BT and dCS Models 15
2.1 Two-field Formulations . . . 16
2.2 Three-field Formulations . . . 16
2.3 Solid-fluid Coupling Effect . . . 17
2.4 FE Solution by Mode Superposition . . . 19

3 Quasi-Steady FE Formulation 20
3.1 Introduction . . . 20
3.2 Poroelasticity Formulations . . . 21
3.2.1 BT governing equations . . . 21
3.2.2 dCS governing equations . . . 22
3.2.3 Comparison between BT and dCS formulations . . . 24
3.2.4 Generalization of the porosity equation: variation under non-reciprocal interactions . . . 27
3.2.5 Weak form of dCS model . . . 28
3.3 Finite Element Formulation . . . 28
3.4 Verification and Convergence Study . . . 31
3.4.1 Verification with Biot model . . . 31
3.4.2 Convergence study . . . 34
3.5 Numerical Examples . . . 36
3.5.1 Two-dimensional footing . . . 36

3.5.2 Two-dimensional injection wells . . . 39
3.6 Discussion . . . 41
3.7 Conclusions . . . 43

4 Dynamic FE Formulation for Wave Propagation **44**
4.1 Introduction . . . 44
4.2 dCS Governing Equations . . . 45
4.3 Finite Element Formulation . . . 48
4.4 Dimensionless Analysis . . . 53
4.5 Verification and Convergence Study . . . 57
4.6 Numerical Examples . . . 59
4.6.1 One-dimensional pulse . . . 59
4.6.2 Two-dimensional wave propagation . . . 65
4.6.3 Two-dimensional injection well . . . 67
4.7 Discussion . . . 70
4.8 Conclusions . . . 73

5 Porous Media Wave Patterns **75**
5.1 Introduction . . . 75
5.2 Porous Media Descriptions . . . 76
5.2.1 dCS governing equations . . . 76
5.2.2 dCS wave equations . . . 77
5.2.3 Wave attenuation and material damping . . . 80
5.3 Wave Velocity and Attenuation Patterns . . . 80
5.3.1 Porosity effective pressure coefficient n . . . 81
5.3.2 Macroscopic shear modulus averaging coefficient δ_μ . . . 81
5.3.3 Critical frequency limits . . . 82
5.3.4 Dynamic fluid viscosity, intrinsic permeability, and initial porosity . . . 84

5.3.5 Added mass coefficient ρ_{12} . . . 87
5.3.6 Variation of porous media constituents . . . 88
5.3.7 Porosity-pressure waves . . . 88
5.4 Discussion . . . 89
5.5 Conclusions . . . 92

6 Dynamic FE Formulation for Low- and High-frequency Applications 93
6.1 Introduction . . . 93
6.2 dCS Governing Equations . . . 94
6.3 Weak Form and FE Discretization . . . 95
6.4 Verification and Convergence Study . . . 98
6.4.1 Verification with Biot model . . . 98
6.4.2 Convergence study . . . 99
6.5 Numerical Examples . . . 100
6.5.1 Three-layer domain with low-frequency wave propagation . . . 100
6.5.2 Two-layer domain with high-frequency wave propagation . . . 106
6.5.3 Laboratory scale sample with high-frequency wave propagation . . . 110
6.6 Discussion . . . 116
6.7 Conclusions . . . 118

7 Conclusions 119
7.1 Concluding Remarks . . . 119
7.2 Research Contributions . . . 121
7.3 Directions for Future Study . . . 123

References 125

APPENDICES 144

A Stress Definition in BT and dCS Theories 145

B Modal Analysis in Porous Media **150**

B.1 Transient Case 151

B.2 Dynamic Case 152

C Porosity-Pressure Coupled Waves **158**

C.1 Wave Equations 158

C.2 Velocity and Attenuation Study 160

C.3 Variation of Solid-Fluid Constituents 161

List of Figures

1.1 Porous media Representative Elementary Volume (REV): composition of solid matrix and connected pore space. 1

1.2 Timeline of the first developments of porous media theories. From left to right: Fillunger [61], Terzaghi [173], Biot [14], Heinrich & Desoyer [81, 82], de la Cruz & Spanos [44, 45, 46], Lopatnikov *et. al.* [119, 120, 121, 122], Coussy *et. al.* [36, 34, 35]. 4

1.3 Porous media Representative Elementary Volume (REV): solid-fluid interface and unit normal vector. 9

2.1 Finite element models for porous media simulation addressed in this thesis. 16

2.2 Two-field relative error norms for unrealistic material parameters (Diff-) and water-saturated sandstone parameters (Reg-) [193]. The convergence rates m for each field are indicated in the legend. Rates are obtained for the same manufactured solution, geometric and discretization parameters. 18

2.3 Dynamic two- and three-field relative error norms for (a) solid displacement and (b) fluid pressure. The convergence rates m for each field are indicated in the legend. Rates are obtained for the same manufactured solution, geometric and discretization parameters. 19

3.1 Comparison of displacement (left) and pressure (right) changes from dCS and BT models and an analytical solution for the one-dimensional consolidation problem. 32

3.2 Variation of (a) solid displacement and (b) fluid pressure throughout the domain over time. 33

3.3 Porosity variation in one-dimensional consolidation problem over the column depth (left) and over time (right). 33

3.4 Porosity and strain variation in one-dimensional consolidation problem over the column depth. 34

3.5 Change in displacement (left) and pressure (right) along the column depth at $t = 10$s. 34

3.6 Convergence study over mesh size refinement considering L2-norm (left) and gradient norm (right). 36

3.7 Two-dimensional footing example. 37

3.8 Solid displacement and fluid pressure distribution for two-dimensional footing problem at $t_{end} = 10$s. In this case of model verification, $\delta_s^{BT} = 0.67$ and $\delta_f^{BT} = 0$. 38

3.9 Change in variables over the simulation time at $x = 5$m, $y = 5$m for the two-dimensional footing problem. 38

3.10 Porosity and volumetric strain variation in two-dimensional footing problem for varying y at right boundary. For this case, solid and fluid materials are considered incompressible, and thus $\delta_s^{BT} = 0.5730$ and $\delta_f^{BT} = 0.0478$. 39

3.11 Two-dimensional injection wells example. 40

3.12 Displacement and pressure distribution at the center of the domain for the two-dimensional injection wells problem $t_{end} = 100$s. 41

3.13 Change in displacement (left) and pressure (right) over the simulation time at $x = 7.46$m, $y = 7.45$m. 41

4.1 Changes in (a) the compliance coefficients δ_f, δ_s and (b) in the dimensionless constants c_9, c_{10} (Table 4.3) for $n = 0$ to $n = K_s/K_f$; the material parameters are taken from Table 4.1. 55

4.2 Convergence study for mesh size refinement considering (a) L2-norm and (b) gradient-norm; the convergence rates m for each field are indicated in the legend for all linear (Lin-) and mixed order elements (Mix-). 58

4.3 Convergence study for time step refinement considering; the convergence rates m for each field are indicated in the legend for all linear (Lin-) and mixed order elements (Mix-). 59

4.4 Impact of the effective pressure coefficient n on (a, b) solid velocity, (c, d) pressure, and (e, f) fluid velocity for one-dimensional wave propagation with permeability $\kappa = 1.88 \times 10^{-13}\text{m}^2$. Figures (a), (c), (e) show variation over the domain at $t_{end} = 5 \times 10^{-2}$s, while Figures (b), (d), (f) show variation over time at $x = 260$m. 61

4.5 Comparison between BT and dCS results for (a) solid velocity, (b) pressure, and (c) fluid velocity considering $\kappa_h = 10^{-8}$ m^2 and $\kappa = 10^{-13}$ m^2. Plots show curves at the final simulation time $t_{end} = 5 \times 10^{-2}$s. 63

4.6 Impact of the effective pressure coefficient n on (a, b) solid velocity, (c, d) pressure, and (e, f) fluid velocity for one-dimensional wave propagation with permeability $\kappa_h = 10^{-8}\text{m}^2$. Figures (a), (c), (e) show variation over the domain at $t_{end} = 5 \times 10^{-2}$s, while Figures (b), (d), (f) show variation over time at $x = 260$m. 64

4.7 Impact of dimensionless parameter δ_μ on (a) solid velocity, (b) pressure, and (c) fluid velocity at $t_{end} = 5 \times 10^{-2}$s. 65

4.8 Distribution of fluid velocity in (a) x and (b) y directions over the domain at $t_{end} = 8 \times 10^{-1}$s; fast P and S waves are identified. 67

4.9 Impact of effective pressure coefficient n on (a,b) solid velocity, (c,d) fluid velocity, and (e) pressure at $t_{end} = 8 \times 10^{-1}$s for two-dimensional pulse; the x-axis refers to a cross-diagonal along the domain. 68

4.10 Impact of effective pressure coefficient n for two-dimensional pulse. Left: variation in (a, c) fluid velocity and (e) pressure at $t_{end} = 8 \times 10^{-1}$s; the x-axis refers to a cross-diagonal along the domain. Right: variation in pressure over time at $x = 2600$m for (b) $n = 1$, (d) n_{min}, and (f) n_{max}. 69

4.11 Geometry and boundary conditions of two-dimensional injection well problem. 70

4.12 Impact of effective pressure coefficient n on (a) solid velocity, (b) pressure, and (c) fluid velocity at $t_{end} = 3 \times 10^{-3}$s for two-dimensional injection. Plots consider both water ($\mu_f = 10^{-3}$Pa·s, w- in legend) and slickwater ($\mu_f = 5 \times 10^{-3}$Pa·s, sw- in legend) fluids; the x-axis refers to the line AB indicated in Figure 4.11. 71

5.1 Velocity and attenuation for (a) fast P, (b) slow P, (c) fast S, and (d) slow S waves in BT and dCS theories, varying the n parameter on the latter. Note that the slow S wave only appears in dCS theory due to the lack of fluid viscous dissipation terms in BT. 82

5.2 Velocity and attenuation for (a) fast P, (b) slow P, (c) fast S, and (d) slow S waves in dCS theory for different values of the parameter δ_μ. 83
5.3 Velocity and attenuation for (a) fast P, (b) slow P, (c) fast S, and (d) slow S waves in dCS theory for highly permeable sandstone. 84
5.4 Velocity for the four wave types in dCS theory. Each row represents the variation in a different material parameter: (a)-(d) is fluid dynamic viscosity, (e)-(h) is intrinsic permeability, and (i)-(l) is initial porosity. Each column indicates a different wave type; first is fast P wave, second is slow P wave, third is fast S wave, and fourth is slow S wave. 85
5.5 Attenuation for the four wave types in dCS theory. Each row represents the variation in a different material parameter: (a)-(d) is fluid dynamic viscosity, (e)-(h) is intrinsic permeability, and (i)-(l) is initial porosity. Each column indicates a different wave type; first is fast P wave, second is slow P wave, third is fast S wave, and fourth is slow S wave. 86
5.6 Wave velocity for different materials considering both BT and dCS models. 89
5.7 Wave attenuation for different materials considering both BT and dCS models. 90

6.1 Verification study for (a) solid displacement, (b) solid velocity, (c) fluid pressure, and (d) relative fluid velocity. Plots show variation over the domain at $t_{end} = 5$s for BT and dCS theories. 99
6.2 Convergence study for (a) mesh size refinement and (b) time step refinement; the convergence rates m for each field are indicated in the legend. 100
6.3 Geometry of two-dimensional three-layer domain. 101
6.4 Two-dimensional wave propagation in three-layer domain: variation of (a,b) solid velocity, (c,d) relative fluid velocity, (e) fluid pressure, and (f) porosity across the diagonal AB (Figure 6.3) at $t_{end} = 0.32$s. 103
6.5 Two-dimensional wave propagation in sandstone (a, c, e) and three-layer (b, d, f) domains at $t_{end} = 0.32$s. The horizontal white lines correspond to lines CD and EF in Figure 6.3. 104
6.6 Synthetic plots at line GH ($x = 2,200$m) for (a) sandstone-only medium and (b) three-layered domain. 105
6.7 Two-dimensional wave propagation in sandstone domain (top row) and shale-sandstone (middle, bottom rows) layered domain. Each column depicts results at a different simulation time. The horizontal white lines correspond to lines CD and EF in Figure 6.3. 107

6.8 Geometry of two-dimensional layered domain. 108

6.9 Two-dimensional wave propagation of $\mathbf{u}_s, \mathbf{w}$ fields in sandstone (a, c) and two-layer (b, d) domains at $t_{end} = 4 \times 10^{-3}$s. The horizontal white line corresponds to the material interface EF indicated in Figure 6.8. 109

6.10 Two-dimensional wave propagation of $p, \dot{\eta}$ fields in sandstone (a, c) and two-layer (b, d) domains at $t_{end} = 4 \times 10^{-3}$s. The horizontal white line corresponds to the material interface EF indicated in Figure 6.8. 110

6.11 Wave types in solid velocity and pressure contour plots at $t_{end} = 4 \times 10^{-3}$s. Original, reflected (Refl.) and transmitted (Tran.) waves are identified. The horizontal white line indicates the shale-sandstone boundary for the layered model. 111

6.12 Two-dimensional wave propagation: (a,b) solid velocity, (c,d) relative fluid velocity, (e) fluid pressure, and (f) porosity variation at $x = 10$m, $t_{end} = 4 \times 10^{-3}$s for sandstone (S-) and shale-sandstone (L-) domains. Legends indicate plots for BT and dCS ($n = 1$) models. 112

6.13 Geometry of sandstone core sample. 113

6.14 Core Sample example: (a, b) solid velocity, (c, d) relative fluid velocity, (e, f) fluid pressure, and (g, h) porosity variation at $t = 2.5 \times 10^{-5}$s (left) and $t_{end} = 2 \times 10^{-4}$s (right). The yellow vertical lines correspond to the cross sections AB, CD, and EF indicated in Figure 6.13. 114

6.15 Wave propagation in sandstone core sample: BT and dCS plots for (a) solid velocity, (b) relative fluid velocity, (c) fluid pressure, and (d) porosity at the cross sections AB (left column), CD (middle column), and EF (right column). 115

6.16 Synthetic plots of pressure field at section EF ($x = 28$cm) BT and dCS models. 116

B.1 First six mode shapes for one-dimensional transient consolidation problem [108]. 153

B.2 One-dimensional transient consolidation: comparison of solid displacement (left) and pressure (right) curves for time discretization and mode superposition solution strategies. 154

B.3 First six mode shapes for (a) solid displacement and (b) fluid pressure in a two-dimensional transient consolidation problem [204]. 155

B.4 First six mode shapes for one-dimensional dynamic porous media. 156

B.5 One-dimensional dynamic consolidation: comparison of solid displacement (left) and pressure (right) curves for time discretization and mode superposition solution strategies. 157

C.1 Velocity and attenuation for porosity-pressure waves in water-saturated sandstone. 161

C.2 Porosity-pressure waves patterns for different solid-fluid combinations. . . . 162

List of Tables

3.1 Material parameters [22] for the column consolidation verification study. . 31

3.2 Material parameters [50] for the two-dimensional footing problem. 37

3.3 Material parameters [193] and problem configuration data for the two-dimensional injection wells problem. 40

4.1 Material parameters [193]for water-saturated sandstone. 46

4.2 Dimensionless parameters from equations (4.9)-(4.11). 48

4.3 Non-dimensional parameters in (4.9)-(4.11) when $c_1 = 1$. 54

4.4 Values of dimensionless parameters, as defined in Table 4.3, for various materials. The combinations are: M1 - water and sandstone, M2 - light oil and sandstone, M3 - heavy oil and sandstone, M4 - water and cancellous bone. 56

4.5 Velocity and wavelength of dCS P and S waves for the water-saturated sandstone [193] and source frequency of 1kHz. 60

4.6 Velocity and wavelength of P and S waves for water-saturated sandstone [193] with $\kappa_h = 10^{-8}$ m^2 and source frequency of 1kHz. 62

4.7 Velocity and wavelength of dCS P and S waves for water-saturated sandstone [171] and source frequency of 10Hz. 66

5.1 Coefficients defined in wave equations (5.10)-(5.13). 78

6.1 Material parameters for water saturated shale [168]. 102

6.2 Velocity and wavelength of dCS P and S waves for water-saturated sandstone [193] and shale [168], considering $\kappa = 10^{-11}$m^2 and source frequency of 10Hz. 102

6.3 Velocity and wavelength of P and S waves for water-saturated sandstone [193] considering $\kappa = 10^{-11}\text{m}^2$ and source frequency of $2 \times 10^5\text{Hz}$. 111

C.1 Peak wave velocity for porosity-pressure P waves. 161

Chapter 1

Introduction

1.1 Porous Media: Definition and Applications

A porous medium is comprised by a solid matrix and a connected pore space, which may be filled by fluids, as depicted in Figure 1.1. Porous structures are found within various areas of study with distinct applications. For instance, the representation of porous soils and rocks is important in the study of seismicity and consolidation processes, predicting constituents behavior and wave patterns. Porous materials are found in the chemical engineering context, for example, in the simulation of solute transport and contaminant removal. Biological tissues can also be represented by a porous space, and understanding its behavior provides tissue characterization and detection of pathologies.

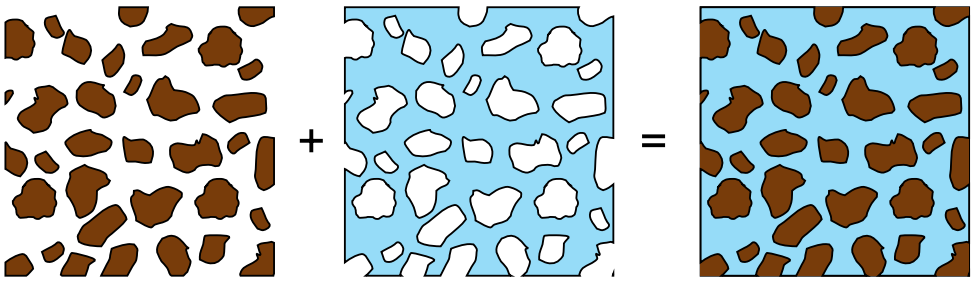


Figure 1.1: Porous media Representative Elementary Volume (REV): composition of solid matrix and connected pore space.

The behavior of solid and fluid/gas constituents can vary significantly. The solid material can have a linear, plastic, elasto-plastic, visco-elastic, or visco-plastic behavior, for instance. The connected pore space can be filled by one or more compressible or incompressible materials. The domain could also be partially or fully saturated, whilst thermal interactions may or may not be introduced into the model. The chosen assumptions depend on the type of problem to be studied and the type of phenomena that it should represent. In this thesis, the main focus is on porous media representation of geological formations, evaluating processes such as rock consolidation and wave propagation. For that, thermal interactions are neglected, the solid matrix has a linear elastic behavior, and it is fully saturated by a unique compressible fluid phase.

Representative Elementary Volume

The characterization of a porous media Representative Elementary Volume (REV) as indicated in Figure 1.1 requires careful consideration. An REV is defined as the minimum volume V where a chosen parameter is independent of the sample size [12, 9]. The maximum size of the REV is such that the gradient of said parameter is negligible, and then the volume can be taken as homogeneous [14]. The definition of the REV also has a correlation with the wave characteristics in a wave propagation phenomena. In this sense, the wavelength must be at least one order of magnitude higher than $V^{1/3}$, and the volume V has to be one order of magnitude higher than the typical dimension of the pores in the medium [151]. These restrictions are usually not an issue for modeling seismic propagation in rock formations, since seismic wavelengths are longer than the pore size. The REV includes both solid and fluid constituents; nonetheless, the constituents might occupy different regions after deformation due to relative solid-fluid movements [134].

The definition of an REV size usually couples an imaging method with a numerical model, such as computed micro-tomography (CMT) with the Lattice Boltzmann method. A typical parameter used for the REV determination is porosity [14]. A series of studies, nonetheless, have been dedicated to analyze the influence of different porous media parameters on the REV size. For instance, Al-Raoush & A. Papadopoulos [2] used X-ray imaging to show that porosity only was insufficient to determine the minimum REV in sand samples. Costanza-Robinson *et. al.* [33] used CMT to study unsaturated sand samples, and moisture saturation and air-water interfacial area were shown to be essential parameters (combined with porosity) for the REV determination. Multiphase flow REV was shown to be larger than a single-phase flow REV, and its size is influenced by the phase interaction and wettability parameters [40, 115].

Typical sizes of REV for sandstone media were observed by Zhang *et. al.* [199], where a

Brent Triassic sandstone had an estimated statistical REV of 0.27mm. In [144] a moving particle semi-implicit method was able to capture highly irregular fluid-solid interfaces; the REV was reported to have linear dimensions of approximately 0.67mm ($V = 0.31\text{m}^3$). The work of Mostaghimi *et. al.* [131] reported REV sizes of a Berea sandstone in the order of $0.8 - 1.2$mm, and linear dimensions determined for permeability were larger than for porosity.

Further works regarding the REV estimation also include the use of a dimensionless range and gradient calculation method [182]; studies by Wollner *et. al.* [181] provided a method to minimize boundary effects on the REV definition, and Zakirov & Khramchenkov [197] focused on evaluating the impact that capillary number and viscous fingering have on REV dimensions. It is noteworthy that rock core sample dimensions vary according to their purpose; usually, such dimensions fall within $5 - 90$mm [1, 172], which could be larger than the REV size. Hence, a core sample may or may not contain an REV depending on the core sample dimensions and the material type. For rock formations the REV is generally well represented within large core samples. On the other hand, high-porosity soils might still have a heterogeneous representation for small samples.

While REV dimensions for rock formations are relatively small compared to sampling sizes, the representative volume V might increase for higher permeability values and more heterogeneous medium. REV dimensions for soil samples – sand, silt, and clay – were found to be in the $20 - 40$mm range [106]. More to that, the work of Zubov *et. al.* [210] encompasses a vector metrics REV study applied to estimate the representative volume V in geomechanics, and it can be further extended to determining reasonable REVs in other media such as composites and biological tissues.

1.2 Poroelasticity Theories

The description of a porous medium requires a theory that accounts for the changes in the solid and fluid constituents, as well as the interactions between both components. For this purpose, several theories have been developed, as depicted in Figure 1.2. Two distinct approaches can be identified: macro-scale theories and mixture theories [36]. Porous media mixture theories consist in restricting mixture theories by the concept of volume fractions [41]; they define the macroscopic behavior of a porous medium through averaging techniques starting from the microscopic response. On the other hand, macro-scale theories assume that the physical concepts – and field equations from continuum mechanics – related to the porous medium hold at the macroscopic level.

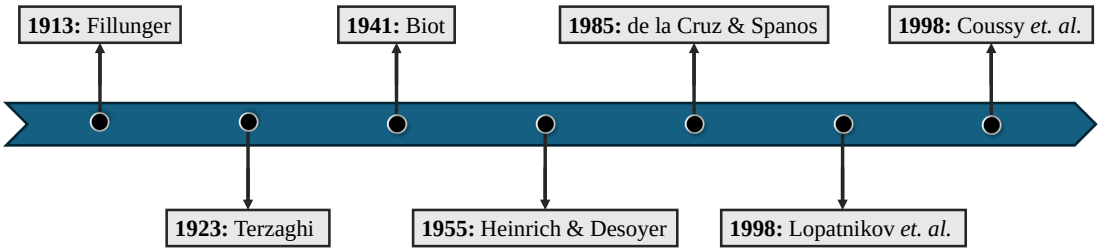


Figure 1.2: Timeline of the first developments of porous media theories. From left to right: Fillunger [61], Terzaghi [173], Biot [14], Heinrich & Desoyer [81, 82], de la Cruz & Spanos [44, 45, 46], Lopatnikov *et. al.* [119, 120, 121, 122], Coussy *et. al.* [36, 34, 35].

The development of macro-scale porous media theories started with Terzaghi's theory of consolidation in the 1920s [41], introducing the concept of effective stress. Following that, the Biot theory of consolidation [14, 15] provided stress-strain relationships for the solid matrix and an expression for the variation in water pressure content while using known material constants and proposing new ones to account for the solid-fluid coupling mechanisms. Concomitantly with Terzaghi's developments, Fillunger [61] presented a porous media theory based on the mixture theory and associated it with mechanical principles [41], applying the volume fractions concept to porous media for the first time [42]. Following that, several authors employed and detailed such porous media mixture theory, e.g., Lopatnikov [121], Coussy [34, 35], and de la Cruz and Spanos [44].

1.2.1 Biot theory

The Biot (BT) theory was initially proposed in the context of consolidation problems [14, 15], and it was extended to account for anisotropic [18] and visco-elastic [19] solid behavior. Early developments also comprised the derivation of wave equations [15, 16, 20]. Examples of applications of the BT model involve soil consolidation [113, 185], seismic explorations [190, 88, 187], and wave propagation at acoustic [155] and ultrasonic [49] frequency ranges. The BT slow wave propagation has also been studied [55, 27], as well as wave analysis using fractional calculus [57, 59]. In the field of nondestructive testing, several authors considered the BT model to compare experimental results in the characterization of bone tissues [93, 132] and in other applications [3, 116].

One of the pillars of the BT theory [14] is the assumption of a unique elastic potential energy U dependent on the fluid and solid phases, which allows the reduction of one poroelastic constant in the formulation. Because of this assumption, which will be more detailed in upcoming sections, the BT theory restricts solid-fluid deformations to reciprocal interactions. This means that both constituents deform to the same extent, and thus porosity is not explicitly modeled. In this sense, the linear porosity equation inferred from Biot equations constrains the change in porosity to solid and fluid pressures, equal in magnitude but in opposite direction [157]. However, further studies show that non-reciprocal interactions are bound to happen due to the micro-inhomogeneous nature of the solid constituent [136, 137, 134]. Hence, the BT porosity definition – or lack thereof – poses a limitation to the simulation of non-reciprocal solid-fluid interactions.

BT wave propagation equations [15, 16] in the context of isotropic poroelastic media yield the existence of three wave types: two compressional (or longitudinal, or P) waves and one shear (or rotational, or S) wave. A fast P wave and a fast S wave are observed to have high velocity and low attenuation characteristics, representing an in-phase solid-fluid motion. The other P wave, also mentioned as slow P, usually has high dissipation and lower velocity due to out of phase solid-fluid motion. Consequently, slow P waves are more difficult to be identified [55], whilst fast P and S waves are easily observed.

By not including fluid viscous dissipation terms (see Section 3.2) in the fluid stress definition, the BT model does not account for the existence of a slow S wave [160], essential in the representation of fluid vorticity at high frequencies [76]. Biot [16] had introduced a correction factor for the wave propagation equations, already acknowledging that the initial theory [15] does not account for fluid viscous effects at such frequency range. Nonetheless, it has been noted that this correction is insufficient to represent fluid shear motion at heterogeneities and discontinuous interfaces [75, 77]. BT theory still contains an unrealistic representation of the velocity dispersion and wave attenuation [151, 152], and its wave motion description seems to be insufficient to represent all porous media dissipation mechanisms. Previous authors identified that the wave attenuation associated with BT theory is significantly smaller than experimental data for rock simulations [129, 105].

To circumvent the underestimation of velocity attenuation and frequency dispersion observed when seismic and ultrasonic waves are modeled using the Biot formulation [189, 195], Dvorkin *et. al.* proposed the Biot-squirt (BISQ) model [54, 53, 52]. It combines the Biot model with the representation of the squirt flow mechanism, which describes the pore-scale phenomenon of water being dissipating through the pores due to a passing wave [104]. Such mechanism seems to be responsible for the viscoelastic response observed in some rock formations – behavior which is defined by the wave frequency and the characteristic squirt-flow length [53]. This characteristic length is introduced into the storage equation,

given by the radius of a cylindrical REV. In later works, the theory was reformulated by [48] to not be dependent on the characteristic length.

Initial studies on wave propagation using the BISQ model showed that the P wave velocity is lower than the Biot prediction at the low-frequency regime; at high frequencies, velocities were reported to be the same [54]. The isotropic BISQ model has been extended to simulate non-isotropic media by Yang & Zhang [189, 190]. In a visco-elastic BISQ model proposed by Feng *et. al.* [195], the dispersion and attenuation were caused by the visco-elastic behavior of the rock rather than the squirt flow. Double porosity models were proposed by Ba *et. al.* to simulate clay squirt flow [8], and by Sharma in the context of propagation of Rayleigh waves [161]. Further developments also include a Biot-spherical squirt model [31], the association of BISQ theory with fractional models [96] and with deep neural networks [186].

Experimental parameter determination

Material parameters are key input data for an accurate representation of porous media. Early studies on the properties of poroelastic systems were presented by Gassman [67] and Geertsma [73]. Biot [17] further described methods to measure essential coefficients in porous media characterization. It was noticed that, due to correlations between parameters, only some constants could be determined, e.g., the shear modulus, drained and undrained bulk modulus, coefficient of fluid content, porosity, and Biot's coefficient α [17].

Detournay & Cheng [47] describe three tests necessary for estimating porous media constants. In the jacketed drained test a load is applied in the core sample, and pressure is allowed to dissipate. An equilibrium is then reached for the pressure field according to the boundary conditions. In this scenario, one is able to measure the sample volume change and the amount of fluid expelled, hence determining the drained bulk modulus and the Biot coefficient.

The second test described is the jacketed undrained test, in which a pressure is applied in the sample but fluid is not allowed to escape. In this scenario, both the undrained bulk modulus and the Skempton coefficient are determined. The third type is an unjacketed test in which the sample is immersed in a fluid, and after the load application one is able to measure the variation in fluid content and the storage coefficient. A list of poroelastic constants experimentally obtained for various types of rocks is presented in [47].

The equipment used in jacketed and unjacketed experiments was described by Zimmerman *et. al.* [208, 207] and Green *et. al.* [78]. Although experimental determination of porous media constants began decades ago, there are still new methods being presented to

improve accuracy and facilitate measurement procedures. For instance, considering that the behavior of the medium could differ under dynamic loading, experiments have been explored for the determination of poroelastic constants in the context of noise vibration and control [4]. Furthermore, the determination of Biot's coefficient was investigated by He [80] for shale formations explored in the oil and gas industry, while Ortiz [142] employed porosity measurement tests under stress.

1.2.2 De la Cruz and Spanos theory

The de la Cruz and Spanos (dCS) poroelasticity theory [44, 45], proposed in the 1990s, assumes that porous medium governing equations [165] are valid at the pore-scale, and need to be averaged throughout the whole domain so that they are suitable to the macroscopic scale. Additionally to the continuity, momentum, and pressure equations, this theory introduces a porosity equation (similarly to the porosity perturbation descriptions in Geertsma [73] and Zimmerman [207], for example). The dCS governing equations also accounts for viscous dissipation terms in the fluid stress definition, yielding the representation a slow S wave [160]. By relying on the complete fluid stress tensor [76], the dCS theory is capable of representing fluid vorticity at high frequencies without the need to introduce a correction factor, as was done in the BT framework [16].

Further developments by Müller and Sahay [135, 157, 134] showed that, by assuming an additive form of the elastic deformation energy potential, the formulation allows the representation of non-reciprocal solid-fluid interactions. These interactions are represented by a parameter called porosity effective pressure coefficient, and it weights the contributions of solid and fluid deformations on the porosity change [157, 134]. The volume averaging technique also yields a macroscopic solid shear modulus [165]; this definition differs from BT theory in the sense that the solid shear modulus at the macro scale in the BT model is simply the average of the solid grain shear modulus, whilst the dCS model accounts for an additional parameter.

Volume-averaging technique

The connection between micro and macro scales in porous media mixture theories is made by using a volume-averaging technique. The governing equations (e.g., momentum and continuity relations) are stated for the individual constituents at the micro scale [165]. These equations are then assumed to be valid at the macroscopic scale by averaging the pore scale quantities over the defined REV.

The volume-averaging process has been studied by various authors, especially since the treatment of the averages of derivatives requires careful evaluation [165]. Initial works of de la Cruz & Spanos [44, 45] had employed the averaging theorems proposed by Whitaker [178, 179], which are still considered in the context of the dCS theory. For solid and fluid field variables G_s, G_f, the average theorem of the spatial derivative over the REV V is given by

$$< \partial_i G_s > = (1 - \eta_0)\partial_i \bar{G}_s + \frac{1}{V}\int_A G_s n_i \, dA, \tag{1.1}$$

$$< \partial_i G_f > = \eta_0 \partial_i \bar{G}_f + \frac{1}{V}\int_A G_f n_i \, dA, \tag{1.2}$$

and the average theorem of the time derivative is

$$< \partial_t G_s > = (1 - \eta_0)\partial_t \bar{G}_s - \int_A G_s \mathbf{v} \cdot \mathbf{n} \, dA, \tag{1.3}$$

$$< \partial_t G_f > = \eta_0 \partial_t \bar{G}_f - \int_A G_f \mathbf{v} \cdot \mathbf{n} \, dA. \tag{1.4}$$

where $\bar{G}_s, \bar{G}_f$ are the averaged quantities (valid at the macro scale), A is the solid-fluid interface area (as depicted in Figure 1.3), $\mathbf{n}$ is a normal unit vector pointing from the solid to the fluid component, η_0 is the initial porosity, and $\mathbf{v}$ is the relative velocity at the solid-fluid interface. Two solid-fluid interface boundary conditions (BCs) are imposed, i.e. the no-slip BC and the traction continuity, as in

$$\left.\frac{\partial u_s}{\partial t}\right|_A = \left.\frac{\partial u_f}{\partial t}\right|_A, \qquad (\boldsymbol{\sigma}_s \mathbf{n})|_A = (\boldsymbol{\sigma}_f \mathbf{n})|_A \, . \tag{1.5}$$

Due to the no-slip boundary condition imposed in the micro scale system, pore-scale solid and fluid velocities at the interface are equal, and thus the relative velocity $\mathbf{v}$ vanishes. When the field variable being averaged is, for instance, solid or fluid displacement, the area integral $\int_A G_{s,f} n_i \, dA$ becomes $\int_A u_i^{s,f} n_i \, dA$, which is the volume swept out of V and can be expressed as $-(\eta - \eta_0)$; η is the porosity variable. More details on employing the volume-averaging technique are presented in Appendix A, where the expressions for averaged (macroscopic) solid and fluid stress tensors are explained. The volume-averaged equations herein presented refer to a linear elastic isotropic medium. Nonetheless, anisotropy can be accounted for in the form of spatially-varying porosity as explored by Sahay *et. al.* [158].

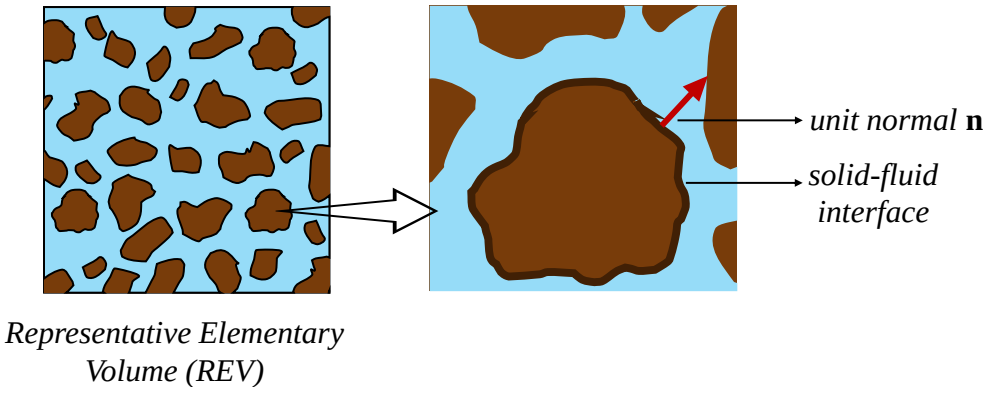


Figure 1.3: Porous media Representative Elementary Volume (REV): solid-fluid interface and unit normal vector.

Porosity-pressure coupling

Due to the explicit representation of porosity, the dCS equations of motion can be rewritten in terms pressure and porosity variables. This allows the study of two additional strongly coupled compressional waves, called porosity-pressure (Por-Pre) waves. The existence of the Por-Pre waves justifies a phenomena called fluid flow enhancement, which consists in a momentary increase in porosity in a certain region that consequently leads to higher fluid flow rate. This process was firstly studied in the early 2000s, when pressure pulse stimulation was noticed to generate such Por-Pre waves and hence enhance fluid flow [74]. Experimental studies were carried out in oil reservoirs, where exceptionally slow pressure waves were continuously applied [39, 51, 209, 166].

In later publications, Lo *et. al.* [117, 118] studied Por-Pre pulsing at seismic frequencies and the effect of acoustic excitation on capillary pressure and water saturation. Laboratory tests were performed by Kahler *et. al.* [94] to analyse acceleration of contaminant removal in aquifers, while Kalisman *et. al.* [95] performed flow cell experiments for solute displacement in unsaturated porous media, and Khasi *et. al.* [98] focused on pore-scale microfluidic experiments using pressure pulsing for remobilization of dense non-aqueous phase liquids. Other applications of pulsed flow can be found in Yoo *et. al.* [194] with the study of cerebrospinal fluid tracer movement and in Li et al. [112] with the investigation of granite rock reservoirs. Although initial studies on fluid flow enhancement used a pressure pulse, any type of pulse source with low enough frequency can lead to the incompressible fluid behavior and consequent flow intensification.

State of the art

The BT theory can be shown to be a particular case of the dCS theory [44, 45]. Hence, the theories can be equated under a few simplifications, i.e., by neglecting the viscous dissipation terms in the fluid stress equation and assuming specific coefficients in the porosity equation such that solid-fluid interactions are reciprocal [165]. Moreover, the material constants employed in both theories require some type of correlation. Concomitantly, volume-averaging porous media theories – such as the dCS model – are also called generalized versions of Biot's theory. Due to the complexity of the governing equations, there is still a need for clarity regarding whether the dCS model can better represent realistic scenarios when compared to the BT theory [151]. One barrier to this evaluation is the lack of numerical methods to simulate problems or practical interest.

Some authors have studied wave propagation phenomena for generalized forms of the BT theory. Hickey *et. al.* [84] used the wave equations in [165] to study phase velocity and attenuation in oil sandstone combinations. Extensive work regarding the dCS model has been done by Quiroga-Goode *et. al.* [151], presenting a comparison between BT and dCS models and analysing wave phase velocity and attenuation in seismic modeling [152]. Quiroga-Goode *et. al.* [150] used Green functions to evaluate the polarization phenomena in porous media, noting that the solid-fluid particle motion is nonuniform along the wave front.

The addition of non-reciprocal solid-fluid interactions was presented in the works of Sahay [157] and Muller [137], where phase velocity of the fast P wave was studied. A comprehensive analysis of wave velocity and attenuation was presented by Zhao *et. al.* [202], where BT results were compared with a simplified form of dCS theory – i.e., the variation in porosity was neglected in the wave equations. In recent works, Gonzalez *et. al.* [76, 75, 77] studied the effect of having the complete fluid stress tensor representation in the dCS theory, highlighting its necessity when dealing with layered domains and high-frequency range.

1.3 Porous Media Numerical Models

Analytical solutions for the BT system of equations have been derived over the years [43, 163, 63], although many simplifications were needed. Therefore, numerical methods to solve the linear coupled system are a widely used alternative [110, 188, 111]. The numerical models vary depending on the adopted main variables; for example, early formulations were derived in terms of the solid and fluid displacements or the solid and relative fluid

displacements [206, 64]. Since the number of unknowns is relatively large for these systems, significantly increasing in two- or three-dimensional simulations, a formulation in terms of solid displacement and fluid pressure is preferred [205, 164]. More specifically, finite element solutions have been derived by Zienkiewicz [205], for instance, and have been used to model a variety of problems, such as dynamic loading [32, 99, 201], wave propagation [86, 79], and fracture propagation [22, 153, 31].

A drawback related to two-field formulations is the assumption that solid and fluid accelerations are the same, which allows the system to be simplified in terms of solid displacement and fluid pressure variables. This assumption limits accuracy when simulating dynamic problems where the relative solid-fluid acceleration is not negligible [206]. Three-field models can consider – additionally to solid displacement and fluid pressure – fluid displacement, fluid velocity, or relative fluid velocity as a main variable. These formulations have been proposed in the context of BT theory, for instance, for consolidation problems [91, 123, 124, 169], three-dimensional models [60], representation of biological tissues [109], and associated with the manifold method [184, 183].

Several authors explored numerical methods to simulate the wave propagation phenomena using the BT framework. Finite difference methods have been employed, for instance, in the context of heterogeneous media [177], viscous materials [156], and explicit time integration schemes [126]. Finite element methods have been employed in the simulation of wave propagation in dynamic response of soils [91, 169], fractured media [31], and cancellous bones [13]. Numerical models for the dCS theory, on the other hand, have been little explored in literature, and are usually related to the investigation of wave propagation.

A numerical model was presented by Quiroga-Goode *et. al.* [151] to investigate the relevance of the dCS fluid viscous dissipation terms; this study, however, does not account for the non-reciprocal solid fluid interactions. The authors expanded their work [152] to analyze the impact of heterogeneity in the model attenuation, and concluded that changes in porosity are enough to enhance the problem attenuation and hence no physical heterogeneity needs to be considered. Gao *et. al.* [65] modeled seismic wave propagation in oil sandstone media using a simplified version of dCS theory, where variation of porosity over time was neglected. The work of Zhao *et. al.* [202] showed a comparison of phase velocity and attenuation obtained through Hickey's [83] system of equations, a framework similar to the dCS model [45, 165]. The authors demonstrated, for a simplified version of the dCS theory, that the velocity and attenuation predicted with both BT and dCS theories are similar unless ultrasonic waves are considered.

1.4 Research Gaps

As it can be seen from the past sections, the BT porous media theory, although commonly employed in analysis and numerical simulations, fails to represent some important phenomena in porous media behaviour – such as variations in porosity and non-reciprocal solid-fluid interactions. The dCS physically-based volume-averaged governing equations lead to a generalized porous media theory. The few existent numerical models are still limited to reciprocal solid-fluid interactions and rely on simplified dCS formulations. Therefore, there is still a lack of a robust dCS numerical framework that accounts for porosity variation, non-reciprocal solid fluid interactions, changes in solid macroscopic shear modulus, and the complete fluid stress tensor.

More specifically, finite element formulations for the dCS theory still need to be developed. A comparison between BT and dCS theories needs to be performed to fully evaluate the contributions of the additional dCS features when compared to BT. The conditions under which the dCS theory could be deemed more useful/accurate (if any) have not been adequately accessed. More to that, the study of wave propagation in dCS theory requires attention, since results at different frequency ranges could digress from BT theory. In this sense, the main research gaps to be tackled in this thesis can be summarized as:

- need of a numerical model for the complete isothermal dCS theory that simulates quasi-steady/transient problems;
- need of a numerical model to study dynamic simulations and wave propagation in the dCS framework;
- need of a detailed study on dCS wave velocity and attenuation patterns and further comparison with BT results;
- need of a dCS numerical model suitable for fluid velocity boundary conditions and study of wave propagation in layered domains.

1.5 Goals and Objectives

The context of porous media theories and numerical developments given in the last section highlighted the need of studying numerical models based on the dCS theory. Having that in mind, the objectives of this thesis are directly related to the research gaps previously presented, and are defined as follows.

1.5.1 Objective 1: Derive and implement a numerical model for the dCS theory in the quasi-steady case

The first objective comprises the derivation of a finite element model based on the dCS theory for the quasi-steady case. The governing equations are written in terms of solid displacement, fluid pressure, and porosity. An advantage of the dCS model compared to the BT theory is the introduction of porosity as an explicit variable. The weak form, semi- and fully-discretized equations are obtained, and a convergence study is performed. The dCS and BT results are compared in one- and two-dimensional problems, highlighting how the BT theory can be considered a specific case of dCS theory under certain simplifications. The non-reciprocal interactions, inherent in the dCS model, lead to distinct curves for solid displacement and fluid pressure. Changes in porosity happen over space and time domains, and are of similar order of the solid strains – showing its relevance in the problem analysis.

This objective is described in Chapter 3 which is based on the article:

B. Campos and R. Gracie, "A FEM for three-field u–p–η poroelasticity with nonreciprocal interactions", *International Journal for Numerical and Analytical Methods in Geomechanics*, vol. 48 (1), p. 332–355, 2024.

1.5.2 Objective 2: Expand the dCS numerical model for dynamic simulations

This second objective focus on the derivation of a dynamic system of equations to represent the dCS porous media description. To this end, inertia (acceleration) terms are now considered into the governing equations, and the system to be solved is written in terms of solid displacement, fluid pressure, and fluid displacement. Fluid and solid accelerations are not necessarily equal, and a coupling inertia term related to the added mass coefficient appears. Similar to the previous objective, the weak form, semi- and fully-discretized equations are obtained, and a convergence study is performed. One- and two-dimensional wave propagation examples are used to show variations in wave patterns due to non-reciprocal interactions. Furthermore, a dimensionless analysis is performed in the dCS equations, showing that the dCS damping terms are only in the same order of the BT damping terms for high fluid viscosity and for small characteristic lengths.

This objective is described in Chapter 4 which is based on the article:

B. Campos and R. Gracie, "A dynamic three-field finite element model for wave propagation in linear elastic porous media". Submitted to *International Journal for Numerical and Analytical Methods in Geomechanics*, May 2024.

1.5.3 Objective 3: Study wave velocity and attenuation patterns in dCS theory

The third objective summarizes the study of the dCS wave equations. A plane wave solution is assumed in the porous media wave equations, and relations in terms of the wavenumber and source frequency are derived. Wave velocity and attenuation for the dCS theory are studied and compared to BT results. Changes in the porosity effective pressure coefficient and in the macroscopic solid shear modulus lead to changes in the P waves behavior. More to that, we show how different material parameters – e.g., fluid dynamic viscosity, intrinsic permeability, initial porosity – affect wave velocity and attenuation in a certain frequency range. Wave patterns for different combinations of solid-fluid constituents are also investigated. At high frequencies, the BT model, accounting for a correction factor, leads to distinct wave patterns than dCS theory.

These findings are presented in Chapter 5 which is based on the article:

B. Campos and R. Gracie, "Wave velocity and attenuation in generalized Biot porous media model". Submitted for publication, September 2024.

1.5.4 Objective 4: Derive a three-field dCS numerical model based on fluid velocity

In the fourth objective the dCS governing equations are written in terms of solid displacement, fluid pressure, and relative fluid velocity. This format is chosen since it facilitates the imposition of fluid flow boundary conditions, commonly found in porous media problems. The weak form, semi- and fully-discretized finite element formulations are presented. One-dimensional examples are used to verify the dCS model implementation against BT results, and to perform convergence studies. dCS model convergence rates are optimal for same-order linear elements. Two-dimensional examples of layered shale-sandstone domains show wave propagation patterns for BT and dCS theories. The results are obtained for low- and high-frequency regime cases, and highlight transmission/reflection wave patterns at material interfaces.

This formulation is presented in Chapter 6 which is based on the article:

B. Campos and R. Gracie, "Fluid velocity finite element formulation for layered porous media domain". Manuscript under preparation, September 2024.

Chapter 2

Numerical Framework of BT and dCS Models

Finite element models to describe porous media behavior can be written in terms of different variables. Over the years, models have been proposed for BT theory and even for simplified versions of dCS theory. In this chapter, we introduce the porous media FE formulations studied in this thesis, highlighting the applicability and assumptions related to each case. The effect of hydro-mechanical coupling on convergence rates is analyzed. Comments on direct integration and mode superposition solution methods are also provided.

A diagram summarizing the FE formulations herein explored is depicted in Figure 2.1. The field variables mentioned are the solid displacement u_s, fluid pressure p, porosity η, fluid displacement u_f, fluid velocity v_f, and fluid velocity relative to the solid w. The diagram also highlights the applicability of the FE models to quasi-steady and dynamic problems.

It is noteworthy that, although these choices of formulations are frequently employed, other alternatives have also been used. One example is the first-order velocity-stress system, commonly employed in wave propagation studies using finite difference schemes [37, 162, 177]. In this case, the main variables are solid velocity, solid stress, and fluid flux. Velocity-stress BT formulations have been used in the context of anisotropic media [200, 203] and seismic wave propagation [125, 5]. Besides the BT model, this framework has also been associated with the Biot-squirt model [28, 191].

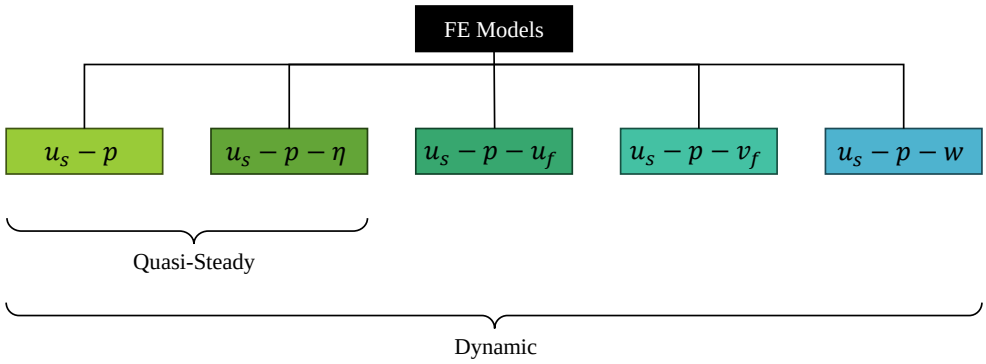


Figure 2.1: Finite element models for porous media simulation addressed in this thesis.

2.1 Two-field Formulations

Two-field formulations, written in terms of solid displacement u_s and fluid pressure p, are the most common way of expressing the porous media equations. They are computationally cheaper than three-field formulations, since the FE mesh results in less degrees of freedom. The $u_s - p$ formulation has been employed, for instance, in the simulation of consolidation problems, where their quasi-steady nature allows one to neglect inertia (acceleration) terms [22, 204, 108, 29].

The $u_s - p$ models have also been utilized in the simulation of dynamic wave propagation problems [99, 107, 111, 188]. In this context, one significant drawback is the fact that, to obtain the two-field system, the relative fluid acceleration is neglected – i.e., we assume that the solid and fluid acceleration are the same. Hence, employing two-field $u_s - p$ formulations in dynamic simulations can lead to loss of accuracy. This system is present in the literature for BT models, and it can be expanded to represent the dCS theory. This step has been computationally implemented and employed in the modal analysis solution reported in Appendix B. For the numerical models detailed in the main scope of this thesis, three-field models were chosen.

2.2 Three-field Formulations

When comparing dCS and BT governing equations, we notice the inclusion of porosity η as a variable in the dCS framework, which is constrained by reciprocal solid-fluid interactions in the BT theory. In this sense, in Chapter 3 a transient $u_s - p - \eta$ dCS formulation is presented, in which we explore the porosity behavior over the problem domain and

throughout the simulation time. This analysis shows how porosity and strains are in the same order of magnitude, and hence the former cannot be ignored. The results of the three-field $u_s - p - \eta$ dCS model are compared to the two-field $u_s - p$ BT model. While it has been shown that BT theory implicitly accounts for porosity variation, it restricts porosity changes to when solid and fluid deform to the same extent.

When the relative fluid acceleration is included, the governing equations cannot be combined into a two-variable system, and thus we retain the fluid displacement alongside solid displacement and fluid pressure variables, originating three-field $u_s - p - u_f$ formulations. Because there is no assumption on the relation between solid and fluid accelerations, this format yields more accuracy for the simulation of dynamic problems such as wave propagation [206, 91, 169]. The $u_s - p - u_f$ dCS formulation for dynamic problems is introduced in Chapter 4, where it is also compared to $u_s - p - u_f$ BT results.

Instead of considering fluid displacement as a variable, three-field formulations have also been explored in terms of fluid velocity v_f and of relative fluid velocity w (with respect to solid velocity). The advantage of $u_s - p - v_f$ and $u_s - p - w$ formulations lies in the fact that the imposition of boundary conditions is more straightforward given that typical porous media problems have velocity (or flux) boundary conditions. The $u_s - p - w$ formulation has been frequently used for BT theory [109, 60, 123, 124, 184] and its dCS equivalent is presented in Chapter 6.

2.3 Solid-fluid Coupling Effect

The coupled system of equations representing porous media models constitute a saddle point problem, and hence it is necessary to ensure that the correspondent solution is unique and independent of the mesh. A well-known condition that is sufficient to ensure such characteristics is the LBB stability condition [11, 21]. The LBB condition [23] is satisfied in two-field formulations by employing, for instance, mixed-order elements – such as Taylor-Hood elements [170]. In this case, linear elements are used for the fluid pressure field, and the solid displacement field is approximated by quadratic elements [22, 64].

In three-field formulations, nonetheless, same-order linear elements have been employed for all fields without numerical locking [206, 91] in BT models. Although stability mathematical proofs in two- and three-fields have been showed for BT theory, they have not been assessed in the context of dCS FE models. Such proofs are also out of the scope of this thesis. Nonetheless, due to the similar structure of the finite element matrices of such theories, we assume that stability requirements in BT models are also applicable to the dCS formulations.

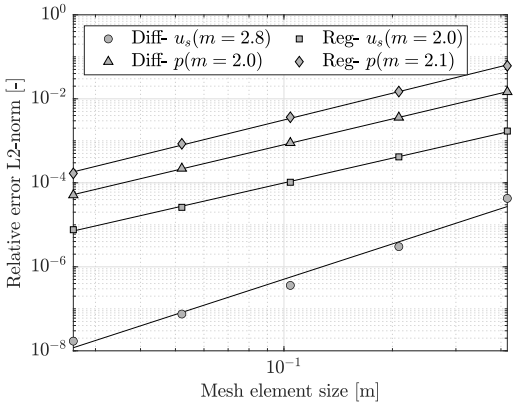
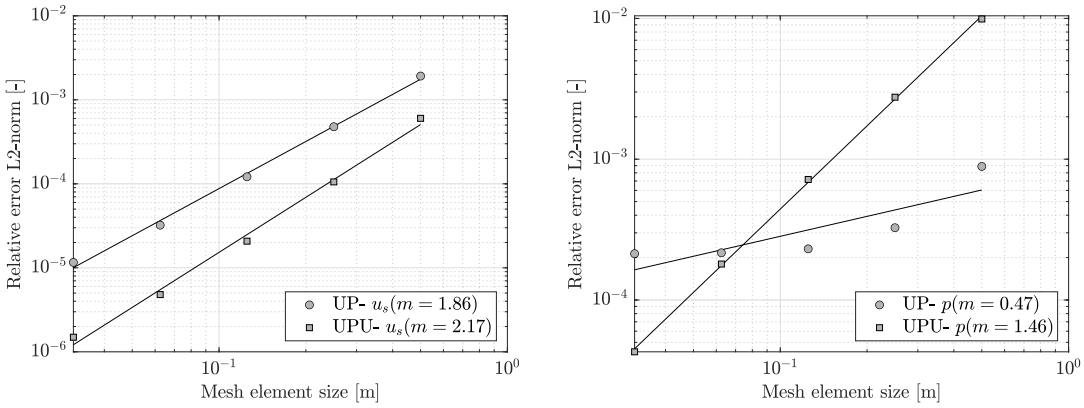


Figure 2.2: Two-field relative error norms for unrealistic material parameters (Diff-) and water-saturated sandstone parameters (Reg-) [193]. The convergence rates m for each field are indicated in the legend. Rates are obtained for the same manufactured solution, geometric and discretization parameters.

Considering mixed-order elements, however, does not ensure a higher convergence rate for the fields with quadratic approximation. Figure 2.2 depicts the convergence of the $u_s - p$ formulation considering (a) unrealistic material parameters and (b) water-saturated sandstone parameters [193]. The water-saturated sandstone example yields the expected convergence rate for the p field, since linear elements are employed. For the u_s field, represented by quadratic elements, a convergence rate of the L2 error norm around $m = 3$ was expected. When the material parameters are altered so that the coupling matrices of the FE system (to be detailed in following chapters) are of much lower order compared to the other matrices, the optimal convergence rate is achieved. Hence, it can be said that convergence rates of porous media FE models are dependent on how strongly coupled the problem is.

Previous to the publications in which this thesis is based, convergence studies on dCS FE models were not reported in literature. Convergence rates for BT models have been presented for same-order elements [101] and for mixed-order elements, although, for the latter, material parameters were not mentioned [138, 139] or randomly chosen [56]. Stability and optimal convergence in BT theory were also proven for split solution methods [102, 128, 127, 38]. Limitations in time convergence for mixed and continuous Galerkin FE method were reported in [145]. Instead of employing mixed-order elements to ensure stability, another strategy is to associate linear-order elements with stabilization techniques [154, 30].

The fact that two-field dynamic formulations are less accurate than three-field models



(a) (b)

Figure 2.3: Dynamic two- and three-field relative error norms for (a) solid displacement and (b) fluid pressure. The convergence rates m for each field are indicated in the legend. Rates are obtained for the same manufactured solution, geometric and discretization parameters.

can also be inferred from their respective convergence rates, as depicted in Figure 2.3. Quadratic elements are considered for the u_s, u_f fields, and linear elements are chosen for the p field. While the optimal convergence rate for quadratic elements is not achieved for both models, the two-field case leads to higher errors.

2.4 FE Solution by Mode Superposition

Modal analysis or mode superposition is an efficient solution method if repetitive analysis of the same configuration are required, if long computing time is necessary, or if the solution can be obtained by a small number of modes [89]. The goal with mode superposition is to transform the equilibrium equations so that the step-by-step solution is computationally cheaper [11]. Appendix B presents a dCS modal analysis based on the two-field $\mathbf{u}_s - p$ system of equations. Due to the form of the three-field matrix systems, the corresponding eigenproblems have zero eigenvalues for the $\eta, \mathbf{u}_f, \mathbf{v}_f, \mathbf{w}$ variables. Mode superposition and direct time integration solution method are shown to yield the same results for one-dimensional test cases.

Chapter 3

Quasi-Steady FE Formulation

3.1 Introduction

In this chapter, the numerical implementation of a finite element model for dCS porous media is proposed. We start by stating the governing equations that, combined, result in a system to be solved in terms of solid displacement, fluid pressure, and porosity. The weak form and the semi- and fully-discrete systems are presented and employed in one- and two-dimensional consolidation problems. The dCS model is compared to the two-field BT model in terms of solid displacement and fluid pressure. We show the similarities and differences between both theories, and highlight how the BT equations can be taken as a specific case of the dCS model. The introduction of a porosity perturbation equation is fundamental in the representation of solid-fluid interactions and consequent determination of porosity changes.

Sections 3.2.1 and 3.2.2 present the governing equations of the two-field BT and three-field dCS theories, whilst Section 3.2.3 compares both and highlights the assumptions required to equate them. The dCS weak formulation is presented in Section 3.2.5, and its finite element formulation is presented in Section 3.3. In Section 3.4, the dCS model is verified through the simulation of a one-dimensional consolidation problem, and a convergence study is performed. In Section 3.5 two-dimensional examples are modeled using the dCS finite element method, confirming the accuracy of the proposed model and showing that the BT model is a specific case of the dCS theory. Additionally, non-reciprocal interactions are studied in both one- and two-dimensional examples. Section 3.7 summarizes the findings of this chapter.

3.2 Poroelasticity Formulations

3.2.1 BT governing equations

Assuming that the only dissipation mechanism is the relative motion between the fluid and solid phases, and neglecting the inertia terms and body forces, the BT equations of motion are [15]

$$\nabla \cdot \boldsymbol{\sigma}_s + \frac{\mu_f \eta_0^2}{\kappa} (\dot{\mathbf{u}}_f - \dot{\mathbf{u}}_s) = 0, \tag{3.1}$$

$$\nabla \cdot \boldsymbol{\sigma}_f - \frac{\mu_f \eta_0^2}{\kappa} (\dot{\mathbf{u}}_f - \dot{\mathbf{u}}_s) = 0, \tag{3.2}$$

in which the divergence of solid and fluid stresses, $\boldsymbol{\sigma}_s$ and $\boldsymbol{\sigma}_f$, are given by

$$\nabla \cdot \boldsymbol{\sigma}_s = N\nabla^2 \mathbf{u}_s + (A+N)\nabla(\nabla \cdot \mathbf{u}_s) + Q\nabla(\nabla \cdot \mathbf{u}_f), \tag{3.3}$$

$$\nabla \cdot \boldsymbol{\sigma}_f = Q\nabla(\nabla \cdot \mathbf{u}_s) + R\nabla(\nabla \cdot \mathbf{u}_f), \tag{3.4}$$

η_0 is the initial porosity of the medium, μ_f is the fluid viscosity, and κ is the intrinsic permeability coefficient. The time-varying terms are the solid and fluid velocities, $\dot{\mathbf{u}}_s$ and $\dot{\mathbf{u}}_f$, respectively. The coefficients A, N are related to the Lamé constants, R is related to the fluid pressure, and Q is related to the solid-fluid coupling [15, 17]. They can be written in terms of more commonly used material elastic constants as in

$$N = \mu, \quad R = \eta_0^2 M, \quad Q = \eta_0(\alpha - \eta_0)M, \quad A = \lambda + \frac{Q^2}{R}, \quad \frac{1}{M} = \frac{\eta_0}{K_f} + \frac{\alpha - \eta_0}{K_s}, \tag{3.5}$$

in which μ is the solid shear modulus, M is the storage coefficient, $\alpha = (Q/R+1)\eta_0$ is the Biot's coefficient, λ is the Lamé constant, and K_f, K_s are the fluid and solid bulk modulus, respectively. The continuity equation for the fluid phase is given by

$$\eta_0 \nabla \cdot (\dot{\mathbf{u}}_s - \dot{\mathbf{u}}_f) + \alpha \nabla \cdot \dot{\mathbf{u}}_s + \frac{\dot{p}}{M} = 0, \tag{3.6}$$

in which p is the fluid pressure. Furthermore, the fluid pressure equation is defined as

$$-\eta_0 \nabla p = Q\nabla(\nabla \cdot \mathbf{u}_s) + R\nabla(\nabla \cdot \mathbf{u}_f), \tag{3.7}$$

which, when compared to the divergence of fluid stress in (3.4), confirms that the fluid stress is only dependent on the fluid pressure, and viscous dissipation within the fluid is not included. In the $u_s - p$ system, solid strain is assumed to be small.

As previously mentioned, the numerical solution of poroelasticity problems can be obtained in terms of different variables. In this chapter, the BT governing equations are written in terms of solid displacement and fluid pressure $\mathbf{u}_s - p$, suitable for quasi-steady simulations. The first equation of the $\mathbf{u}_s - p$ coupled system is obtained by summing up the equations of motion (3.1) and (3.2). For the second equation, the divergence of fluid stress in the fluid equation of motion (3.2) is written in terms of pressure as $\nabla \cdot \boldsymbol{\sigma}_f = -\eta_0 \nabla p$ and the fluid displacement term is isolated as in

$$\dot{\mathbf{u}}_f = -\frac{\kappa}{\mu_f \eta_0} \nabla p + \dot{\mathbf{u}}_s, \tag{3.8}$$

and replaced into the pressure equation (3.7)

$$\begin{aligned} \eta_0 \nabla \dot{p} - Q \nabla (\nabla \cdot \dot{\mathbf{u}}_s) - R \nabla (\nabla \cdot \mathbf{u}_f) = 0, \\ \eta_0 \nabla \dot{p} - Q \nabla (\nabla \cdot \dot{\mathbf{u}}_s) - R \nabla \left[\nabla \cdot \left(-\frac{\kappa}{\mu_f \eta_0} \nabla p + \dot{\mathbf{u}}_s \right) \right] = 0, \end{aligned} \tag{3.9}$$

and, after rearranging the terms, the following system is obtained

$$\begin{cases} \nabla \cdot \boldsymbol{\tau} = 0, \\ -\dfrac{\kappa}{\mu_f} \nabla^2 p + \alpha \nabla \cdot \dot{\mathbf{u}}_s + \dfrac{1}{M} \dot{p} = 0, \end{cases} \tag{3.10}$$

in which the total stress $\boldsymbol{\tau} = \boldsymbol{\sigma}_s + \boldsymbol{\sigma}_f$ can be written as a sum of the effective stress $\boldsymbol{\sigma}$ (depending only on solid deformation) and the pore pressure p as in

$$\boldsymbol{\tau} = \boldsymbol{\sigma}_s + \boldsymbol{\sigma}_f = \boldsymbol{\sigma} - \alpha \mathbf{m} p, \tag{3.11}$$

where $\mathbf{m} = [1, 1, 0]^\top$ is a mapping vector [205].

3.2.2 dCS governing equations

In contrast to Biot's approach, the dCS theory [44, 45] begins with the assumption that the governing equations are valid at the pore scale (i.e., the defined REV), and are then extended to the whole domain by employing a volume averaging technique [178]. The volume-averaged momentum equations of the solid matrix and fluid are given by [165]

$$(1 - \eta_0) \nabla \cdot \boldsymbol{\sigma}_s + \frac{\mu_f \eta_0^2}{\kappa} (\dot{\mathbf{u}}_f - \dot{\mathbf{u}}_s) = 0, \tag{3.12}$$

$$\eta_0 \nabla \cdot \boldsymbol{\sigma}_f - \frac{\mu_f \eta_0^2}{\kappa} (\dot{\mathbf{u}}_f - \dot{\mathbf{u}}_s) = 0, \tag{3.13}$$

and the divergence of the averaged solid $\boldsymbol{\sigma}_s$ and fluid $\boldsymbol{\sigma}_f$ stresses are given by

$$(1-\eta_0)\nabla\cdot\boldsymbol{\sigma}_s = \mu_M\nabla^2\mathbf{u}_s + (1-\eta_0)\left[K_s + \frac{\mu_M}{3}\right]\nabla(\nabla\cdot\mathbf{u}_s) - K_s\nabla\eta, \tag{3.14}$$

$$\eta_0\cdot\boldsymbol{\sigma}_f = \eta_0 K_f\nabla(\nabla\cdot\mathbf{u}_f) + K_f\nabla\eta + \eta_0\mu_f\nabla^2\dot{\mathbf{u}}_f + \eta_0\left(\xi_f + \frac{\mu_f}{3}\right)\nabla\left(\nabla\cdot\dot{\mathbf{u}}_f\right) + \xi_f\nabla\dot{\eta} + (1-\eta_0)\mu_f\left(\frac{\mu_M}{(1-\eta_0)\mu_s} - 1\right)\left[\nabla^2\dot{\mathbf{u}}_s + \frac{1}{3}\nabla\left(\nabla\cdot\dot{\mathbf{u}}_s\right)\right]. \tag{3.15}$$

in which μ_M is a macroscopic solid shear modulus given by $\mu_M = (1-\eta_0)\mu_s(1-\delta_\mu)$ and δ_μ is a dimensionless parameter, ξ_f is the fluid bulk viscosity, and η is the porosity variable. There is a correspondence between the stresses definitions from both theories, which can be noted as the first two right-hand side terms are similar to those from BT (3.1). Furthermore, the porosity term has a correspondence with the fluid displacement term. This correlation will be clarified in upcoming sections.

The continuity equation for the solid and fluid components are, respectively,

$$\frac{\rho_s - \rho_s^0}{\rho_s^0} - \frac{\eta-\eta_0}{1-\eta_0} + \nabla\cdot\mathbf{u}_s = 0, \tag{3.16}$$

$$\frac{1}{\rho_f^0}\dot{\rho_f} + \frac{1}{\eta_0}\dot{\eta} + \nabla\cdot\dot{\mathbf{u}}_f = 0, \tag{3.17}$$

in which ρ_s^0 and ρ_f^0 are the initial densities of the solid and fluid, respectively; ρ_s and ρ_f are time-dependent counterparts. A continuity equation for the solid phase is not presented in the Biot theory framework; however, it is implied when matrix deformations are compatible. Similarly to the BT system, in the dCS $u_s - p - \eta$ system the solid strain is assumed to be small. The fluid continuity equation from BT and dCS theories can be equated when using the porosity equation.

The pressure equations for the solid and fluid are given by

$$\frac{p_s}{K_s} = -\nabla\cdot\mathbf{u}_s + \frac{\eta-\eta_0}{1-\eta_0}, \tag{3.18}$$

$$\frac{1}{K_f}\dot{p} = -\nabla\cdot\dot{\mathbf{u}}_f - \frac{1}{\eta_0}\dot{\eta}. \tag{3.19}$$

where p_s is the solid pressure.

The first two terms on the right-hand side in equation (3.15) correspond to the averaged fluid pressure; thus, the subsequent terms in (3.15) represent the viscous dissipation neglected in the BT theory. To complete the system of equations necessary to determine

all unknowns, an additional constitutive equation must be introduced. When the porous media is deformed, the fluid and solid phases might change in different proportions and, therefore, introduce changes in porosity. Hence, a linear constitutive equation relating the porosity variation to the deformation of the components is adopted [85, 165]

$$\dot{\eta} = \delta_s \nabla \cdot \dot{\mathbf{u}}_s - \delta_f \nabla \cdot \dot{\mathbf{u}}_f, \tag{3.20}$$

in which δ_s and δ_f are the solid and fluid compliance coefficients [151] that act as weighting parameters for the impact of solid and fluid volumetric strains. These dimensionless parameters were defined by Hickey et. al. [85] in terms of macroscopic compressibilities of the medium, which can be obtained through laboratory experiments. These are valid, however, only for low-frequency wave propagation, and need to be experimentally determined for different problem configurations and materials [152]. For certain compliance parameters, the porosity equation can be substituted into the previous momentum and continuity equations so that one can return to the Biot framework.

It is possible to obtain a coupled system in terms of solid displacement, fluid pressure, and porosity, assuming that solid and fluid components have constant densities. For that purpose, the first equation in the system is given by the summation of the solid and fluid equations of motion, leading to a total stress given by $\boldsymbol{\tau} = (1-\eta_0)\nabla \cdot \boldsymbol{\sigma}_s + \eta_0 \nabla \cdot \boldsymbol{\sigma}_f$. The second equation is obtained by isolating the fluid displacement term in (3.17) and replacing it into the pressure equation (3.19). Finally, the third equation comes from the substitution of the fluid displacement term from (3.17) into the porosity equation (3.20), yielding

$$\begin{cases} \nabla \cdot \boldsymbol{\tau} = 0, \\ -\dfrac{\kappa}{\mu_f}\nabla^2 p + \eta_0 \nabla \cdot \dot{\mathbf{u}}_s + \dfrac{\eta_0}{K_f}\dot{p} + \dot{\eta} = 0, \\ \dot{\eta} + (\delta_f - \delta_s)\nabla \cdot \dot{\mathbf{u}}_s - \dfrac{\delta_f}{\eta_0}\dfrac{\kappa}{\mu_f}\nabla^2 p = 0. \end{cases} \tag{3.21}$$

3.2.3 Comparison between BT and dCS formulations

By establishing a specific multiplicative form for the energy potential as a starting point for the development of the porous media equations, Biot theory implies that there is a reciprocity between the stresses of both phases. The elastic energy potential is assumed to be dependent on both displacement and pressure fields [14, 15], as in

$$U = U(\epsilon_s, \zeta), \tag{3.22}$$

where ϵ_s is the solid volumetric strain, ζ is the variation in fluid content, and the stresses are written as

$$\sigma_{ij} = \frac{\partial U}{\partial \varepsilon_{s,ij}}, \qquad p = \frac{\partial U}{\partial \zeta}. \tag{3.23}$$

However, an alternative form of the energy potential, such as the additive form, is commonly adopted in multi-body dynamics [46, 34]. Müller [134] mentions, based on the work of de la Cruz [46], that solid and fluid fields have two different energy potentials U_s, U_f, and that the total energy of the porous media can be written as

$$U = \underbrace{(1-\eta_0)\sigma_{s,ij}\varepsilon_{s,ij} - \eta_0 p \varepsilon_{f,ll}}_{\text{bulk energy}} + \underbrace{(p-p_s)(\eta-\eta_0)}_{\text{pore-interface energy}}. \tag{3.24}$$

In this sense, the change in porosity is implicitly defined in a restrictive way in BT in terms of macroscopic fluid and solid strain. On the other hand, the dCS theory considers the porosity as a primary variable. Furthermore, the definition of the fluid stress in the dCS approach in (3.14) includes the dissipation effects due to viscous mechanisms within the fluid [45, 151, 157]. Despite the differences between the theories, it is possible to show that BT formulation can be taken as a specific case of dCS theory (i.e., the systems of equations (3.10) and (3.21) can be equated) when the following assumptions are made:

(i) The terms in the fluid stress related to viscous dissipation within the fluid are neglected, leaving only $\nabla \cdot \boldsymbol{\sigma}_f = -\nabla p$ in equation (3.15). This assumption holds, for example, by assuming the fluid has very low viscosity;

(ii) The stresses from the BT approach are an averaged value of the pore-scale stresses presented in the dCS theory, as in

$$\boldsymbol{\sigma}_s^{BT} = (1-\eta_0)\boldsymbol{\sigma}_s^{dCS}, \qquad \boldsymbol{\sigma}_f^{BT} = \eta_0 \boldsymbol{\sigma}_f^{dCS}, \tag{3.25}$$

(iii) There is a correspondence between the material parameters given by [44, 45]

$$N = (1-\eta_0)\mu_s(1-\delta_\mu), \tag{3.26a}$$
$$Q = K_f\delta_s = K_s\delta_f, \tag{3.26b}$$
$$R = \eta_0 K_f(1-\frac{\delta_f}{\eta_0}), \tag{3.26c}$$
$$A = (1-\eta_0-\delta_s)K_s - \frac{2}{3}(1-\eta_0)\mu_s(1-\delta_\mu); \tag{3.26d}$$

(iv) The solid and fluid compliances, δ_s and δ_f, are defined so that we return to the implicit form of the porosity equation in BT theory [44, 45]. Given the correspondence between materials in (3.26), this leads to

$$\frac{\delta_f^{BT}}{\delta_s^{BT}} = \frac{K_f}{K_s}, \tag{3.27}$$

and $\delta_s^{BT}, \delta_f^{BT}$ can be obtained through [157, 134] [1]

$$\delta_s^{BT} = \frac{Q}{K_f} = \frac{\eta_0(\alpha-\eta_0)}{K_f\left(\dfrac{\eta_0}{K_f}+\dfrac{\alpha-\eta_0}{K_s}\right)}, \qquad \delta_f^{BT} = \frac{Q}{K_s} = \frac{\eta_0(\alpha-\eta_0)}{K_s\left(\dfrac{\eta_0}{K_f}+\dfrac{\alpha-\eta_0}{K_s}\right)}; \tag{3.28}$$

(v) The constant δ_μ in the macroscopic shear modulus μ_M is zero, meaning that $\mu_M = \mu = (1-\eta_0)\mu_s$. The parameter δ_μ in the dCS model appears in the solid-fluid interface terms obtained through the volume-averaging technique.

When comparing the stress forms in the BT and dCS theories, it is noteworthy that whilst the solid and fluid stresses are obtained in different ways, the total stress relation in (3.11) is maintained, where the averaged effective stress term $\boldsymbol{\sigma}$ is given by

$$\boldsymbol{\sigma} = 2\mu\nabla\mathbf{u}_s + \mathbf{I}\lambda\nabla\cdot\mathbf{u}_s \tag{3.29}$$

and, for numerical implementation purposes, its Voigt form can be expressed as

$$\boldsymbol{\sigma} = \begin{Bmatrix}\sigma_{xx}\\ \sigma_{yy}\\ \sigma_{xy}\end{Bmatrix} = \begin{bmatrix}2\mu+\lambda & \lambda & 0\\ \lambda & 2\mu+\lambda & 0\\ 0 & 0 & \lambda\end{bmatrix}\begin{Bmatrix}\varepsilon_{xx}\\ \varepsilon_{yy}\\ 2\varepsilon_{xy}\end{Bmatrix} \tag{3.30}$$

for a two-dimensional problem, where ε_{ij} are the effective strains dependent only on the solid displacement. Details on the derivation of $\boldsymbol{\sigma}$ and the full correlation between the BT and dCS stresses can be found in Appendix A.

[1] These expressions for δ_s, δ_f are adapted from de la Cruz and Spanos [45] to account for $\alpha \neq 1$, and they are obtained using the definitions of Q and M in (3.5).

3.2.4 Generalization of the porosity equation: variation under non-reciprocal interactions

The unique energy potential in BT theory leads to a simplification in the governing equations and therefore reduction in the number of elastic constants [14, 24]. The Biot coefficient α is taken to be the same as the effective pressure coefficient α^*; while α indicates the change in fluid volume caused by changes in bulk volume for the drained condition, α^* represents the change in confining pressure with respect to changes in fluid pressure at constant bulk volume. Hence, the term reciprocal interactions refer to the assumption that $\alpha = \alpha^*$.

By generalizing the energy potential into the additive form, separating fluid and solid contributions, the assumption $\alpha = \alpha^*$ is removed and thus the constituents are allowed to deform independently of each other. These are called non-reciprocal interactions, as proposed by Sahay [157]. In such generalization an additional parameter, named the porosity effective pressure coefficient n, is introduced into the porosity equation coefficients (3.28) as

$$\delta_s = (\alpha - \eta_0)\frac{\eta_0 M^*}{K_f}, \qquad \delta_f = (\alpha - \eta_0)\frac{\eta_0 M^*}{K_s} n, \tag{3.31}$$

where M^* is a modified storage coefficient defined as

$$\frac{1}{M^*} = \frac{1}{M} - (1 - n)\frac{\alpha - \eta_0}{K_s}. \tag{3.32}$$

By adding the n coefficient to the porosity equation, it is possible to obtain interactions in which solid and fluid have different contributions to the change in porosity. According to Sahay [157], a valid range of n can be obtained based on the physically acceptable limits of the bulk modulus, and it is comprised within the interval $0 \leq n \leq K_s/K_f$. The lower bound $n_{min} = 0$ indicates that the fluid does not affect the porosity (and hence $\delta_f = 0$), while the upper bound $n_{max} = K_s/K_f$ leads to no porosity changes (meaning that $\delta_f = \delta_s$). Further studies [136, 137] showed, based on quasi-steady experimental data, that n is dependent on the solid properties and solid and fluid pressures, likely varying around 1 for water-saturated rocks. By assuming $n = 1$, the porosity perturbation equation returns to the form implicitly present in Biot theory. In this case, both phases are assumed to be homogeneous at pore scale, hence limiting the applicability range of the theory.

Non-reciprocal solid-fluid interactions indicate situations where energy concentration happens in different parts of the solid-fluid bulk or material interface. Nonetheless, overall equilibrium is still achieved. Expressions of n validated with quasi-steady simulations have

been derived in terms of α, α^*, and η_0 [133, 136, 137]. Specifically for the upper limit n_{max}, Sahay & Muller [157, 134] highlighted how it would represent a response to a sudden load. Since it is not a state of equilibrium, the system would still reach equilibrium after some time and thus the correspondent value of n would also change.

3.2.5 Weak form of dCS model

The dCS coupled system of equations (3.21) can be transformed into a Galerkin weak formulation by using weight functions $\delta\mathbf{u}, \delta p, \delta\eta$ and integrating the equations over a domain Ω with boundary Γ. The latter is composed by the sets $\Gamma_u, \Gamma_t, \Gamma_p, \Gamma_q$ referring to the surfaces with prescribed displacement, traction, pressure, and flux, respectively; the essential boundary conditions are applied to Γ_u and Γ_p. Assuming appropriate function spaces for the displacement, pressure, porosity fields, and the respective weight functions, the weak form of the dCS set of equations is given by

$$\int_\Omega (\nabla\delta\mathbf{u}_s)^\top \boldsymbol{\sigma}\, d\Omega - \alpha \int_\Omega (\nabla\delta\mathbf{u}_s)^\top \mathbf{m} p\, d\Omega - \int_{\Gamma_t} \delta\mathbf{u}_s^\top \bar{\mathbf{t}}\, d\Gamma_t = 0, \tag{3.33a}$$

$$\frac{\kappa}{\mu_f}\int_\Omega (\nabla\delta p)^\top \nabla p\, d\Omega - \int_{\Gamma_q} \delta p\, \bar{q}\, d\Gamma_q + \eta_0 \int_\Omega \delta p (\nabla\cdot\dot{\mathbf{u}}_s)\, d\Omega + \frac{\eta_0}{K_f}\int_\Omega \delta p\, \dot{p}\, d\Omega + \int_\Omega \delta p\, \dot{\eta}\, d\Omega = 0, \tag{3.33b}$$

$$\int_\Omega \delta\eta\, \dot{\eta}\, d\Omega + (\delta_f - \delta_s)\int_\Omega \delta\eta\, (\nabla\cdot\dot{\mathbf{u}}_s)\, d\Omega + \frac{\delta_f}{\eta_0}\frac{\kappa}{\mu_f}\int_\Omega (\nabla\delta\eta)^\top \nabla p\, d\Omega - \frac{\delta_f}{\eta_0}\frac{\kappa}{\mu_f}\int_{\Gamma_q} \delta\eta\, \bar{q}\, d\Gamma_t = 0, \tag{3.33c}$$

where $\bar{\mathbf{t}}$ is the prescribed traction on Γ_t and $\bar{q}$ is the prescribed flux on Γ_q. When compared to the BT weak formulation, the porosity term in (3.33b) is not present, the coefficients of the remaining terms are changed, and the porosity variation is implicitly considered in the constituents stresses.

3.3 Finite Element Formulation

The discretization in space of the weak forms obtained in (3.33) is made by approximating the unknowns with the following interpolation

$$\mathbf{u}_s = \mathbf{N}_s\hat{\mathbf{u}}, \qquad \mathbf{p} = \mathbf{N}_p\hat{\mathbf{p}}, \qquad \boldsymbol{\eta} = \mathbf{N}_\eta\hat{\boldsymbol{\eta}}, \tag{3.34}$$

where $\mathbf{N}_s, \mathbf{N}_p, \mathbf{N}_\eta$, are the Lagrangian shape functions, and $\hat{\mathbf{u}}_s, \hat{\mathbf{p}}, \hat{\boldsymbol{\eta}}$ are the nodal displacement vectors. To ensure a stabilized FE formulation, linear elements are employed for the pressure and porosity fields while quadratic elements are considered for the solid displacement field [22, 64, 123]. It is noteworthy that we have adopted mixed-order Taylor-Hood elements [170] because they are known to satisfy the LBB stability condition [23] for the BT theory. We have not proven that the dCS model with Taylor-Hood elements satisfies the LBB conditions; however, we have not observed evidence of LBB instabilities. The semi-discrete system of equations for the dCS theory are given by

$$\begin{cases} \mathbf{K}_{ss}^{dCS}\hat{\mathbf{u}}_s - \mathbf{K}_{sp}^{dCS}\hat{\mathbf{p}} = \mathbf{f}_s, \\ \mathbf{K}_{ps}^{dCS}\dot{\hat{\mathbf{u}}}_s + \mathbf{K}_{pp}^{dCS}\hat{\mathbf{p}} + \mathbf{S}^{dCS}\dot{\hat{\mathbf{p}}} + \mathbf{K}_{p\eta}^{dCS}\dot{\hat{\boldsymbol{\eta}}} = \mathbf{f}_p, \\ \mathbf{K}_{\eta u}^{dCS}\dot{\hat{\mathbf{u}}}_s + \mathbf{K}_{\eta p}^{dCS}\hat{\mathbf{p}} + \mathbf{K}_{\eta\eta}^{dCS}\dot{\hat{\boldsymbol{\eta}}} = \mathbf{f}_\eta; \end{cases} \tag{3.35}$$

they can be compared to the correspondent system of equations for the BT theory, which consists in

$$\begin{cases} \mathbf{K}_{ss}^{BT}\hat{\mathbf{u}}_s - \mathbf{K}_{sp}^{BT}\hat{\mathbf{p}} = \mathbf{f}_s, \\ \mathbf{K}_{ps}^{BT}\dot{\hat{\mathbf{u}}}_s + \mathbf{K}_{pp}^{BT}\hat{\mathbf{p}} + \mathbf{S}^{BT}\dot{\hat{\mathbf{p}}} = \mathbf{f}_p. \end{cases} \tag{3.36}$$

The matrices for the BT model in (3.36) are

$$\mathbf{K}_{ss}^{BT} = \int_\Omega \mathbf{B}_s^\top \mathbf{D}\mathbf{B}_s \; d\Omega, \tag{3.37}$$

$$\mathbf{K}_{sp}^{BT} = \alpha \int_\Omega \mathbf{B}_s^\top \mathbf{m}\mathbf{N}_p \; d\Omega, \tag{3.38}$$

$$\mathbf{K}_{ps}^{BT} = (\mathbf{K}_{sp}^{BT})^\top, \tag{3.39}$$

$$\mathbf{K}_{pp}^{BT} = \frac{\kappa}{\mu_f}\int_\Omega \mathbf{B}_p^\top \mathbf{B}_p \; d\Omega, \tag{3.40}$$

$$\mathbf{S}^{BT} = \frac{1}{M}\int_\Omega \mathbf{N}_p^\top \mathbf{N}_p \; d\Omega, \tag{3.41}$$

where the $\mathbf{D}$ matrix in (3.37) is the constitutive matrix for linear elasticity problems relating stresses and strains defined in (3.30); the $\mathbf{B}$ matrices contain the derivatives of the shape functions $\mathbf{N}$. For the dCS equations in (3.35), the matrices are defined as

$$\mathbf{K}_{ss}^{dCS} = \mathbf{K}_{ss}^{BT} \tag{3.42}$$

$$\mathbf{K}_{sp}^{dCS} = \mathbf{K}_{sp}^{BT} \tag{3.43}$$

$$\mathbf{K}_{pp}^{dCS} = \mathbf{K}_{pp}^{BT} \tag{3.44}$$

$$\mathbf{K}_{ps}^{dCS} = \eta_0 \int_\Omega \mathbf{N}_p^\top \mathbf{B}_s \; d\Omega \tag{3.45}$$

$$\mathbf{S}^{dCS} = \frac{\eta_0}{K_f}\int_\Omega \mathbf{N}_p^\top \mathbf{N}_p \; d\Omega \tag{3.46}$$

$$\mathbf{K}_{p\eta}^{dCS} = \int_\Omega \mathbf{N}_p^\top \mathbf{N}_\eta \; d\Omega \tag{3.47}$$

$$\mathbf{K}_{\eta s}^{dCS} = (\delta_f - \delta_s)\int_\Omega \mathbf{N}_\eta^\top \mathbf{B}_s \; d\Omega \tag{3.48}$$

$$\mathbf{K}_{\eta p}^{dCS} = \frac{\delta_f}{\eta_0}\frac{\kappa}{\mu_f}\int_\Omega \mathbf{B}_\eta^\top \mathbf{B}_p \; d\Omega \tag{3.49}$$

$$\mathbf{K}_{\eta\eta}^{dCS} = \int_\Omega \mathbf{N}_\eta^\top \mathbf{N}_\eta \; d\Omega \tag{3.50}$$

The load and flux vectors are given by

$$\mathbf{f}_s = \int_{\Gamma_t} \mathbf{N}_s^\top \bar{\mathbf{t}} \; d\Gamma_t, \qquad \mathbf{f}_p = -\int_{\Gamma_q} \mathbf{N}_p^\top \bar{q} d\Gamma_q, \qquad \mathbf{f}_\eta = -\int_{\Gamma_q} \mathbf{N}_\eta^\top \bar{q} d\Gamma_q. \tag{3.51}$$

For the discretization in time, a Backward Euler fully implicit scheme [89] is used. The fully discretized system for the dCS model is given by

$$\begin{bmatrix} \hat{\mathbf{K}}_{ss}^{dCS} & \hat{\mathbf{K}}_{sp}^{dCS} & \mathbf{0} \\ \hat{\mathbf{K}}_{ps}^{dCS} & \hat{\mathbf{K}}_{pp}^{dCS} & \hat{\mathbf{K}}_{p\eta}^{dCS} \\ \hat{\mathbf{K}}_{\eta s}^{dCS} & \hat{\mathbf{K}}_{\eta p}^{dCS} & \hat{\mathbf{K}}_{\eta\eta}^{dCS} \end{bmatrix} \begin{Bmatrix} \hat{\mathbf{u}}_s^{n+1} \\ \hat{\mathbf{p}}^{n+1} \\ \hat{\boldsymbol{\eta}}^{n+1} \end{Bmatrix} = \begin{Bmatrix} \hat{\mathbf{f}}_s^{n+1} \\ \hat{\mathbf{f}}_p^{n+1} \\ \hat{\mathbf{f}}_\eta^{n+1} \end{Bmatrix}, \tag{3.52}$$

which can be compared to the BT model as in

$$\begin{bmatrix} \hat{\mathbf{K}}_{ss}^{BT} & \hat{\mathbf{K}}_{sp}^{BT} \\ \hat{\mathbf{K}}_{ps}^{BT} & \hat{\mathbf{K}}_{pp}^{BT} \end{bmatrix} \begin{Bmatrix} \hat{\mathbf{u}}_s^{n+1} \\ \hat{\mathbf{p}}^{n+1} \end{Bmatrix} = \begin{Bmatrix} \hat{\mathbf{f}}_s^{n+1} \\ \hat{\mathbf{f}}_p^{n+1} \end{Bmatrix}. \tag{3.53}$$

The matrices for the dCS fully discrete system in (3.52) are given by

$$\hat{\mathbf{K}}_{uu} = \Delta t \mathbf{K}_{uu}^{dCS} \tag{3.54}$$

$$\hat{\mathbf{K}}_{up} = -\Delta t \mathbf{K}_{up}^{dCS} \tag{3.55}$$

$$\hat{\mathbf{K}}_{pu} = \mathbf{K}_{pu}^{dCS} \tag{3.56}$$

$$\hat{\mathbf{K}}_{pp} = \Delta t \mathbf{K}_{pp}^{dCS} + \mathbf{S}^{dCS} \tag{3.57}$$

$$\hat{\mathbf{K}}_{p\eta} = \mathbf{K}_{p\eta}^{dCS} \tag{3.58}$$

$$\hat{\mathbf{K}}_{\eta u} = \mathbf{K}_{\eta u}^{dCS} \tag{3.59}$$

$$\hat{\mathbf{K}}_{\eta p} = \Delta t \mathbf{K}_{\eta p}^{dCS} \tag{3.60}$$

$$\hat{\mathbf{K}}_{\eta\eta} = \mathbf{K}_{\eta\eta}^{dCS} \tag{3.61}$$

$$\hat{\mathbf{f}}_u^{n+1} = \Delta t \mathbf{f}_u^{n+1} \tag{3.62}$$

$$\hat{\mathbf{f}}_p^{n+1} = \mathbf{K}_{pu}^{dCS} \hat{\mathbf{u}}^n + \mathbf{S}^{dCS} \hat{\mathbf{p}}^n + \mathbf{K}_{p\eta} \hat{\boldsymbol{\eta}}^n + \Delta t \mathbf{f}_p^{n+1} \tag{3.63}$$

$$\hat{\mathbf{f}}_\eta^{n+1} = \mathbf{K}_{\eta u} \hat{\mathbf{u}}^n + \mathbf{K}_{\eta\eta} \hat{\boldsymbol{\eta}}^n + \Delta t \mathbf{f}_\eta^{n+1} \tag{3.64}$$

and for the BT fully discrete system in (3.53) the correspondent matrices are

$$\hat{\mathbf{K}}_{uu} = \Delta t \mathbf{K}_{uu}^{BT} \tag{3.65}$$

$$\hat{\mathbf{K}}_{up} = -\Delta t \mathbf{K}_{up}^{BT} \tag{3.66}$$

$$\hat{\mathbf{K}}_{pu} = \mathbf{K}_{pu}^{BT} \tag{3.67}$$

$$\hat{\mathbf{K}}_{pp} = \Delta t \mathbf{K}_{pp}^{BT} + \mathbf{S}^{BT} \tag{3.68}$$

$$\hat{\mathbf{f}}_u^{n+1} = \Delta t \mathbf{f}_u^{n+1} \tag{3.69}$$

$$\hat{\mathbf{f}}_p^{n+1} = \mathbf{K}_{pu}^{BT} \hat{\mathbf{u}}^n + \mathbf{S}^{BT} \hat{\mathbf{p}}^n + \Delta t \mathbf{f}_p^{n+1} \tag{3.70}$$

3.4 Verification and Convergence Study

3.4.1 Verification with Biot model

An initial study is carried out to verify the validity of the proposed numerical method for the dCS model. A one-dimensional consolidation problem is studied, in which the material parameters listed in Table 3.1 are taken from Boone and Ingraffea [22]. The column length is taken as $L = 6\text{m}$ with a unit cross sectional area. For the boundary conditions, the column displacement is fixed at the bottom ($x = 6\text{m}$) and a compression load of $\bar{t} = 1$ kPa is applied at the top ($x = 0\text{m}$); the column is assumed to be impervious at the bottom and drained at the top ($p = 0$).

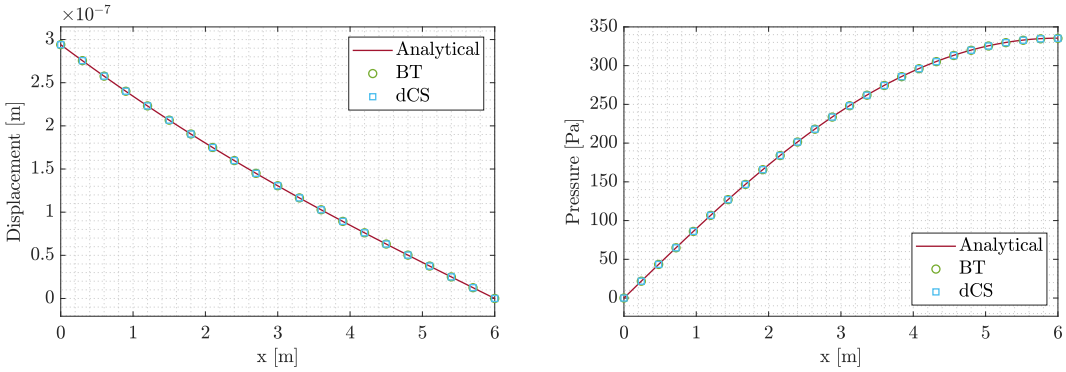
Table 3.1: Material parameters [22] for the column consolidation verification study.

Parameter	Value	Unit	Parameter	Value	Unit
μ	6	GPa	K_f	3	GPa
ν	0.2	-	K_s	36	GPa
κ	2×10^{-14}	m^2	η_0	0.19	-
μ_f	10^{-12}	GPa $\cdot$ s	δ_s	0.5977	-
α	1	-	δ_f	0.0498	-

The column geometry is discretized into $ne = 100$ elements, and a time step of $\Delta t = 0.1\text{s}$ is used. The total simulation time is $t_{end} = 600\text{s}$. Figure 3.1 shows the variation in displacement and pressure over the column depth for both theories at an early simulation time of $t = 10\text{s}$, which are compared to an analytical solution for the Terzaghi's consolidation problem [60]. Both numerical approximations lead to the same results, and these are in agreement with the analytical solution. Figure 3.2 depicts the evolution of the displacement and pressure distribution in the domain over the total simulation time. The displacement field tends to a linear distribution over depth. Meanwhile, the pressure reaches a peak value after the sudden load application, and it dissipates over time to stabilize at zero. The pressure plots herein presented refer to the variation of such field; for the total pressure, one can expect a linear behavior along the column depth.

Furthermore, Fig. 3.3a shows the normalized change in porosity $(\eta - \eta_0)/\eta_0$ along the domain at t_{end}, whilst Fig. 3.3b depicts the normalized change in porosity over time; both plots refer to the case where $n = 1$, i.e., equivalent to the BT model. It is noticeable that there is an oscillation in the porosity at the top of the column which is still present at t_{end}, when the simulation has already reached an steady state. This perturbation is caused

by the sudden application of the load at the first step; since there is no natural damping for η in the weak form (3.33)c, such initial perturbation is carried out throughout the simulation time. Figure 3.4 shows the porosity variation and the solid strain variation over the column depth; for visualization purposes, the results at the first 0.4m of the column are not included, where the porosity oscillation is present. It is noticeable that, although the variation in porosity seem to be small at first sight, in the order of 10^{-6}, the solid strain is in the order of 10^{-7}, yielding that porosity changes are relevant in the context of the problem behavior.

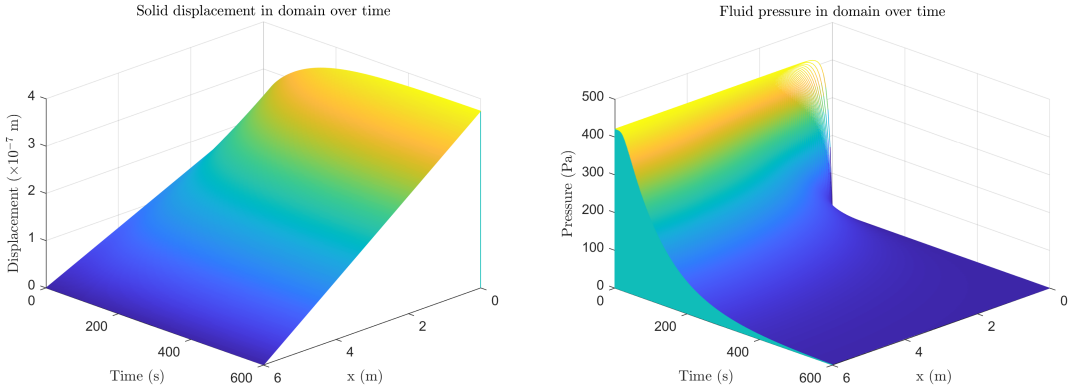


(a) Solid displacement at $t = 10$s (b) Fluid pressure at $t = 10$s

Figure 3.1: Comparison of displacement (left) and pressure (right) changes from dCS and BT models and an analytical solution for the one-dimensional consolidation problem.

To verify the impact of the porosity effective pressure coefficient introduced in Section 3.2.4, different values of n are adopted for the column consolidation problem. Figure 3.5 shows the results for displacement and pressure variables for various n. The minimum and maximum values of n show significant discrepancy from $n = 1$ (equivalent to BT theory). Small variations in n, however, yield almost the same results as $n = 1$. Since the range of n is established solely based on physically acceptable boundaries, these can be very conservative. More to that, n can assume different values depending on the system behavior under sudden load application, and thus n values might change throughout the simulation.

When $n = 0$, the fluid pressure has no effect on the boundary movements, hence it is concentrated in the bulk region. This leads to an increase in the bulk fluid pressure (see total energy relation in (3.24)) when compared to $n = 1$, as seen in Fig. 3.5b. At the same time, since the solid deformation is the only responsible for pore boundary movements, its contribution to the bulk potential energy decreases (Fig. 3.5a). More generally, for $n < 1$



(a) Solid displacement at $t = 600$s (b) Fluid pressure at $t = 600$s

Figure 3.2: Variation of (a) solid displacement and (b) fluid pressure throughout the domain over time.

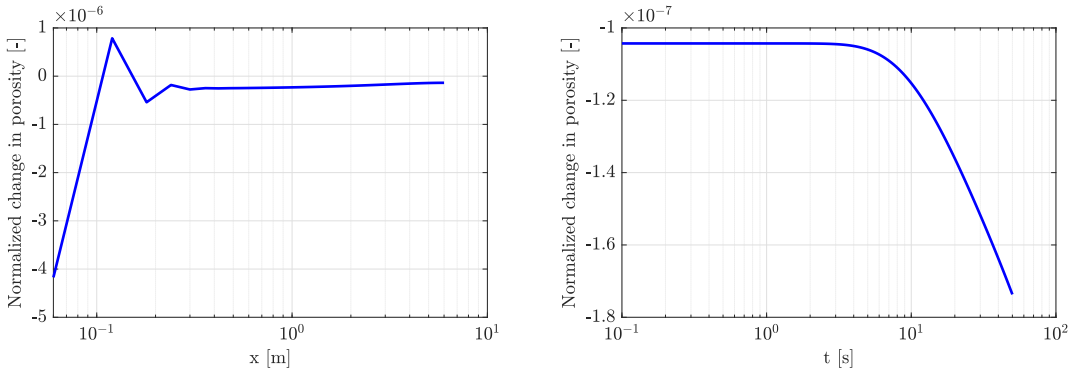


Figure 3.3: Porosity variation in one-dimensional consolidation problem over the column depth (left) and over time (right).

the deformational potential energy is localized in the pore-interface or in the solid bulk.

When $n = K_s/K_f$, the fluid presents maximum resistance against the pore interface, and hence the bulk pressure decreases in Fig. 3.5b. In this case, the volumetric proportions of solid and fluid are maintained, and $\eta - \eta_0 = 0$; thus, the solid deformation increases (Fig. 3.5a) to balance out the bulk potential energy. For $n > 1$, the potential energy is localized in the fluid space due to the lack of time for it to be stabilized in the porous media. Since equilibrium is not yet achieved, values of $n > 1$ should be temporary until the system is equilibrated. Such discussion regarding the effects of n on the constituents and its characteristics can be found in the work of Müller and Sahay [135, 157, 133, 136, 137].

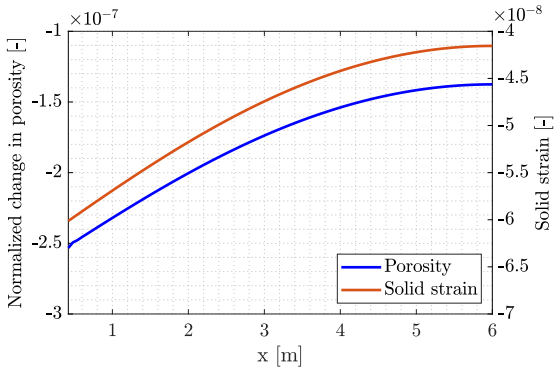
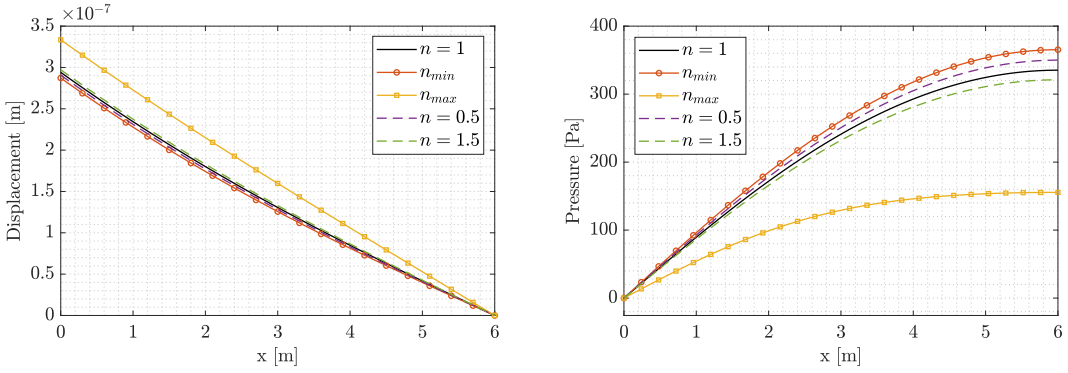


Figure 3.4: Porosity and strain variation in one-dimensional consolidation problem over the column depth.



(a) (b)

Figure 3.5: Change in displacement (left) and pressure (right) along the column depth at $t = 10$s.

3.4.2 Convergence study

To further validate the numerical implementation of the poroelasticity model, a convergence study is simulated for the dCS model when recovering the BT formulation (i.e., under the assumptions described in section 3.2.3). In this sense, a consolidation model is employed, considering the same material parameters, geometry, and boundary conditions from the previous section. The mesh refinement convergence considers a structured mesh with decreasing element size and constant time step of $\Delta t = 1 \times 10^{-5}$s after $t_{end} = 1$s of simulation. The relative errors for both displacement and pressure fields are computed

using the expressions of the L2-norm as in [62]

$$e^u_{L2} = \frac{\|\mathbf{u}_s^{ex} - \mathbf{u}_s^h\|_{L2}}{\|\mathbf{u}_s^{ex}\|_{L2}} = \frac{\left[\sum^{ne} \int_{\Omega^e} (\mathbf{u}_s^{ex} - \mathbf{u}_s^h)^2 \, d\Omega^e\right]^{1/2}}{\left[\sum^{ne} \int_{\Omega^e} (\mathbf{u}_s^{ex})^2 \, d\Omega^e\right]^{1/2}} \tag{3.71}$$

$$e^p_{L2} = \frac{\|p^{ex} - p^h\|_{L2}}{\|p^{ex}\|_{L2}} = \frac{\left[\sum^{ne} \int_{\Omega^e} (p^{ex} - p^h)^2 \, d\Omega^e\right]^{1/2}}{\left[\sum^{ne} \int_{\Omega^e} (p^{ex})^2 \, d\Omega^e\right]^{1/2}}, \tag{3.72}$$

and, for the energy norm, the expressions are given by

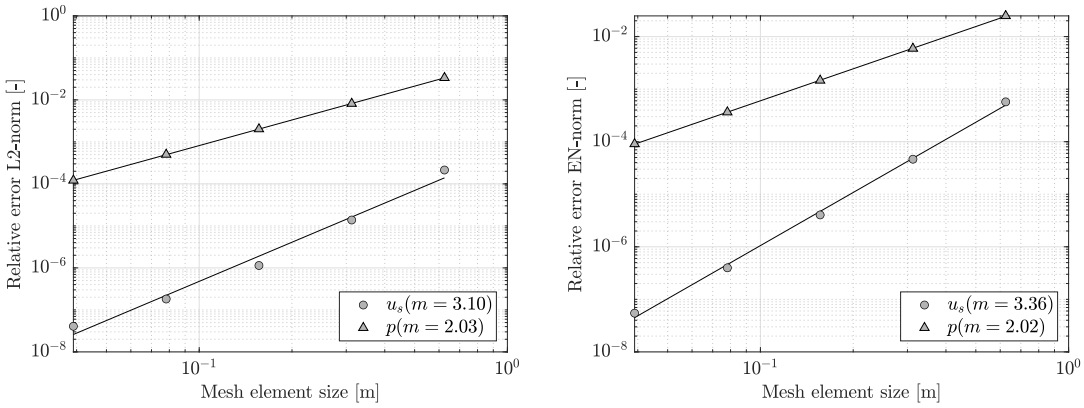
$$e^u_{EN} = \frac{\|\nabla\mathbf{u}_s^{ex} - \nabla\mathbf{u}_s^h\|_{EN}}{\|\nabla\mathbf{u}_s^{ex}\|_{EN}} = \frac{\left[\sum^{ne} \int_{\Omega^e} (\nabla\mathbf{u}_s^{ex} - \nabla\mathbf{u}_s^h)^2 \, d\Omega^e\right]^{1/2}}{\left[\sum^{ne} \int_{\Omega^e} (\nabla\mathbf{u}_s^{ex})^2 \, d\Omega^e\right]^{1/2}}, \tag{3.73}$$

$$e^p_{EN} = \frac{\|\nabla p^{ex} - \nabla p^h\|_{EN}}{\|\nabla p^{ex}\|_{EN}} = \frac{\left[\sum^{ne} \int_{\Omega^e} (\nabla p^{ex} - \nabla p^h)^2 \, d\Omega^e\right]^{1/2}}{\left[\sum^{ne} \int_{\Omega^e} (\nabla p^{ex})^2 \, d\Omega^e\right]^{1/2}}, \tag{3.74}$$

where $\mathbf{u}_s^h, p^h, \nabla\mathbf{u}_s^h, \nabla p^h$ are the approximate FE solutions and $\mathbf{u}_s^{ex}, p^{ex}, \nabla\mathbf{u}_s^{ex}, \nabla p^{ex}$ are the exact values obtained with the analytical solution [174]. The obtained rates of convergence are $\mathcal{O}(h^{1.97})$ for $\mathbf{u}_s$ and $\mathcal{O}(h^{2.03})$ for p in the L2-norm, $\mathcal{O}(h^{1.51})$ for $\mathbf{u}_s$, $\mathcal{O}(h^{1.98})$ for p in the energy norm. It is noticeable that the convergence rate for the displacement field is not the same as one would expect for an uncoupled problem, having in mind that quadratic shape functions are being employed. This deterioration in convergence can be attributed to the nature of the porous media problem, where the coupling matrix and the difference in magnitude of the solid and fluid material parameters interfere in the quadratic convergence for the displacement field, thus restricting the convergence order to the lowest approximation.

A manufactured solution with unrealistic material parameters is proposed to verify whether the optimal convergence for both fields is achieved. For that, we assume that the displacement and pressure fields are given by $u_s(x,t) = \sin(xt)$, $p(x,t) = \cos(xt)$, and the boundary conditions are properly adapted according to the governing equations of the problem. Figure 3.6a shows the convergence of both displacement and pressure fields, now with rates of $\mathcal{O}(h^{3.10})$ for $\mathbf{u}_s$, $\mathcal{O}(h^{2.03})$ for p in the L2-norm. The time step size is still responsible for some part of the error, which explains why convergence is still deteriorated even when mesh size is reduced. Furthermore, the energy norm observed (Figure 3.6b) had a convergence rate of $\mathcal{O}(h^{3.36})$ for $\mathbf{u}_s$, $\mathcal{O}(h^{2.02})$ for p, also in accordance with the numerical approximation for the respective fields. It is noteworthy that the numerical convergence of the Biot model has been previously studied by Murad and Loula [138] and in later works [60, 130, 176], and the poor convergence of the porous media model when simulating a consolidation problem

has been reported [145]. Although the choice of combining linear and quadratic elements ensure a higher convergence rate for the displacement, using only linear elements is a viable alternative once stabilization techniques are considered [180, 148, 154, 111, 68].



(a) L2 norm (b) Gradient norm

Figure 3.6: Convergence study over mesh size refinement considering L2-norm (left) and gradient norm (right).

3.5 Numerical Examples

3.5.1 Two-dimensional footing

A two-dimensional footing problem is simulated in this section for validation purposes. The correspondent geometry is depicted in Fig. 3.7, where a load of $\bar{t} = 15$ kPa is applied in part of the top boundary. The domain boundaries are undrained except for the segment AB, and all boundaries except the top have the normal displacements fixed. The material properties are taken from Diebels & Ehlers [50] and listed in Table 3.2, where solid and fluid constituents are assumed to be incompressible. Hence, $K_s, K_f \to \infty$, and the expressions for δ_s, δ_f need to be adapted within this limit. Evaluating Eq. (3.28) for this case, we have that $\delta_s^{BT} = \alpha - \eta_0$ and $\delta_f^{BT} = 0$.

A uniform FE mesh composed by $ne = 400$ quadrilateral elements is adopted, with a bi-linear approximation of the pressure and porosity fields and a bi-quadratic approximation for the displacement field. The simulation is carried out with a time step of $\Delta t = 10^{-2}$ s and a final simulation time of $t_{end} = 10$ s. Figure 3.8 shows the variation of the displacement and

Table 3.2: Material parameters [50] for the two-dimensional footing problem.

Parameter	Value	Unit	Parameter	Value	Unit
λ	5.583×10^{-3}	GPa	α	1	-
μ	8.375×10^{-3}	GPa	η_0	0.33	-
ν	0.2	-	δ_s	0.67	-
κ	10^{-9}	m^2	δ_f	0	-
μ_f	10^{-12}	GPa $\cdot$ s			

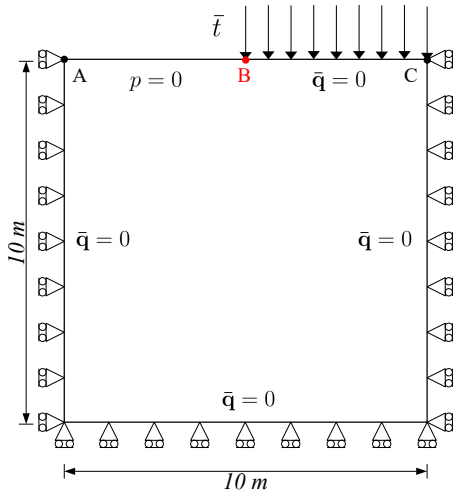
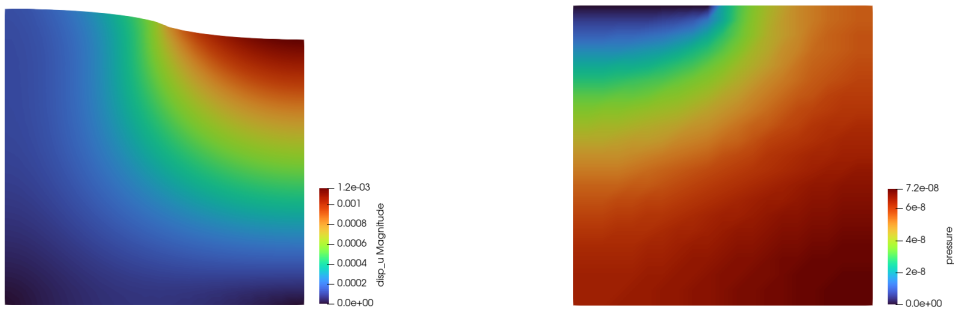


Figure 3.7: Two-dimensional footing example.

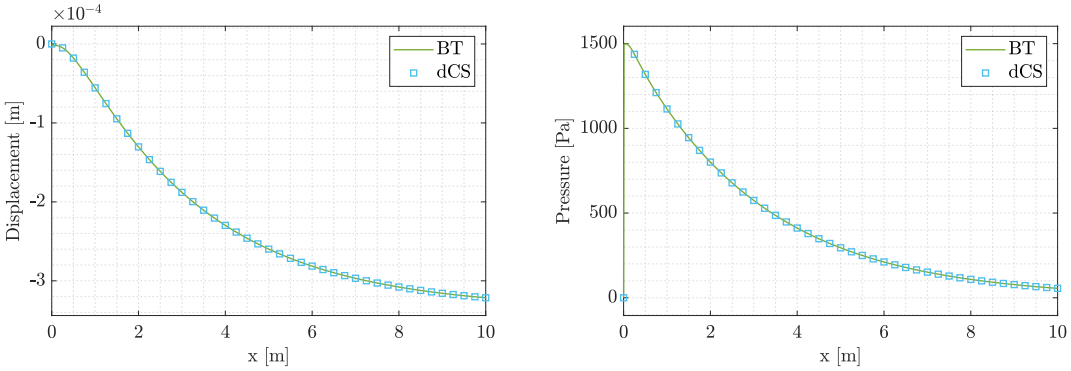
pressure at t_{end}, and Fig. 3.9 depicts the change in pressure and displacement throughout time at a point in the middle of the domain ($x = 5$m, $y = 5$m). At the very beginning, the model has an undrained response to the suddenly applied load – the fluid is trapped within the domain. As time passes, the long-term drained response leads to a dissipation in the pore pressure [50]. Furthermore, results obtained with the dCS model are the same as the ones obtained with the BT model and represented in Diebels & Ehlers [50].

It is noteworthy that, since in this example both solid and fluid are assumed to be incompressible, and $\delta_s^{BT} = \alpha - \eta_0$, $\delta_f^{BT} = 0$, the porosity effective pressure coefficient n presented in section 3.2.4 does not appear in the formulation. In order to verify the impact that n would have in the simulation, an additional simulation was carried out considering both constituents as compressible, assuming $K_f = 3$GPa and $K_s = 36$GPa. Because of the different material parameters (e.g., lower Young's modulus, higher permeability, higher porosity), the variation in n did not yield any significant changes in the problem behaviour.



(a) Displacement (b) Pressure

Figure 3.8: Solid displacement and fluid pressure distribution for two-dimensional footing problem at $t_{end} = 10$s. In this case of model verification, $\delta_s^{BT} = 0.67$ and $\delta_f^{BT} = 0$.



(a) Displacement (b) Pressure

Figure 3.9: Change in variables over the simulation time at $x = 5$m, $y = 5$m for the two-dimensional footing problem.

An interesting conclusion in this example comes from the variation in porosity, as depicted in Figure 3.10, plotted along the right boundary of the domain. Although it presents the same behaviour as the one-dimensional case, the two-dimensional example shows that the initial oscillation in porosity near the point of load application is dissipated throughout the domain, and it vanishes once steady state is reached. The variation of volumetric strain over the boundary is compared to the porosity in the same graph, showing that both are in the order of 10^{-4}.

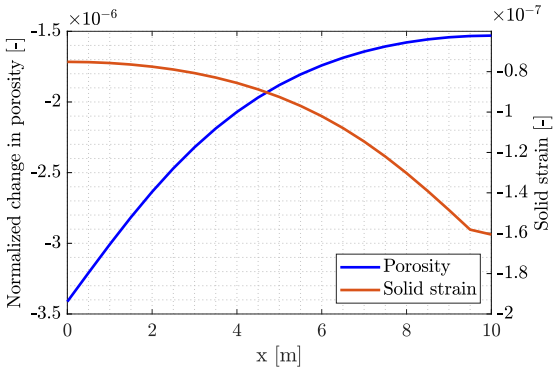


Figure 3.10: Porosity and volumetric strain variation in two-dimensional footing problem for varying y at right boundary. For this case, solid and fluid materials are considered incompressible, and thus $\delta_s^{BT} = 0.5730$ and $\delta_f^{BT} = 0.0478$.

3.5.2 Two-dimensional injection wells

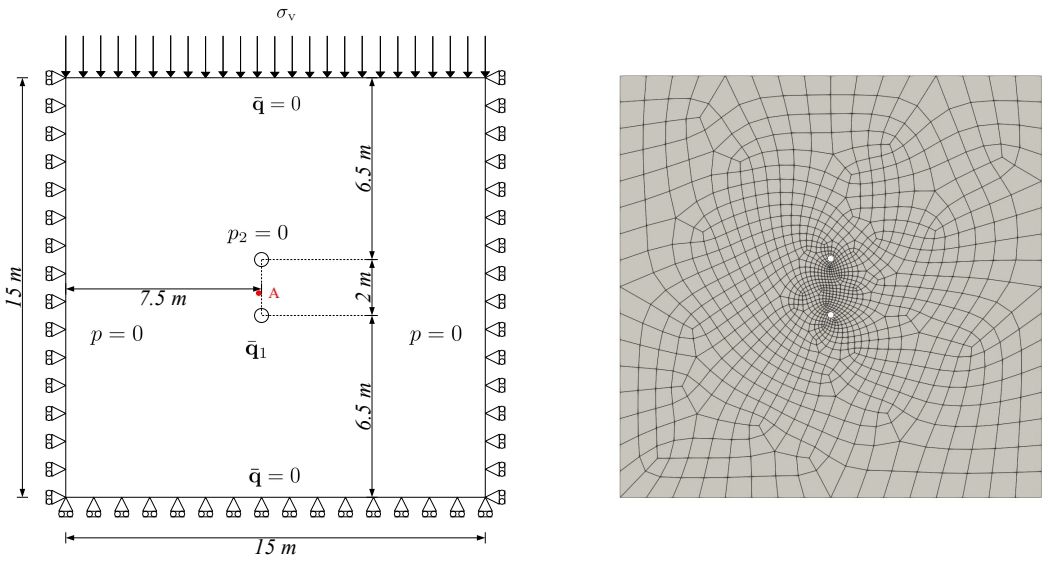
A two-dimensional injection wells problem is simulated with the proposed dCS finite element model. The problem geometry is illustrated in Fig. 3.11, and the material is assumed to be a Berea sandstone with properties indicated in Table 3.3. The external left, right, and bottom boundaries have the normal displacement restrained; the left and right boundaries are drained while the top and bottom ones are impervious. The wells are situated at (1) $x = 7.5$m, $y = 6.5$m and (2) $x = 7.5$m, $y = 8.5$m with a diameter of 8 ¾ in. A prescribed flux of 1 MPa is prescribed at the well 1, and $p = 0$ at the well 2. The problem domain is considered to be at a depth of 400m, and the overburden material is assumed to have a density of 2300 kg/m^3; the in situ stresses and the initial pore pressure are included in Table 3.3.

The domain is discretized into $ne = 1164$ quadrilateral elements with a mixed order of approximation – bi-linear for the pressure and porosity and bi-quadratic for the displacement field. For the time discretization process, a time step of $\Delta t = 1$s is used throughout $t_{end} = 50$s. Figure 3.12 illustrates the displacement and pressure distributions close to the wells at the final simulation time. The pressure distribution increases over time around well 1, where the flux is prescribed. The displacements in the same region are consistent with the boundary conditions applied in terms of in situ stress – the vertical stress caused by the overburden has more significant effects than the horizontal stress.

Figure 3.13 shows the displacement and pressure variations in time at the point A in the domain ($x = 7.46$m, $y = 7.45$m) for different values of the porosity effective pressure coefficient n. There is a visible difference between the results for $n = 1$ and the limit

Table 3.3: Material parameters [193] and problem configuration data for the two-dimensional injection wells problem.

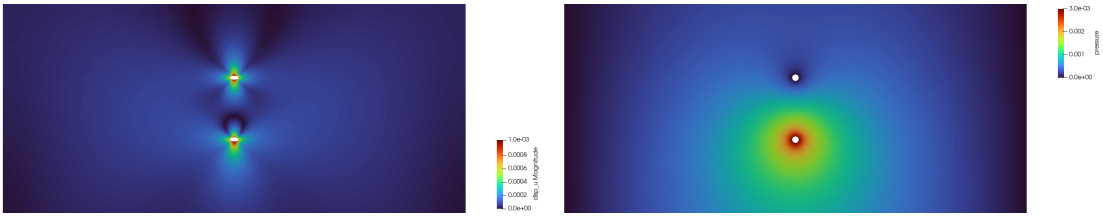
Parameter	Value	Unit	Parameter	Value	Unit
E	14.4	GPa	δ_s	0.4653	-
ν	0.2	-	δ_f	0.0427	-
k	1.88×10^{-13}	m^2	H_{datum}	400	m
μ_f	10^{-12}	GPa $\cdot$ s	$\rho_{\text{overburden}}$	2300	kg/m^3
α	0.79	-	σ_{V}	9.02	MPa
η_0	0.19	-	σ_{H}	2.26	MPa
K_f	3.3	GPa	p_0	3.92	MPa
K_s	36	GPa			



(a) Geometry (b) Mesh

Figure 3.11: Two-dimensional injection wells example.

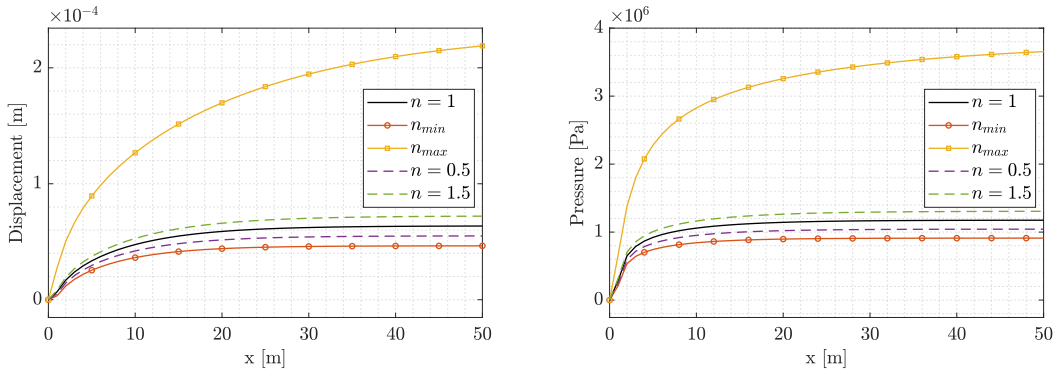
cases $n_{min} = 0, n_{max} = K_s/K_f$. Small changes around $n = 1$ (i.e., $n = 0.5, n = 1.5$), nonetheless, lead to small differences in the displacement and pressure results. In the column consolidation problem, the variation of n over the column depth followed different patterns for displacement and pressure fields – as explained in section 3.4.1. In the injection wells problem, on the other hand, the variation of the porosity effective pressure coefficient n over time affected the solid and pressure variables in a similar way. This difference is



(a) Displacement, $t = 50$s (b) Pressure, $t = 50$s

Figure 3.12: Displacement and pressure distribution at the center of the domain for the two-dimensional injection wells problem $t_{end} = 100$s.

likely related to the boundary conditions, which are more complex for the injection wells problem and therefore the predictions made in the column consolidation example are no longer valid.



(a) (b)

Figure 3.13: Change in displacement (left) and pressure (right) over the simulation time at $x = 7.46$m, $y = 7.45$m.

3.6 Discussion

Biot theory is commonly used in practice and there are well known methodologies for determining material parameters. However, the dCS theory introduces additional parameters, values of which have not yet been widely reported in the literature outside theoretical discussions. In part to fill this gap, the above studies of dCS versus BT theories rely on the work of Sahay [157] to define the additional material parameters (δ_s, δ_f) that appear

in the porosity equation (3.31). The present study provides a verification of the numerical method and its implementation to solve boundary values problems based on dCS theory. However, validation of the use of dCS versus BT for a particular application remains to be completed. Therefore, the present study did not aim to prove or disprove the utility of either dCS or BT theories, but rather provide a FEM tool to enable validation and comparisons in the future.

The developed FE model does not account for inertia terms in the governing equations, leading to numerical simulations in a quasi-static/transient flow context. As an initial study of the dCS FE model, this simpler set of governing equations was adopted so that both the physics and the numerical methods could be investigated thoroughly. Further investigations will extend to the dynamics, where more significant differences between the dCS and BT models may be expected.

Besides the numerical implementation of the dCS model, this study also thoroughly compared the governing equations used in both BT and dCS theories. In the BT approach, the fluid effect on the solid stress – represented by the fluid pressure term – is included in the definition of such stress field. Meanwhile, such effect appears in the dCS approach as a consequence of the volume averaging technique, hence resulting from the solid-fluid interactions. Nevertheless, both theories still rely on an effective stress and a fluid pressure contribution to the total stress relation.

For the verification stage, the governing equations from dCS theory are firstly simplified so that the dCS model would contain BT as a special case. In particular, the compliance coefficients in the porosity equation are defined so that the model accounts for reciprocal solid-fluid interactions when $n = 1$. Moreover, the macroscopic solid shear modulus introduced in the de la Cruz and Spanos theory is herein taken as an averaged version of the pore-scale shear modulus. Lastly, the fluid stress is defined only in terms of the averaged fluid pressure, meaning that viscous dissipation, which appears in the dCS theory (but not BT), is neglected.

After the verification step, non-reciprocal interactions were introduced to the model by varying the coefficient n. Some of the results presented show modest deviations from BT theory. However, the magnitude of the deviation was restricted by the design of the numerical examples, which aimed to incorporate BT as a special case of the dCS framework. Non-reciprocal interactions allow the representation of energy concentrated at the solid or fluid constituents; regardless, the overall equilibrium of the system is not violated. More to that, it is noteworthy that the latter theory admits more general additive energy potentials, in a manner akin to multi-body dynamics and mixture theory.

3.7 Conclusions

In this chapter a FE Method for the dCS poroelasticity theory for transient problems has been presented. The model is formulated in terms of three fields: solid displacement u_s, pore pressure p, and total porosity η. The governing equations are pore-scale volume-average statements of conservation of momentum and conservation of mass plus a compatibility equation for fluid and solid deformations (the porosity equation). Numerical approximations are derived using mixed-order elements and implicit time integration.

The model was verified in one- and two-dimensional problems. The convergence rates of the one-dimensional consolidation problem are optimal for the displacement and pressure fields. The dCS model was constrained to incorporate the two-field $u_s - p$ BT model as a special case. The FEM dCS model was applied to a footing problem and a subsurface injection problem in two-dimensions, where the effects of non-reciprocal interactions were assessed. Non-reciprocal interactions had a modest impact on results in the footing problem, but were significant in some cases in the subsurface injection problem. The next step on this topic comprises using the developed numerical model as a basis for fully dynamic simulations, in which significant differences between the BT and dCS model may be expected.

Chapter 4

Dynamic FE Formulation for Wave Propagation

4.1 Introduction

Expanding on the numerical implementation from the previous chapter, the dCS theory is now modeled accounting for inertia terms, allowing the representation of dynamic processes. A dimensionless form of the governing equations is introduced, allowing further studies on the relevance of dCS terms in comparison with BT theory. The weak formulation, semi- and fully-discrete forms are presented for the three-field model in terms of solid displacement, fluid pressure, and fluid displacement. The choice of such main variables does not assume that solid and fluid accelerations are the same, which is an assumption made on two-field (solid displacement-pressure) dynamic models. The dynamic FE model also allows the study of wave propagation in porous media, which is done in one- and two-dimensional examples.

Section 4.2 details the governing equations, while Section 4.3 presents the correspondent weak formulation and FE discretization. Section 4.4 presents a dimensionless analysis of the dCS model and assesses the relative contribution of the fluid viscous dissipation term from the dCS theory. In Section 4.5, the developed FE dCS model is verified against a manufactured solution, and a convergence study is performed to attest the robustness of the numerical implementation. In Section 4.6, one- and two-dimensional wave propagation examples are presented, and changes in the porosity effective pressure coefficient and in the macroscopic shear modulus are evaluated. Section 4.7 includes a discussion of the presented results, whilst Section 4.8 summarizes the findings herein reported.

4.2 dCS Governing Equations

The system of governing equations for the dCS theory is taken from Spanos [165]. For the Lagrangian point of view herein adopted, solid and fluid strains are assumed to be small. A dimensionless form of such equations is obtained through the correspondence

$$\boldsymbol{\sigma}_s = E\bar{\boldsymbol{\sigma}}_s, \qquad \mathbf{u}_s = L\bar{\mathbf{u}}_s, \qquad \nabla = \frac{1}{L}\bar{\nabla}, \qquad p = K_f\bar{p}, \tag{4.1}$$

$$\boldsymbol{\sigma}_f = E\bar{\boldsymbol{\sigma}}_f, \qquad \mathbf{u}_f = L\bar{\mathbf{u}}_f, \qquad t = t_d\bar{t}. \tag{4.2}$$

where the overbar indicates a dimensionless variable, $\boldsymbol{\sigma}_s$ is the solid stress, $\boldsymbol{\sigma}_f$ is the fluid stress, $\mathbf{u}_s$ is the solid displacement, $\mathbf{u}_f$ is the fluid displacement, p is the fluid pressure, ∇ is the gradient operator, t is the time variable, L is a characteristic length (e.g., taken as the domain length for one-dimensional problems), and t_d is a time scaling parameter. The momentum equations for the solid and fluid are given by

$$\begin{aligned}(1-\eta_0)\rho_s\frac{L}{t_d^2}\bar{\ddot{\mathbf{u}}}_s = {} & \frac{E}{L}\bar{\nabla}\cdot\bar{\boldsymbol{\sigma}}_s + \frac{\mu_f\eta_0^2 L}{\kappa t_d}(\bar{\dot{\mathbf{u}}}_f - \bar{\dot{\mathbf{u}}}_s) - \frac{\rho_{12}L}{t_d^2}(\bar{\ddot{\mathbf{u}}}_f - \bar{\ddot{\mathbf{u}}}_s) \\ & - \frac{\mu_s\delta_\mu}{L}\left[\bar{\nabla}^2\bar{\mathbf{u}}_s + \frac{1}{3}\bar{\nabla}(\bar{\nabla}\cdot\bar{\mathbf{u}}_s)\right] + \mathbf{b}_s, \end{aligned} \tag{4.3}$$

$$\begin{aligned}\eta_0\rho_f\frac{L}{t_d^2}\bar{\ddot{\mathbf{u}}}_f = {} & \frac{E}{L}\bar{\nabla}\cdot\bar{\boldsymbol{\sigma}}_f - \frac{\mu_f\eta_0^2 L}{\kappa t_d}(\bar{\dot{\mathbf{u}}}_f - \bar{\dot{\mathbf{u}}}_s) + \frac{\rho_{12}L}{t_d^2}(\bar{\ddot{\mathbf{u}}}_f - \bar{\ddot{\mathbf{u}}}_s) \\ & - (1-\eta_0)\frac{\mu_f\delta_\mu}{Lt_f}\left[\bar{\nabla}^2\bar{\mathbf{u}}_s + \frac{1}{3}\bar{\nabla}(\bar{\nabla}\cdot\bar{\mathbf{u}}_s)\right] + \mathbf{b}_f \end{aligned} \tag{4.4}$$

where $\mathbf{b}_s$, $\mathbf{b}_f$ are body force terms, and δ_μ is a dimensionless parameter related to the macroscopic shear modulus μ_M by

$$\mu_M = (1-\eta_0)\mu_s(1-\delta_\mu), \tag{4.5}$$

The constant δ_μ was mentioned in the works of Hickey et. al.[85], Sahay [159], and Spanos [165], where it was either referred as c or δ_μ ($c = -\delta_\mu$). Such constant establishes a difference between the averaged solid grain shear modulus $(1-\eta_0)\mu_s$ and the macroscopic shear modulus μ_M, obtained through the volume averaging technique [178]. Hence, μ_M includes the effect that the solid-fluid interface has on the macroscopic behavior of the medium. Values of δ_μ have been reported in Hickey [83] based on experimental data for quasi-steady rock consolidation, and are within the range $0 \leq \delta_\mu \leq 1$. Nonetheless, determination of δ_μ through dynamic experiments is still a gap to be addressed in the literature.

The correspondent solid and fluid stresses are

$$\bar{\boldsymbol{\sigma}}_s = (1-\eta_0-\delta_s)\frac{K_s}{E}\bar{\nabla}\cdot\bar{\mathbf{u}}_s + \frac{K_s\delta_f}{E}\bar{\nabla}\cdot\bar{\mathbf{u}}_f + (1-\eta_0)\frac{\mu_s}{E}(\bar{\nabla}\bar{\mathbf{u}}_s + \frac{1}{3}\bar{\nabla}\cdot\bar{\mathbf{u}}_s), \tag{4.6}$$

$$\bar{\boldsymbol{\sigma}}_f = -\eta_0\frac{K_f}{E}\mathbf{I}\bar{p} + \frac{\eta_0\mu_f}{Et_d}\bar{\nabla}\cdot\dot{\bar{\mathbf{u}}}_f + (\eta_0\xi_f + \eta_0\frac{\mu_f}{3} - \xi_f\delta_f)\frac{1}{Et_d}\bar{\nabla}\cdot\dot{\bar{\mathbf{u}}}_f + \frac{\xi_f\delta_s}{Et_d}\bar{\nabla}\cdot\dot{\bar{\mathbf{u}}}_s; \tag{4.7}$$

the fluid pressure equation is

$$\dot{\bar{p}} + (1-\frac{\delta_f}{\eta_0})\bar{\nabla}\cdot\dot{\bar{\mathbf{u}}}_f + \frac{\delta_s}{\eta_0}\bar{\nabla}\cdot\dot{\bar{\mathbf{u}}}_s = s, \tag{4.8}$$

where s is a source/sink term. Table 4.1 lists the material parameters included in the previous equations, followed by typical values for water-saturated sandstone media which will be employed in upcoming numerical examples. The single and double dots indicate respectively the velocity and acceleration fields, and the solid and fluid compliance coefficients are defines as in (3.31).

Table 4.1: Material parameters [193]for water-saturated sandstone.

Parameter	Symbol	Value	Unit
Young's modulus	E	14.4	GPa
Poisson's ratio	ν	0.2	-
Intrinsic permeability	κ	1.88×10^{-13}	m^2
Biot coefficient	α	0.79	-
Initial porosity	η_0	0.19	-
Dynamic viscosity of fluid	μ_f	10^{-3}	$Pa\cdot s$
Bulk viscosity of fluid	ξ_f	2.8×10^{-3}	Pa·s
Bulk modulus of solid	K_s	36	GPa
Bulk modulus of fluid	K_f	3.3	GPa
Density of solid	ρ_s	2600	kg/m^3
Density of fluid	ρ_f	1000	kg/m^3
Added mass density	ρ_{12}	0	kg/m^3
Compliance of solid	$\delta_s(n=1)$	0.4653	-
Compliance of fluid	$\delta_f(n=1)$	0.0427	-

It is noteworthy that the variables indicated in the dCS theory are averaged values of the ones referred in BT theory, such that $\boldsymbol{\sigma}_s^{BT} = (1-\eta_0)\boldsymbol{\sigma}_s, \boldsymbol{\sigma}_f^{BT} = \eta_0\boldsymbol{\sigma}_f$. As mentioned in Section 3.2.4, the parameter n is called the porosity effective pressure coefficient [157], and it represents the effect of non-reciprocal solid-fluid interactions. For $n=1$, solid and fluid

have the same effect in porosity changes, and the system of equations from the Biot theory are recovered – apart from the fluid viscous dissipation from the fluid stress definition. While expressions to determine n have been reported by Müller [135, 136] and values were in the range $0.5 < n < 1.5$, these were obtained under quasi-static consolidation conditions. For dynamic loading, n is yet to be defined through appropriate experiments [152]. The reported bounds for n are very conservative values, meaning that better approximations for dynamic simulations could yield a more restrictive range.

The system of equations to be solved is obtained from a combination of the solid and fluid momentum equations, the pressure equation, and the porosity relation arranged in a way so that the correspondent matrix system is well conditioned. Considering that the main variables are solid displacement, fluid pressure, and fluid displacement, the first equation of the three-field formulation is obtained by summing the momentum equations (4.3) and (4.4), substituting the fluid acceleration from (4.4). The second equation is given by the pressure equation (4.8), and the third equation is given by the fluid equation of motion (4.4), yielding

$$\bar{\nabla}\cdot\bar{\boldsymbol{\tau}} - c_1\ddot{\bar{\mathbf{u}}}_s - c_2\ddot{\bar{\mathbf{u}}}_f + c_3\bar{\nabla}\bar{p} - c_4\bar{\nabla}^2\dot{\bar{\mathbf{u}}}_f - c_5\bar{\nabla}(\bar{\nabla}\cdot\dot{\bar{\mathbf{u}}}_s) - c_6\bar{\nabla}(\bar{\nabla}\cdot\dot{\bar{\mathbf{u}}}_f) + c_7(\dot{\bar{\mathbf{u}}}_f - \dot{\bar{\mathbf{u}}}_s) + c_8\left[\bar{\nabla}^2\bar{\mathbf{u}}_s + \frac{1}{3}\bar{\nabla}(\bar{\nabla}\cdot\bar{\mathbf{u}}_s)\right] + \bar{\mathbf{b}}_s = 0, \tag{4.9}$$

$$c_9\bar{\nabla}\cdot\bar{\mathbf{u}}_s + \bar{p} + c_{10}\bar{\nabla}\cdot\bar{\mathbf{u}}_f = s, \tag{4.10}$$

$$-c_{11}\ddot{\bar{\mathbf{u}}}_f - c_2\ddot{\bar{\mathbf{u}}}_s - c_3\bar{\nabla}\bar{p} + c_4\bar{\nabla}^2\dot{\bar{\mathbf{u}}}_f + c_5\bar{\nabla}(\bar{\nabla}\cdot\dot{\bar{\mathbf{u}}}_s) + c_6\bar{\nabla}(\bar{\nabla}\cdot\dot{\bar{\mathbf{u}}}_f) - c_7(\dot{\bar{\mathbf{u}}}_f - \dot{\bar{\mathbf{u}}}_s) + c_{12}\left[\bar{\nabla}^2\dot{\bar{\mathbf{u}}}_s + \frac{1}{3}\bar{\nabla}(\bar{\nabla}\cdot\dot{\bar{\mathbf{u}}}_s)\right] + \bar{\mathbf{b}}_f = 0. \tag{4.11}$$

where the dimensionless coefficients introduced are listed in Table 4.2; $\bar{\mathbf{b}}_s = \mathbf{b}_s L/E$, $\bar{\mathbf{b}}_f = \mathbf{b}_f L/E$, and $\bar{\boldsymbol{\tau}}$ is the dimensionless form of the total stress tensor. The total stress tensor is defined either as a summation of solid and fluid stresses $\boldsymbol{\tau} = \boldsymbol{\sigma}_s + \boldsymbol{\sigma}_f$ or as a decomposition in terms of effective stress $\boldsymbol{\sigma}$ and fluid pressure p, $\boldsymbol{\tau} = \boldsymbol{\sigma} - \alpha\mathbf{m}p$. The effective stress alludes to its similar definition in linear elasticity, dependent solely on the solid displacement.

It should be noticed that in BT theory the constant c_7 is modified by a high-frequency correction factor F, dependent on the source frequency ω and on the pore geometry [16]. A commonly used expression for this correction factor is $F = \sqrt{1 + 0.5\mathrm{i}(\omega/\omega_c)}$ [92], where ω_c is the BT critical frequency limit. For the low-frequency regime where $\omega \leq \omega_c$, $F = 1$. The correction is necessary in BT theory since it is not able to represent fluid behavior at high frequency. In the dCS theory, nonetheless, because it includes the complete fluid stress tensor, fluid motion is fully represented regardless of the frequency range [76].

Table 4.2: Dimensionless parameters from equations (4.9)-(4.11).

$c_1 = [(1-\eta_0)\rho_s - \rho_{12}]\,\dfrac{L^2}{Et_d^2}$	$c_5 = \dfrac{\xi_f \delta_s}{Et_d}$	$c_9 = \dfrac{\delta_s}{\eta_0}$
$c_2 = \dfrac{\rho_{12} L^2}{Et_d^2}$	$c_6 = \left(\eta_0 \xi_f + \dfrac{\eta_0 \mu_f}{3} - \xi_f \delta_f\right) \dfrac{1}{Et_d}$	$c_{10} = (1 - \dfrac{\delta_f}{\eta_0})$
$c_3 = \dfrac{\eta_0 K_f}{E}$	$c_7 = \dfrac{\mu_f \eta_0^2 L^2}{\kappa E t_d}$	$c_{11} = [\eta_0 \rho_f - \rho_{12}] \dfrac{L^2}{Et_d^2}$
$c_4 = \dfrac{\eta_0 \mu_f}{Et_d}$	$c_8 = -\dfrac{\delta_\mu \mu_s}{E}$	$c_{12} = -(1-\eta_0) \dfrac{\delta_\mu \mu_f}{Et_f}$

The above three-field system of equations for the dCS model is similar to previously proposed three-field models for BT theory [91]. The three-field formulation is suitable for dynamic simulations and a wide frequency range. While a two-field formulation in terms of solid displacement and fluid pressure is commonly employed for consolidation problems [206, 154] due their to quasi-static behavior, such framework is developed under the assumption that solid and fluid accelerations are equal. Nonetheless, applications of two-field formulations in dynamic cases have also been reported in literature [140, 114, 143], when neglecting the relative solid-fluid acceleration is justified for low frequencies.

4.3 Finite Element Formulation

The coupled system of equations (4.9)-(4.11) is transformed into a weak formulation by considering arbitrary and sufficiently smooth weight functions $\delta\mathbf{v}$, δw, $\delta\mathbf{g}$ and performing an integration over a domain Ω with boundary Γ. The boundary Γ can be divided into the sets $\Gamma = \Gamma_s \cup \Gamma_{ts} = \Gamma_p \cup \Gamma_q = \Gamma_f \cup \Gamma_{tf}$, for the solid displacement, fluid pressure, and fluid displacement fields, respectively. Also, $\Gamma_s \cap \Gamma_{ts} = \Gamma_p \cap \Gamma_q = \Gamma_f \cap \Gamma_{tf} = \varnothing$. For appropriate

functions spaces of the main variables and the weight functions, the weak form of (4.9) is

$$
\begin{aligned}
&c_1\int_{\bar\Omega}(\delta\mathbf{v})^\top\ddot{\bar{\mathbf{u}}}_s d\bar\Omega + c_2\int_{\bar\Omega}(\delta\mathbf{v})^\top\ddot{\bar{\mathbf{u}}}_f d\bar\Omega + \int_{\bar\Omega}(\nabla\delta\mathbf{v})^\top\bar{\boldsymbol{\sigma}}d\bar\Omega - (\alpha-c_3)\int_{\bar\Omega}(\nabla\delta\mathbf{v})^\top\bar p d\bar\Omega\\
&\quad - c_4\int_{\bar\Omega}(\nabla\delta\mathbf{v})^\top\nabla\dot{\bar{\mathbf{u}}}_f d\bar\Omega - c_5\int_{\bar\Omega}(\nabla\delta\mathbf{v})^\top\nabla\cdot\dot{\bar{\mathbf{u}}}_s d\bar\Omega - c_6\int_{\bar\Omega}(\nabla\delta\mathbf{v})^\top\nabla\cdot\dot{\bar{\mathbf{u}}}_f d\bar\Omega\\
&\quad - c_7\int_{\bar\Omega}(\delta\mathbf{v})^\top\dot{\bar{\mathbf{u}}}_f d\bar\Omega + c_7\int_{\bar\Omega}(\delta\mathbf{v})^\top\dot{\bar{\mathbf{u}}}_s d\bar\Omega + c_8\int_{\Omega}(\nabla\delta\mathbf{v})^\top\nabla\bar{\mathbf{u}}_s d\Omega + \frac{c_8}{3}\int_{\Omega}(\nabla\delta\mathbf{v})^\top\nabla\cdot\bar{\mathbf{u}}_s d\Omega\\
&\quad = \int_{\bar\Gamma_{ts}}(\delta\mathbf{v})^\top(\bar{\boldsymbol{\sigma}}\cdot\mathbf{n})d\bar\Gamma - (\alpha-c_3)\int_{\bar\Gamma_{ts}}(\delta\mathbf{v})^\top(\bar p\cdot\mathbf{n})d\bar\Gamma - c_4\int_{\bar\Gamma_{ts}}(\delta\mathbf{v})^\top(\nabla\cdot\dot{\bar{\mathbf{u}}}_f)\cdot\mathbf{n}d\bar\Gamma\\
&\quad - c_5\int_{\bar\Gamma_{ts}}(\delta\mathbf{v})^\top(\nabla\cdot\dot{\bar{\mathbf{u}}}_s)\cdot\mathbf{n}d\bar\Gamma - c_6\int_{\bar\Gamma_{f}}(\delta\mathbf{v})^\top(\nabla\cdot\dot{\bar{\mathbf{u}}}_f)\cdot\mathbf{n}d\bar\Gamma + c_8\int_{\Gamma}(\delta\mathbf{v})^\top(\nabla\bar{\mathbf{u}}_s\cdot\mathbf{n})d\Gamma\\
&\quad + \frac{c_8}{3}\int_{\Gamma}(\delta\mathbf{v})^\top(\nabla\cdot\bar{\mathbf{u}}_s)\cdot\mathbf{n}d\Gamma + \int_{\Omega}(\delta\mathbf{v})^\top\bar{\mathbf{b}}_s d\Omega,
\end{aligned}
\tag{4.12}
$$

where $\delta\mathbf{v}=0$ on $\bar\Gamma_s$; for equation (4.10), the weak form is

$$
c_9\int_{\bar\Omega}(\delta w)^\top\nabla\cdot\bar{\mathbf{u}}_s d\bar\Omega + \int_{\bar\Omega}(\delta w)^\top\bar p d\bar\Omega + c_{10}\int_{\bar\Omega}(\delta w)^\top\nabla\cdot\bar{\mathbf{u}}_f d\bar\Omega = \int_{\Omega}(\delta w)^\top s d\Omega,
\tag{4.13}
$$

where $\delta w=0$ on $\bar\Gamma_p$, and for equation (4.11), the correspondent weak form is

$$
\begin{aligned}
&c_{11}\int_{\bar\Omega}(\delta\mathbf{g})^\top\ddot{\bar{\mathbf{u}}}_f d\bar\Omega + c_2\int_{\bar\Omega}(\delta\mathbf{g})^\top\ddot{\bar{\mathbf{u}}}_s d\bar\Omega - c_3\int_{\bar\Omega}(\delta\mathbf{g})^\top\bar p d\bar\Omega + c_4\int_{\bar\Omega}(\nabla\delta\mathbf{g})^\top\nabla\dot{\bar{\mathbf{u}}}_f d\bar\Omega\\
&\quad + c_5\int_{\bar\Omega}(\nabla\delta\mathbf{g})^\top\nabla\cdot\dot{\bar{\mathbf{u}}}_s d\bar\Omega + c_6\int_{\bar\Omega}(\nabla\delta\mathbf{g})^\top\nabla\cdot\dot{\bar{\mathbf{u}}}_f d\bar\Omega + c_7\int_{\bar\Omega}(\delta\mathbf{g})^\top\dot{\bar{\mathbf{u}}}_f d\bar\Omega - c_7\int_{\bar\Omega}(\delta\mathbf{g})^\top\dot{\bar{\mathbf{u}}}_s d\bar\Omega\\
&\quad + c_{12}\int_{\Omega}(\nabla\mathbf{g})^\top\nabla\dot{\bar{\mathbf{u}}}_s d\Omega + \frac{c_{12}}{3}\int_{\Omega}(\nabla\mathbf{g})^\top\nabla\cdot\dot{\bar{\mathbf{u}}}_s d\Omega\\
&\quad = -c_3\int_{\bar\Gamma_{tf}}(\delta\mathbf{g})^\top(\bar p\cdot\mathbf{n})d\bar\Gamma + c_4\int_{\bar\Gamma_{tf}}(\delta\mathbf{g})^\top(\nabla\dot{\bar{\mathbf{u}}}_f\cdot\mathbf{n})d\bar\Gamma + c_5\int_{\bar\Gamma_{tf}}(\delta\mathbf{g})^\top(\nabla\cdot\dot{\bar{\mathbf{u}}}_s\cdot\mathbf{n})d\bar\Gamma\\
&\quad + c_6\int_{\bar\Gamma_{tf}}(\delta\mathbf{g})^\top(\nabla\cdot\dot{\bar{\mathbf{u}}}_f\cdot\mathbf{n})d\bar\Gamma + c_{12}\int_{\Gamma_{tf}}(\delta\mathbf{g})^\top(\nabla\dot{\bar{\mathbf{u}}}_s\cdot\mathbf{n})d\Gamma + \frac{c_{12}}{3}\int_{\Gamma_{tf}}(\delta\mathbf{g})^\top(\nabla\cdot\dot{\bar{\mathbf{u}}}_s)\cdot\mathbf{n}d\Gamma\\
&\quad + \int_{\Omega}(\delta\mathbf{g})^\top\bar{\mathbf{b}}_f d\Omega,
\end{aligned}
\tag{4.14}
$$

where $\delta\mathbf{g}=0$ on $\bar\Gamma_f$. The prescribed traction is expressed as $\bar{\mathbf{t}}=(\bar{\boldsymbol{\sigma}}\cdot\mathbf{n})$, whilst the prescribed pressure is $(\bar p\cdot\mathbf{n})$; the vector $\mathbf{n}$ is an outward normal to the dimensionless domain $\bar\Omega$. The spacial discretization of the weak form is obtained by using the interpolation

$$
\bar{\mathbf{u}}_s=\mathbf{N}_s\hat{\mathbf{u}}_s,\qquad \bar p=\mathbf{N}_p\hat{\mathbf{p}},\qquad \bar{\mathbf{u}}_f=\mathbf{N}_f\hat{\mathbf{u}}_f
\tag{4.15}
$$

to approximate the solid displacement, fluid pressure, and fluid displacement fields, in which $\hat{\mathbf{u}}_s$, $\hat{\mathbf{p}}$, $\hat{\mathbf{u}}_f$ are the vectors of nodal values, and $\mathbf{N}_s$, $\mathbf{N}_p$, and $\mathbf{N}_f$ are Lagrangian shape functions. The resulting system is

$$\begin{cases} \mathbf{M}_{ss}\ddot{\hat{\mathbf{u}}}_s + \mathbf{M}_{sf}\ddot{\hat{\mathbf{u}}}_f + \mathbf{C}_{ss}\dot{\hat{\mathbf{u}}}_s - \mathbf{C}_{sf}\dot{\hat{\mathbf{u}}}_f + \mathbf{K}_{ss}\hat{\mathbf{u}}_s - \mathbf{K}_{sp}\hat{\mathbf{p}} = \mathbf{f}_s, \\ \mathbf{K}_{ps}\hat{\mathbf{u}}_s + \mathbf{K}_{pp}\hat{\mathbf{p}} + \mathbf{K}_{pf}\hat{\mathbf{u}}_f = \mathbf{f}_p, \\ \mathbf{M}_{ff}\ddot{\hat{\mathbf{u}}}_f + \mathbf{M}_{fs}\ddot{\hat{\mathbf{u}}}_s - \mathbf{C}_{fs}\dot{\hat{\mathbf{u}}}_s + \mathbf{C}_{ff}\dot{\hat{\mathbf{u}}}_f - \mathbf{K}_{fp}\hat{\mathbf{p}} = \mathbf{f}_f \end{cases} \tag{4.16}$$

or, in matrix form,

$$\underbrace{\begin{bmatrix} \mathbf{M}_{ss} & \mathbf{0} & \mathbf{M}_{sf} \\ \mathbf{0} & \mathbf{0} & \mathbf{0} \\ \mathbf{M}_{fs} & \mathbf{0} & \mathbf{M}_{ff} \end{bmatrix}}_{\mathbf{M}} \begin{Bmatrix} \ddot{\hat{\mathbf{u}}}_s \\ \ddot{\hat{\mathbf{p}}} \\ \ddot{\hat{\mathbf{u}}}_f \end{Bmatrix} + \underbrace{\begin{bmatrix} \mathbf{C}_{ss} & \mathbf{0} & -\mathbf{C}_{sf} \\ \mathbf{0} & \mathbf{0} & \mathbf{0} \\ -\mathbf{C}_{fs} & \mathbf{0} & \mathbf{C}_{ff} \end{bmatrix}}_{\mathbf{C}} \begin{Bmatrix} \dot{\hat{\mathbf{u}}}_s \\ \dot{\hat{\mathbf{p}}} \\ \dot{\hat{\mathbf{u}}}_f \end{Bmatrix} + \underbrace{\begin{bmatrix} \mathbf{K}_{ss} & -\mathbf{K}_{sp} & \mathbf{0} \\ \mathbf{K}_{ps} & \mathbf{K}_{pp} & \mathbf{K}_{pf} \\ \mathbf{0} & -\mathbf{K}_{fp} & \mathbf{0} \end{bmatrix}}_{\mathbf{K}} \begin{Bmatrix} \hat{\mathbf{u}}_s \\ \hat{\mathbf{p}} \\ \hat{\mathbf{u}}_f \end{Bmatrix} = \begin{Bmatrix} \mathbf{f}_s \\ \mathbf{f}_p \\ \mathbf{f}_f \end{Bmatrix}, \tag{4.17}$$

where $\mathbf{M}$ is the overall mass matrix, $\mathbf{C}$ is the overall damping matrix, and $\mathbf{K}$ is the overall stiffness matrix. Entries of the mass matrix $\mathbf{M}$ are defined as

$$\mathbf{M}_{ss} = c_1 \int_{\bar{\Omega}} \mathbf{N}_s^\top \mathbf{N}_s d\bar{\Omega}, \tag{4.18}$$

$$\mathbf{M}_{sf} = c_2 \int_{\bar{\Omega}} \mathbf{N}_s^\top \mathbf{N}_f d\bar{\Omega}, \tag{4.19}$$

$$\mathbf{M}_{ff} = c_{11} \int_{\bar{\Omega}} \mathbf{N}_f^\top \mathbf{N}_f d\bar{\Omega}, \tag{4.20}$$

$$\mathbf{M}_{fs} = c_2 \int_{\bar{\Omega}} \mathbf{N}_f^\top \mathbf{N}_s d\bar{\Omega}, \tag{4.21}$$

which are the same as in Biot theory. The entries of the damping matrix $\mathbf{C}$ are

$$\mathbf{C}_{ss} = \underbrace{-c_5 \int_{\bar{\Omega}} \mathbf{B}_s^\top \mathbf{B}_s d\bar{\Omega}}_{\text{dCS addition}} + c_7 \int_{\bar{\Omega}} \mathbf{N}_s^\top \mathbf{N}_s d\bar{\Omega}, \tag{4.22}$$

$$\mathbf{C}_{sf} = \underbrace{(c_4 + c_6) \int_{\bar{\Omega}} \mathbf{B}_s^\top \mathbf{B}_f d\bar{\Omega}}_{\text{dCS addition}} + c_7 \int_{\bar{\Omega}} \mathbf{N}_s^\top \mathbf{N}_f d\bar{\Omega}, \tag{4.23}$$

$$\mathbf{C}_{ff} = \underbrace{(c_4 + c_6) \int_{\bar{\Omega}} \mathbf{B}_f^\top \mathbf{B}_f d\bar{\Omega}}_{\text{dCS addition}} + c_7 \int_{\bar{\Omega}} \mathbf{N}_f^\top \mathbf{N}_f d\bar{\Omega}, \tag{4.24}$$

$$\mathbf{C}_{fs} = \underbrace{(-c_5 - \frac{4}{3} c_{12}) \int_{\bar{\Omega}} \mathbf{B}_f^\top \mathbf{B}_s d\bar{\Omega}}_{\text{dCS addition}} + c_7 \int_{\bar{\Omega}} \mathbf{N}_f^\top \mathbf{N}_s d\bar{\Omega}, \tag{4.25}$$

where the terms marked as a dCS addition come from the fluid stress definition in such theory, which includes viscous dissipation within the fluid. Terms involving the c_7 parameter are present in both BT and dCS theories. For the stiffness matrix $\mathbf{K}$ the entries are

$$\mathbf{K}_{ss} = \int_{\bar{\Omega}} \mathbf{B}_s^\top \mathbf{C} \mathbf{B}_s d\bar{\Omega} + \underbrace{\frac{4}{3} c_8 \int_{\bar{\Omega}} \mathbf{B}_s^\top \mathbf{B}_s d\bar{\Omega}}_{\text{dCS addition}}, \tag{4.26}$$

$$\mathbf{K}_{sp} = (\alpha - c_3) \int_{\bar{\Omega}} \mathbf{B}_s^\top \mathbf{m} \mathbf{N}_p d\bar{\Omega}, \tag{4.27}$$

$$\mathbf{K}_{ps} = c_9 \int_{\bar{\Omega}} \mathbf{N}_p^\top \mathbf{m}^\top \mathbf{B}_s d\bar{\Omega}, \tag{4.28}$$

$$\mathbf{K}_{pp} = \int_{\bar{\Omega}} \mathbf{N}_p^\top \mathbf{N}_p d\bar{\Omega}, \tag{4.29}$$

$$\mathbf{K}_{pf} = c_{10} \int_{\bar{\Omega}} \mathbf{N}_p^\top \mathbf{m}^\top \mathbf{B}_f d\bar{\Omega}, \tag{4.30}$$

$$\mathbf{K}_{fp} = c_3 \int_{\bar{\Omega}} \mathbf{B}_f^\top \mathbf{m} \mathbf{N}_p d\bar{\Omega}, \tag{4.31}$$

where $\mathbf{K}_{ps}$ and $\mathbf{K}_{pf}$ can represent BT theory if δ_s, δ_f are chosen accordingly, i.e., $n = 1$ in equation (3.31). The additional dCS term in $\mathbf{K}_{ss}$ comes from the dimensionless parameter δ_μ, and vanishes for $\delta_\mu = 0$ (thus returning to BT). The entries for the force vector are given by

$$\begin{aligned}\mathbf{f}_s = &\int_{\Gamma_{ts}} \mathbf{N}_s^\top \bar{\mathbf{t}} d\Gamma - (\alpha - c_3) \int_{\Gamma_{ts}} \mathbf{N}_s^\top (\bar{p} \cdot \mathbf{n}) d\Gamma - (c_4 + c_6) \int_{\Gamma_{ts}} \mathbf{N}_s^\top \mathbf{B}_f (\bar{\mathbf{u}}_f \cdot \mathbf{n}) d\Gamma \\ &- c_5 \int_{\Gamma_{ts}} \mathbf{N}_s^\top \mathbf{B}_s (\bar{\dot{\mathbf{u}}}_s \cdot \mathbf{n}) d\Gamma + \frac{4}{3} c_8 \int_{\Gamma_{ts}} \mathbf{N}_s^\top \mathbf{B}_s (\bar{\mathbf{u}}_s \cdot \mathbf{n}) d\Gamma + \int_{\Omega} \mathbf{N}_s^\top \bar{\mathbf{b}}_s d\Omega,\end{aligned} \tag{4.32}$$

$$\mathbf{f}_p = \int_{\Omega} \mathbf{N}_p^\top s d\Omega, \tag{4.33}$$

$$\begin{aligned}\mathbf{f}_f = &-c_3 \int_{\Gamma_{tf}} \mathbf{N}_f^\top (\bar{p} \cdot \mathbf{n}) d\Gamma + (c_4 + c_6) \int_{\Gamma_{tf}} \mathbf{N}_f s^\top \mathbf{B}_f (\bar{\dot{\mathbf{u}}}_f \cdot \mathbf{n}) d\Gamma \\ &+ (c_5 + \frac{4}{3} c_{12}) \int_{\Gamma_{tf}} \mathbf{N}_f^\top \mathbf{B}_s (\bar{\dot{\mathbf{u}}}_s \cdot \mathbf{n}) d\Gamma + \int_{\Omega} \mathbf{N}_f^\top \bar{\mathbf{b}}_f d\Omega.\end{aligned} \tag{4.34}$$

Considering the generalized Newmark method [141] for time integration, the fully discretized system is written as

$$\begin{bmatrix} \hat{\mathbf{K}}_{ss} & \hat{\mathbf{K}}_{sp} & \hat{\mathbf{K}}_{sf} \\ \mathbf{K}_{ps} & \mathbf{K}_{pp} & \mathbf{K}_{pf} \\ \hat{\mathbf{K}}_{fs} & \hat{\mathbf{K}}_{fp} & \hat{\mathbf{K}}_{ff} \end{bmatrix} \begin{Bmatrix} \hat{\mathbf{u}}_s^{n+1} \\ \hat{\mathbf{p}}^{n+1} \\ \hat{\mathbf{u}}_f^{n+1} \end{Bmatrix} = \begin{Bmatrix} \hat{\mathbf{f}}_s^{n+1} \\ \mathbf{f}_p^{n+1} \\ \hat{\mathbf{f}}_f^{n+1} \end{Bmatrix}; \tag{4.35}$$

and the sub-matrices from (4.35) are given by

$$\bar{\mathbf{K}}_{ss} = \frac{1}{\beta\Delta t^2}\mathbf{M}_{ss} + \frac{\gamma}{\beta\Delta t}\mathbf{C}_{ss} + \mathbf{K}_{ss}, \quad (4.36) \qquad \bar{\mathbf{K}}_{fs} = \frac{1}{\beta\Delta t^2}\mathbf{M}_{fs} - \frac{\gamma}{\beta\Delta t}\mathbf{C}_{fs}, \quad (4.39)$$

$$\bar{\mathbf{K}}_{sp} = -\mathbf{K}_{sp}, \quad (4.37) \qquad \bar{\mathbf{K}}_{fp} = -\mathbf{K}_{fp}, \quad (4.40)$$

$$\bar{\mathbf{K}}_{sf} = \frac{1}{\lambda\Delta t^2}\mathbf{M}_{sf} - \frac{\zeta}{\lambda\Delta t}\mathbf{C}_{sf}, \quad (4.38) \qquad \bar{\mathbf{K}}_{ff} = \frac{1}{\lambda\Delta t^2}\mathbf{M}_{ff} + \frac{\zeta}{\lambda\Delta t}\mathbf{C}_{ff} \quad (4.41)$$

$$\begin{aligned}\hat{\mathbf{f}}_s^{n+1} = \mathbf{f}_s^{n+1} &+ \mathbf{M}_{ss}\left(\frac{1}{\beta\Delta t^2}\hat{\mathbf{u}}_s^n + \frac{1}{\beta\Delta t}\dot{\hat{\mathbf{u}}}_s^n + (\frac{1}{2\beta}-1)\ddot{\hat{\mathbf{u}}}_s^n\right)\\ &+ \mathbf{M}_{sf}\left(\frac{1}{\lambda\Delta t^2}\hat{\mathbf{u}}_f^n + \frac{1}{\lambda\Delta t}\dot{\hat{\mathbf{u}}}_f^n + (\frac{1}{2\lambda}-1)\ddot{\hat{\mathbf{u}}}_f^n\right)\\ &+ \mathbf{C}_{ss}\left(\frac{\gamma}{\beta\Delta t}\hat{\mathbf{u}}_s^n + (\frac{\gamma}{\beta}-1)\dot{\hat{\mathbf{u}}}_s^n + \Delta t(\frac{\gamma}{2\beta}-1)\ddot{\hat{\mathbf{u}}}_s^n\right)\\ &+ \mathbf{C}_{sf}\left(-\frac{\zeta}{\lambda\Delta t}\hat{\mathbf{u}}_f^n - (\frac{\zeta}{\lambda}-1)\dot{\hat{\mathbf{u}}}_f^n - \Delta t(\frac{\zeta}{2\lambda}-1)\ddot{\hat{\mathbf{u}}}_f^n\right), \end{aligned} \quad (4.42)$$

$$\begin{aligned}\hat{\mathbf{f}}_f^{n+1} = \mathbf{f}_f^{n+1} &+ \mathbf{M}_{fs}\left(\frac{1}{\beta\Delta t^2}\hat{\mathbf{u}}_s^n + \frac{1}{\beta\Delta t}\dot{\hat{\mathbf{u}}}_s^n + (\frac{1}{2\beta}-1)\ddot{\hat{\mathbf{u}}}_s^n\right)\\ &+ \mathbf{M}_{ff}\left(\frac{1}{\lambda\Delta t^2}\hat{\mathbf{u}}_f^n + \frac{1}{\lambda\Delta t}\dot{\hat{\mathbf{u}}}_f^n + (\frac{1}{2\lambda}-1)\ddot{\hat{\mathbf{u}}}_f^n\right)\\ &+ \mathbf{C}_{fs}\left(-\frac{\gamma}{\beta\Delta t}\hat{\mathbf{u}}_s^n - (\frac{\gamma}{\beta}-1)\dot{\hat{\mathbf{u}}}_s^n - \Delta t(\frac{\gamma}{2\beta}-1)\ddot{\hat{\mathbf{u}}}_s^n\right)\\ &+ \mathbf{C}_{ff}\left(\frac{\zeta}{\lambda\Delta t}\hat{\mathbf{u}}_f^n + (\frac{\zeta}{\lambda}-1)\dot{\hat{\mathbf{u}}}_f^n + \Delta t(\frac{\zeta}{2\lambda}-1)\ddot{\hat{\mathbf{u}}}_f^n\right). \end{aligned} \quad (4.43)$$

For the numerical examples herein presented, the Newmark parameters are taken as $\beta = \gamma = \lambda = \zeta = 0.7$ so that some numerical damping is added to the problem without significantly impacting the solution. Other combinations of $\beta, \gamma, \lambda, \zeta$ led to significant artificial damping.

Regarding the shape functions considered, mixed-order Taylor-Hood elements [170] are suitable and often employed in two-field BT formulations [64] so that the LBB stability condition is satisfied [204, 108]. It has been observed that three-field $u_s - p - u_f$ BT formulation allows the adoption of shape functions of the same (linear) order without numerical

locking [206, 91]. In the upcoming examples, the use of same- and mixed-order elements is investigated. Regardless, it is noteworthy that the fulfillment of stability requirements for either all-linear or mixed elements in the dCS theory has not been mathematically proven.

4.4 Dimensionless Analysis

The system of governing equations (4.9)-(4.11) for the dCS theory involves three aspects that are neglected in the Biot theory. The first aspect comes from the definition of the fluid stress, since

$$\boldsymbol{\sigma}_f^{BT} = -\eta_0 \mathbf{I} p, \qquad \boldsymbol{\sigma}_f^{dCS} = -\eta_0 \mathbf{I} p + \eta_0 \mu_f \nabla \dot{\mathbf{u}}_f + \eta_0 (\xi_f + \frac{\mu_f}{3}) \nabla \cdot \dot{\mathbf{u}}_f + \xi_f \dot{\eta}; \tag{4.44}$$

meaning that in the BT theory the fluid stress is defined only in terms of the fluid pressure, whilst in the dCS model the viscous dissipation within the fluid is included. The second aspect to be studied comes from the fact that porosity is taken as a dynamic variable in the dCS theory. Even though it is implicitly present in (4.9)-(4.11), new parameters are added to the problem: the compliance coefficients δ_s, δ_f. More to that, such coefficients are dependent on the porosity effective pressure coefficient n [157] as in (3.31). In this sense, only when $n = 1$ one can recover the results from Biot theory. The third aspect to be mentioned is the addition of the parameter δ_μ, which connects the solid shear modulus to a macroscopic averaged value (4.5). In BT theory the parameter δ_μ is non existent, and thus the macroscopic shear modulus is given by $\mu_M = (1-\eta_0)\mu_s$. Hence, the dCS FE model can deviate from BT FE results due to (i) the addition of fluid viscous dissipation terms, (ii) variations in the n coefficient, and (iii) nonzero values of the dimensionless parameter δ_μ.

The dimensionless formulation herein presented is considered to evaluate the relative impact that these differences in dCS theory have when comparing to BT. Firstly, an expression for the time scaling parameter is derived assuming that

$$c_1 = [(1-\eta_0)\rho_s - \rho_{12}] \frac{L^2}{E t_d^2} = 1 \longrightarrow t_d = L\sqrt{\frac{(1-\eta_0)\rho_s - \rho_{12}}{E}}. \tag{4.45}$$

Substituting t_d into (4.9)-(4.11), the dimensionless constants are rewritten as in Table 4.3. Let us assume first that $\delta_\mu = 0$, and compare the damping contributions of the BT theory and the addition of the dCS theory. From $\mathbf{C}_{ss}$ and $\mathbf{C}_{fs}$, we have a relation between the dimensionless coefficients as in

$$\frac{c_5}{c_7} = \frac{\xi_f \delta_s \kappa}{\mu_f \eta_0^2 L^2}, \tag{4.46}$$

Table 4.3: Non-dimensional parameters in (4.9)-(4.11) when $c_1 = 1$.

$c_1 = 1$	$c_5 = c_4 \dfrac{\xi_f \delta_s}{\eta_0 \mu_f}$	$c_9 = \dfrac{\delta_s}{\eta_0}$
$c_2 = \dfrac{\rho_{12}}{(1-\eta_0)\rho_s - \rho_{12}}$	$c_6 = c_4 \dfrac{(\eta_0 \xi_f + \eta_0 \mu_f/3 - \xi_f \delta_f)}{\eta_0 \mu_f}$	$c_{10} = 1 - \dfrac{\delta_f}{\eta_0}$
$c_3 = \dfrac{\eta_0 K_f}{E}$	$c_7 = c_4 \dfrac{\eta_0 L^2}{\kappa}$	$c_{11} = \dfrac{\eta_0 \rho_f - \rho_{12}}{(1-\eta_0)\rho_s - \rho_{12}}$
$c_4 = \dfrac{\eta_0 \mu_f}{L\sqrt{E[\eta_0 \rho_f - \rho_{12}]}}$	$c_8 = -\dfrac{\mu_s}{E}\delta_\mu$	$c_{12} = -c_4 \dfrac{(1-\eta_0)\delta_\mu}{\eta_0}$

and similar from the matrices $\mathbf{C}_{sf}$, $\mathbf{C}_{ff}$,

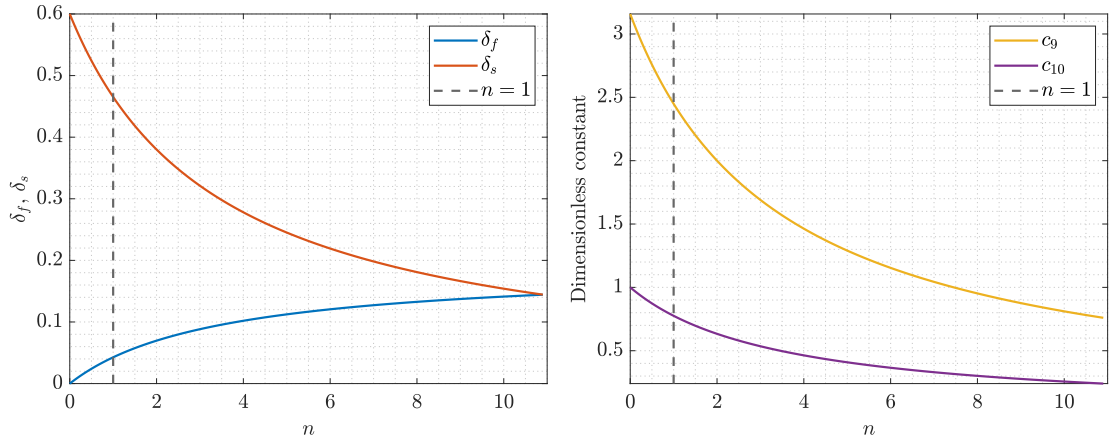
$$\frac{c_4 + c_6}{c_7} = \frac{\kappa}{\mu_f \eta_0^2 L^2}\left[\eta_0 \xi_f + \frac{4}{3}\eta_0 \mu_f - \xi_f \delta_f\right]. \tag{4.47}$$

One can infer that, for ratios close to zero, the added terms from dCS theory have little impact in the overall damping of the system. When focusing on porous media applications in geomechanics, the coupled problem to be solved usually combines water and some type of soil/rock material. The water viscosity μ_f and bulk viscosity ξ_f are of the same order, i.e. $\mu_f = 1 \times 10^{-3}$ Pa $\cdot$ s, $\xi_f = 2.8 \times 10^{-3}$ Pa $\cdot$ s (Table 4.1). Hence, their relative ratio does not contribute to the relations in (4.46), (4.47). The initial porosity η_0 varies from 0 to 1, thus not being of significant influence. The range of δ_s relies on the parameters involved in its definition

$$\delta_s = \frac{(\alpha - \eta_0)\eta_0}{K_f\left[\dfrac{1}{M} - (1-n)\dfrac{(\alpha - \eta_0)}{K_s}\right]}; \tag{4.48}$$

since $0 \leq \alpha \leq 1$ and $0 \leq \eta_0 \leq 1$, the most significant changes in δ_s come from the bulk modulus of the constituents. Considering typical values of fluid bulk modulus K_f and solid bulk modulus K_s for a water-saturated sandstone (Table 4.1), Figure 4.1a depicts the variation of δ_s, δ_f with n. Due to the small range that δ_s, δ_f assume, such parameters also have modest impact in (4.46), (4.47).

We reiterate that the constant c_7 in BT theory accounts for a high-frequency correction factor F. Additional tests showed that, even for high frequencies, F is still in the order 10^0 to 10^1 and hence do not significantly contribute to the ratios expressed in (4.46), (4.47). Therefore, they depend heavily on the adopted values for intrinsic permeability κ



(a) Variation of δ_f, δ_f (b) Variation of c_9, c_{10}

Figure 4.1: Changes in (a) the compliance coefficients δ_f, δ_s and (b) in the dimensionless constants c_9, c_{10} (Table 4.3) for $n = 0$ to $n = K_s/K_f$; the material parameters are taken from Table 4.1.

and characteristic length L. For instance, κ can approximately vary between 10^{-9}m^2 and 10^{-20}m^2 for rocks and soils [90]. If the characteristic length is taken in the order of meters or kilometers, the ratio between dCS and BT contributions varies between 10^{-11} to 10^{-26}. Consequently, the contribution of the viscous dissipation from dCS theory is negligible for water-saturated sandstone.

To increase the overall contribution of viscous dissipation within the fluid, one could think about reducing the value of L. The constant c_5 from dCS theory is inversely proportional to L, while c_7, related to the damping from BT theory, is directly proportional to L. Therefore, decreasing the characteristic length would lead to an increase in c_5, which would be somewhat limited by the order ξ_f and, hence, not significant. More to that, a decrease in L means reducing c_7, term responsible for most of the damping. When L is small, there is little damping in either BT or dCS model. Nonetheless, as L decreases, the order of magnitude of BT and dCS approximate, and thus dCS contributions become relatively significant.

Although the damping contribution from the dCS model is negligible when considering water-saturated sandstone, other solid-fluid combinations should be investigated. Table 4.4 shows the values obtained for the c_7 constant, representing the damping from BT theory, and for the c_4, c_5, c_6 constants, the additional damping in dCS theory, for different porous media systems. Regardless of the medium considered, the dCS additional damping

is negligible compared to the damping intrinsic to the BT theory. In a limiting case, for instance, let us consider $\xi_f = 100$ GPa $\cdot$ s. If the other parameters are taken from a water-saturated sandstone, the dimensionless coefficients would be $c_7 = 348.69$ and $c_5 = 844.94$. Therefore, the dCS addition to the damping matrix would be in the same order of BT damping given that bulk viscosity assumes high values.

Table 4.4: Values of dimensionless parameters, as defined in Table 4.3, for various materials. The combinations are: M1 - water and sandstone, M2 - light oil and sandstone, M3 - heavy oil and sandstone, M4 - water and cancellous bone.

	M1 [193]	M2 [83]	M3 [175]	M4 [58]
c_7 (BT)	348.69	1.01×10^{6}	8.19×10^{5}	0.53
c_5 (dCS addition)	2.36×10^{-11}	1.39×10^{-11}	7.54×10^{-6}	4.42×10^{-8}
$c_4 + c_6$ (dCS addition)	1.21×10^{-11}	2.40×10^{-9}	3.44×10^{-6}	3.21×10^{-7}

Besides the addition of the fluid viscous dissipation terms, the dCS model deviates from BT theory when $n \neq 1$. Changes in n happen through the compliance coefficients δ_s, δ_f, as seen in (3.31). Such changes have negligible impact on the parameters c_5, c_6, associated with damping. On the other hand, n also appears in the sub-matrices $\mathbf{K}_{ps}$ (4.28) and $\mathbf{K}_{pf}$ (4.30), with respective dimensionless coefficients c_9 and c_{10}. Figure 4.1b shows the behaviour of such constants as n varies; an increase in the porosity effective pressure coefficient n leads to a reduction in the contributions of both parameters and, consequently, of $\mathbf{K}_{ps}$ and $\mathbf{K}_{pf}$. The extent of these changes will be assessed in the upcoming numerical examples.

When the dimensionless parameter δ_μ is nonzero, the coefficients c_8, c_{12} are nonzero, thus affecting the submatrices $\mathbf{K}_{ss}$ and $\mathbf{C}_{fs}$, respectively. There are few studies in the literature that explore the effects of δ_μ – and include the constant into the porous media model [151, 152]. The work of Hickey [83, 85] is one example; considering a sandstone material of $\mu_s = 23$ GPa, the experimentally obtained macroscopic modulus is $\mu_M = 4.9$ GPa [83]. For a porosity of $\eta_0 = 0.25$, this leads to $\delta_\mu = 0.72$. Other values of δ_μ for a fixed μ_s and different η_0 were reported by Quiroga-Goode et. al. [152], also yielding values in the range of $0.50 < \delta_\mu < 0.93$. One can observe that, for values of $\delta_\mu > 0$, the contributions from $\mathbf{C}_{fs}$, $\mathbf{K}_{ss}$ are reduced. In terms of the relative magnitude of the term in $\mathbf{C}_{fs}$, the typical values of c_5 listed in Table 4.4 and the aforementioned range for δ_μ yields $c_8 \gg c_5$, and the order of magnitude of the ratio c_{12}/c_7 depends on the material. On the other hand, looking at $\mathbf{K}_{ss}$, the additional term containing c_8 is in the same order of the BT term, which may lead to significant changes when $\delta_\mu \neq 0$. The following numerical examples will also explore the extent of this effect.

4.5 Verification and Convergence Study

The robustness of the developed FE model is verified through the simulation of a one-dimensional case. The manufactured solution adopted is of the form

$$u_s(x,t) = \sin(xt)/1000 \ \ [\text{m}], \tag{4.49}$$

$$u_f(x,t) = \cos(xt)/1000 \ \ [\text{m}], \tag{4.50}$$

$$p(x,t) = \sin(xt)\cos(xt)/1000 \ \ [\text{GPa}]; \tag{4.51}$$

the choice of functions for the field variables was made so that the solution was smooth; trigonometric functions were also employed in previous convergence studies for BT theory [66, 56].

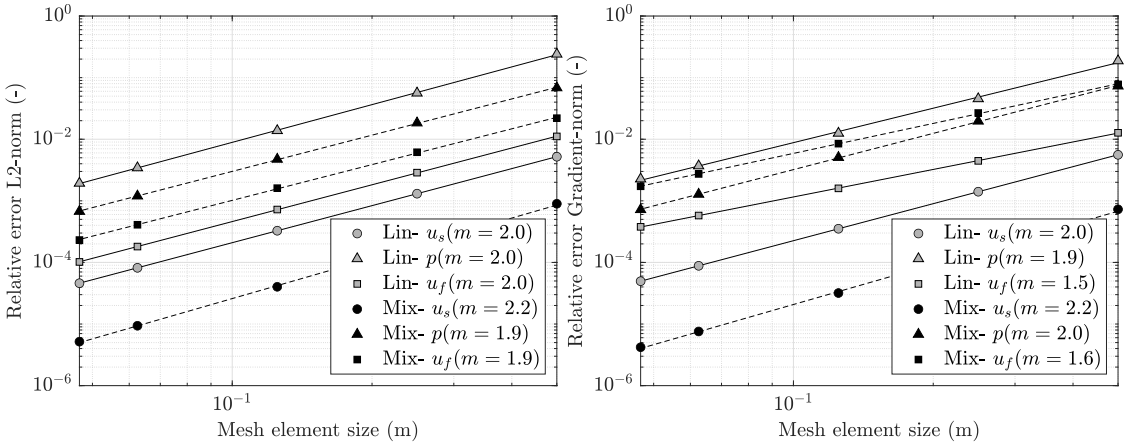
The material parameters represent a water-saturated sandstone material (Table 4.1). The domain has a length of $L = 6\text{m}$; initial and essential boundary conditions are properly prescribed according to the manufactured solution. The time step considered is $\Delta t = 10^{-5}\text{s}$ for a final simulation time of $t_{end} = 1\text{s}$. To perform a convergence study, Δt is fixed as the mesh is refined. Figures 4.2a and 4.2b depict the relative errors for the L2-norm and the gradient-norm considering (i) linear elements for all fields and (ii) linear elements for the fluid pressure field, and quadratic elements for the solid and fluid displacement fields. For the first case (i), the convergence rates for the L2-norm are $\mathcal{O}(h^{2.0})$ for $\mathbf{u}_s$, $\mathcal{O}(h^{2.0})$ for p, $\mathcal{O}(h^{2.0})$ for $\mathbf{u}_f$. For the gradient-norm, the convergence rates are $\mathcal{O}(h^{2.0})$ for $\mathbf{u}_s$, $\mathcal{O}(h^{1.9})$ for p, $\mathcal{O}(h^{1.5})$ for $\mathbf{u}_f$. Considering case (ii), the convergence rate for $\mathbf{u}_s$ slightly improves to $\mathcal{O}(h^{2.2})$ in both norms; for p, the L2-norm rate decreases to $\mathcal{O}(h^{1.9})$ and the gradient-norm rate increases to $\mathcal{O}(h^{2.0})$. Considering the $\mathbf{u}_f$ field, L2-norm rate is deteriorated to $\mathcal{O}(h^{1.9})$ and gradient-norm improves to $\mathcal{O}(h^{1.6})$.

The convergence rate for the solid displacement field is higher than for the fluid pressure field, which seems reasonable since the former is approximated with quadratic shape functions. Considering that the same approximation is used for the fluid displacement field, its relative lower convergence rate could be related to the form of the discrete formulation. The entries for the fluid displacement field in (4.17) are in terms of its first and second time derivatives, leading to zero entries in the $\mathbf{K}$ matrix. We believe that the lack of fluid displacement terms in two of the three semi-discrete equations could account in part for the difference between u_s and u_f convergence rates. It is also noteworthy that there is little difference between the convergence rate when considering all linear fields or a mixed order formulation.

The obtained convergence rates are lower than optimal rates found in uncoupled problems. This has been previously observed for BT theory by Mikelic et. al. [127], who noted

that coupled-problem rates decrease as the coupling strength is increased. Convergence is then limited by the lowest approximation order, i.e. linear pressure field. Previous works that reported optimal convergence rates for the BT framework have omitted the chosen material parameters [138, 139] or have considered random parameters [56]. Due to the coupled nature of the problem, it is still unclear what value the convergence rates should assume, and how to quantify the coupling strength effect on them. More to that, existent literature is based on the BT theory, and thus there is still uncertainty regarding how convergence for the dCS FE model should behave.

A secondary convergence study was performed in terms of time step refinement. To this end, a mesh of $ne = 100$ elements was fixed as the time step was reduced; the adopted reference solution is associated with a time step of $\Delta t = 10^{-5}$s. Linear elements were used on the pressure field discretization, while quadratic elements were employed on the solid and fluid displacement fields. The study showed that the convergence rates for the relative L2-norm error are equal to $\mathcal{O}(h^{1.01})$ for $\mathbf{u}_s$, $\mathcal{O}(h^{0.99})$ for p, and $\mathcal{O}(h^{1.02})$ for $\mathbf{u}_f$; see Figure 4.3. These rates are as predicted for the generalized Newmark method [141] with coefficients equal to 0.7, providing a first order accuracy in time. The use of an alternative set of Newmark parameters can lead to different results.



(a) L2 norm (b) Gradient norm

Figure 4.2: Convergence study for mesh size refinement considering (a) L2-norm and (b) gradient-norm; the convergence rates m for each field are indicated in the legend for all linear (Lin-) and mixed order elements (Mix-).

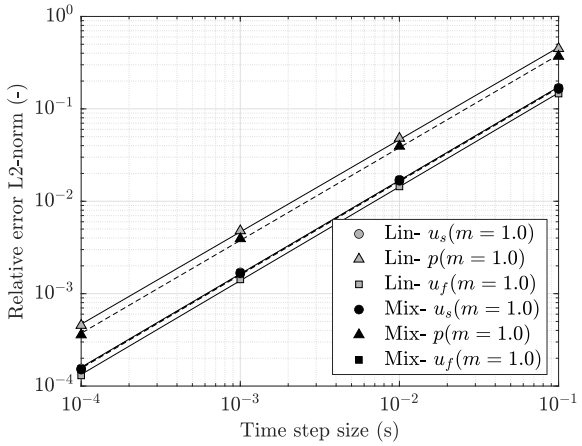


Figure 4.3: Convergence study for time step refinement considering; the convergence rates m for each field are indicated in the legend for all linear (Lin-) and mixed order elements (Mix-).

4.6 Numerical Examples

4.6.1 One-dimensional pulse

A one-dimensional problem is considered to evaluate the wave propagation patterns and the differences between BT and dCS theories. The material parameters considered refer to a water-saturated sandstone, as listed in Table 4.1, and $\delta_\mu = 0$. A sinusoidal variation is applied in the solid displacement field in the middle of the domain with dimension $L = 500$m, expressed as

$$u(t) = P_0[\sin(\pi f t) - 0.5\sin(2\pi t f)], t < 1/f \tag{4.52}$$

where $f = 1$kHz is the source frequency and $P_0 = 1$GN is the amplitude. Table 4.5 lists the speed and wavelength of all dCS wave types for the analyzed water-saturated sandstone and valid at the frequency range $0 - 1$kHz. For a dry sandstone material, the wave speed of P and S waves would be $v_P^{dry} = 2481$ m/s and $v_S^{dry} = 1519$ m/s, respectively.

A mesh of $ne = 5 \times 10^3$ elements is considered, and a linear interpolation is used for solid displacement, fluid pressure, and fluid displacement fields. The final simulation time is taken as $t_{end} = 5 \times 10^{-2}$s for a time step of $\Delta t = 10^{-5}$s. Figure 4.4 shows the solid velocity, pressure, and fluid velocity distribution for BT and dCS theories, assuming different values of n for the latter.

Table 4.5: Velocity and wavelength of dCS P and S waves for the water-saturated sandstone [193] and source frequency of 1kHz.

Parameter	Fast P	Slow P	Fast S	Slow S
Wave velocity [m/s]	4433.32	68.85	3086.30	2.01
Wavelength [m]	4.43	0.07	3.09	0.0020

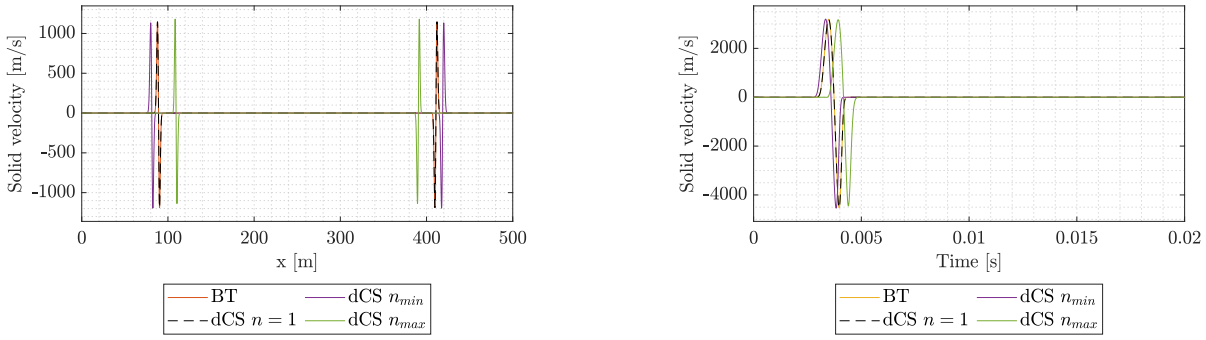
There are no noticeable differences between the results for BT and dCS ($n = 1$) theories, showing that the addition of the viscous dissipation terms within the fluid yields no changes in the solid/fluid behavior – as predicted in the dimensionless analysis. The difference between the two curves is in the order of 10^{-12}. It is noteworthy to reiterate that, for $n = 1$ in the dCS theory, the fluid viscous dissipation terms in the damping submatrices (4.22)-(4.25) are the sole difference when compared to the BT formulation.

The second result to notice is the variation in the curves due to the parameter n introduced in dCS theory. For $n < 1$ the fluid pressure reaches higher values, and the opposite happens to $n > 1$, when taking the case $n = 1$ as a reference. For the solid and fluid velocities this variation is more subtle, and the maximum and minimum values seem to be approximately the same. It is possible, nonetheless, to notice a small shift in the wave propagation pattern; for $n > 1$ the wave speed is increased, and consequently so is the wave length. The opposite behavior is observed for $n < 1$.

When $n < 1$, fluid presents less resistance to boundary (solid-fluid interface) movements. Hence, as the boundary moves more freely, porosity increases and so does the pressure in the bulk, compared to the case where $n = 1$. Since the fluid pressure is higher, the solid constituent movement is somewhat restricted, and thus solid displacements are relatively smaller. On the other hand, when $n > 1$ the fluid resistance to boundary movements increases, showing a rigid-like behavior. Because of that, changes in porosity are reduced, and so is the fluid pressure. Consequently, the lower pressure allows solid grains to move more easily, and hence solid displacements are augmented when compared to $n = 1$.

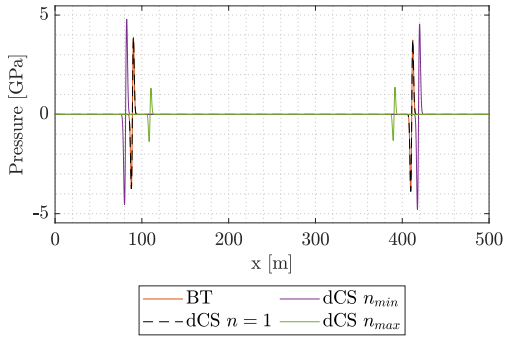
Critical frequency limit

As observed in Figure 4.4, the imposed boundary conditions lead to the propagation of a fast P wave. Nevertheless, the slow P wave mentioned in Biot formulation [15] is not visible. This can be explained by the characteristics of such wave, as mentioned in previous literature and shown through experimental and numerical data [147, 156]. There is a critical frequency limit that separates two distinct behaviors of the slow P wave [177]; below this

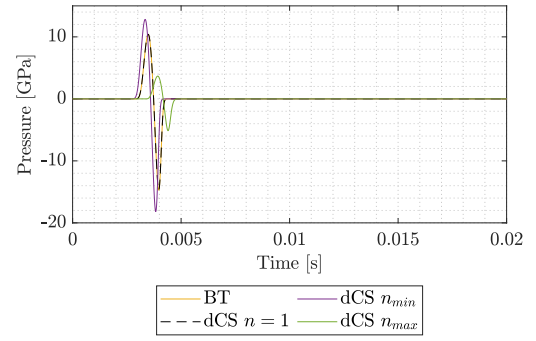


(a) $\dot{u}_s$, $t_{end} = 5 \times 10^{-2}$s

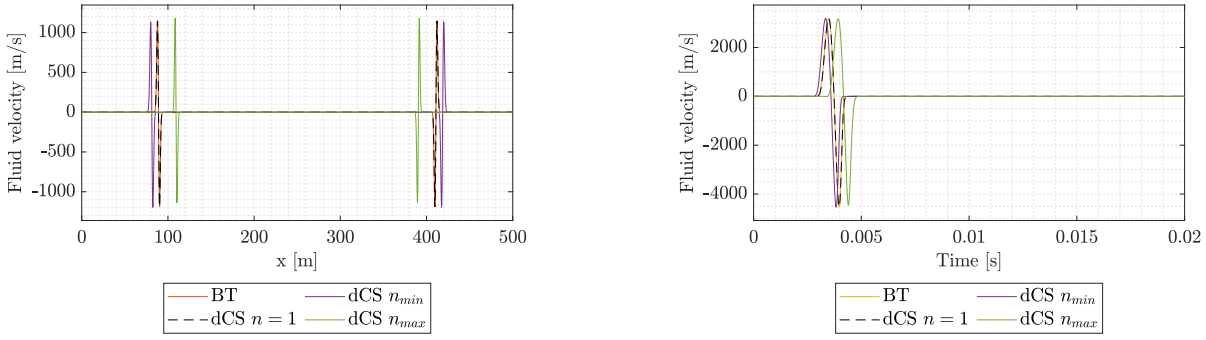
(b) $\dot{u}_s$, $x = 260$m



(c) p, $t_{end} = 5 \times 10^{-2}$s



(d) p, $x = 260$m



(e) $\dot{u}_f$, $t_{end} = 5 \times 10^{-2}$s

(f) $\dot{u}_f$, $x = 260$m

Figure 4.4: Impact of the effective pressure coefficient n on (a, b) solid velocity, (c, d) pressure, and (e, f) fluid velocity for one-dimensional wave propagation with permeability $\kappa = 1.88 \times 10^{-13}\text{m}^2$. Figures (a), (c), (e) show variation over the domain at $t_{end} = 5 \times 10^{-2}$s, while Figures (b), (d), (f) show variation over time at $x = 260$m.

critical value, slow P waves are highly attenuated and have slow speed. Above this value,

however, such wave becomes propagatory – being known for higher propagation speeds and small dispersion.

The critical frequency limit can be expressed as [177]

$$\omega_c = \frac{\mu_f \eta_0}{\kappa \rho_f}, \tag{4.53}$$

and thus being restricted to the material parameters of the medium. In order to see the propagation of slow P waves in the current example, for the same frequency of $f = 1$kHz, we increase the intrinsic permeability κ. Let us consider a high permeability value of $\kappa_h = 10^{-8}$ m^2. In this case, since the source frequency is greater than the critical frequency limit, we enter the high-frequency BT regime. The correction factor F, as mentioned in Section 4.2, is introduced in the BT framework using the expression given by Johnson [92]. Table 4.6 lists the updated values of wave velocity and wavelength for the permeability κ_h; the remaining material parameters are as listed in Table 4.1. At the high-frequency regime, wave velocity for BT and dCS theories is slightly different; changes in wavelength are even less noticeable.

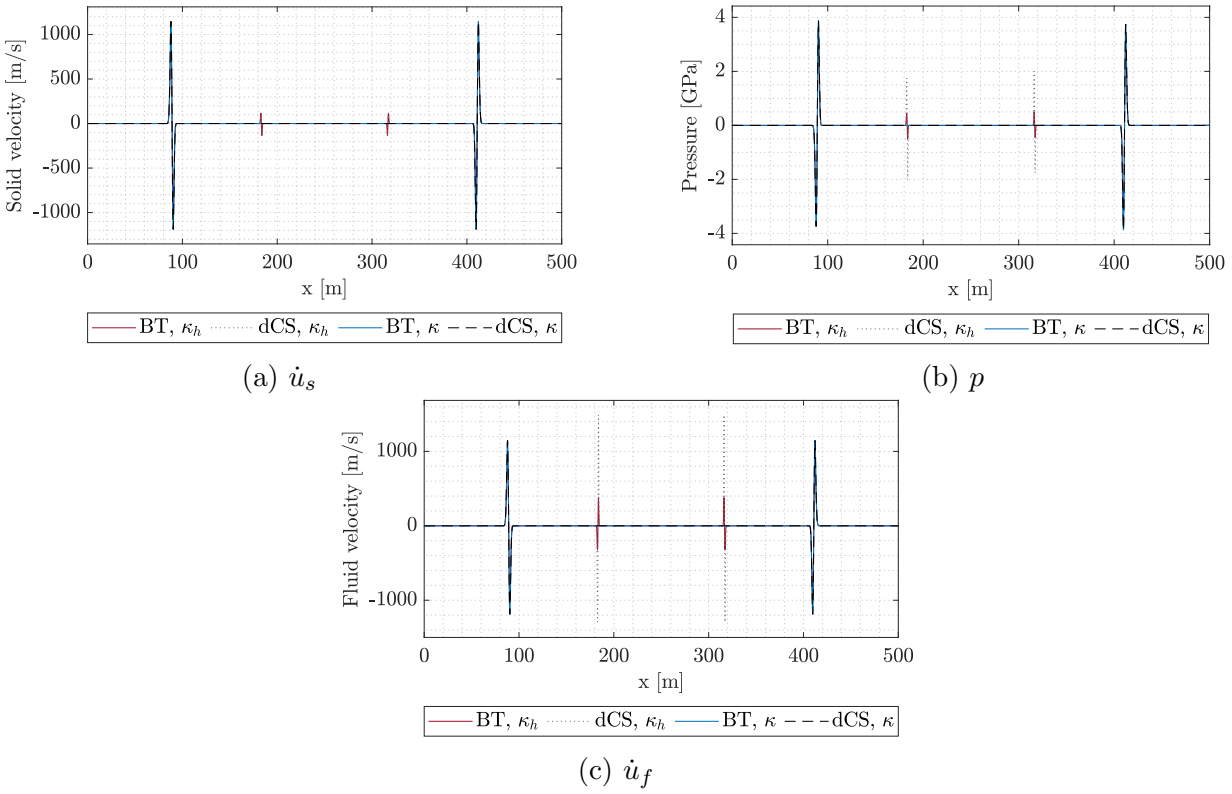
Table 4.6: Velocity and wavelength of P and S waves for water-saturated sandstone [193] with $\kappa_h = 10^{-8}$ m^2 and source frequency of 1kHz.

Parameter	Fast P	Slow P	Fast S	Slow S
dCS Wave velocity [m/s]	4480.45	1490.80	3222.48	0.04
dCS Wavelength [m]	4.48	1.49	3.22	4.21×10^{-5}
BT Wave velocity [m/s]	4484.54	1550.40	3231.59	-
BT Wavelength [m]	4.48	1.55	3.23	-

For simulations with κ_h, the mesh discretization is refined to $ne = 5 \times 10^4$ elements, while the time step size and final simulation time are maintained. The increase in the number of elements compared to the previous simulation ($\kappa = 1.88 \times 10^{-13}$m^2) is due to the fact that the mesh discretization of $ne = 5 \times 10^3$ elements was insufficient to capture the slow wave propagation for the high-permeability (κ_h) case.

Figure 4.5 depicts the solid velocity, pressure, and fluid velocity distribution throughout the domain at the final simulation time for both permeability values and both BT theory and dCS theory with $n = 1$. It is noticeable that the higher intrinsic permeability yields propagation of slow waves, which is not visible when adopting κ. The BT slow P wave is more attenuated for the fluid component than the correspondent dCS wave; the difference

in attenuation is less noticeable for the solid component. The fast wave is almost identical for both permeability values, with a slightly smaller amplitude for κ.

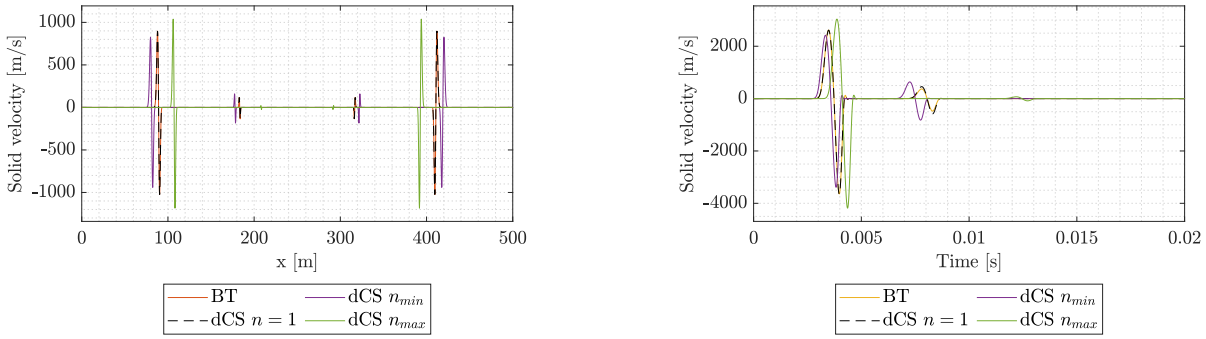


(a) $\dot{u}_s$ (b) p

(c) $\dot{u}_f$

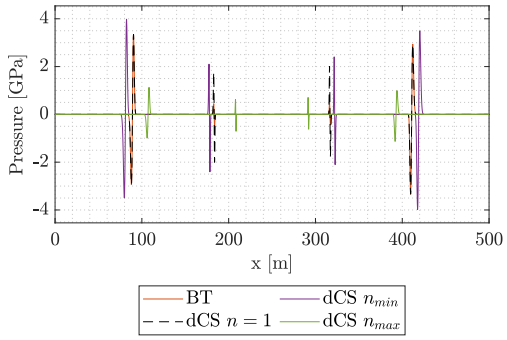
Figure 4.5: Comparison between BT and dCS results for (a) solid velocity, (b) pressure, and (c) fluid velocity considering $\kappa_h = 10^{-8}$ m^2 and $\kappa = 10^{-13}$ m^2. Plots show curves at the final simulation time $t_{end} = 5 \times 10^{-2}$s.

For the new permeability $\kappa_h = 10^{-8}$ m^2, Figure 4.6 depicts the distribution of solid velocity, pressure, and fluid velocity for different n. The slow P wave yields the same behavior for all three fields regarding changes in n: $n > 1$ leads to more attenuation, when $n < 1$ causes less attenuation. Furthermore, attenuation is higher in the solid than in the fluid component. The dimensionless analysis in Section 4.4 showed that the dCS model adds a negligible amount of damping to the $\mathbf{C}$ matrix components (4.22) - (4.25). However, in this example we notice that there are attenuation changes for different values of n. This is related to the fact that n is present in submatrices (4.26) - (4.31) of the stiffness matrix $\mathbf{K}$. Therefore, changes in n do not affect the damping matrix by itself, but attenuation is still present since n alters the physical properties of the medium.

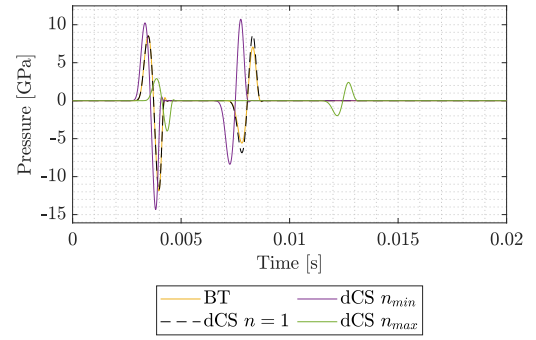


(a) $\dot{u}_s$, $t_{end} = 5 \times 10^{-2}$s

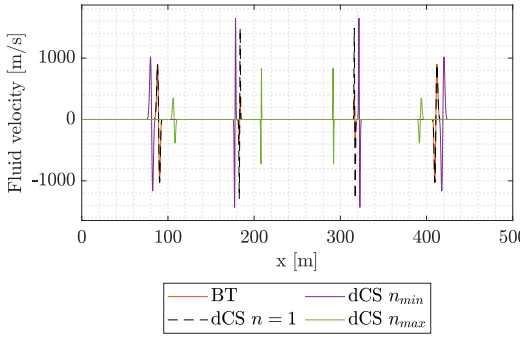
(b) $\dot{u}_s$, $x = 260$m



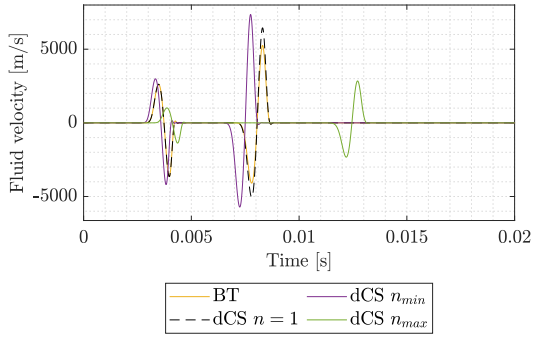
(c) p, $t_{end} = 5 \times 10^{-2}$s



(d) p, $x = 260$m



(e) $\dot{u}_f$, $t_{end} = 5 \times 10^{-2}$s



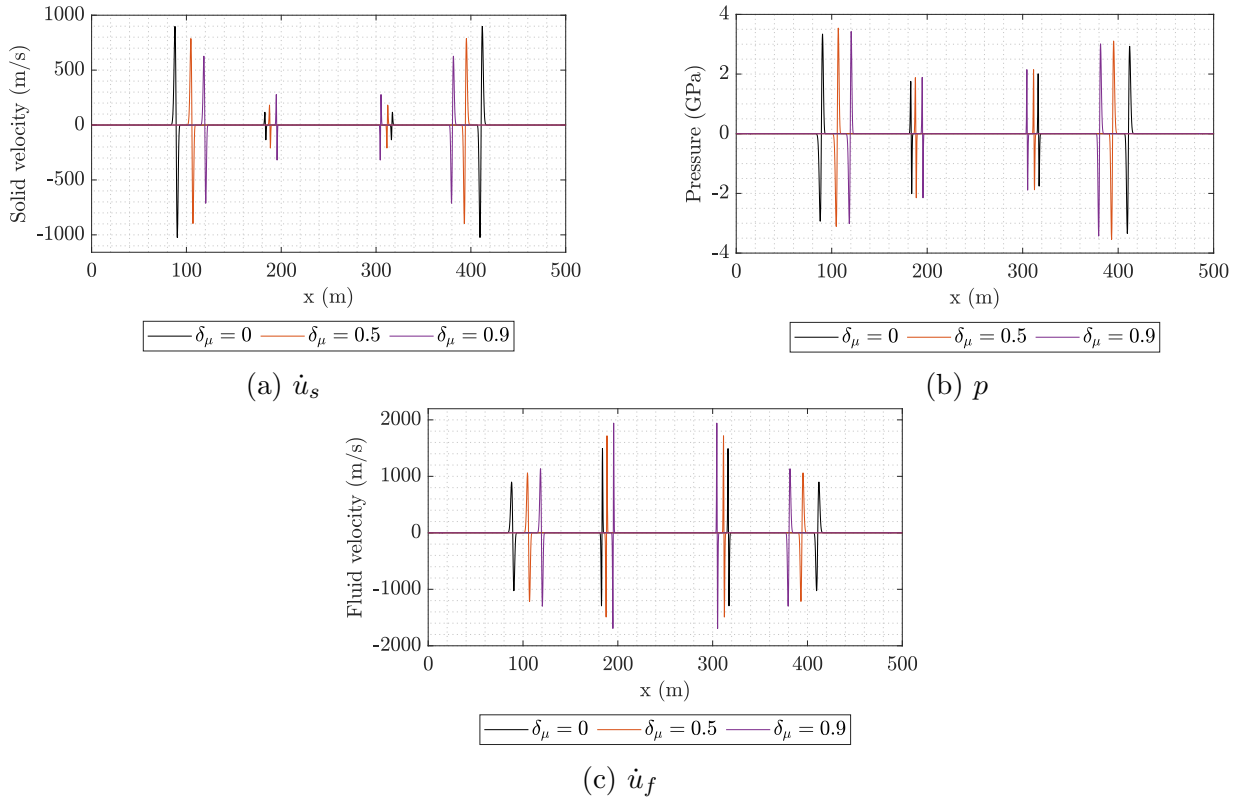
(f) $\dot{u}_f$, $x = 260$m

Figure 4.6: Impact of the effective pressure coefficient n on (a, b) solid velocity, (c, d) pressure, and (e, f) fluid velocity for one-dimensional wave propagation with permeability $\kappa_h = 10^{-8}\text{m}^2$. Figures (a), (c), (e) show variation over the domain at $t_{end} = 5 \times 10^{-2}$s, while Figures (b), (d), (f) show variation over time at $x = 260$m.

Macroscopic shear modulus

Maintaining the intrinsic permeability at $\kappa_h = 10^{-8}$ m^2, we now evaluate the impact of the

constant δ_μ on the results for the dCS model. For that, we maintain the same geometry, mesh and time discretization, and remaining material parameters as in Table 4.1. Figure 4.7 depicts the results for solid velocity, pressure, and fluid velocity for different values of δ_μ – chosen within the range of typical values reported in Hickey [85] through the definition of μ_M. Existing data for the determination of δ_μ is limited and thus the exact value related to the data in Table 4.1 is unknown. When $\delta_\mu \neq 0$ the P waves propagate at a lower speed, and attenuation decreases in all wave types but the fast P wave in the solid.



(a) $\dot{u}_s$ (b) p

(c) $\dot{u}_f$

Figure 4.7: Impact of dimensionless parameter δ_μ on (a) solid velocity, (b) pressure, and (c) fluid velocity at $t_{end} = 5 \times 10^{-2}$s.

4.6.2 Two-dimensional wave propagation

A two-dimensional wave propagation problem is simulated to verify the proposed FE model for the dCS theory. A square domain with side dimensions of $L = 5000$m is considered to

reproduce the results in Tian et. al. [171]. The material properties are as mentioned in the paper, and the source function $S(t)$ is also taken as a Ricker wavelet of the form

$$S(t) = [1 - 2\pi^2 f^2 (t - t_0)^2] \exp[-\pi^2 f^2 (t - t_0)^2], \tag{4.54}$$

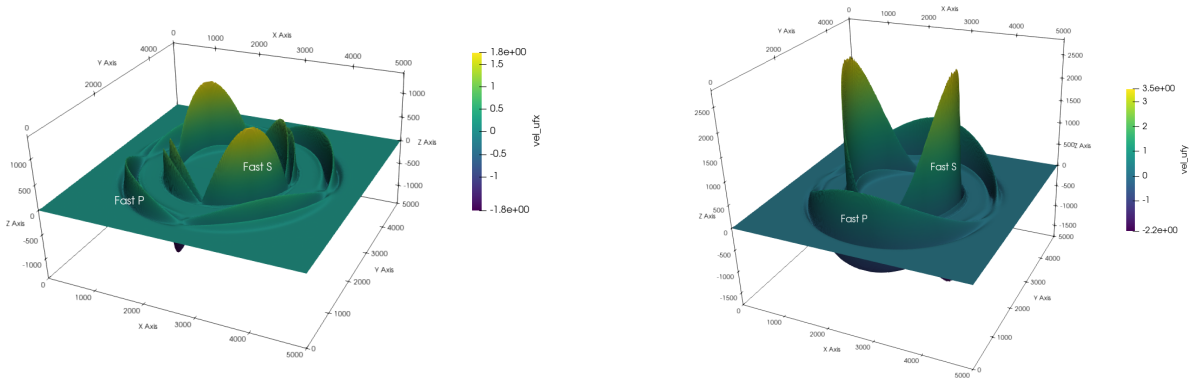
in which $f = 10$Hz is the dominant frequency, $t_0 = 1/f = 0.05$s is the peak location, and t is the current simulation time. This source is applied to the vertical component of the solid displacement at the central node; the final simulation time is taken as $t_{end} = 0.8$s for a time step of $\Delta t = 8 \times 10^{-4}$s. For the water-saturated rock parameters in Tian et. al. [171], the correspondent wave velocity and wavelength are reported in Table 4.7; there are no differences between dCS and BT values. The dry wave speed of P and S waves is $v_P^{dry} = 2439$ m/s and $v_S^{dry} = 1493$ m/s, respectively.

Table 4.7: Velocity and wavelength of dCS P and S waves for water-saturated sandstone [171] and source frequency of 10Hz.

Parameter	Fast P	Slow P	Fast S	Slow S
Wave velocity [m/s]	2769.07	4.73	1569.55	0.67
Wavelength [m]	276.91	0.47	156.96	0.07

Considering a mesh of 500×500 Q4 quadrilateral elements and $n = 1$ in (3.31), Figure 4.8 depicts the fluid velocity distribution in x and y, where fast P and S waves are identified. The slow waves cannot be identified due to their high attenuation combined with the current choice of mesh and time step size. The results herein obtained match the plots in Figure 3 of the aforementioned work, where Biot theory was used. The similarity between BT and dCS ($n = 1$) theories is, as mentioned in the one-dimensional example, due to the fact that the addition of fluid viscous dissipation terms in the dCS theory leads to negligible increments when compared to the BT for water-saturated sandstone domains.

To evaluate the impact that the changes in n have in the wave propagation phenomena, Figure 4.10(a, c, e) depicts the fluid velocity in x and y directions and the fluid pressure diagonally across the domain (i.e. $x = y$ coordinates) at the final simulation time. The curves are almost identical for the fluid velocities, with a small shift in the wave pattern noticed for the upper bound $n_{max} = K_s/K_f$. Changes in pressure distribution are a little more pronounced, with higher values for n_{min} and smaller values for n_{max}. Figure 4.10(b, d, f) shows synthetic plots of the pressure field at $x = 2600$m, for different n, which follow the same propagation pattern in all three cases. Variations in pressure attenuation, previously noticed in Figure 4.10(c), are very subtle. This result is coincident with the one-dimensional case. Furthermore, the lower frequency imposed in this example leads to less differences when n assumes its minimum or maximum limits.



(a) Fluid velocity in x [m/s]

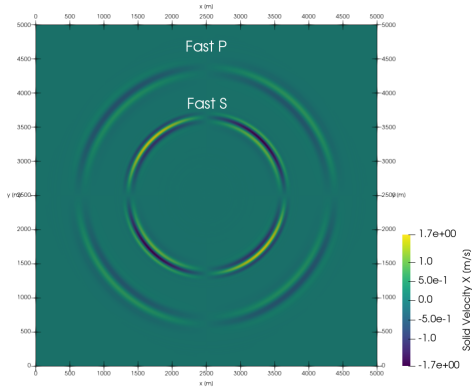
(b) Fluid velocity in y [m/s]

Figure 4.8: Distribution of fluid velocity in (a) x and (b) y directions over the domain at $t_{end} = 8 \times 10^{-1}$s; fast P and S waves are identified.

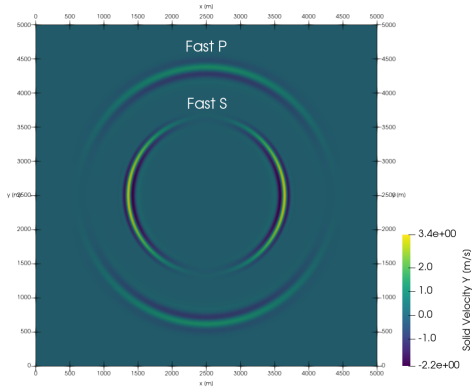
4.6.3 Two-dimensional injection well

A two-dimensional injection well is simulated for a water-saturated sandstone medium (Table 4.1), for which the geometry considered is depicted in Figure 4.11. The symmetry of the problem allows the simulation of a quarter of the domain with dimensions $L = 10$m; the injection well has a diameter of $r = 22$cm. The associated boundary conditions are indicated in Figure 4.11; the normal solid displacements are restricted in all boundaries except for the well, where fluid pressure is prescribed using a cosine relation give by $p(t) = A_0(1 - \cos(2\pi ft))/2$ for $t < 1/f$. Such relation indicates a pulsed fluid injection during 10^{-3}s with a frequency of $f = 1$ kHz and an amplitude of $A_0 = 10^{-2}$ GN. The dry wave speeds, as well as P and S wave velocity and wavelengths, are the same as reported in Section 4.6.1 for κ (low permeability case).

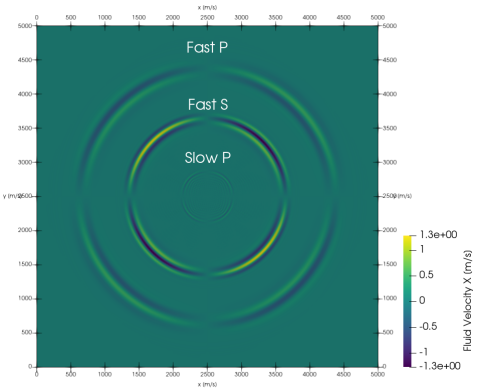
The vertical and horizontal in situ stresses are determined based on an overburden with density $\rho_{ov} = 2600\,\mathrm{kg/m^3}$ and gravitational acceleration at a depth of 1 km, also accounting for the hydrostatic pressure. The domain is discretized into $ne = 11,200$ quadrilateral elements; although bi-linear elements should suitable for the three-field formulation herein employed [91, 169], preliminary tests showed instability due to the pressure boundary condition. Hence, in this example we consider bi-linear Q4 elements for the fluid pressure field discretization and bi-quadratic Q9 elements for the solid and fluid displacement fields. The final simulation time is taken as $t_{end} = 3 \times 10^{-3}$s with a time step of $\Delta t = 10^{-5}$s.



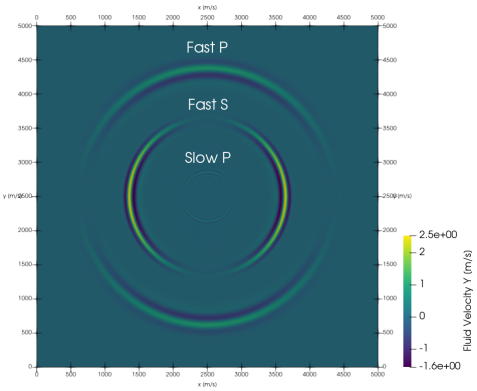
(a) Solid velocity in x



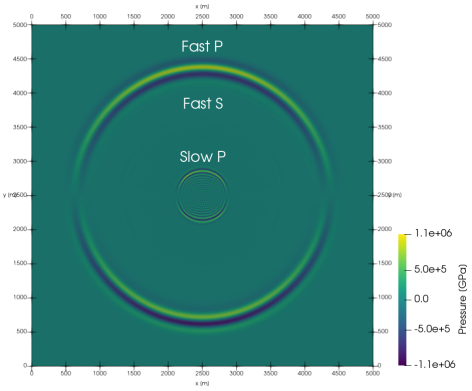
(b) Solid velocity in y



(c) Fluid velocity in x

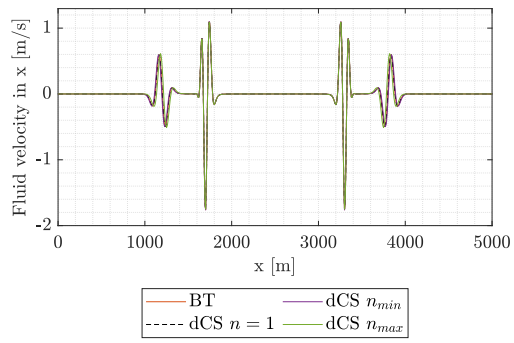


(d) Fluid velocity in y

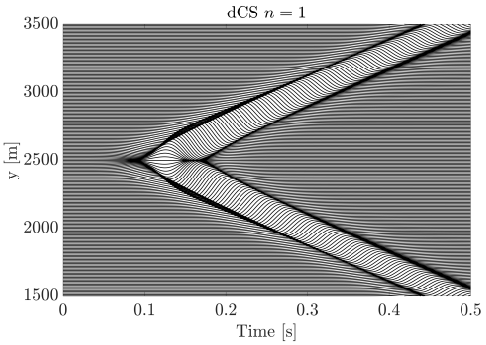


(e) Pressure

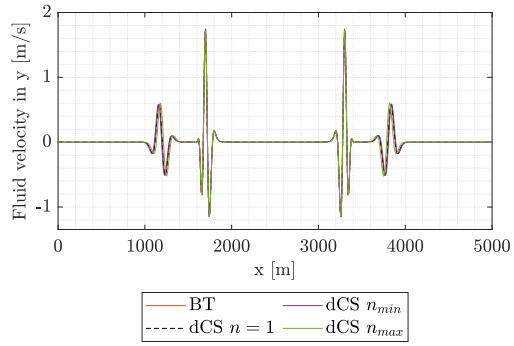
Figure 4.9: Impact of effective pressure coefficient n on (a,b) solid velocity, (c,d) fluid velocity, and (e) pressure at $t_{end} = 8 \times 10^{-1}$s for two-dimensional pulse; the x-axis refers to a cross-diagonal along the domain.



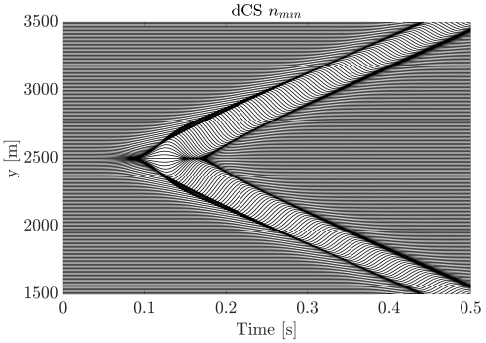
(a) Fluid velocity in x



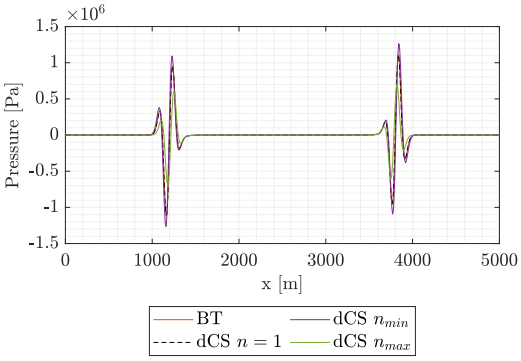
(b) Pressure, $n = 1$



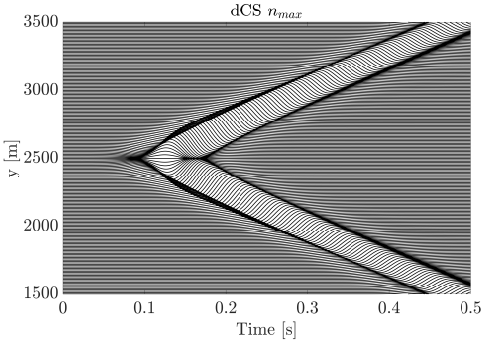
(c) Fluid velocity in y



(d) Pressure, $n_{min} = 0$



(e) Pressure



(f) Pressure, $n_{max} = K_s/K_f$

Figure 4.10: Impact of effective pressure coefficient n for two-dimensional pulse. Left: variation in (a, c) fluid velocity and (e) pressure at $t_{end} = 8 \times 10^{-1}$s; the x-axis refers to a cross-diagonal along the domain. Right: variation in pressure over time at $x = 2600$m for (b) $n = 1$, (d) n_{min}, and (f) n_{max}.

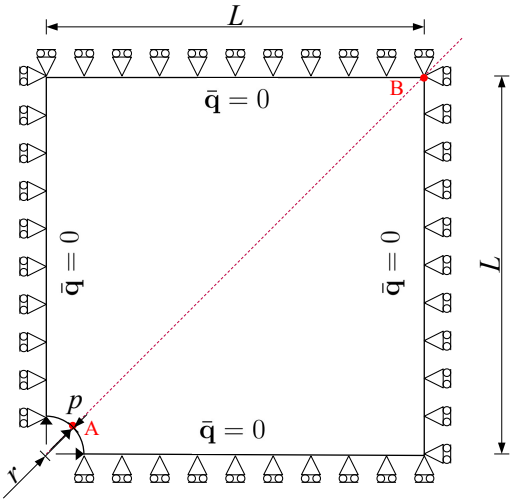
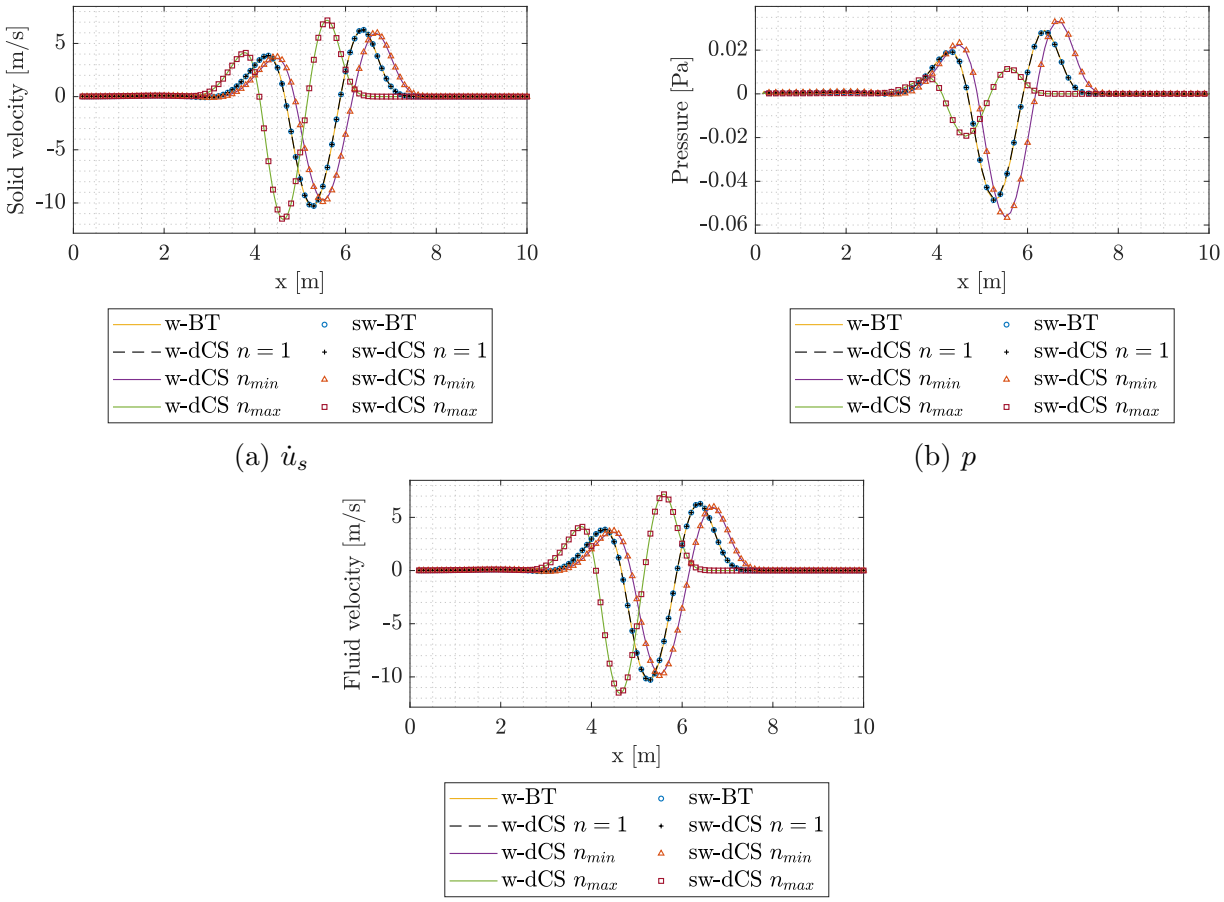


Figure 4.11: Geometry and boundary conditions of two-dimensional injection well problem.

Figure 4.12 depict the solid velocity, pressure, and fluid velocity over the line AB (Figure 4.11) at the final simulation time. The plots show the distribution considering water as the fluid component ($\mu_f = 10^{-3}$Pa·s), as well as slickwater ($\mu_f = 5 \times 10^{-3}$Pa·s), and variation in n is presented for both cases. The applied pulse leads to the propagation of a fast P wave along the domain, registered at $x = 3$ to 7m approximately. As noticed in the previous examples, higher values of n decrease the wave speed, while lower values of n lead to the opposite behavior. Attenuation on the solid and fluid velocity fields is inversely proportional to n. For the pressure field, nonetheless, n_{max} yields more wave attenuation. The curves obtained with BT and dCS ($n = 1$) coincide for both fluid components, showing that the increase in viscosity is not enough to yield differences between these theories due to fluid viscous dissipation mechanism. Furthermore, the substitution of water for slickwater leads to more attenuation, consequence of the higher viscosity.

4.7 Discussion

The constitutive equations employed in Biot theory carry some assumptions to the resulting coupled system. For instance, the definition of the fluid stress is dependent only on the fluid pressure, leading to the representation of one rotational wave instead of two. Furthermore, by including viscous dissipation terms within the fluid stress, a new form of attenuation can be included in the problem. The proposed framework based on the dCS theory accounts for such viscous dissipation terms, yielding a new slow S wave in the formulation.



(a) $\dot{u}_s$ (b) p

(c) $\dot{u}_f$

Figure 4.12: Impact of effective pressure coefficient n on (a) solid velocity, (b) pressure, and (c) fluid velocity at $t_{end} = 3 \times 10^{-3}$s for two-dimensional injection. Plots consider both water ($\mu_f = 10^{-3}$Pa·s, w- in legend) and slickwater ($\mu_f = 5 \times 10^{-3}$Pa·s, sw- in legend) fluids; the x-axis refers to the line AB indicated in Figure 4.11.

The introduction of the porosity effective pressure coefficient n allows one to account for nonreciprocal solid-fluid interactions, when then constituents affect the change in porosity to a different extent. This happens due to the presence of micro-heterogeneity in the media, causing the deformation energy of the medium to be localized in either the fluid bulk, solid bulk, or the solid-fluid interface. Even though different n might represent an uneven distribution of deformation energy between the solid and fluid constituents, overall equilibrium of the system is still achieved (i.e. there is no violation of Newton's law).

The dimensionless analysis was employed to evaluate the contribution of the dissipation terms added in the dCS theory. For water-saturated sandstone models, fluid viscous dissipation adds negligible damping to the system. When substituting water for oil, or when considering a cancellous bone medium, the newly included terms adds little damping. Changes in this behaviour could be noticed in extreme cases, for instance when bulk viscosity is high, when the characteristic length is small, or when there is a combination of high dynamic viscosity and high frequency. Although the complete fluid stress tensor in dCS theory does not seem to change significantly the solid-fluid behaviour, it becomes essential in the representation of fluid shear motion at high frequencies and in layered media [76, 75, 77].

Through the dimensionless analysis, the effect of the constant δ_μ was also evaluated. The terms added to the submatrices related to δ_μ can be of similar order of the BT damping, depending on the material. Contributions from $\delta_\mu \neq 0$, thus, can significantly affect the numerical results. Nonetheless, the use of such constant is little explored in the literature, and further studies are required to determine adequate values.

The FE model developed was based on three field variables: solid displacement, fluid pressure, and fluid displacement. While two-field solid displacement-fluid pressure formulations are common for the simulation of consolidation problems due to their quasi-steady nature, they assume that solid and fluid accelerations are equal. Two-field formulations in dynamic simulations have their accuracy restricted to low frequency ranges. Meanwhile, three-field formulations are suited for dynamic problems in all frequency ranges, since there are no assumptions regarding accelerations. The convergence study showed that the coupled nature of the porous media problem leads to some deterioration in convergence rates, when compared to optimal values in uncoupled problems.

In two-field $u_s - p$ formulations, mixed-order elements can be used to ensure numerical stability in BT theory, and it is reasonable to extend such mixed-order elements requirement for the dCS model. It is noteworthy that low-order linear elements are also a viable option when coupled with stabilization techniques. For three-field formulations such as the one herein presented, the use of linear elements is generally enough to avoid numerical locking. As mentioned on the two-dimensional injection well problem, however, the imposed pressure boundary condition leads to numerical instabilities, which were solved by employing mixed-order elements. Further developments of the presented model include the derivation of specific requirements for satisfying stability in the dCS FE framework.

In the one- and two-dimensional examples, a comparison between the results associated to the Biot and dCS ($n = 1$) theories confirmed what was noticed in the dimensionless analysis, and the addition of fluid viscous dissipation terms had modest effect in the curves.

Significant differences were noticed, nonetheless, for wave propagation above the BT critical frequency limit. The BT high-frequency correction factor leads to discrepancies from dCS ($n = 1$) results, showing higher attenuation in the fluid motion for BT theory. However, the fluid viscous dissipation terms added in dCS theory should be responsible for completely representing fluid motion at all frequencies. This wave behavior is going to be further discussed in the following chapter.

Variation of the coefficient n showed changes in the velocity and pressure curves, which were more or less pronounced depending on the source frequency. Regarding the parameter introduced in the solid macroscopic shear modulus, for $\delta_\mu \neq 0$, waves propagate at a slower speed, since stiffness and damping matrices are altered. Nonetheless, such parameter δ_μ is often neglected in literature, and further studies are still necessary to determine an expression for δ_μ valid at different frequency ranges and material types. The two-dimensional injection well problem exemplified how the developed FE model can be employed in a boundary value problem, where wave propagation is represented. The comparison between water and slickwater fluids shows how the latter increases wave attenuation due to its higher viscosity.

The wave propagation phenomena herein represented could also be assessed from a frequency-domain point of view, by using a Helmholtz decomposition on the momentum equations and obtaining a correspondent eigenproblem to be solved in terms of the solid/fluid wave number. The derivation of such eigenproblem form, however, relies on the assumption that waves propagate at the same wavelength in the solid and fluid constituents, which is violated as can be observed in the wave patterns. Nevertheless, the eigenproblem solution is still an important tool to study the changes in wave velocity and attenuation, and relate that to the source frequency and material parameters; such analysis will be explored on the following chapter.

4.8 Conclusions

This chapter presented a FE model for the dCS theory based on a three-field dynamic formulation in terms of solid displacement, fluid pressure, and fluid displacement. It differs from BT theory due to the addition of viscous dissipation terms in the fluid stress definition, nonreciprocal solid-fluid interactions (represented by n), and the dimensionless constant δ_μ in the macroscopic shear modulus definition. The convergence study showed that the field convergence rates differ from optimal rates attributed to uncoupled variables. The deterioration of the convergence rate increases as the problem is more strongly coupled.

The dimensionless analysis performed showed that the dCS model adds negligible damping; dCS damping terms are only significant at high frequencies and for high fluid viscosity. For small characteristic lengths – i.e, for laboratory-scale experiments, dCS and BT damping are close in order of magnitude. Effects of the complete fluid stress tensor in the dCS model are visible at the high-frequency BT range, when the BT model lead to higher attenuation of the slow P wave. Still, the BT correction factor is insufficient to represent the fluid motion especially at layered media.

In one- and two-dimensional examples, variations in n and δ_μ led to changes in wave propagation patterns. Furthermore, low frequencies lead to modest changes in plots for different n. The simulation of a two-dimensional injection well for both water and slick-water depicted higher attenuation for the latter. In the next chapter, wave velocity and attenuation patterns at different frequencies and for different solid-fluid combinations are explored. The goal is to have a better understanding of the changes that the dCS model yields compared to BT results.

Chapter 5

Porous Media Wave Patterns

5.1 Introduction

The goal of this chapter is to analyse the wave patterns related to the dCS model, showing how wave velocity and attenuation change due to the non-reciprocal solid-fluid interactions, as well as due to variations in the macroscopic solid shear modulus. The resultant eigenproblem, based on a plane waves assumption, leads to a dependency between the wavenumber and the applied frequency, which is observed for different sets of material parameters. The effect of such features herein considered is observed separately, followed by discussions on how the wave patterns are affected and under which circumstances the dCS model differs from BT. Moreover, we raise the discussion on the representation of fluid effects at high-frequency by the BT and dCS theories.

Section 5.2 details the derivation of dCS wave equations, highlighting the related assumptions and the differences to the BT model. Section 5.3 shows the effect of non-reciprocal interactions and variation in the macroscopic solid shear modulus; changes in the critical frequency limit and the added mass coefficient are also addressed. Wave velocity and attenuation are evaluated at different frequencies and ranges of specific material parameters. Section 5.3.7 explains the porosity-pressure coupling effect, when low-frequency pulses lead to fluid flow enhancement. Section 5.4 presents a discussion on the obtained results, while Section 5.5 summarizes the chapter findings.

5.2 Porous Media Descriptions

5.2.1 dCS governing equations

The system of equations that describe a porous medium are taken from Spanos [165] and herein reproduced, assuming (i) an isothermal behavior, (ii) constant solid and fluid densities, and (iii) non-zero solid and fluid acceleration terms. The solid and fluid equations of motion are given by

$$(1-\eta_0)\rho_s\ddot{\mathbf{u}}_s = \nabla\cdot\boldsymbol{\sigma}_s + \frac{\mu_f\eta_0^2}{\kappa}(\dot{\mathbf{u}}_f - \dot{\mathbf{u}}_s) - \rho_{12}(\ddot{\mathbf{u}}_f - \ddot{\mathbf{u}}_s) \tag{5.1}$$

$$\eta_0\rho_f\ddot{\mathbf{u}}_f = \nabla\cdot\boldsymbol{\sigma}_f - \frac{\mu_f\eta_0^2}{\kappa}(\dot{\mathbf{u}}_f - \dot{\mathbf{u}}_s) + \rho_{12}(\ddot{\mathbf{u}}_f - \ddot{\mathbf{u}}_s), \tag{5.2}$$

where $\mathbf{u}_s$, $\mathbf{u}_f$ are the solid and fluid displacements, and the single and double dots indicate a first and second time derivative, respectively; ρ_s, ρ_f are the solid and fluid densities, ρ_{12} is the added mass coefficient, μ_f is the fluid dynamic viscosity, κ is the intrinsic permeability, and η_0 is the initial porosity. The divergence of solid $\nabla\cdot\boldsymbol{\sigma}_s$ and fluid $\nabla\cdot\boldsymbol{\sigma}_f$ stresses are defined as

$$\nabla\cdot\boldsymbol{\sigma}_s = (1-\eta_0)K_s\nabla(\nabla\cdot\mathbf{u}_s) - K_s\nabla\eta + \mu_M[\nabla^2\mathbf{u}_s + \frac{1}{3}\nabla(\nabla\cdot\mathbf{u}_s)], \tag{5.3}$$

$$\begin{aligned}\nabla\cdot\boldsymbol{\sigma}_f = &-\eta_0\nabla p + \eta_0\mu_f\nabla^2\dot{\mathbf{u}}_f + \eta_0(\xi_f + \frac{\mu_f}{3})\nabla(\nabla\cdot\dot{\mathbf{u}}_f) + \xi_f\nabla\dot{\eta}\\ &+ (1-\eta_0)\mu_f(\frac{\mu_M}{(1-\eta_0)\mu_s} - 1)[\nabla^2\dot{\mathbf{u}}_s + \frac{1}{3}\nabla(\nabla\cdot\dot{\mathbf{u}}_s)],\end{aligned} \tag{5.4}$$

in which p is the pressure variable and η is the porosity variable, K_s is the solid bulk modulus, ξ_f is the fluid bulk viscosity, and $\mu_M = (1-\eta_0)\mu_s(1-\delta_\mu)$ is the macroscopic shear modulus, where δ_μ is a parameter that relates μ_M to the averaged quantity $(1-\eta_0)\mu_s$ [159, 165, 152]. The storage equation is given by

$$\frac{\dot{p}}{K_f} = -\nabla\cdot\dot{\mathbf{u}}_f - \frac{\dot{\eta}}{\eta_0}, \tag{5.5}$$

where K_f is the fluid bulk modulus. The porosity variable η is related to $\mathbf{u}_s, \mathbf{u}_f$ by

$$\dot{\eta} = \delta_s\nabla\cdot\dot{\mathbf{u}}_s - \delta_f\nabla\cdot\dot{\mathbf{u}}_f, \tag{5.6}$$

in which δ_s, δ_f are dimensionless parameters that can be written as

$$\delta_s = (\alpha-\eta_0)\frac{\eta_0 M^*}{K_f}, \quad \delta_f = (\alpha-\eta_0)\frac{\eta_0 M^*}{K_s}n, \tag{5.7}$$

where n is the porosity effective pressure coefficient introduced by Sahay [157] and the other parameters are defined in Section 3.2.4. Sections 3.4.1 and 4.6.1 include further discussions on the definition, meaning, and determination of the compliance coefficients δ_s, δ_f and the parameter n. Here we reiterate that δ_s, δ_f weight the extent to which solid and fluid deformations affect porosity change, and that acceptable boundaries for n are $0 \leq n \leq K_s/K_f$. BT equations can be recovered when $n = 1$, assuming that $\delta_\mu = 0$ and neglecting fluid viscous dissipation terms in (5.4). Therefore, we aim to compare the effect of (5.4) in dCS and BT theory by assuming $n = 1$ and $\delta_\mu = 0$, as well as evaluate changes due to non-reciprocal interactions by varying n.

By substituting relations (5.3)-(5.6) into (5.1)-(5.2), we can write the equations of motion only in terms of $\mathbf{u}_s$ and $\mathbf{u}_f$ as in

$$\begin{aligned}\ddot{\mathbf{u}}_s &- \frac{\mu_M}{\rho_s(1-\eta_0)}\nabla^2\mathbf{u}_s - \left(\frac{K_s}{\rho_s} + \frac{\mu_M}{3\rho_s(1-\eta_0)}\right)\nabla(\nabla\cdot\mathbf{u}_s) + \frac{K_s\delta_s}{\rho_s(1-\eta_0)}\nabla(\nabla\cdot\mathbf{u}_s) \\ &- \frac{K_s\delta_f}{\rho_s(1-\eta_0)}\nabla(\nabla\cdot\mathbf{u}_f) - \frac{\mu_f\eta_0^2}{\rho_s\kappa(1-\eta_0)}(\dot{\mathbf{u}}_f - \dot{\mathbf{u}}_s) + \frac{\rho_{12}}{\rho_s(1-\eta_0)}(\ddot{\mathbf{u}}_f - \ddot{\mathbf{u}}_s) = 0,\end{aligned} \tag{5.8}$$

$$\begin{aligned}\ddot{\mathbf{u}}_f &- \frac{K_f}{\rho_f}\nabla(\nabla\cdot\mathbf{u}_f) - \frac{K_f\delta_s}{\rho_f\eta_0}\nabla(\nabla\cdot\mathbf{u}_s) + \frac{K_f\delta_f}{\rho_f\eta_0}\nabla(\nabla\cdot\mathbf{u}_f) + \frac{\mu_f\eta_0}{\rho_f\kappa}(\dot{\mathbf{u}}_f - \dot{\mathbf{u}}_s) \\ &- \frac{\rho_{12}}{\rho_f\eta_0}(\ddot{\mathbf{u}}_f - \ddot{\mathbf{u}}_s) + (\frac{\xi_f\delta_f}{\rho_f\eta_0} - \frac{\xi_f}{\rho_f} - \frac{\mu_f}{3\rho_f})\nabla(\nabla\cdot\dot{\mathbf{u}}_f) - \frac{\mu_f}{\rho_f}\nabla^2\dot{\mathbf{u}}_f - \frac{\xi_f\delta_s}{\rho_f\eta_0}\nabla(\nabla\cdot\dot{\mathbf{u}}_s) \\ &- \frac{(1-\eta_0)\mu_f}{\rho_f\eta_0}(\frac{\mu_M}{(1-\eta_0)\mu_s} - 1)[\nabla^2\dot{\mathbf{u}}_s + \frac{1}{3}\nabla(\nabla\cdot\dot{\mathbf{u}}_s)] = 0.\end{aligned} \tag{5.9}$$

This form of the dCS momentum equations are used in the derivation of the correspondent wave equations. These were previously presented in literature [165] in a similar form as the one herein detailed. The next section summarize such equations, further showing the steps and assumptions made and highlighting the role that some parameters have on the wave velocity and attenuation patterns.

5.2.2 dCS wave equations

The compressional wave equations are obtained by applying the divergence operator in (5.8)-(5.9). Considering that $\nabla\cdot\mathbf{u}_s = \varepsilon_s$, $\nabla\cdot\mathbf{u}_f = \varepsilon_f$,

$$\ddot{\varepsilon}_s - a_{ps}\nabla^2\varepsilon_s - b_{ps}\nabla^2\varepsilon_f - c_s(\dot{\varepsilon}_f - \dot{\varepsilon}_s) + d_s(\ddot{\varepsilon}_f - \ddot{\varepsilon}_s) = 0, \tag{5.10}$$

$$\ddot{\varepsilon}_f - a_{pf}\nabla^2\varepsilon_f - b_{pf}\nabla^2\varepsilon_s + c_f(\dot{\varepsilon}_f - \dot{\varepsilon}_s) - d_f(\ddot{\varepsilon}_f - \ddot{\varepsilon}_s) + g_{pf}\nabla^2\dot{\varepsilon}_f - h_{pf}\nabla^2\dot{\varepsilon}_s = 0. \tag{5.11}$$

For the rotational (shear) wave equations, the curl operator is applied in (5.8)-(5.9); using $\nabla \times \mathbf{u}_s = \Omega_s$, $\nabla \times \mathbf{u}_f = \Omega_f$,

$$\ddot{\Omega}_s - a_{ss}\nabla^2\Omega_s - c_s(\dot{\Omega}_f - \dot{\Omega}_s) + d_s(\ddot{\Omega}_f - \ddot{\Omega}_s) = 0, \tag{5.12}$$

$$\ddot{\Omega}_f - a_{sf}\nabla^2\dot{\Omega}_f + c_f(\dot{\Omega}_f - \dot{\Omega}_s) - d_f(\ddot{\Omega}_f - \ddot{\Omega}_s) = 0; \tag{5.13}$$

the coefficients introduced in (5.10)-(5.13) are listed in Table 5.1.

Table 5.1: Coefficients defined in wave equations (5.10)-(5.13).

$a_{ps} = \left(\dfrac{K_s + 4\mu_s(1-\delta_\mu)/3}{\rho_s} - \dfrac{K_s\delta_s}{\rho_s(1-\eta_0)}\right)$	$a_{pf} = \left(\dfrac{K_f}{\rho_f} - \dfrac{K_f\delta_f}{\rho_f\eta_0}\right)$
$b_{ps} = \dfrac{K_s\delta_f}{\rho_s(1-\eta_0)}$	$b_{pf} = \dfrac{K_f\delta_s}{\rho_f\eta_0}$
$c_s = \dfrac{\mu_f\eta_0^2}{\rho_s\kappa(1-\eta_0)}$	$c_f = \dfrac{\mu_f\eta_0}{\rho_f\kappa}$
$d_s = \dfrac{\rho_{12}}{\rho_s(1-\eta_0)}$	$d_f = \dfrac{\rho_{12}}{\rho_f\eta_0}$
$g_{pf} = \left(\dfrac{\xi_f\delta_f}{\rho_f\eta_0} - \dfrac{\xi_f}{\rho_f} - \dfrac{4\mu_f}{3\rho_f}\right)$	$h_{pf} = \dfrac{\xi_f\delta_s}{\rho_f\eta_0} - \dfrac{4(1-\eta_0)\mu_f\delta_\mu}{3\rho_f\eta_0}$
$a_{ss} = \dfrac{\mu_s}{\rho_s}$	$a_{sf} = \dfrac{\mu_f}{\rho_f}$

We assume a plane wave solution for the compressional waves such that

$$\varepsilon_s = \bar{\varepsilon}_s \exp[\mathrm{i}(k_{px}x + k_{py}y) - \mathrm{i}\omega t], \tag{5.14}$$

$$\varepsilon_f = \bar{\varepsilon}_f \exp[\mathrm{i}(k_{px}x + k_{py}y) - \mathrm{i}\omega t], \tag{5.15}$$

where $\bar{\varepsilon}_s$, $\bar{\varepsilon}_f$ are the wave amplitudes, ω is the source frequency, and k_{px}, k_{py} are the wavenumbers in x and y directions. Substituting (5.14)-(5.15) into (5.10)-(5.11), we have

$$(-\omega^2 + a_{ps}k_p^2 - c_s\mathrm{i}\omega + d_s\omega^2)\bar{\varepsilon}_s + (b_{ps}k_p^2 + c_s\mathrm{i}\omega - d_s\omega^2)\bar{\varepsilon}_f = 0, \tag{5.16}$$

$$(b_{pf}k_p^2 + c_f\mathrm{i}\omega - d_f\omega^2 - h_{pf}\mathrm{i}\omega k_p^2)\bar{\varepsilon}_s + (-\omega^2 + a_{pf}k_p^2 - c_f\mathrm{i}\omega + d_f\omega^2 + g_{pf}\mathrm{i}\omega k_p^2)\bar{\varepsilon}_f = 0, \tag{5.17}$$

where $k_p^2 = k_{px}^2 + k_{py}^2$. From the correspondent coefficient matrix, a polynomial equation in terms of the wavenumber can be written as

$$A_p k_p^4 + B_p k_p^2 + C_p = 0, \tag{5.18}$$

in which

$$A_p = (a_{ps}g_{pf} + b_{ps}h_{pf})\mathrm{i}\omega + a_{pf}a_{ps} - b_{pf}b_{ps}, \tag{5.19}$$

$$B_p = (d_s g_{pf} - d_s h_{pf} - g_{pf})\mathrm{i}\omega^3 + (-a_{pf}c_s - a_{ps}c_f - b_{pf}c_s - b_{ps}c_f)\mathrm{i}\omega + (a_{pf}d_s + a_{ps}d_f + b_{pf}d_s + b_{ps}d_f + c_s g_{pf} - c_s h_{pf} - a_{pf} - a_{ps})\omega^2, \tag{5.20}$$

$$C_p = (c_f + c_s)\mathrm{i}\omega^3 + (1 - d_f - d_s)\omega^4. \tag{5.21}$$

Assuming a similar plane wave solution for rotational waves,

$$\Omega_s = \bar{\Omega}_s \exp[\mathrm{i}(k_{sx}x + k_{sy}y) - \mathrm{i}\omega t], \tag{5.22}$$

$$\Omega_f = \bar{\Omega}_f \exp[\mathrm{i}(k_{sx}x + k_{sy}y) - \mathrm{i}\omega t], \tag{5.23}$$

we have that $\bar{\Omega}_s$, $\bar{\Omega}_f$ are the wave amplitudes, and k_{sx}, k_{sy} are the wavenumbers for the rotational wave in x and y directions. Replacing (5.22)-(5.23) into (5.12)-(5.13) yields

$$(-\omega^2 + a_{ss}k_s^2 - c_s\mathrm{i}\omega + d_s\omega^2)\bar{\Omega}_s + (c_s\mathrm{i}\omega - d_s\omega^2)\bar{\Omega}_f = 0, \tag{5.24}$$

$$(c_f\mathrm{i}\omega - d_f\omega^2)\bar{\Omega}_s + (-\omega^2 a_{sf}\mathrm{i}\omega k_s^2 - c_f\mathrm{i}\omega + d_f\omega^2)\bar{\Omega}_f = 0, \tag{5.25}$$

and the polynomial equation for $k_s^2 = k_{sx}^2 + k_{sy}^2$ obtained is equal to

$$A_s k_s^4 + B_s k_s^2 + C_s = 0, \tag{5.26}$$

in which

$$A_s = -a_{sf}a_{ss}\mathrm{i}\omega, \tag{5.27}$$

$$B_s = (-a_{sf}d_s + a_{sf})\mathrm{i}\omega^3 - a_{ss}c_f\mathrm{i}\omega + (a_{sf}c_s + a_{ss}d_f - a_{ss})\omega^2, \tag{5.28}$$

$$C_s = (c_f + c_s)\mathrm{i}\omega^3 + (1 - d_f - d_s)\omega^4. \tag{5.29}$$

From Table 5.1, the coefficients g_{pf}, h_{pf} in the fluid equation represent the fluid viscous dissipation mechanism present in dCS theory, but not in BT. Furthermore, the porosity effective pressure coefficient n is implicitly related to the coefficients a_{ps}, b_{ps}, a_{pf}, b_{pf}. The parameter δ_μ appears in the terms a_{ps} and h_{pf}. Therefore, changes in n and δ_μ only affect P (compressional) waves, and have no impact on the behavior of S (rotational) waves. In the following section, we explore the impact that changes in n, δ_μ have on the dCS wave velocity and dispersion patterns, and how they differ from BT results.

5.2.3 Wave attenuation and material damping

The upcoming examples evaluate wave attenuation patterns through the inverse of quality factor $1/Q$. Nonetheless, material damping is another significant source of wave attenuation. In general, two types of attenuation can be identified: geometric and material damping. While the former happens due to the location and type of the wave source, the latter is related to the ground properties and wave amplitude [100]. The determination of material damping, however, can be a cumbersome task. Kim & Lee [100] used 3D geophones to measure ground vibrations due to different sources, such as train loading and hydraulic hammer compaction. Athanasopoulos et. al. [6] compared experimental data with information reported in literature for attenuation coefficients of geomaterials, which were found to provide less seismic wave attenuation when compared to soft soils. Karl et. al. [97] used the bender element technique to verify that material damping is frequency-dependent.

Pritz [149] used a frequency power law to describe material damping, which was verified through experimental observation however was proven to be valid only within a finite bandwidth. The estimation of damping has also been done by analyzing surface waves. The work of Badsar et. al. [10] presented a method to determine material damping in shallow layers by employing spectral analysis, and the attenuation plots were obtained from the spectrum of frequency-wavenumber. Furthermore, Yang et. al. [192] presented a technique to measure material damping by wavelet transforms. Estimation of material damping has been done in a variety of materials such as concrete [167], composite bars [198], and granular materials [196].

In porous media BT and dCS models, material damping is included in the form of Darcy-like resistance $(\dot{u}_f - \dot{u}_s)\mu_f \eta_0^2/\kappa$ [165], indicating solid-fluid interactions. Additional material damping is represented in the dCS model by fluid viscous dissipation terms. Quantifying such material attenuation, however, was out of the scope of this research. It is still noteworthy that material damping might be a more relevant source of wave attenuation than solid-fluid interface effects, and it is an important topic for future studies.

5.3 Wave Velocity and Attenuation Patterns

A study of the wave velocity and attenuation patterns using the dCS model and the wave propagation equations herein derived is presented. Unless stated otherwise, the material parameters considered for the analysis represent a water-saturated sandstone [193] and are reproduced in Table 4.1. The phase velocity and quality factor are computed as detailed

in [26]. For the BT theory, the correction factor for the high-frequency range [16] is taken as in [92]. The impact of two material parameters is evaluated: (a) the porosity effective pressure coefficient n, and (b) the parameter δ_μ present in the macroscopic shear modulus.

5.3.1 Porosity effective pressure coefficient n

The first study performed is to compare the wave characteristics from BT and dCS theories, and analyze variations of the parameter n in the latter. In this case, we consider $\delta_\mu = 0$ and $\rho_{12} = 0$. It is noteworthy that the minimum ($n_{min} = 0$) and maximum ($n_{max} = K_s/K_f$) values adopted for n are physically sound limits defined in [157]. While $n = 1$ indicates that solid and fluid affect the porosity change to the same extent, for $n_{min} = 0$ the fluid pressure does not cause variations in porosity. On the other hand, $n_{max} = K_s/K_f$ indicates that there are no changes in porosity ($\delta_s = \delta_f$). In the range $0 \leq n < 1$, fluid pressure affects the porosity change to a lesser extent than solid pressure; the opposite behavior is noticed for $1 < n \leq K_s/K_f$ [134]. While such lower and upper bounds might be deemed as very conservative, realistic porous materials might be far from these extremes.

Figure 5.1 depicts the velocity and attenuation for the four dCS wave types. For $n = 1$ the only difference between BT and dCS results is related to the fluid viscous dissipation terms in dCS. The wave velocity seems to be the same for BT and dCS models except for the second P wave, were dCS shows lower values at high frequencies. Regarding the attenuation patterns, BT shows higher values at high frequencies for both P waves and the fast S wave.

As demonstrated in the wave equations, the porosity effective pressure coefficient n does not affect the behavior of S waves, for which the velocity and attenuation are the same regardless of n. For the fast P wave (or P wave of the first kind), $n < 1$ leads to lower velocity and lower attenuation; $n > 1$ increases the velocity, but further decreases the attenuation when compared to $n = 1$. For the second or slow P wave, $n < 1$ actually increases its velocity, and the opposite happens for $n > 1$. Interesting enough, the correspondent attenuation is not significantly altered with n.

5.3.2 Macroscopic shear modulus averaging coefficient δ_μ

The effect of changes in the macroscopic shear modulus due to the parameter δ_μ is depicted in Figure 5.2. The porosity effective pressure coefficient is now fixed at $n = 1$, and the added mass density is maintained as zero. Typical values of μ_M for water saturated sandstone are reported by [152], from which δ_μ can be inferred; the values of δ_μ herein evaluated are

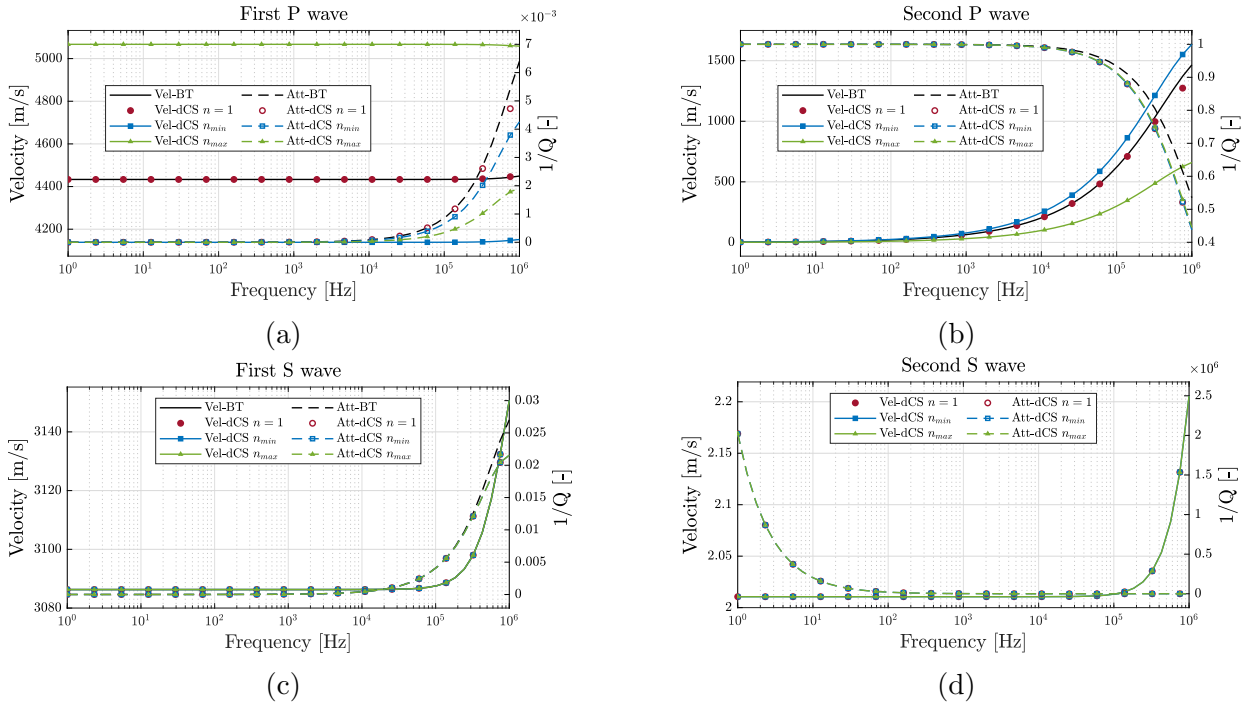


Figure 5.1: Velocity and attenuation for (a) fast P, (b) slow P, (c) fast S, and (d) slow S waves in BT and dCS theories, varying the n parameter on the latter. Note that the slow S wave only appears in dCS theory due to the lack of fluid viscous dissipation terms in BT.

$\delta_\mu = 0$, $\delta_\mu = 0.5$, and $\delta_\mu = 1.0$. Similarly to the previous analysis, δ_μ is not present in the coefficients of the rotational wave equations, and thus has no impact in velocity and attenuation of S waves. Alterations in the behavior of the second P wave are also small, leading to a slight decrease in velocity for $\delta_\mu > 0$ and no visible changes in attenuation. The fast P wave, on the other hand, presents lower velocity when $\delta_\mu > 0$; attenuation decreases for $\delta_\mu = 0.5$, and it increases for $\delta_\mu = 1.0$.

5.3.3 Critical frequency limits

The slow P wave behavior is known to vary according to the applied frequency [177, 156]. There is a critical frequency value, given by (4.53) that determines such behavior. For a certain frequency ω, if $\omega < \omega_c$, the slow P wave has low velocity and very high attenuation, and thus the latter effect is dominant. When $\omega > \omega_c$, however, the slow P wave attenuation decreases, its velocity increases, and it now has a propagatory characteristic. For the

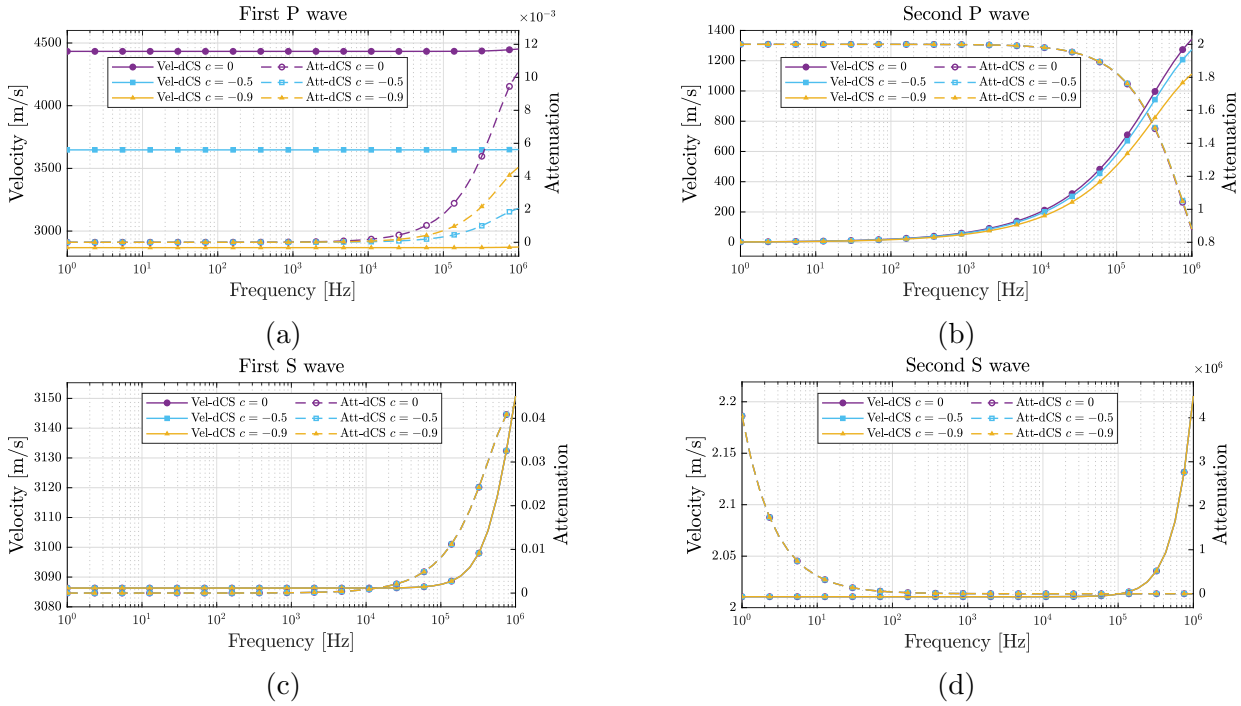


Figure 5.2: Velocity and attenuation for (a) fast P, (b) slow P, (c) fast S, and (d) slow S waves in dCS theory for different values of the parameter δ_μ.

parameters in Table 4.1, the critical frequency is $\omega_c = 1.01 \times 10^6$ Hz; since this is a high frequency close to the upper boundary of the previous examples, the effects above this limit are not observed. To better understand the wave behavior above ω_c, let us for instance increase the intrinsic permeability by two orders of magnitude, i.e. $\kappa_h = 1.88 \times 10^{-11}$ m^2, corresponding to a highly permeable sandstone.

Figure 5.3 depicts the wave velocity and attenuation for the new permeability value κ_h, where the vertical orange line indicates the new critical frequency of $\omega_c = 1.01 \times 10^4$ Hz. We notice how P wave velocity does not change significantly for $\omega > \omega_c$, reaching a plateau. The exception is the BT slow P wave, which has a peak close to the critical limit; the fast S wave velocity shows this same behavior. Attenuation of the fast P and S waves diverges more between BT and dCS theories, reaching a difference of approximately 40% between BT and dCS ($n = 1$) for the fast P wave, and of approximately 50% for the fast S wave. For the slow P wave, this difference in attenuation is small. Attenuation for the slow S wave is unchanged, while its velocity significantly increases after ω_c.

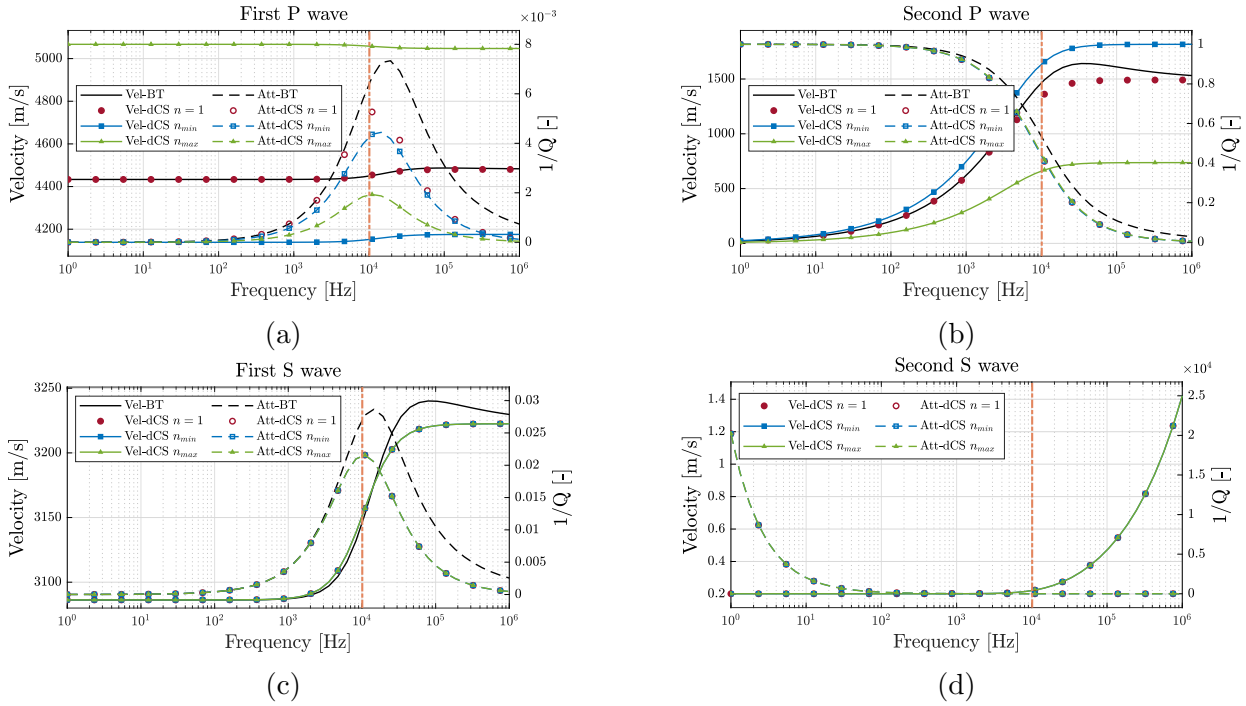


Figure 5.3: Velocity and attenuation for (a) fast P, (b) slow P, (c) fast S, and (d) slow S waves in dCS theory for highly permeable sandstone.

5.3.4 Dynamic fluid viscosity, intrinsic permeability, and initial porosity

For a determined frequency range, alterations in the porous medium material parameters could lead to changes in wave velocity and attenuation. In this sense, changes in three parameters are chosen to be evaluated: (a) the dynamic fluid viscosity μ_f, (b) the intrinsic permeability κ, and (c) the initial porosity η_0. While the dynamic fluid viscosity might vary depending on the porous fluid constituent, the permeability and porosity vary significantly depending on the type of solid constituent. In the following figures, the contour plots represent changes in either velocity or attenuation for a fixed range of frequency (x axis) and a material parameter (y axis).

Figures 5.4 and 5.5 (a)-(d) depict changes in velocity and attenuation, respectively, for different frequencies over a range of dynamic fluid viscosity from $\mu_f = 10^{-3}$ to 10^{0} Pa·s. For the P waves and the fast S wave, an increase in velocity is noticed for low values of μ_f and at high frequencies. The fast S wave velocity is significantly higher as μ_f increases,

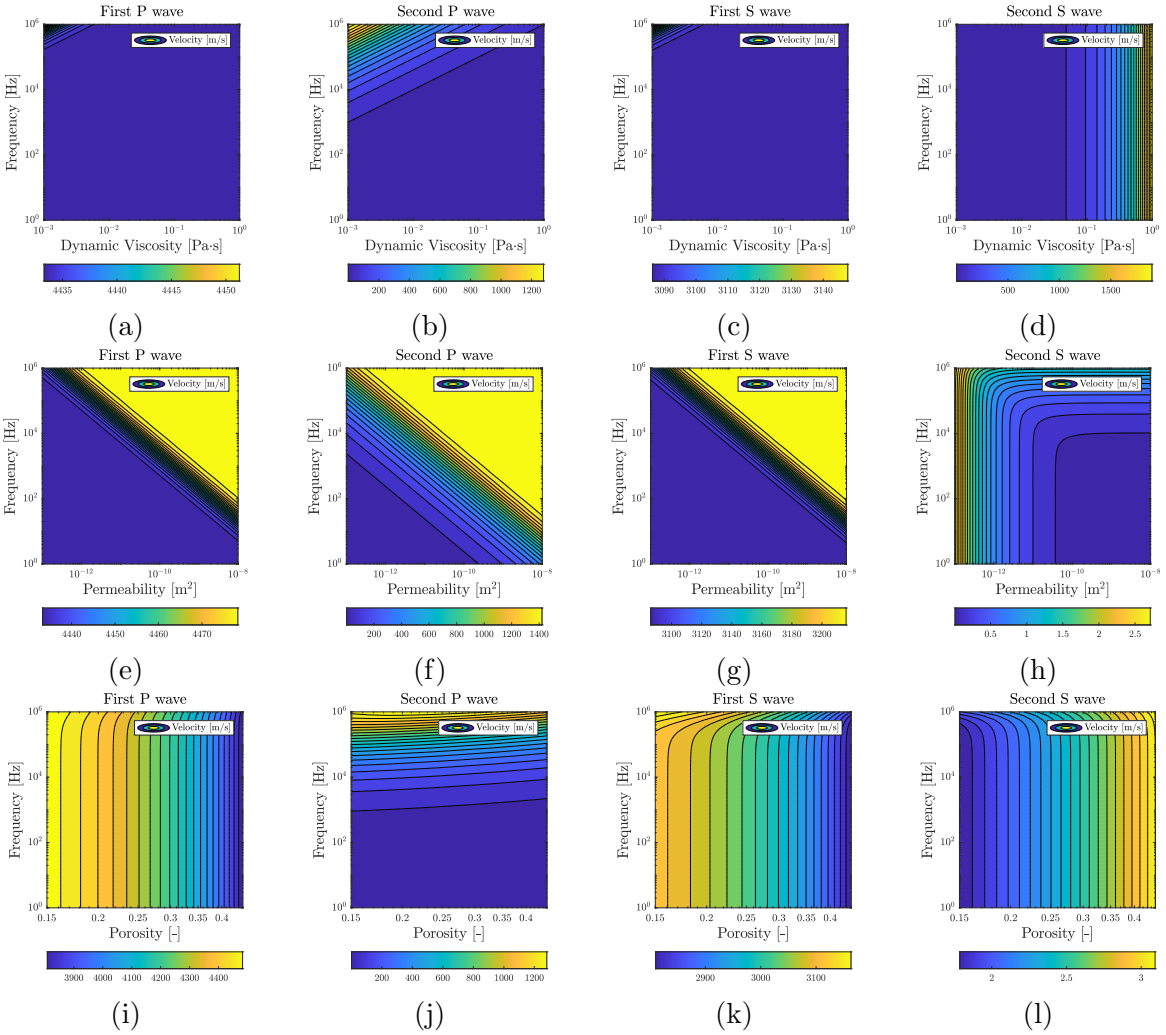


Figure 5.4: Velocity for the four wave types in dCS theory. Each row represents the variation in a different material parameter: (a)-(d) is fluid dynamic viscosity, (e)-(h) is intrinsic permeability, and (i)-(l) is initial porosity. Each column indicates a different wave type; first is fast P wave, second is slow P wave, third is fast S wave, and fourth is slow S wave.

however changes in frequency do not seem to affect it. Regarding the attenuation values, a similar behavior is presented in both P and S fast waves: higher attenuation appears at low μ_f and high frequencies. The opposite happens to the second P wave, having higher attenuation as μ_f increases; frequency, however, seems to have an influence only for low

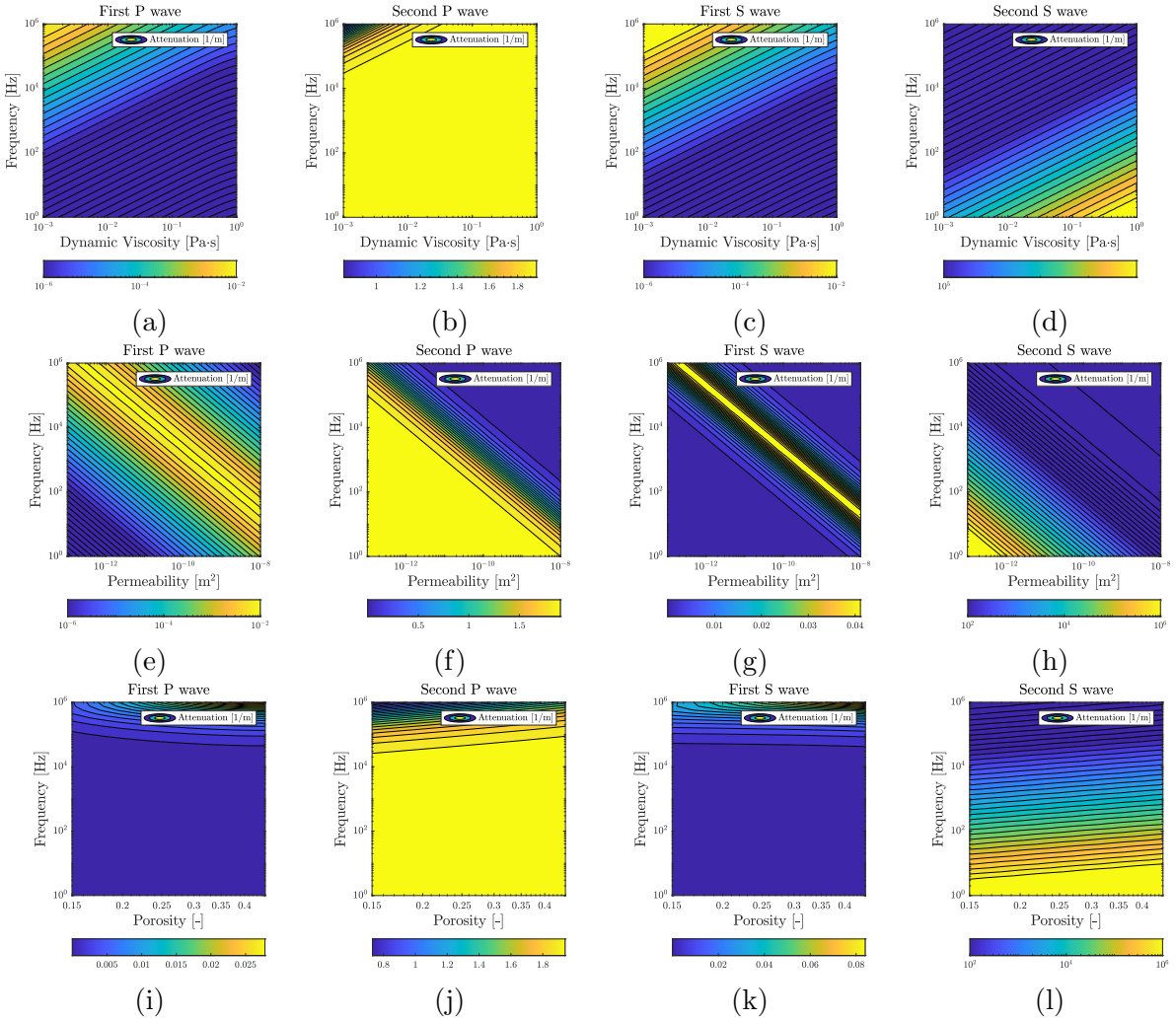


Figure 5.5: Attenuation for the four wave types in dCS theory. Each row represents the variation in a different material parameter: (a)-(d) is fluid dynamic viscosity, (e)-(h) is intrinsic permeability, and (i)-(l) is initial porosity. Each column indicates a different wave type; first is fast P wave, second is slow P wave, third is fast S wave, and fourth is slow S wave.

μ_f, and changes in ω become irrelevant for high μ_f. Furthermore, a peak in attenuation of the slow S wave happens for high μ_f and low frequencies.

Changes in velocity and attenuation values due to the intrinsic permeability κ can be

observed in Figures 5.4 and 5.5 (e) - (h). Velocities of both P waves and the fast S wave seem to increase for both high κ and high frequency. Frequency has a small effect on the slow S wave velocity, which decreases as permeability increases. With respect to the attenuation factor, the slow S wave has very high attenuation for low κ at low frequency. The slow P wave attenuation increases as both κ and frequency decrease. For the fast P and S waves, there is a region in the middle of the observed range where attenuation is higher.

The effect of porosity in wave patterns is depicted in Figures 5.4 and 5.5 (i)-(l). While fast P, S waves and slow S wave are not affected by changes in frequency, the slow P wave is not affected by porosity variations. The velocity in fast waves increases for low η_0, and it decreases for low η_0 in the slow S wave. Tle slow P wave velocity shows significant increase at high frequency. Attenuation for the four wave types does has very little dependency on porosity. Whilst attenuation is increased for high frequency in fast P and S waves, the opposite behavior is found in slow P, S waves.

5.3.5 Added mass coefficient ρ_{12}

The added mass coefficient ρ_{12} is an inertia coupling term introduced in Biot [15]. Hickey et. al. [84] mention that acceptable boundaries for this coefficient at the (seismic) low frequency level are $-\eta_0\rho_f/3 \leq \rho_{12} \leq 0$. For the material parameters listed in Table 4.1, such upper bound is given by $\rho_{12} = -63$ kg/m^3. When solving the porous media governing equations with two-field formulations, in terms of solid displacement and fluid pressure, we assume that solid and fluid accelerations are the same, and thus the ρ_{12} term in (5.1)-(5.2) vanishes.

When dealing with three-field formulations (adding fluid displacement as a main variable), however, this assumption is no longer made, and such term should be present. The coupling mass coefficient is, nonetheless, often neglected in three-field modeling [123, 169, 184]. In this sense, we performed additional tests to verify the difference that non-zero ρ_{12} values cause in the wave velocity and attenuation patterns. We noticed that even at the lower bound, for a water-saturated sandstone porous media, changes in ρ_{12} lead to negligible variations in wave patterns. Hence, neglecting the added mass term ρ_{12} does not lead to significant differences in the context of wave propagation.

5.3.6 Variation of porous media constituents

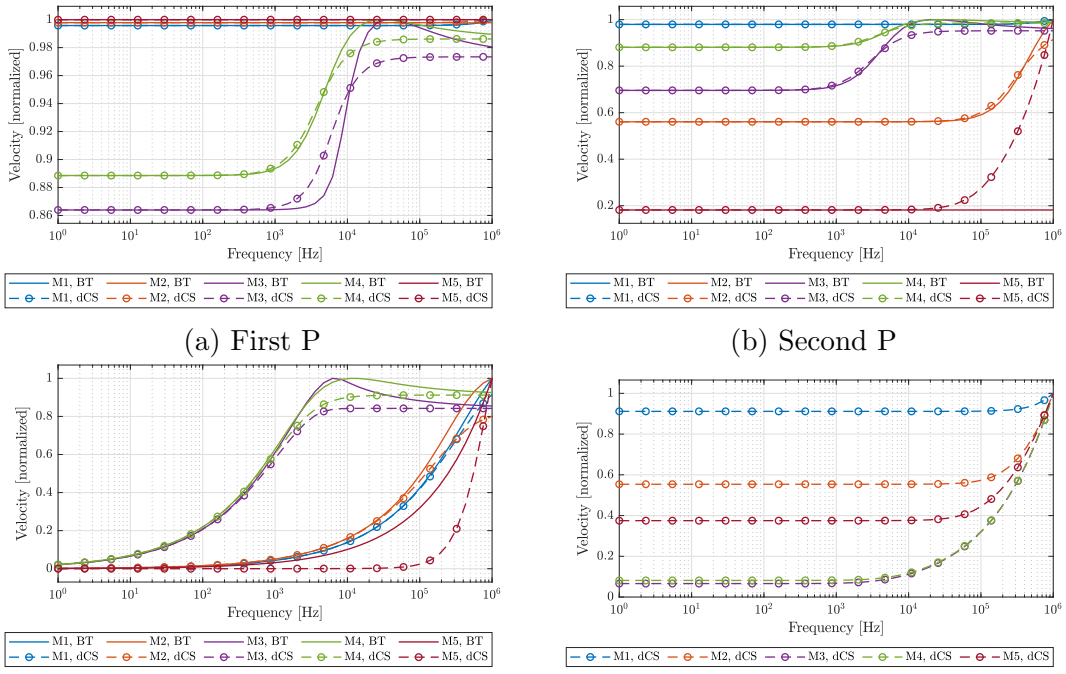
The material constituents herein considered represent a water-saturated sandstone medium. Nevertheless, a wide range of materials can be simulated using porous media theories. In this sense, further analysis are performed and a comparison between wave patterns is made considering five solid-fluid combinations: (M1) water and sandstone [193], (M2) water and cancellous bone tissue [87], (M3) fluidized snow and ice [146], (M4) brine and marine sediments [103], and (M5) heavy oil and marine sediments. Figures 5.6 and 5.7 depict the normalized velocity and attenuation values, respectively, of the four evaluated wave types for the BT and dCS models.

Regarding wave velocity, BT and dCS patterns are very similar for combinations M1 and M2, with deviations for the fast S wave at high frequency. Combination M5 shows similar fast P wave velocity, but differences are more pronounced for the slow P and fast S waves as frequency increases. For the combinations M3 and M4, the critical frequency limit is in the order of 10^3, and we can notice how BT and dCS behavior diverges after such limit – there is a peak velocity around the critical limit and it reaches a plateau after that.

On the other hand, wave attenuation seems to show more discrepancies between BT and dCS models. We observe how attenuation in combinations M3 and M4 diverge significantly after the critical frequency limit. Also, M5 yields higher attenuation for dCS theory when compared to BT. Fast P wave attenuation seems similar between BT and dCS theories for M1 and M2 combinations, and higher attenuation for such solid-fluid porous media is noticed for BT model in the slow P and fast S waves. It is noteworthy that attenuation for M3 is three times higher for BT than dCS curve for the fast P wave, and attenuation is almost doubled for the fast S wave. Furthermore, absolute velocity of slow P and fast S waves are significantly smaller for the M4 combination than others.

5.3.7 Porosity-pressure waves

Considering the introduction of the explicit porosity variable, the dCS theory allows the representation of the solid and fluid equations of motion in terms of pressure and porosity variables, instead of the solid displacement - fluid displacement pairing previously considered [165]. This representation yields wave equations that indicate the existence of two new strongly coupled compressional waves. One of these waves is a porosity diffusion wave, characterized by slow speed and an occurrence dependent on the fluid behaving incompressibly [165].



(a) First P

(b) Second P

(c) First S

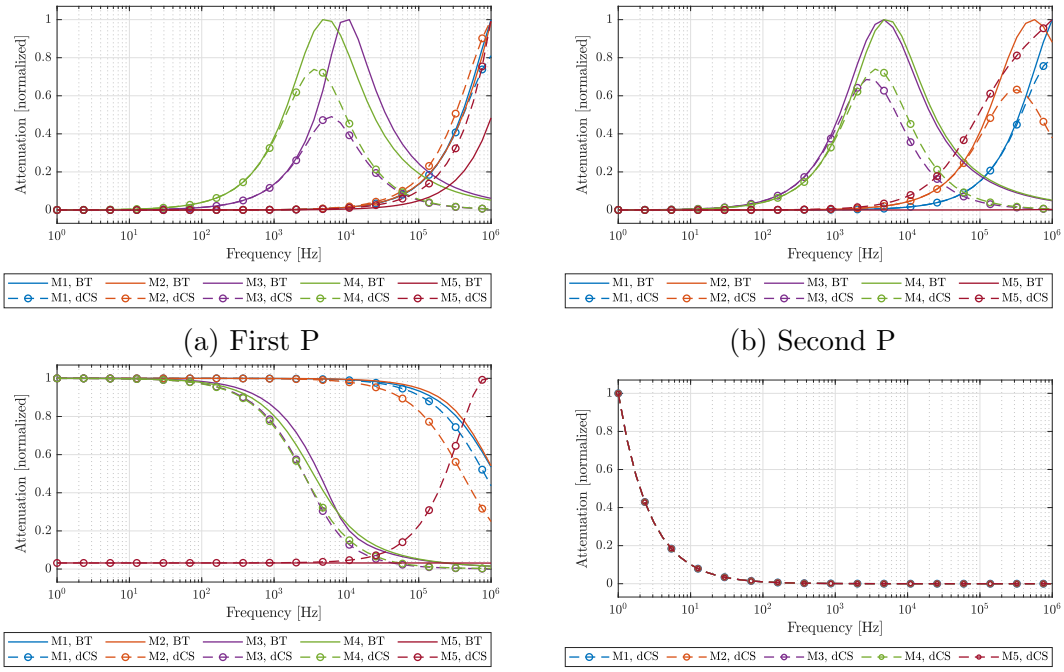
(d) Second S

Figure 5.6: Wave velocity for different materials considering both BT and dCS models.

The existence of porosity-pressure waves justifies a phenomena called fluid flow enhancement, which consists in a momentary increase in porosity in a certain region that consequently leads to higher fluid flow rates. A literature review on experiments with fluid flow enhancement based on wave pulses was presented in Chapter 1. The derivation of the porosity-pressure wave equations, as well as observations on the related wave patterns, are presented in Appendix C. Velocity and attenuation of these coupled waves are strongly dependent on the coefficient n.

5.4 Discussion

The governing equations in the dCS theory are written in terms of solid and fluid constituents, and they yield a set of wave equations that relate the wavenumber to a source frequency. It is noteworthy that, for obtaining such equations, one has to rely on the assumption that solid and fluid constituents propagate at the same wavelength, and consequently the same velocity. This assumption has been present in the previous studies on



(a) First P

(b) Second P

(c) First S

(d) Second S

Figure 5.7: Wave attenuation for different materials considering both BT and dCS models.

wave propagation in porous media [7, 202]. The extent to which such assumption is valid is a topic for future studies, as well as the discrepancy between BT and dCS results when this premise is disregarded.

The wave equations obtained for the dCS model account for additional phenomena when compared to BT. First, that are terms in the dCS fluid stress definition representing the viscous dissipation within the fluid. For the water-sandstone material herein studied, the inclusion of such terms lead to small differences between BT and dCS models. Nonetheless, the representation of fluid viscous dissipation is essential for capturing fluid vorticity effects at high frequencies and at discontinuities [76].

More to that, variations in the porosity effective pressure coefficient n can lead to changes in the wave propagation. Different values of n only affect compressional waves, and thus being related to volumetric deformations. For the minimum and maximum physically sound values of n, curves for velocity and attenuation in dCS theory show some discrepancy from BT theory. Realistic values have been determined for water-saturated media [136] through experiments in a quasi-static condition. However, different values could be expected for

dynamic problems and different material parameters [152].

Another difference between BT and dCS theories that can be pointed out is the coefficient δ_μ, only present on the latter. While the averaged shear modulus of the REV is given by $(1-\eta_0)\mu_s$, the macroscopic shear modulus in dCS is written as $\mu_M = (1-\delta_\mu)(1-\eta_0)\mu_s$, accounting for the difference between the averaged solid shear modulus and the value valid at the macroscopic scale after the volume averaging. As observed in the results, $\delta_\mu > 0$ yields some differences in the wave velocity and attenuation curves. As noted for the n parameter, the determination of δ_μ is also dependent on experiment settings, and might be different for static and dynamic simulations.

Aiming to study the wave velocity and attenuation patterns for frequencies above the critical value ω_c defined in (4.53), we considered a highly permeable sandstone. The curve trends changed after ω_c, showing significant difference between dCS and BT attenuation curves. Meanwhile, the velocity represented by BT theory reached a peak value after ω_c. As frequency increases, nonetheless, wave velocity becomes constant. Further tests with different solid-fluid combinations showed similar behavior after the critical frequency limit. We also performed additional tests to verify the effect of the added mass coefficient ρ_{12} on wave patterns, since this coefficient is sometimes neglected in numerical modeling. Values of $\rho_{12} \neq 0$ led to negligible differences in wave velocity and attenuation.

Through the contour plots over a frequency range from 10^0 to 10^6 Hz, we observed the impact of dynamic viscosity, permeability, and porosity on the wave velocity and attenuation. The general trend noticed is that such variables yield more changes for the P waves and the fast S wave at high frequencies, and the slow S wave usually presents the opposite behavior. This analysis shows insightful trends on the dependency of wave patterns on the material parameters, and how frequency may also have an influence in these patterns.

Wave velocity and attenuation showed significant discrepancies for BT and dCS theory at high frequencies. In the initial developments of BT theory, a correction factor was already introduced to represent fluid shear motion at high frequencies. Recent developments on the dCS theory, however, showed how this correction seems to be insufficient to represent the fluid vorticity in heterogeneous media and at porous media interfaces. In this sense, the complete fluid stress tensor in dCS theory seems to rightfully reproduce wave patterns, especially because the representation of a slow S wave justifies the changes in deformation energy. The results herein reported depict how these two methods lead to distinct wave behavior at the high-frequency range, considering that the BT correction factor is insufficient to fully capture fluid motion.

5.5 Conclusions

This chapter determines the planar P- and S-waves velocity and attenuation stemming from wave equations for porous media based on the de la Cruz and Spanos model. Since the dCS theory accounts for the complete fluid stress tensor, it leads to the representation of a slow S wave, not present in BT theory. Although this wave is characterized by low velocity and high attenuation, it is crucial in the representation of fluid viscous dissipation phenomena at high frequency, as well as in the representation of potential energy in wave reflection and transmission at porous media interfaces. This generalized dCS formulation leads to different wave attenuation than BT at high frequencies, to which we can observe that the BT frequency correction factor might not fully capture and incorrectly represent fluid behavior in such frequency range.

Changes in the porosity effective pressure coefficient and in the macroscopic solid shear modulus yield distinct results between dCS and BT models, and the most significant differences appear at high frequencies for the water-saturated sandstone combination. The effect of permeability, porosity, and dynamic viscosity on wave patterns were analysed for a wide frequency range. Different trends were observed for each material parameter; for instance, different values of initial porosity lead to changes in wave velocity for a same frequency, however changing the initial porosity does not affect attenuation. The results herein shown provide valuable insights on the wave patterns related to the dCS model and how they might change depending on the material parameters and frequency source. The comparison between BT and dCS theories raises important questions regarding the representation of fluid dissipation mechanisms at high frequencies. Regarding the correlation of the current study with practical applications, these results are directly related to nondestructive testing and laboratory measurements, for example, where higher frequencies are commonly used.

Chapter 6

Dynamic FE Formulation for Low- and High-frequency Applications

6.1 Introduction

In this chapter a three-field dCS formulation is presented, where the main variables are solid displacement, fluid pressure, and relative fluid velocity. This formulation has an advantage over the $u_s - p - u_f$ formulation since boundary and initial conditions are more easily prescribed, considering that in most applications the fluid velocity is known/desired instead of the fluid displacement. The $u_s - p - w$ system also allows a straightforward extension to inertia-dominant flows, when Darcy's law is replaced by nonlinear relations representing more complex fluid behavior.

Section 6.2 details the three-field governing equations, while 6.3 shows the corresponding weak formulation and the FE approximation to be solved. A verification and convergence study are presented in Section 6.4, where the derived formulation is compared to BT results. Convergence rates for linear elements are optimal, and those for mixed-order elements are once more shown to be sub-optimal due to solid-fluid coupling. In Section 6.5 numerical simulations of shale-sandstone layered domains are presented, where wave transmission and reflection effects are shown. An example of wave propagation in a sandstone core sample show how BT and dCS results diverge, also considering wave boundary reflections. The results are discussed in Section 6.6 and the conclusions are summarized in Section 6.7.

6.2 dCS Governing Equations

The solid and fluid momentum equations in the dCS theory are given by

$$(1-\eta_0)\rho_s\ddot{\mathbf{u}}_s = \nabla\cdot\boldsymbol{\sigma}_s + \frac{\mu_f\eta_0}{\kappa}F\mathbf{w} + \mathbf{b}_s, \tag{6.1}$$

$$\eta_0\rho_f\ddot{\mathbf{u}}_f = \nabla\cdot\boldsymbol{\sigma}_f - \frac{\mu_f\eta_0}{\kappa}F\mathbf{w} + \mathbf{b}_f, \tag{6.2}$$

where $\mathbf{u}_s$ is the solid displacement, $\mathbf{u}_f$ is the fluid displacement, and $\mathbf{w}$ is the fluid velocity relative to the solid, written as

$$\mathbf{w} = \eta_0(\dot{\mathbf{u}}_f - \dot{\mathbf{u}}_s); \tag{6.3}$$

for $u_s - p - w$ systems, solid strain and gradient of fluid velocity are assumed to be small. These form of the equations is adapted from [165] to explicitly include the field variable $\mathbf{w}$.

The parameter F is a high-frequency correction factor introduced by Biot [16], which assumes a unity value at the low frequency regime. Since this correction is not used in the dCS framework (see related discussions in Chapters 4 and 5), we use $F = 1$ for the dCS equations regardless of the frequency. The single and double dots indicate first and second time derivative, respectively; $\mathbf{b}_s, \mathbf{b}_f$ are body forces, and the averaged stresses are defined as in (3.14), (3.15). The storage equation is given by

$$\frac{\dot{p}}{K_f} + (1-\frac{\delta_f}{\eta_0})\frac{1}{\eta_0}\nabla\cdot\mathbf{w} + (1+\frac{\delta_s-\delta_f}{\eta_0})\nabla\cdot\dot{\mathbf{u}}_s = s. \tag{6.4}$$

Combining relations (6.1), (6.2), (6.4), and the porosity perturbation equation (3.20), the system to be solved in terms of $\mathbf{u}_s, p, \mathbf{w}$ is

$$\begin{cases} \nabla\cdot\boldsymbol{\tau} - \rho\ddot{\mathbf{u}}_s - \rho_f\dot{\mathbf{w}} + \mathbf{b} = 0, \\ \rho_f\ddot{\mathbf{u}}_s + \dfrac{\rho_f}{\eta_0}\dot{\mathbf{w}} + \nabla p - \dfrac{\mu_f}{\eta_0}\nabla^2\mathbf{w} - \mu_f\nabla^2\dot{\mathbf{u}}_s - \dfrac{1}{\eta_0}(\xi_f + \dfrac{\mu_f}{3} - \dfrac{\xi_f\delta_f}{\eta_0})\nabla(\nabla\cdot\mathbf{w}) \\ \qquad -\dfrac{1}{\eta_0}[\eta_0(\xi_f + \dfrac{\mu_f}{3}) + \xi_f\delta_s - \xi_f\delta_f]\nabla(\nabla\cdot\dot{\mathbf{u}}_s) + \dfrac{\mu_f}{\kappa}F\mathbf{w} - \mathbf{b}_f = 0, \\ \dfrac{\dot{p}}{K_f} + (1-\dfrac{\delta_f}{\eta_0})\dfrac{1}{\eta_0}\nabla\cdot\mathbf{w} + (1+\dfrac{\delta_s-\delta_f}{\eta_0})\nabla\cdot\dot{\mathbf{u}}_s = s, \end{cases} \tag{6.5}$$

where $\boldsymbol{\tau} = \boldsymbol{\sigma}_s + \boldsymbol{\sigma}_f = \boldsymbol{\sigma} - \alpha\mathbf{m}p$ is the total stress, $\rho = (1-\eta_0)\rho_s + \eta_0\rho_f$ is the total density, $\mathbf{b} = \mathbf{b}_s + \mathbf{b}_f$ is the body force term, and the material parameters are as given in Chapter 3.2.

6.3 Weak Form and FE Discretization

The correspondent weak form for (6.5) is given as follows. $\delta\mathbf{u}, \delta\mathbf{g}, \delta p$ are weight functions defined on appropriate function spaces, Ω is the simulation domain, and Γ is the correspondent boundary.

$$\begin{aligned}
&\rho \int_\Omega (\nabla\delta\mathbf{u})^\top \ddot{\mathbf{u}}_s \, d\Omega + \rho_f \int_\Omega (\nabla\delta\mathbf{u})^\top \dot{\mathbf{w}} \, d\Omega + \int_\Omega (\nabla\delta\mathbf{u})^\top \boldsymbol{\sigma} \, d\Omega - \alpha \int_\Omega (\nabla\delta\mathbf{u})^\top \mathbf{m} p \, d\Omega \\
&\quad = \int_{\Gamma_t} (\delta\mathbf{u})^\top \bar{\mathbf{t}} \, d\Gamma_t + \int_\Omega (\nabla\delta\mathbf{u})^\top \mathbf{b} \, d\Omega, \qquad (6.6)
\end{aligned}$$

$$\begin{aligned}
&\rho_f \int_\Omega (\delta\mathbf{g})^\top \ddot{\mathbf{u}}_s \, d\Omega + \frac{\rho_f}{\eta_0} \int_\Omega (\delta\mathbf{g})^\top \dot{\mathbf{w}} \, d\Omega - \int_\Omega (\nabla\delta\mathbf{g})^\top p \, d\Omega + \frac{\mu_f}{\eta_0} \int_\Omega (\nabla\delta\mathbf{g})^\top \nabla\mathbf{w} \, d\Omega \\
&\quad + \mu_f \int_\Omega (\nabla\delta\mathbf{g})^\top \nabla\dot{\mathbf{u}}_s \, d\Omega + \frac{1}{\eta_0}(\xi_f + \frac{\mu_f}{3} - \frac{\xi_f\delta_f}{\eta_0}) \int_\Omega (\nabla\delta\mathbf{g})^\top \nabla\cdot\mathbf{w} \, d\Omega \\
&\quad + \frac{1}{\eta}[\eta_0(\xi_f + \frac{\mu_f}{3}) + \xi_f\delta_s - \xi_f\delta_f] \int_\Omega (\nabla\delta\mathbf{g})^\top \nabla\cdot\dot{\mathbf{u}}_s \, d\Omega + \frac{\mu_f}{\kappa} \int_\Omega (\delta\mathbf{g})^\top \mathbf{w} \, d\Omega \\
&\quad = \int_\Omega (\delta\mathbf{g})^\top \mathbf{b}_f \, d\Omega - \int_{\Gamma_f} (\delta\mathbf{g})^\top \bar{p} \, d\Gamma_f + \frac{\mu_f}{\eta_0} \int_{\Gamma_f} (\delta\mathbf{g})^\top \nabla\mathbf{w}\cdot\mathbf{n} \, d\Gamma_f \\
&\quad + \mu_f \int_{\Gamma_f} (\delta\mathbf{g})^\top \nabla\dot{\mathbf{u}}_s \cdot\mathbf{n} \, d\Gamma_f + \frac{1}{\eta_0}(\xi_f + \frac{\mu_f}{3} - \frac{\xi_f\delta_f}{\eta_0}) \int_{\Gamma_f} (\delta\mathbf{g})^\top (\nabla\cdot\mathbf{w})\cdot\mathbf{n} d\Gamma_f \\
&\quad + \frac{1}{\eta_0}[\eta_0(\xi_f + \frac{\mu_f}{3}) + \xi_f\delta_s - \xi_f\delta_f] \int_{\Gamma_f} (\delta\mathbf{g})^\top (\nabla\cdot\dot{\mathbf{u}}_s)\cdot\mathbf{n} \, d\Gamma_f, \qquad (6.7)
\end{aligned}$$

$$\begin{aligned}
&\frac{1}{K_f} \int_\Omega (\delta p)^\top \dot{p} \, d\Omega + (1 - \frac{\delta_f}{\eta_0}) \frac{1}{\eta_0} \int_{\Gamma_q} (\delta p)^\top \nabla\cdot\mathbf{w} \, d\Omega + (1 + \frac{\delta_s - \delta_f}{\eta_0}) \int_\Omega (\delta p)^\top \nabla\cdot\dot{\mathbf{u}}_s \, d\Omega \\
&\quad = \int_\Omega (\delta p)^\top s \, d\Omega, \qquad (6.8)
\end{aligned}$$

The FE approximation is obtained using an interpolation for the $\mathbf{u}_s, \mathbf{w}, p$ fields as in

$$\mathbf{u}_s = \mathbf{N}_s\hat{\mathbf{u}}_s, \qquad \mathbf{w} = \mathbf{N}_f\hat{\mathbf{w}}, \qquad p = \mathbf{N}_p\hat{\mathbf{p}} \qquad (6.9)$$

in which $\mathbf{N}_s, \mathbf{N}_f, \mathbf{N}_p$ are Lagrangian shape functions and $\hat{\mathbf{u}}_s, \hat{\mathbf{w}}, \hat{\mathbf{p}}$ are vectors of nodal unknowns. The resulting semi-discretized matrix system is given by

$$\begin{cases}
\mathbf{M}_{ss}\ddot{\hat{\mathbf{u}}}_s + \mathbf{M}_{sf}\dot{\hat{\mathbf{w}}} + \mathbf{K}_{ss}\hat{\mathbf{u}}_s - \mathbf{K}_{sp}\hat{\mathbf{p}} = \mathbf{f}_s, \\
\mathbf{M}_{fs}\ddot{\hat{\mathbf{u}}}_s + \mathbf{M}_{ff}\dot{\hat{\mathbf{w}}} + \mathbf{C}_{fs}\dot{\hat{\mathbf{u}}}_s - \mathbf{K}_{fp}\hat{\mathbf{p}} + \mathbf{K}_{ff}\hat{\mathbf{w}} = \mathbf{f}_f, \\
\mathbf{C}_{ps}\dot{\hat{\mathbf{u}}}_s + \mathbf{K}_{pf}\hat{\mathbf{w}} + \mathbf{C}_{pp}\dot{\hat{\mathbf{p}}} = \mathbf{f}_p
\end{cases} \qquad (6.10)$$

in which the submatrices are

$$\mathbf{M}_{ss} = \rho \int_\Omega \mathbf{N}_s^\top \mathbf{N}_s \ d\Omega, \tag{6.11}$$

$$\mathbf{M}_{sf} = \rho_f \int_\Omega \mathbf{N}_s^\top \mathbf{N}_f \ d\Omega, \tag{6.12}$$

$$\mathbf{M}_{fs} = \mathbf{M}_{sf}^\top, \tag{6.13}$$

$$\mathbf{M}_{ff} = \frac{\rho_f}{\eta_0} \int_\Omega \mathbf{N}_f^\top \mathbf{N}_f \ d\Omega, \tag{6.14}$$

$$\mathbf{K}_{ss} = \int_\Omega \mathbf{B}_s^\top \mathbf{D} \mathbf{B}_s \ d\Omega, \tag{6.15}$$

$$\mathbf{K}_{sp} = \alpha \int_\Omega \mathbf{B}_s^\top \mathbf{m} \mathbf{N}_p \ d\Omega, \tag{6.16}$$

$$\mathbf{K}_{fp} = \int_\Omega \mathbf{B}_f^\top \mathbf{m} \mathbf{N}_p \ d\Omega, \tag{6.17}$$

$$\mathbf{C}_{pp} = \frac{1}{K_f} \int_\Omega \mathbf{N}_p^\top \mathbf{N}_p \ d\Omega \tag{6.18}$$

$$\mathbf{K}_{pf} = (1 - \frac{\delta_f}{\eta_0}) \frac{1}{\eta_0} \int_\Omega \mathbf{N}_p^\top \mathbf{m}^\top \mathbf{B}_f \ d\Omega, \tag{6.19}$$

$$\mathbf{C}_{ps} = (1 + \frac{\delta_s - \delta_f}{\eta_0}) \int_\Omega \mathbf{N}_p^\top \mathbf{m}^\top \mathbf{B}_s \ d\Omega, \tag{6.20}$$

$$\mathbf{K}_{ff} = \frac{\mu_f}{\kappa} \int_\Omega \mathbf{N}_f^\top \mathbf{N}_f \ d\Omega + \frac{1}{\eta_0} (\frac{4\mu_f}{3} + \xi_f - \frac{\xi_f \delta_f}{\eta_0}) \int_\Omega \mathbf{B}_f^\top \mathbf{B}_f \ d\Omega, \tag{6.21}$$

$$\mathbf{C}_{fs} = \frac{1}{\eta_0} [\eta_0 (\xi_f + \frac{4\mu_f}{3}) + \xi_f \delta_s - \xi_f \delta_f] \int_\Omega \mathbf{B}_f^\top \mathbf{B}_s \ d\Omega. \tag{6.22}$$

As highlighted in the derivations of FE formulations presented in previous chapters, this dCS system can also be simplified into the BT theory, if we assume a specific form of δ_s, δ_f as in (3.28) and if the fluid stress tensor in (3.15) is simplified to depend only on the fluid pressure, i.e. viscous dissipation terms are neglected.

Similarly to Chapter 4, in the following examples both low-order (linear approximation for all fields) and mixed-order (quadratic approximation for u_s, w fields, linear approximation for p field) elements are studied. The mixed-order elements herein used are the so-called Taylor-Hood elements [170]. BT two-field $u_s - p$ models have considered, for instance, mixed-order elements [204, 108] or low-order stabilized elements [154, 30]. Three-field $u_s - p - u_f$ BT models have been shown to allow the use of low-order elements without stabilization [91, 169], while $u_s - p - w$ BT models employed Raviart-Thomas elements to ensure stability [60, 123, 124]. Since no formal derivation of stability requirements for the dCS theory has been presented yet, we assume that the findings for BT theory hold for the dCS framework.

Using the generalized Newmark method as the time integration scheme [141], the main variables at time step $n+1$ are discretized as

$$\ddot{\hat{\mathbf{u}}}_s^{n+1} = \frac{1}{\beta\Delta t^2}(\hat{\mathbf{u}}_s^{n+1} - \hat{\mathbf{u}}_s^n) - \frac{1}{\beta\Delta t}\dot{\hat{\mathbf{u}}}_s^n - (\frac{1}{2\beta} - 1)\ddot{\hat{\mathbf{u}}}_s^n, \tag{6.23}$$

$$\dot{\hat{\mathbf{u}}}_s^{n+1} = \frac{\gamma}{\beta\Delta t}(\hat{\mathbf{u}}_s^{n+1} - \hat{\mathbf{u}}_s^n) - (\frac{\gamma}{\beta} - 1)\dot{\hat{\mathbf{u}}}_s^n - \Delta t(\frac{\gamma}{2\beta} - 1)\ddot{\hat{\mathbf{u}}}_s^n, \tag{6.24}$$

$$\dot{\hat{\mathbf{w}}}^{n+1} = \frac{1}{\theta\Delta t}(\hat{\mathbf{w}}^{n+1} - \hat{\mathbf{w}}^n) + (1 - \frac{1}{\theta})\dot{\hat{\mathbf{w}}}^n, \tag{6.25}$$

$$\dot{\hat{\mathbf{p}}}^{n+1} = \frac{1}{\zeta\Delta t}(\hat{\mathbf{p}}^{n+1} - \hat{\mathbf{p}}^n) + (1 - \frac{1}{\zeta})\dot{\hat{\mathbf{p}}}^n, \tag{6.26}$$

where $\beta, \gamma, \theta, \zeta$ are constant parameters. To add some numerical damping to the problem, we choose $\beta = \gamma = \theta = \zeta = 0.7$. The fully discretized system is given by

$$\begin{bmatrix} \overline{\mathbf{K}}_{ss} & \overline{\mathbf{K}}_{sf} & \overline{\mathbf{K}}_{sp} \\ \overline{\mathbf{K}}_{fs} & \overline{\mathbf{K}}_{ff} & \overline{\mathbf{K}}_{fp} \\ \overline{\mathbf{K}}_{ps} & \overline{\mathbf{K}}_{pf} & \overline{\mathbf{K}}_{pp} \end{bmatrix} \begin{Bmatrix} \hat{\mathbf{u}}_s^{n+1} \\ \hat{\mathbf{w}}^{n+1} \\ \hat{\mathbf{p}}^{n+1} \end{Bmatrix} = \begin{Bmatrix} \bar{\mathbf{f}}_s^{n+1} \\ \bar{\mathbf{f}}_f^{n+1} \\ \bar{\mathbf{f}}_p^{n+1} \end{Bmatrix}, \tag{6.27}$$

in which the matrix entries are

$$\overline{\mathbf{K}}_{ss} = \frac{\mathbf{M}_{ss}}{\beta\Delta t^2} + \mathbf{K}_{ss}, \tag{6.28}$$

$$\overline{\mathbf{K}}_{fs} = \frac{\mathbf{M}_{fs}}{\beta\Delta t^2} + \mathbf{C}_{fs}\frac{\gamma}{\beta\Delta t}, \tag{6.29}$$

$$\overline{\mathbf{K}}_{ps} = \mathbf{C}_{ps}\frac{\gamma}{\beta\Delta t}, \tag{6.30}$$

$$\overline{\mathbf{K}}_{sf} = \frac{\mathbf{M}_{sf}}{\theta\Delta t}, \tag{6.31}$$

$$\overline{\mathbf{K}}_{ff} = \frac{\mathbf{M}_{ff}}{\theta\Delta t} + \mathbf{K}_{ff}, \tag{6.32}$$

$$\overline{\mathbf{K}}_{pf} = \mathbf{K}_{pf}, \tag{6.33}$$

$$\overline{\mathbf{K}}_{sp} = -\mathbf{K}_{sp}, \tag{6.34}$$

$$\overline{\mathbf{K}}_{fp} = -\mathbf{K}_{fp}, \tag{6.35}$$

$$\overline{\mathbf{K}}_{pp} = \frac{\mathbf{C}_{pp}}{\zeta\Delta t}, \tag{6.36}$$

and the vectors are defined as

$$\bar{\mathbf{f}}_s^{n+1} = \mathbf{f}_s^{n+1} + \mathbf{M}_{ss}\left[\frac{1}{\beta\Delta t^2}\hat{\mathbf{u}}_s^n + \frac{1}{\beta\Delta t}\dot{\hat{\mathbf{u}}}_s^n + (\frac{1}{2\beta}-1)\ddot{\hat{\mathbf{u}}}_s^n\right] + \mathbf{M}_{sf}\left[\frac{1}{\theta\Delta t}\hat{\mathbf{w}}^n - (1-\frac{1}{\theta})\dot{\hat{\mathbf{w}}}^n\right], \tag{6.37}$$

$$\begin{aligned}\bar{\mathbf{f}}_f^{n+1} =& \mathbf{f}_f^{n+1} + \mathbf{M}_{fs}\left[\frac{1}{\beta\Delta t^2}\hat{\mathbf{u}}_s^n + \frac{1}{\beta\Delta t}\dot{\hat{\mathbf{u}}}_s^n + (\frac{1}{2\beta}-1)\ddot{\hat{\mathbf{u}}}_s^n\right] + \mathbf{M}_{ff}\left[\frac{1}{\theta\Delta t}\hat{\mathbf{w}}^n - (1-\frac{1}{\theta})\dot{\hat{\mathbf{w}}}^n\right] \\ &+ \mathbf{C}_{fs}\left[\frac{\gamma}{\beta\Delta t}\hat{\mathbf{u}}_s^n + (\frac{\gamma}{\beta}-1)\dot{\hat{\mathbf{u}}}_s^n + \Delta t(\frac{\gamma}{2\beta}-1)\ddot{\hat{\mathbf{u}}}_s^n\right],\end{aligned} \tag{6.38}$$

$$\bar{\mathbf{f}}_p^{n+1} = \mathbf{f}_p^{n+1} + \mathbf{C}_{ps}\left[\frac{\gamma}{\beta\Delta t}\hat{\mathbf{u}}_s^n + (\frac{\gamma}{\beta}-1)\dot{\hat{\mathbf{u}}}_s^n + \Delta t(\frac{\gamma}{2\beta}-1)\ddot{\hat{\mathbf{u}}}_s^n\right] + \mathbf{C}_{pp}\left[\frac{1}{\zeta\Delta t}\hat{\mathbf{p}}^n - (1-\frac{1}{\zeta})\dot{\hat{\mathbf{p}}}^n\right]. \tag{6.39}$$

6.4 Verification and Convergence Study

6.4.1 Verification with Biot model

The developed dCS formulation is verified against BT results for a dynamic one-dimensional consolidation problem. The material parameters for a water-saturated sandstone are taken from [50, 43]; the domain has a length of $L = 10$m, the solid displacement is fixed at the bottom ($x = 0$m) and a point load of $\bar{t} = 3$kN is applied at the top ($x = 10$m). The column has a fixed pressure $p = 0$ at $x = 10$m and an impervious behavior at $x = 0$m. The domain is discretized into $ne = 400$ elements with a linear approximation for p and a quadratic approximation for u_s, w fields. The final simulation time is taken as $t_{end} = 5$s and the time step is $\Delta t = 10^{-2}$s.

Figure 6.1 depicts the variation of $u_s, \dot{u}_s, p, w$ over the domain at the final simulation time. We observe that the dCS theory ($n = 1$) yields the same behavior as BT theory, as expected. For the behavior over time, initial instability was noticed in the pressure and relative fluid velocity fields; such instability, related to the step load application, was dissipated before $t = 1$s.

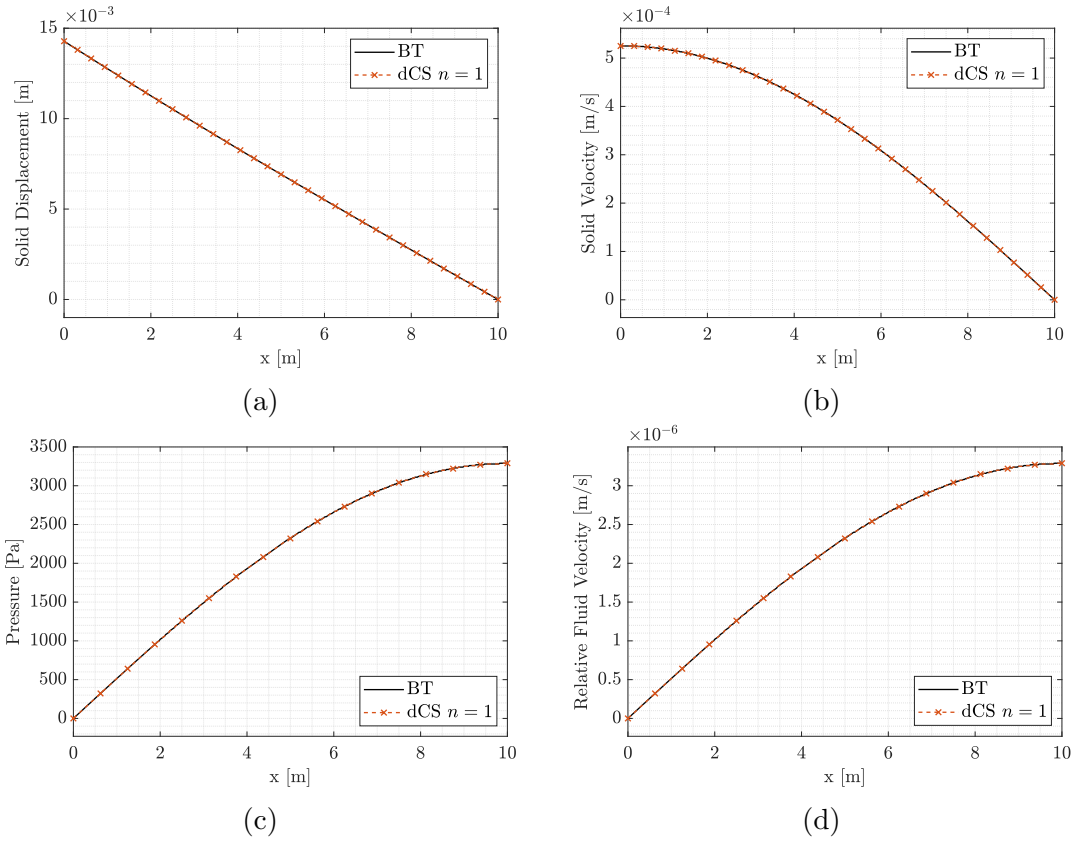


Figure 6.1: Verification study for (a) solid displacement, (b) solid velocity, (c) fluid pressure, and (d) relative fluid velocity. Plots show variation over the domain at $t_{end} = 5$s for BT and dCS theories.

6.4.2 Convergence study

The convergence of the three-field dCS numerical model is studied by using a manufactured solution of the type

$$u_s = \sin(xt)/1000 \quad [\text{m}], \tag{6.40}$$

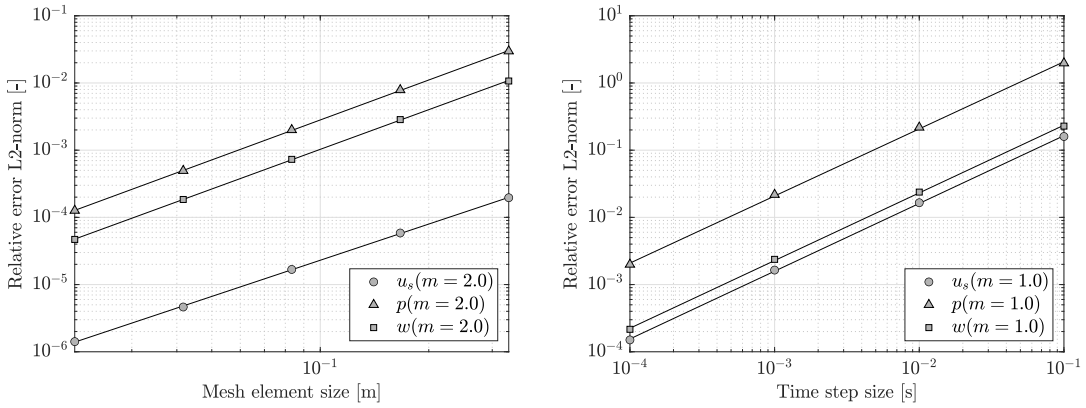
$$w = \cos(xt)/1000 \quad [\text{m}], \tag{6.41}$$

$$p = \sin(xt)\cos(xt)/1000 \quad [\text{GPa}]. \tag{6.42}$$

The one-dimensional example has a length of $L = 4$m and the material parameters are given by [193]; a linear approximation is adopted for all fields. For the mesh size refinement,

a time step of $\Delta t = 10^{-5}$s is fixed for a final simulation time of $t_{end} = 1$s, while mesh element size is decreased. Figure 6.2a depicts the mesh size convergence for the three fields, showing optimal rates for the choice of same-order linear elements. It is noteworthy that, although optimal mesh size convergence rates are reported for linear elements, additional tests showed that the same does not hold for mixed-order elements. In this case, the quadratic approximation is deteriorated due to the solid-fluid coupling effect, and poorer convergence rates are expected the more the coupling terms differ from the uncoupled ones [127, 25].

For the time step convergence, the number of elements is fixed at $ne = 100$, while the time step is decreased. A reference solution using $\Delta t = 10^{-5}$s is employed for comparison. Results in Figure 6.2b depict a first order convergence for all three fields, as expected due to the chosen time integration scheme and related parameters.



(a) (b)

Figure 6.2: Convergence study for (a) mesh size refinement and (b) time step refinement; the convergence rates m for each field are indicated in the legend.

6.5 Numerical Examples

6.5.1 Three-layer domain with low-frequency wave propagation

The three-field $u_s - p - w$ dCS is employed in the simulation of a two-dimensional wave propagation through a water-saturated domain. The problem geometry is depicted in Figure 6.3, where a sandstone layer of 400m thickness is adjacent to two 800m-thickness

shale layers; lines CD and EF indicate the material interfaces. The whole domain has dimensions 2000×4000m, and the material parameters of both constituents are listed in Tables 4.1 (sandstone) and 6.1 (shale). The sandstone has a permeability of $\kappa = 10^{-11}\text{m}^2$ and a porosity of $\eta_0 = 0.19$, whilst the shale permeability is given by $\kappa = 10^{-21}\text{m}^2$ and the porosity is $\eta_0 = 0.08$. The normal solid displacement is fixed at all boundaries, where also $p = 0$. A Ricker wavelet source is applied in the solid displacement field at the center of the domain with a frequency of 10Hz.

Table 6.2 reports the wave velocity and wavelength for the aforementioned parameters for sandstone and shale; differences for dCS and BT models are negligible. Due to the low permeability and porosity of shale, the slow S wave velocity has an attenuation of the order of 10^{13}, and thus it is not propagatory. The dry wave speed of the sandstone material for P and S waves are $v_P^{dry} = 2481$ m/s and $v_S^{dry} = 1519$ m/s, respectively. For the shale material, the correspondent velocities are $v_P^{dry} = 3977$ m/s and $v_S^{dry} = 2552$ m/s.

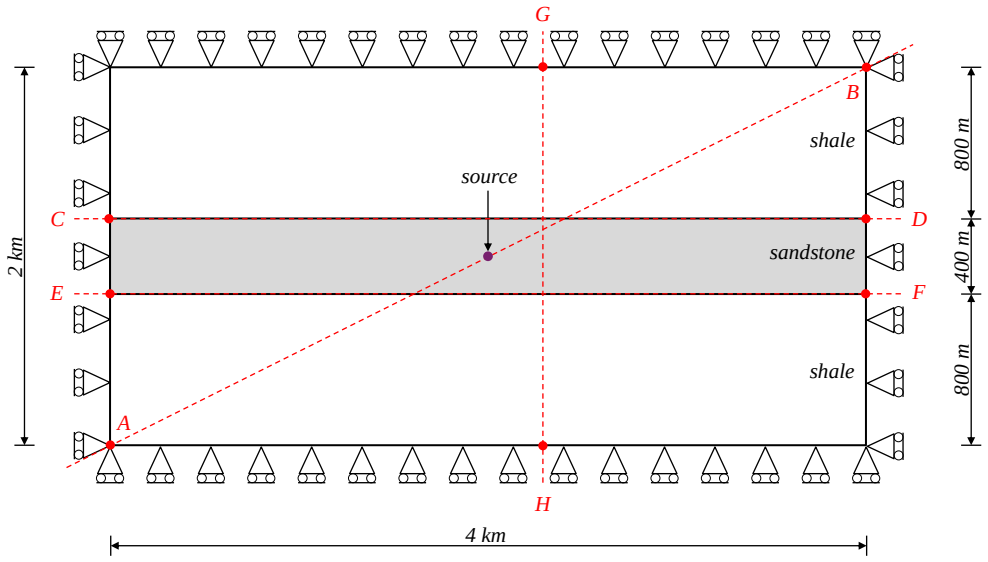


Figure 6.3: Geometry of two-dimensional three-layer domain.

The domain is discretized into $ne = 15,400$ elements considering a linear approximation for all fields. The total simulation time is of $t_{end} = 3.2 \times 10^{-1}$s and the time step is $\Delta t = 8 \times 10^{-4}$s. Figure 6.4 compares the solid and fluid behavior using BT and dCS theories at the diagonal AB (Figure 6.3), as well as variations in the porosity effective pressure coefficient for the latter. BT and dCS models yield very similar behavior when $n = 1$; in this case, the only difference between BT and dCS formulations is the fluid stress definition. Variations are more significant for n_{max} than n_{min}, when n_{max} leads to less

Table 6.1: Material parameters for water saturated shale [168].

Parameter	Symbol	Value	Unit
Young's modulus	E	38.93	GPa
Poisson's ratio	ν	0.15	-
Intrinsic permeability	κ	1×10^{-21}	m^2
Biot coefficient	α	0.47	-
Initial porosity	η_0	0.08	-
Dynamic viscosity of fluid	μ_f	10^{-3}	$Pa \cdot s$
Bulk viscosity of fluid	ξ_f	2.8×10^{-3}	Pa·s
Bulk modulus of solid	K_s	35	GPa
Bulk modulus of fluid	K_f	3.3	GPa
Density of solid	ρ_s	2600	kg/m^3
Density of fluid	ρ_f	1000	kg/m^3
Added mass density	ρ_{12}	0	kg/m^3
Compliance of solid	$\delta_s(n=1)$	0.2672	-
Compliance of fluid	$\delta_f(n=1)$	0.0252	-

Table 6.2: Velocity and wavelength of dCS P and S waves for water-saturated sandstone [193] and shale [168], considering $\kappa = 10^{-11} m^2$ and source frequency of 10Hz.

Parameter	Fast P	Slow P	Fast S	Slow S
Sandstone - Wave velocity [m/s]	4433.32	45.72	3086.30	0.28
Sandstone - Wavelength [m]	443.33	4.57	308.63	0.03
Shale - Wave velocity [m/s]	4377.21	6.84×10^-4	2616.85	-
Shale - Wavelength [m]	437.71	6.84×10^{-5}	261.68	-

attenuation in the u_s field and more attenuation in the p field, when compared to $n = 1$. For n_{max} we notice how there is no variation in porosity, meaning that at the upper bound n_{max} when $\delta_s = \delta_f$, porosity remains unchanged.

Figure 6.5 shows the wave propagation contours for solid velocity, relative fluid velocity, fluid pressure, and porosity variation for (i) the three-layer case and (ii) a sandstone-only domain – so that material interface effects can be better visualized. We notice how P waves travel faster once they reach the shale layer, and are also more attenuated. The reflected waves are easily identified in the solid velocity plots, and relative fluid velocity is more significant in the sandstone layer. The pressure distribution in the layered domain shows

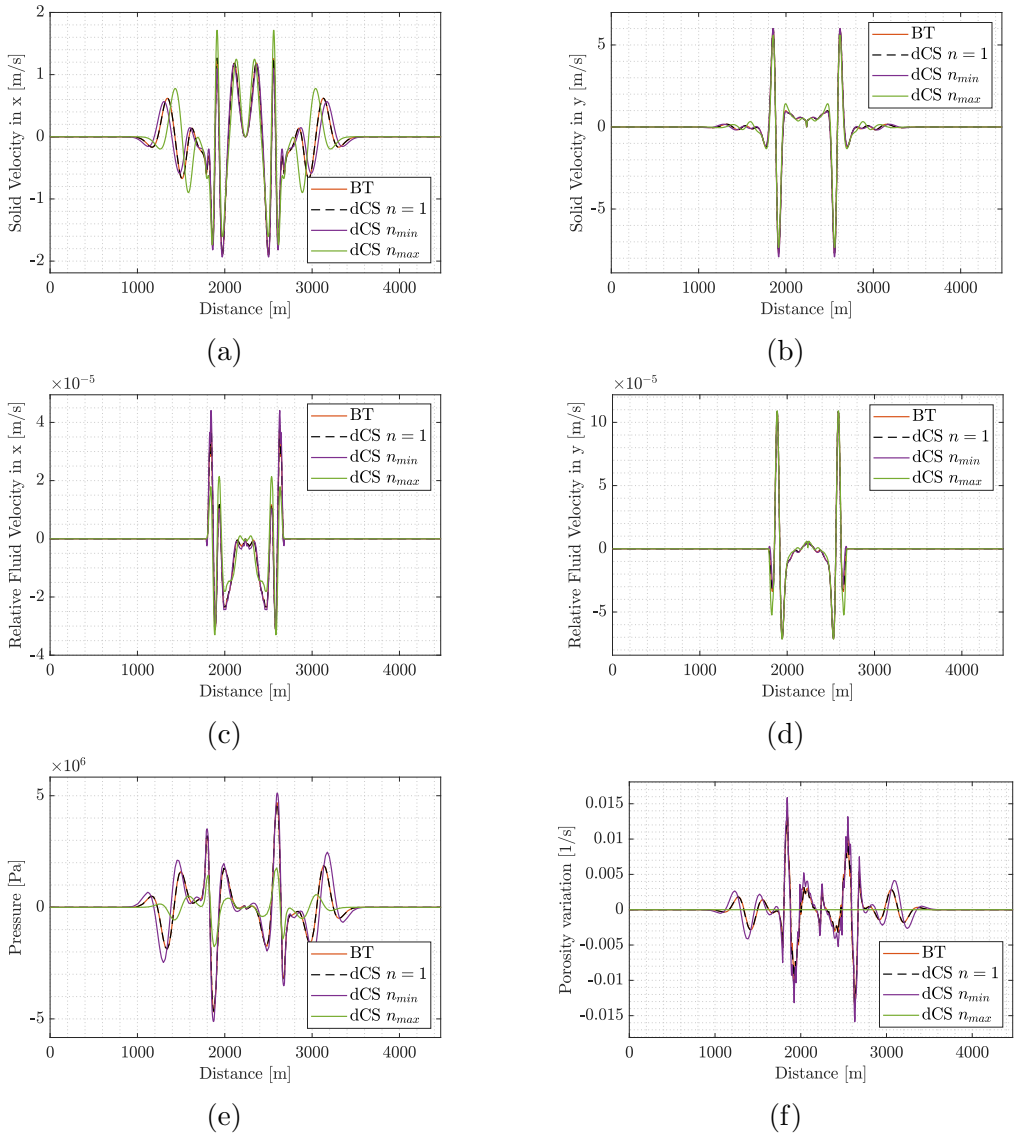
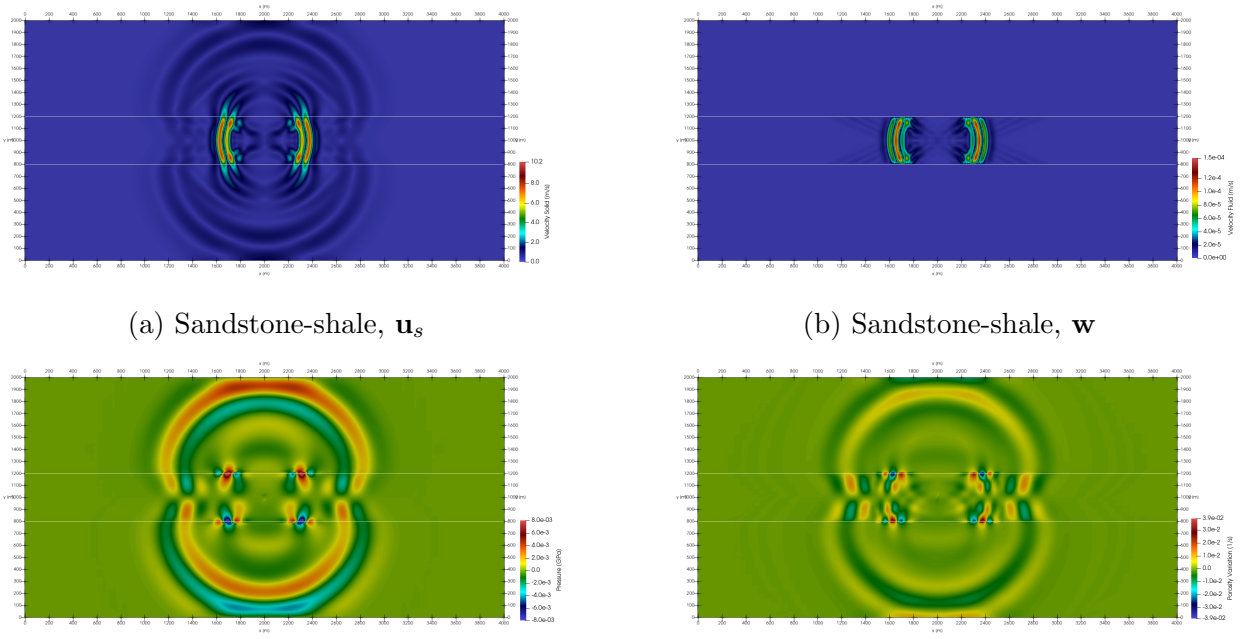


Figure 6.4: Two-dimensional wave propagation in three-layer domain: variation of (a,b) solid velocity, (c,d) relative fluid velocity, (e) fluid pressure, and (f) porosity across the diagonal AB (Figure 6.3) at $t_{end} = 0.32$s.

that not only waves are more attenuated when reaching the shale formation, but also that there are peak pressure wave points at the material interface.

In Figure 6.6 the wave patterns for solid velocity, relative fluid velocity, and fluid pressure

are depicted in synthetic plots. The behavior at the line GH (indicated in Figure 6.3) is monitored throughout the simulation. We compare the results in the layered domain with a sandstone-only medium, so that the effects caused by the material interface are better understood. More oscillations are found in the $\dot{\mathbf{u}}_s$ field for the layered domain; the relative fluid velocity $\mathbf{w}$ vanishes at the shale layer. For the pressure field, we notice how new wave patterns are formed at the material interface, when compared to the sandstone-only medium.



(a) Sandstone-shale, $\mathbf{u}_s$

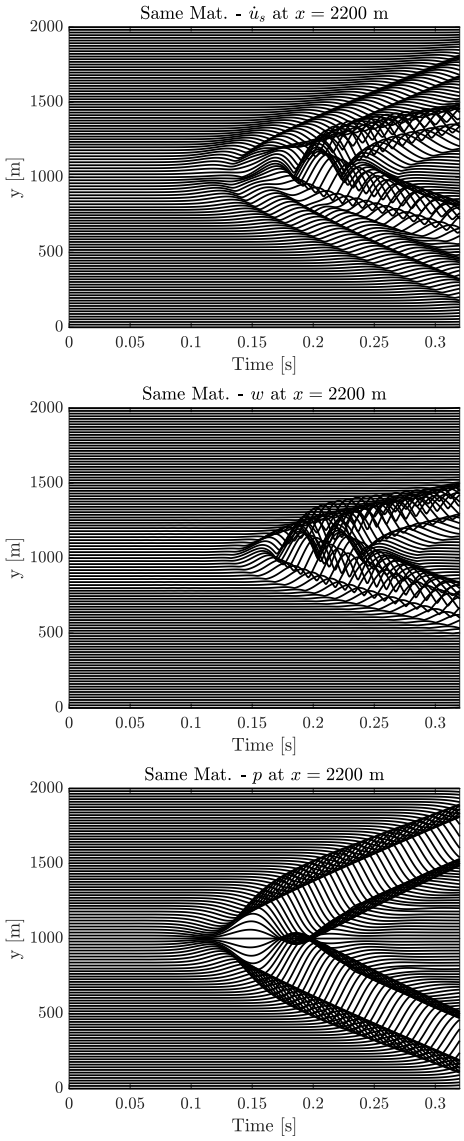
(b) Sandstone-shale, $\mathbf{w}$

(c) Sandstone-shale, p

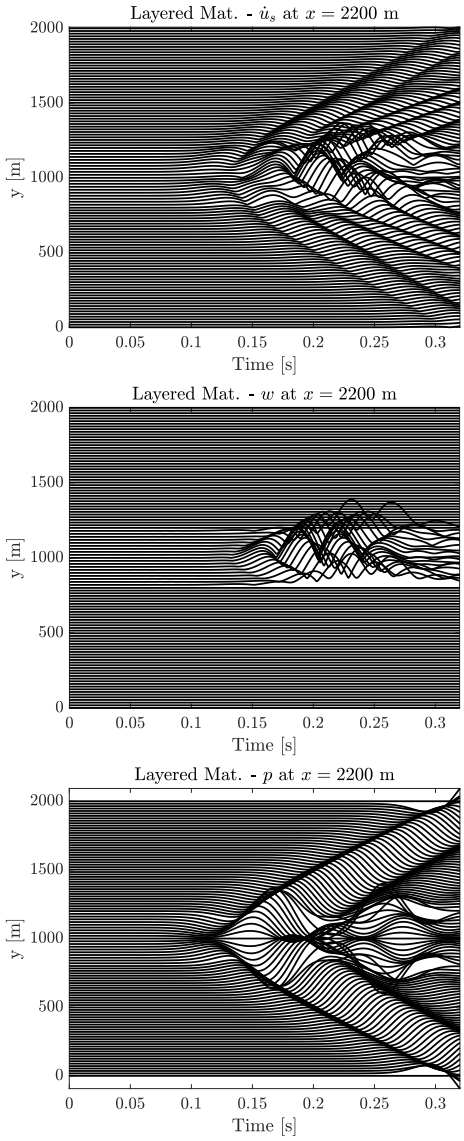
(d) Sandstone-shale, $\dot{\eta}$

Figure 6.5: Two-dimensional wave propagation in sandstone (a, c, e) and three-layer (b, d, f) domains at $t_{end} = 0.32$s. The horizontal white lines correspond to lines CD and EF in Figure 6.3.

Figure 6.7 shows the pressure and fluid velocity evolution over time. Each column indicates a different time step, i.e. $t = 0.136$s, $t = 0.2$s, $t = 0.24$s, and $t = 0.28$s. While the top row depicts pressure variation at a sandstone-only medium, the other two rows show the wave patterns at the three-layer domain. At $t = 0.136$s the waves are still concentrated at the sandstone layer, and at $t = 0.2$s they start to spread into the shale layer. We notice already how the outer waves are attenuated when reaching the shale material, characterized by lower porosity and lower permeability. Due to such characteristics, it is indeed expected



(a) Same Material



(b) Layered Material

Figure 6.6: Synthetic plots at line GH ($x = 2,200$m) for (a) sandstone-only medium and (b) three-layered domain.

that waves travel faster and are more attenuated in shale compared to sandstone.

At $t = 0.24$s we observe how the waves continue to propagate through the shale layer,

however part of the waves seem to split from the wave front, being held at the shale-sandstone interface. This happens due to the phenomena of wave propagation through material interfaces – while part of the wave is transmitted, part of it is reflected and another part propagates at the interface. Although this phenomena is more noticeable for the pressure field, it was also observed in the behavior of solid velocity and relative fluid velocity to a lesser extent. Additional tests with a sandstone-shale-sandstone layered domain, where the wave source was applied in the sandstone layer, did not show the same prominent wave propagation at the interface.

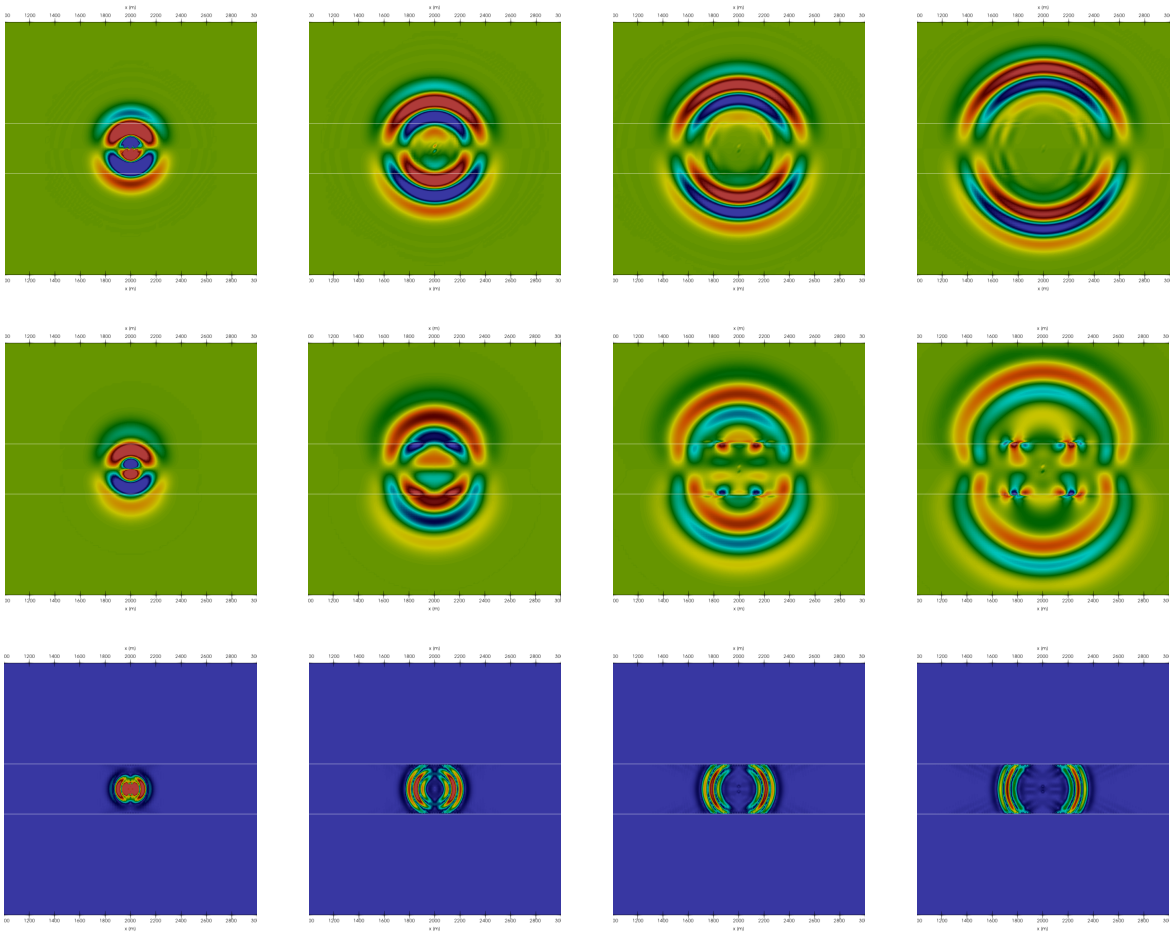
6.5.2 Two-layer domain with high-frequency wave propagation

A two-dimensional two-layer domain with geometry depicted in Figure 6.8 is simulated with the developed three-field dCS model. The sandstone and shale formations have the same properties as the previous example, and boundary conditions are also the same. The cross section EF indicates the material interface. The wave source is applied in the middle of the domain to the solid velocity field so that cylindrical waves are generated. Differently from Section 6.5.1, it is now a high-frequency pulse given by $S(t) = \sin(2\pi t f) - 0.5\sin(4\pi t f)$, where $f = 20$kHz. The wave characteristics of P and S wave are as reported in Table 6.2 except from the slow P wave, which now has a velocity of 633.74 m/s in sandstone.

The 30×30m domain is discretized into a 400×400 mesh with a bi-linear approximation for all fields. The final simulation time is $t_{end} = 4 \times 10^{-3}$s and the correspondent time step is $\Delta t = 10^{-5}$s. Since the critical frequency limit is $\omega_c = 1.01 \times 10^4$Hz and the applied pulse is 20kHz, the simulation fits into the high-frequency BT regime. Nonetheless, the correction factor F is still close to unity, and thus BT and dCS results were noticed to yield similar behavior.

Figures 6.9 and 6.10 depict the contours of solid velocity, relative fluid velocity, fluid pressure, and porosity variation at the final simulation time. In the solid velocity plot, we notice how the fast P wave propagates faster and it is more attenuated at the shale layer. The transition from sandstone to shale domain leads to negligible values of the relative fluid velocity (order of 10^{-16}) and hence transmitted waves are not identified. Still, the reflected waves are noticed. It is also interesting how the fast P waves are not detected in the relative fluid velocity field due to negligible magnitude. For the pressure field, fast P and S waves are reflected and transmitted; surface waves at the material interface also appear. Similar behavior is observed in the porosity variation plots, where the effects of fast S waves are slightly more visible.

Figure 6.11 indicates the waves types in both solid velocity and fluid pressure contour



(a) $t = 0.136$s (b) $t = 0.2$s (c) $t = 0.24$s (d) $t = 0.28$s

Figure 6.7: Two-dimensional wave propagation in sandstone domain (top row) and shale-sandstone (middle, bottom rows) layered domain. Each column depicts results at a different simulation time. The horizontal white lines correspond to lines CD and EF in Figure 6.3.

plots. For the former, we notice how the transmitted fast P and S waves are split into two fronts. Also, the slow P wave is slightly noticeable, and it interferes in the reflected fast P wave shape. For the pressure contour plot, it is possible to identify the reflection and transmission of fast P and S waves. More to that, the fast S wave is divided into a surface wave contribution, which propagates at the material interface. In both solid and fluid fields, the shale domain clearly allows faster wave propagation since the P wave is

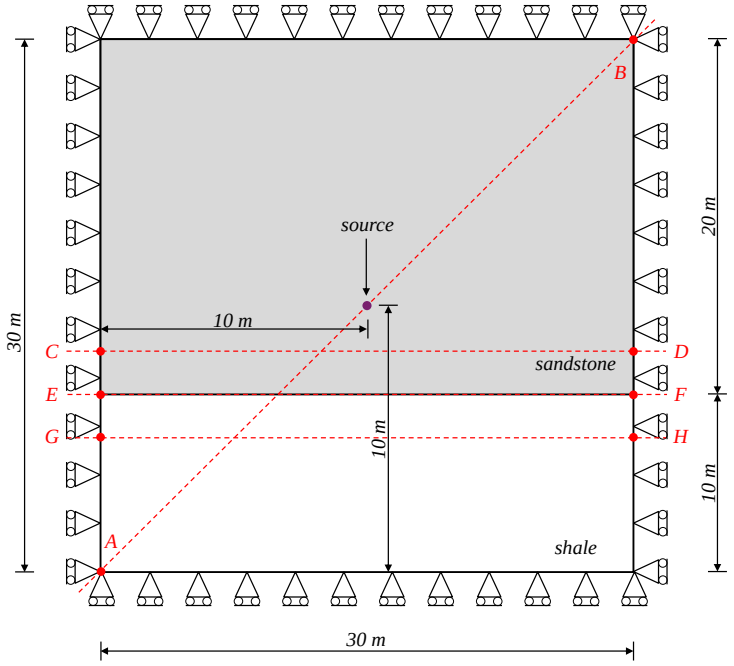
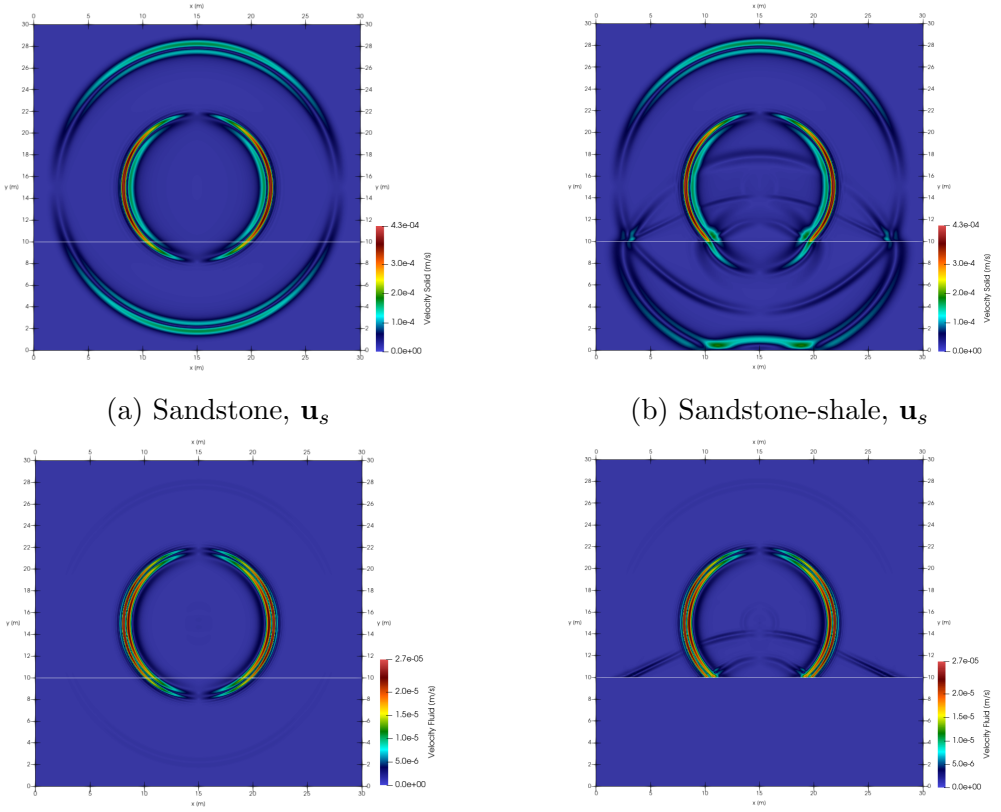


Figure 6.8: Geometry of two-dimensional layered domain.

being reflected at the shale boundary whilst its upper counterpart (in sandstone) did not reach the domain boundary.

A comparison between the BT and dCS ($n = 1$) wave patterns at $y = 10$m (line EF in Figure 6.8) for the sandstone-only and for the shale-sandstone domains is shown in Figure 6.12. In the two-layer domain, $y = 10$m indicates the location of the material interface. For the solid velocity and fluid velocity field, the patterns are somewhat similar, apart from variations in wave attenuation. The y component of the relative fluid velocity is the most affected component at the interface, with a significant lower attenuation for the layered domain. For the pressure field and porosity variation, differences on the two-layer problem are more pronounced. Besides changes in attenuation on the fast P wave, the reflection/transmission of the fast S wave leads to a surface wave propagating at the interface. Compared to the sandstone-only domain, the this wave propagation pattern is barely noticed in pressure plots. For all fields, there is a slight distinction between BT and dCS curves for the fast S wave, however fast P wave remains the same.

Additional analysis were performed to observe wave patterns at $x = 8$m (line GH in Figure 6.8, transmitted waves) and $x = 12$m (line CD in 6.8, reflected waves) in the layered domain. The transmitted waves showed small differences in BT and dCS ($n = 1$) curves



(a) Sandstone, $\mathbf{u}_s$

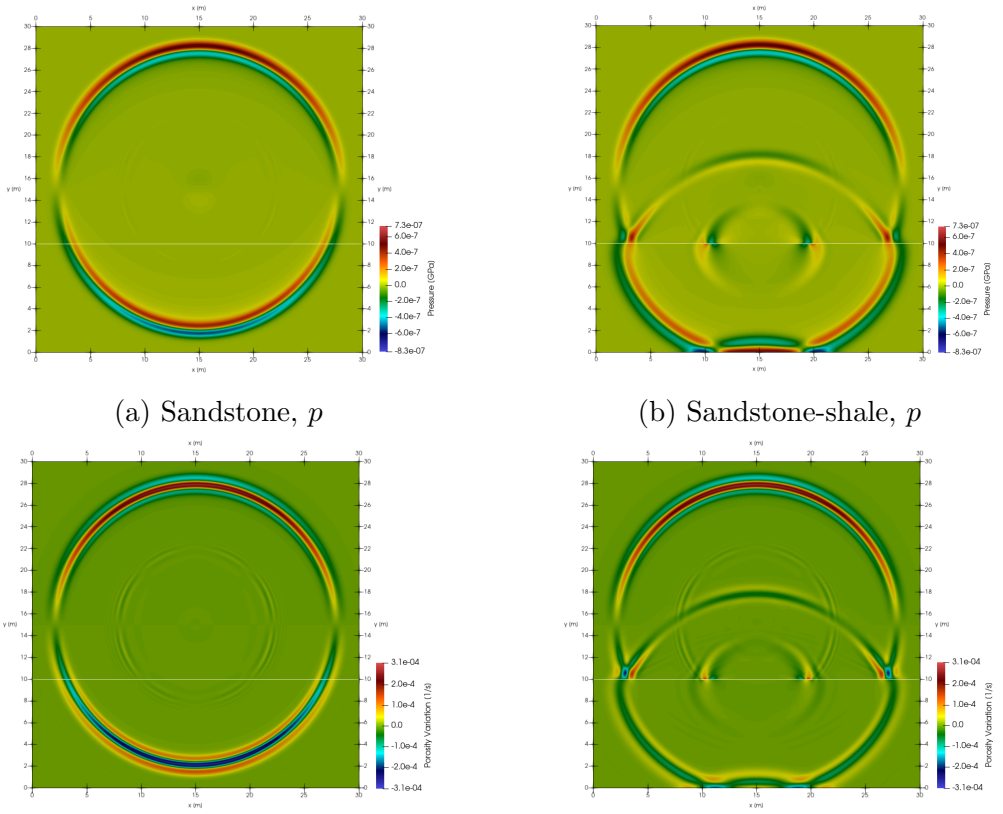
(b) Sandstone-shale, $\mathbf{u}_s$

(c) Sandstone, $\mathbf{w}$

(d) Sandstone-shale, $\mathbf{w}$

Figure 6.9: Two-dimensional wave propagation of $\mathbf{u}_s, \mathbf{w}$ fields in sandstone (a, c) and two-layer (b, d) domains at $t_{end} = 4 \times 10^{-3}$s. The horizontal white line corresponds to the material interface EF indicated in Figure 6.8.

for the relative velocity field; nonetheless, $\mathbf{w}$ has very small magnitude in the shale domain. BT and dCS curves are the same for the reflected waves at $x = 12$m. Further studies also comprised the variation of n in the dCS model. Solid velocity and relative fluid velocity plots showed same behavior for fast S wave, and reduced wave attenuation and speed for the fast P wave when $n = n_{max}$. Still for n_{max}, pressure and porosity variation plots showed more attenuation for fast P and S waves; $\dot{\eta} = 0$ for n_{max}. For the lower bound n_{min}, more attenuated results are observed for $\dot{\mathbf{u}}_s, \mathbf{w}$ fields. The described behavior as n changes is noticed at the material interface $x = 10$m, as well as at $x = 8$m and $x = 12$m.



(a) Sandstone, p

(b) Sandstone-shale, p

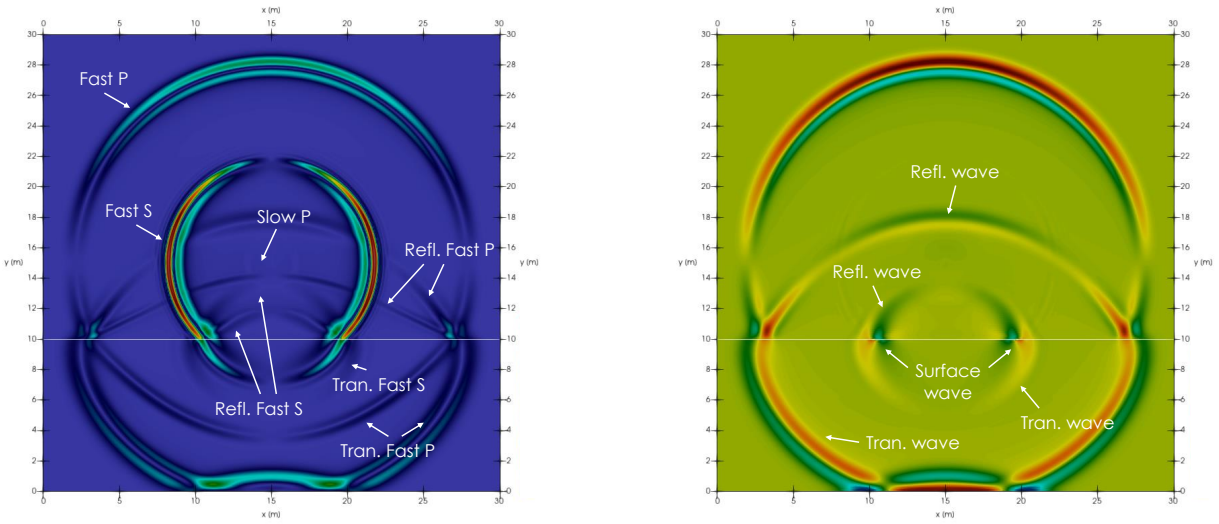
(c) Sandstone, $\dot{\eta}$

(d) Sandstone-shale, $\dot{\eta}$

Figure 6.10: Two-dimensional wave propagation of $p, \dot{\eta}$ fields in sandstone (a, c) and two-layer (b, d) domains at $t_{end} = 4 \times 10^{-3}$s. The horizontal white line corresponds to the material interface EF indicated in Figure 6.8.

6.5.3 Laboratory scale sample with high-frequency wave propagation

The developed $u_s - p - w$ model is employed to simulate wave propagation in a sandstone core sample. The material parameters for the sandstone are reported in Table 4.1 with a permeability of $\kappa = 10^{-11}\text{m}^2$, whilst the problem geometry is represented in Figure 6.13. The sample is considered fixed and impervious at the left and right boundaries, while flow is allowed at the top and bottom regions. A wave pulse of the form $S(t) = \sin(2\pi f) - 0.5\sin(4\pi f), t < 1/f$ is applied on the solid displacement field, on the left side of the domain. The given source frequency is taken as $f = 2 \times 10^5$ Hz which, combined



(a) Solid velocity

(b) Pressure

Figure 6.11: Wave types in solid velocity and pressure contour plots at $t_{end} = 4 \times 10^{-3}$s. Original, reflected (Refl.) and transmitted (Tran.) waves are identified. The horizontal white line indicates the shale-sandstone boundary for the layered model.

with the water-saturated sandstone configuration, indicates that the solution is on the high-frequency regime. In this case, the BT correction factor is $F > 1$, meaning that differences between BT and dCS models should be more prominent. Table 6.3 lists the wave velocity and wavelength for BT and dCS theories for the current problem. Although wave velocities in dCS and BT theories are different, the correspondent wavelengths are similar.

Table 6.3: Velocity and wavelength of P and S waves for water-saturated sandstone [193] considering $\kappa = 10^{-11}\text{m}^2$ and source frequency of 2×10^5Hz.

Parameter	Fast P	Slow P	Fast S	Slow S
dCS Wave velocity [m/s]	4479.76	1488.69	3220.95	0.64
dCS Wavelength [cm]	2.24	0.74	1.61	3.20×10^{-4}
BT Wave velocity [m/s]	4486.95	1611.37	3240.07	-
BT Wavelength [cm]	2.24	0.81	1.62	-

The domain is discretized into a mesh with 600×200 bi-linear elements. The simulation is

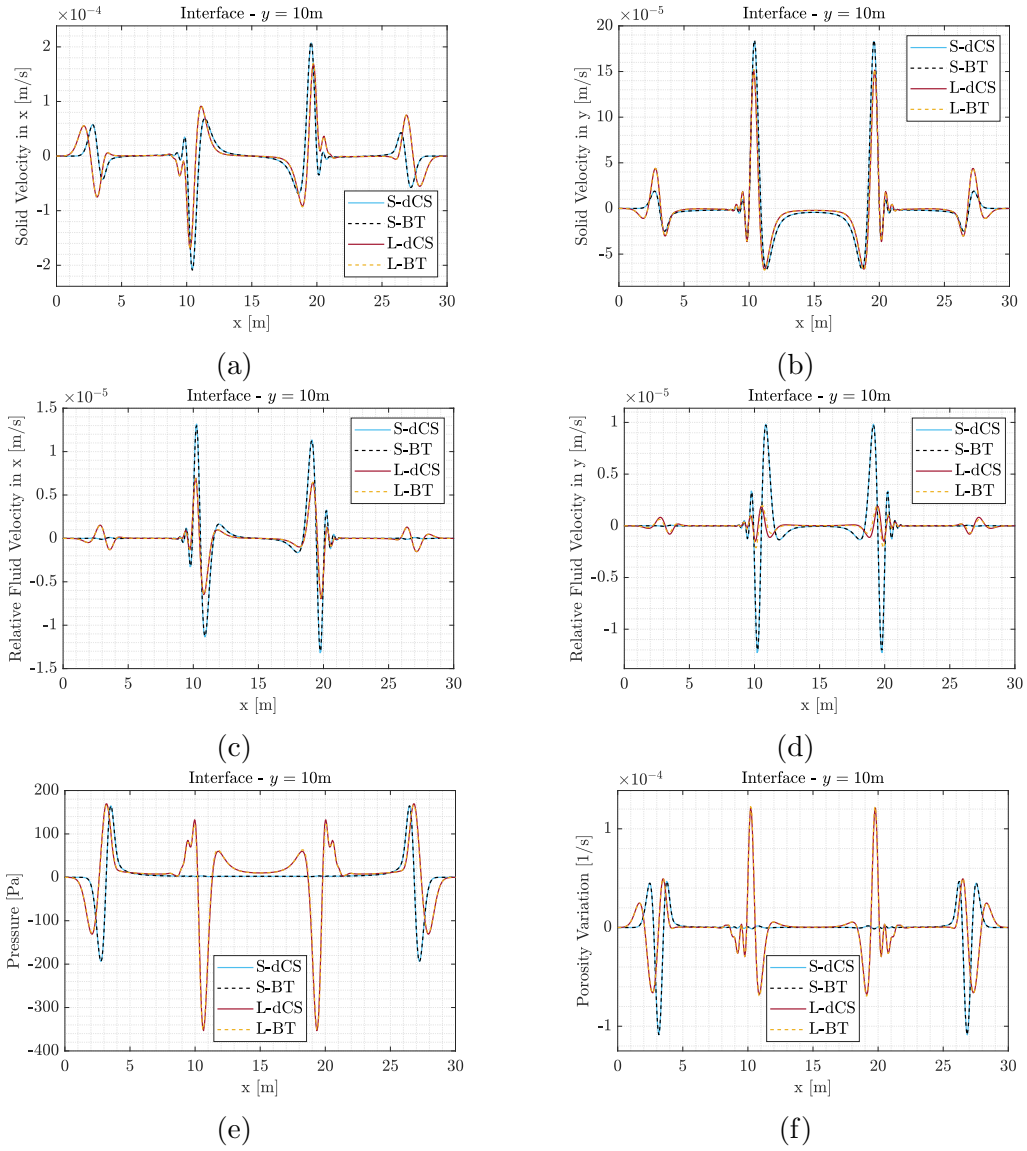


Figure 6.12: Two-dimensional wave propagation: (a,b) solid velocity, (c,d) relative fluid velocity, (e) fluid pressure, and (f) porosity variation at $x = 10$m, $t_{end} = 4 \times 10^{-3}$s for sandstone (S-) and shale-sandstone (L-) domains. Legends indicate plots for BT and dCS ($n = 1$) models.

carried out for $t_{end} = 2 \times 10^{-4}$s with a time step of $\Delta t = 5 \times 10^{-7}$s. Figure 6.14 depicts the behavior of solid displacement, relative fluid velocity, fluid pressure, and porosity variation

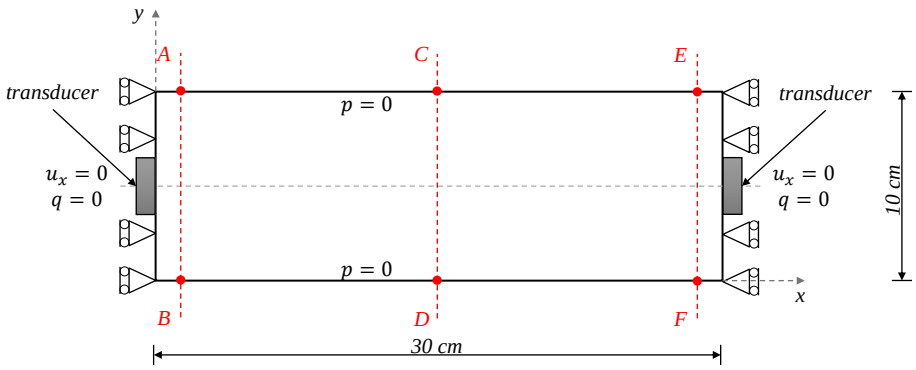


Figure 6.13: Geometry of sandstone core sample.

at an initial simulation time of $t = 2.5 \times 10^{-5}$s and at the final simulation time $t_{end} = 2 \times 10^{-4}$s. The applied pulse is visible at $t = 2.5 \times 10^{-5}$s; as the generated waves propagate, various boundary reflections take place. To understand the wave patterns along the sample, three cross sections are analyzed at different times: (i) $x = 2$cm (line AB), $t = 2.5 \times 10^{-5}$s, (ii) $x = 15$cm (line CD), $t = 1 \times 10^{-}4$, and (iii) $x = 20$cm (line EF), $t_{end} = 2 \times 10^{-4}$s.

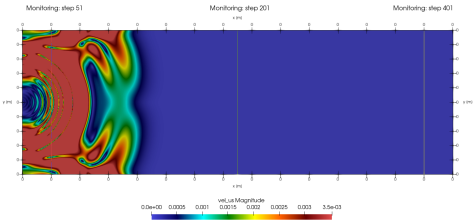
Figure 6.15 depicts the curves of solid velocity, relative fluid velocity, fluid pressure, and porosity variation at the aforementioned combinations (i), (ii), and (iii). Discrepancies between BT and dCS ($n = 1$) are less pronounced in the solid field, where they have the same behavior but BT curves are more attenuated. Similar behavior is also noticed for the fluid pressure and porosity variation fields. Results for the relative fluid velocity show that, at the end of the simulation, differences between BT and dCS ($n = 1$) at $x = 28$cm are more visible. Wave patterns for dCS n_{max} differ significantly from the other curves, likely due to more interactions between the transmitted/reflected waves.

It is noteworthy that the porosity variation $\dot{\eta}$ does not vanish at the upper bound n_{max}, where $\delta_s = \delta_f$. From the porosity perturbation equation (5.6), $\dot{\eta} = 0$ for $\delta_s = \delta_f$ only if the divergence of solid and fluid velocity are of the same order. This equation could also be rewritten in terms of solid velocity and relative fluid velocity as in

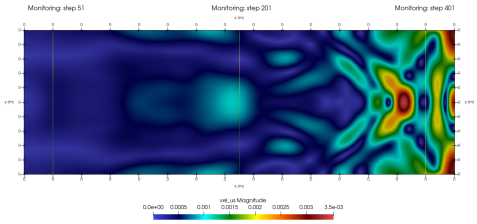
$$\dot{\eta} = (\delta_s - \delta_f)\nabla \cdot \dot{\mathbf{u}}_s - \frac{\delta_f}{\eta_0}\nabla \cdot \mathbf{w} \tag{6.43}$$

meaning that, if $\delta_s = \delta_f$, the divergence of relative fluid velocity should vanish for the porosity to remain unchanged. Although this holds true for the low-frequency example in Section 6.5.1, it does not happen on the laboratory-scale high-frequency example.

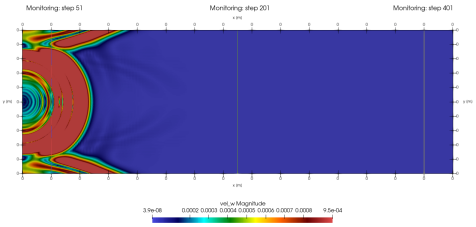
Synthetic plots of the fluid pressure field are shown in Figure 6.16 for BT and dCS models. The figures show the pressure behavior at $x = 28$cm from $t = 1 \times 10^{-4}$s to $t = 2 \times 10^{-4}$s,



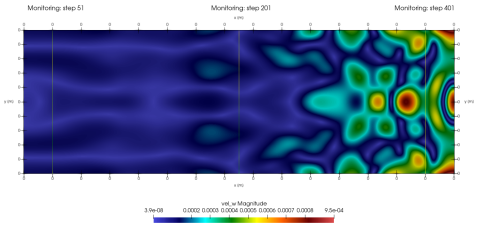
(a) $\dot{\mathbf{u}}_s$, $t = 2.5 \times 10^{-5}$s



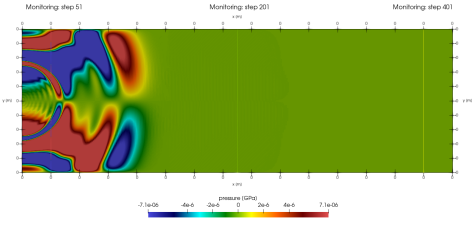
(b) $\dot{\mathbf{u}}_s$, $t_{end} = 2 \times 10^{-4}$s



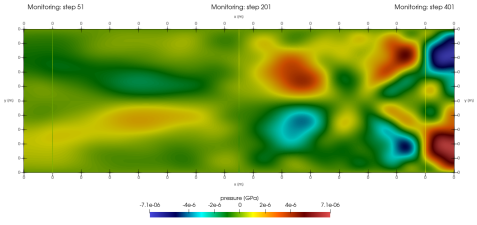
(c) $\mathbf{w}$, $t = 2.5 \times 10^{-5}$s



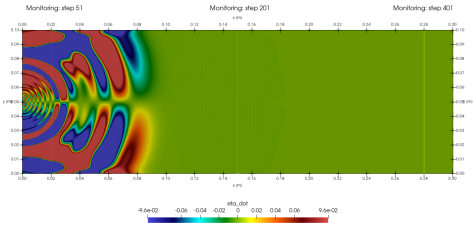
(d) $\mathbf{w}$, $t_{end} = 2 \times 10^{-4}$s



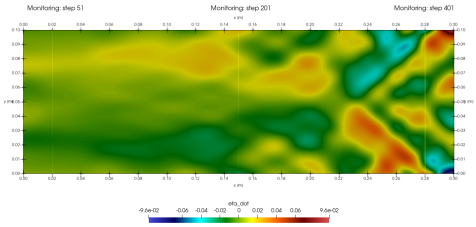
(e) p, $t = 2.5 \times 10^{-5}$s



(f) p, $t_{end} = 2 \times 10^{-4}$s



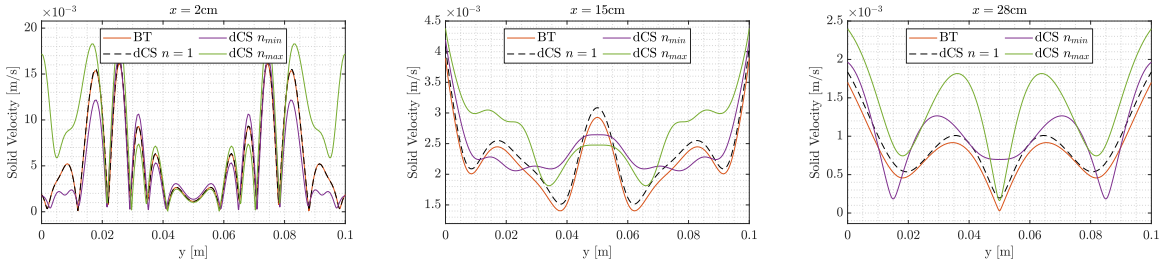
(g) $\dot{\eta}$, $t = 2.5 \times 10^{-5}$s



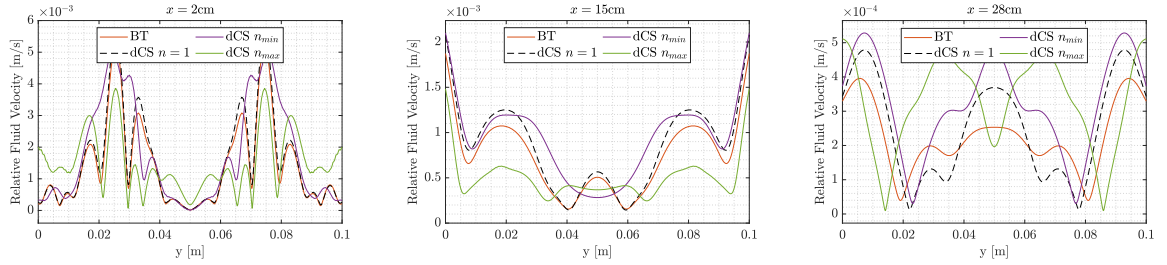
(h) $\dot{\eta}$, $t_{end} = 2 \times 10^{-4}$s

Figure 6.14: Core Sample example: (a, b) solid velocity, (c, d) relative fluid velocity, (e, f) fluid pressure, and (g, h) porosity variation at $t = 2.5 \times 10^{-5}$s (left) and $t_{end} = 2 \times 10^{-4}$s (right). The yellow vertical lines correspond to the cross sections AB, CD, and EF indicated in Figure 6.13.

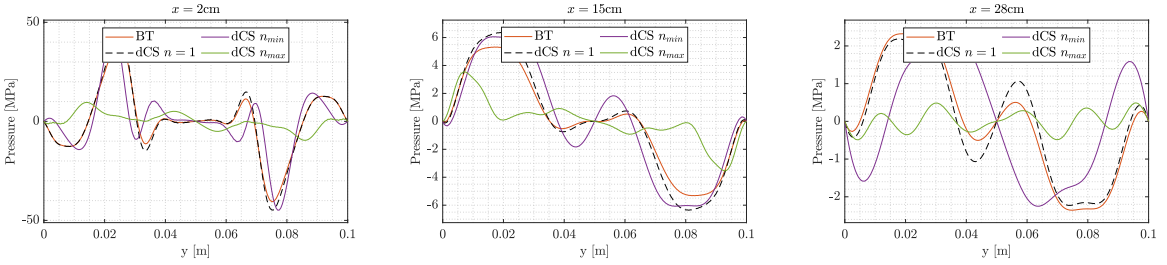
when the pulse propagation is noticed at the right side of the domain. BT and dCS ($n = 1$) patterns are quite similar, as was also observed in Figure 6.15. Wave propagation happens



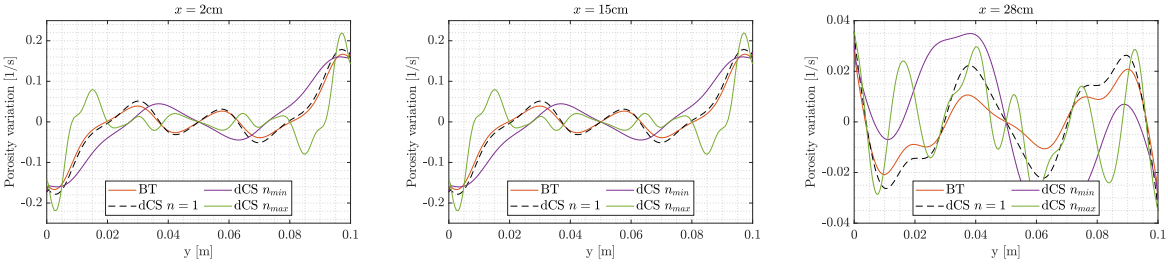
(a) $\dot{\mathbf{u}}_s$



(b) $\mathbf{w}$



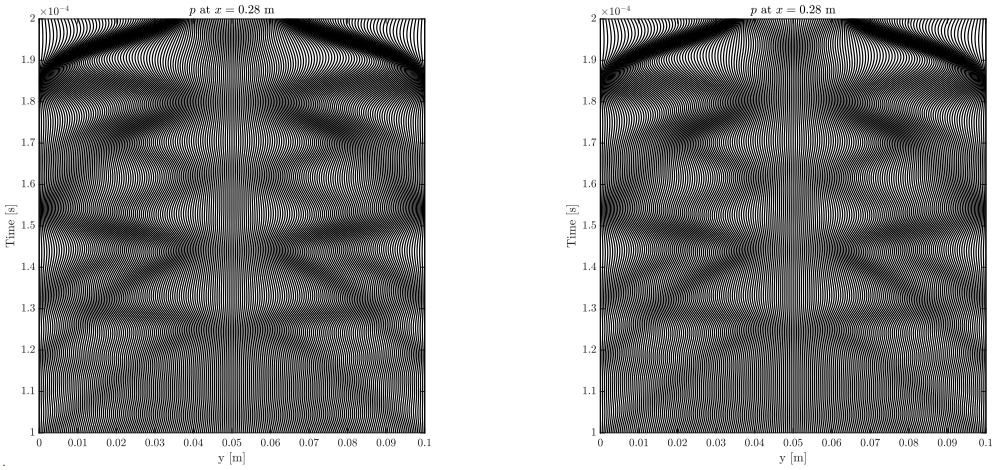
(c) p



(d) $\dot{\eta}$

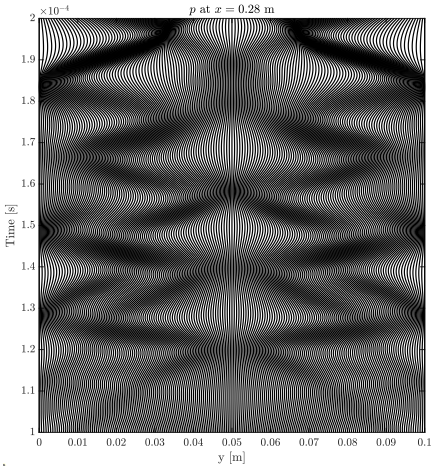
Figure 6.15: Wave propagation in sandstone core sample: BT and dCS plots for (a) solid velocity, (b) relative fluid velocity, (c) fluid pressure, and (d) porosity at the cross sections AB (left column), CD (middle column), and EF (right column).

with shorter wavelength for dCS n_{min}, and larger wavelength for dCS n_{max}.

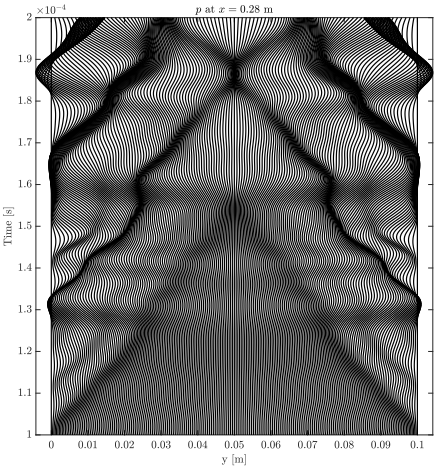


(a) Pressure, BT

(b) Pressure, dCS $n = 1$



(c) Pressure, dCS n_{min}



(d) Pressure, dCS n_{max}

Figure 6.16: Synthetic plots of pressure field at section EF (x = 28cm) BT and dCS models.

6.6 Discussion

A three-field dCS porous media model was proposed in terms of solid displacement, fluid pressure, and relative fluid velocity. The three-field formulation does not require that solid

and fluid accelerations are the same, hence providing accurate results when the relative solid-fluid motion is significant. Furthermore, considering that typical porous media problems deal with either pressure or flow boundary conditions for the fluid constituent, the definition of such boundary conditions becomes more straightforward.

In terms of stability requirements, $u_s - p - u_f$ BT models have been used without causing numerical locking, while $u_s - p - w$ BT models have employed mixed order Raviart-Thomas elements. Since the derivation of stability requirements for dCS finite element models is yet to be presented, we studied results using both linear and mixed-order elements, and assumed that requirements for BT theory should also hold for the dCS models. For the numerical examples herein presented, low-order linear elements for all u_s, p, w fields were enough to yield stable results.

The governing equations incorporate Darcy's law, hence restricting the model to the simulation of viscous-dominated flows with low fluid velocity. The assumption of small variations is related to the fluid velocity and, therefore, the model can still represent large fluid displacements. More to that, the choice of three-field $u_s - p - w$ variables allows an easy transition from Darcy's law to relations representing inertia-dominated flows, such as Forchheimer's equation.

The verification study showed that dCS theory still yields same results as BT theory when $n = 1$, since fluid viscous dissipation terms in dCS theory do not change solid/fluid load bearing capacity. These terms are important, nonetheless, in the representation of shear fluid motion and transmission/reflection waves at high frequencies. In this scenario, BT theory fails to represent interface non-slip boundary condition. The convergence study considered a one-dimensional manufactured solution, and showed optimal mesh-refinement convergence (for low-order elements) and time-step convergence. Employing mixed-order Taylor-Hood elements did not improve the convergence rates for fields with quadratic approximation.

The two-dimensional three-layer domain example showed how variations in the n parameter lead to significant changes in wave attenuation, but wave velocity seems to be less affected. For the two-layer domain, wave patterns at the interface also presented differences in attenuation. The propagation in a sandstone-shale domain showed that waves have higher speed and attenuation in shale, and that changing from sandstone to shale material generates transmitted and reflected waves, as well as surface waves traveling at the material interface. Surface waves are better visualized in the pressure field, although they can also be noticed on the solid velocity and relative fluid velocity plots.

The simulation of wave propagation in a laboratory-scale sandstone core sample showed that, at high enough frequencies, BT and dCS ($n = 1$) yields different results. This happens

due to the BT high-frequency correction factor, which is not applied to the dCS model since fluid motion is already properly represented by the complete fluid stress tensor. At such high-frequencies, nonetheless, the assumption of Poiseuille flow might break, and numerical results should be carefully analyzed. The presented simulation also clarified that the upper bound n_{max} of the porosity effective pressure coefficient leads to an unchanged porosity only at the low-frequency regime. Complex interactions of reflected waves – either at the layer interfaces or at the domain boundaries – could be observed in a two-dimensional F-K (frequency-wavenumber) plot obtained by Fast Fourier Transform, which is a topic for future studies.

6.7 Conclusions

In this chapter a three-field $u_s - p - w$ dCS formulation for porous media simulation was presented. The set of governing equations led to a FE discretization in terms of solid displacement, fluid pressure, and relative fluid velocity. A verification study showed how dCS results yield similar results from BT when the only difference between the theories is the dCS complete fluid stress tensor. Convergence rates were shown to be optimal for low-order linear elements, and rates associated with the quadratic approximation in mixed-order elements are deteriorated due to solid-fluid coupling effects. The two-dimensional layered domain examples showed how variations in the porosity effective pressure coefficient lead to changes in wave attenuation, while wave velocity seems to be less affected. The transition from sandstone to shale layers lead to reflected, transmitted, and surface waves. Both fast and slow waves were identified. The slow wave, although less prominent and more attenuated, interfered in reflected waves patterns.

High-frequency wave propagation in a sandstone core sample showed that discrepancies between BT and dCS models are more pronounced than in the low-frequency case. This happens due to the presence of the high-frequency BT correction factor, which is not part of the dCS model since fluid motion at all frequencies is properly represented by the complete fluid stress tensor. The core sample simulation also showed how the upper bound of n does not necessarily lead to unchanged porosity; this feature holds only for cases where relative fluid deformations are negligible. The presented formulation has the advantage of including w as a main variable, facilitating the implementation of fluid boundary conditions (usually given in terms of velocity instead of displacement) and the extension to non-Darcy flows.

Chapter 7

Conclusions

7.1 Concluding Remarks

The existent research gap in deriving and implementing numerical models for the dCS theory has been addressed in this thesis. Finite element dCS models were derived for transient and dynamic cases, one- and two-dimensional problems, and considering both time and frequency domain solutions.

Due to its similarity with BT theory in some aspects, one of the goals of this research was to compare dCS and BT results and understand under which circumstances, if any, these theories would lead to distinct outcomes. A detailed investigation of the governing equations showed that, under certain simplifications, the dCS theory can reproduce BT results – and hence dCS model can be said to be a generalized version of BT model.

Some interesting results were related to the dCS numerical models. The convergence study, for instance, showed how convergence rates are dependent on the solid-fluid coupling terms. When coupling matrices have a significant contribution to the overall system, convergence of mixed-order elements is limited by the lowest polynomial approximation order. The same behavior was noticed to be valid for BT theory.

One of the reasons of the discrepancy between the dCS and BT theories is the presence of fluid viscous dissipation terms on the fluid stress definition of the former. The dimensionless analysis performed based on the dCS dynamic model confirmed that fluid viscous dissipation terms do not yield differences on the solid-fluid general behavior per se, but are important in the representation of an additional rotational wave. This complete stress tensor in the dCS theory should be enough to represent fluid behavior at high frequencies,

while BT theory needs to account for a high-frequency viscosity correction factor. These approaches, however, were shown to lead to different wave patterns. A questioning is then raised about the ability of BT theory to fully represent fluid behavior at high frequencies, even accounting for its correction factor.

Another difference between BT and dCS models is that dCS theory, due to the introduction of a porosity perturbation equation and compliance coefficients, allows the representation of non-reciprocal solid-fluid interactions. Contrary to reciprocal interactions (intrinsic to BT theory), non-reciprocal effects originate from the adoption of an additive form of the deformation energy potential. One additional elastic constant is introduced to the system, indicating that the deformation energy might be unevenly concentrated in the solid and fluid constituents. These interactions happen when the constituents affect porosity changes to different extents, and can be responsible for significant changes in the solid and fluid behavior – at low and high frequencies.

The porosity effective pressure coefficient n is responsible for representing said solid-fluid interactions. The interval $n_{min} \leq n < 1$ indicates micro-heterogeneity of solid grains, and deformation energy tends to concentrate in solid bulk or interface regions due to irregular grain shapes or grain surface roughness. At the interval $1 < n \leq n_{max}$, energy is concentrated in the fluid constituent, indicating cases where fluid has yet to find its equilibrium position within the coupled medium. Hence, values of n within such range should change once the system regains its equilibrium state. Regardless of the configuration, it should be noted that the reference to non-reciprocal interactions does not allude to a violation of Newton's law of equilibrium.

The presented FE dCS models were written in terms of different main variables according to the type of problem simulated. While $u_s - p$ and $u_s - p - \eta$ formulations are suitable for quasi-steady problems, they are derived assuming that solid and fluid accelerations are the same. Hence, for accurate dynamic simulations, the introduction of the fluid displacement (or fluid velocity) variable is required. The dCS $u_s - p - u_f$ formulation was used for the simulation of wave propagation and injection wells. The $u_s - p - w$ formulation was employed in the simulation of consolidation problem and layered domains.

Numerical stability requirements, previously derived for BT theory, were assumed to be valid for the dCS models. Mixed-order Taylor-Hood elements were employed for $u_s - p$ and $u_s - p - \eta$ models, while low-order all-linear elements were tested for $u_s - p - u_f$ and $u_s - p - w$ models. The pressure injection well showed instabilities that were solved with mixed-order elements; for the remaining examples, low-order elements were enough to generate stable results. It is noteworthy that the derivation of stability requirements specifically for dCS theory is still a gap to be studied.

The dCS theory is a reasonable choice for porous media representation due to its physical foundation and explicit connection between micro and macro pore scales. The FE frameworks derived and verified in this thesis comprise a robust foundation for dCS numerical simulations. Besides, they are an important step in comprehending the dCS theory and its capabilities.

7.2 Research Contributions

The work reported in this thesis comprised novel FE models for the dCS theory, which are capable of simulating quasi-steady and dynamic behavior. A study on wave propagation in porous media showed velocity and attenuation patterns for different material parameters and frequency ranges. The formulations were presented in terms of different combinations of main variables, and for each system of equations (i) verification analysis, (ii) convergence study, and (iii) use of same- and mixed-order elements were explored. The main contributions of this research were disseminated in journal papers and conferences, summarized as follows.

First objective: comprised the derivation and implementation of a numerical model for the dCS theory in the quasi-steady case. This research is disseminated in:

B. Campos and R. Gracie, "A FEM for three-field u–p–η poroelasticity with non-reciprocal interactions", *International Journal for Numerical and Analytical Methods in Geomechanics*, vol. 48 (1), p. 332–355, 2024.

The key contributions of this work are:

- A finite element dCS model to simulate quasi-steady porous media behavior was derived. The system of equations to be solved was written in terms of solid displacement, fluid pressure, and porosity.
- A thorough comparison between BT and dCS formulations showed how, under some simplifications, dCS formulation can be reduced to Biot's theory.
- The FE dCS model showed that, by accounting for non-reciprocal solid-fluid interactions, changes in the deformation pattern of the constituents are noticed.
- Convergence studies showed that the use of a polynomial approximation one order higher for the solid field does not necessarily increase the convergence rate in one order. Such rate is restricted by the solid-fluid coupling and deteriorates more as

the coupling is stronger, i.e., the coupling matrices are of similar order compared to uncoupled terms.

Second objective: aimed to expand the developed dCS FE model to the simulation of dynamic behavior and study of wave propagation. This research is disseminated in:

B. Campos and R. Gracie, "A dynamic three-field finite element model for wave propagation in linear elastic porous media". Submitted to *International Journal for Numerical and Analytical Methods in Geomechanics*, May 2024.

The key contributions of this work are:

- The previously quasi-steady FE model was extended to account for inertial (acceleration) terms. The system to be solved was written in terms of solid displacement, fluid pressure, and fluid displacement. Porosity changes can still be monitored through the porosity perturbation equation.
- A dimensionless analysis confirmed that the dCS addition to the damping matrices is not relevant to the solid-fluid behavior. Such addition however, comprised by the complete fluid stress tensor, is essential in the representation of a slow S wave.
- The three-field model involving fluid displacement as a variable does not require mixed-order elements to satisfy the LBB condition. Nonetheless, two-dimensional examples showed that the use of mixed-order approximation might be needed depending on the type of boundary value problem.
- One- and two-dimensional wave propagation examples showed how solid-fluid non-reciprocal interactions affect wave velocity and attenuation. Pattern variations are shown to be dependent on the adopted parameters for the porous media constituents.

Third objective: focused on the study of wave velocity and attenuation patterns in the dCS theory. This research is disseminated in:

B. Campos and R. Gracie, "Wave velocity and attenuation in generalized Biot porous media model". Submitted for publication, September 2024.

The key contributions of this work are:

- A detailed study of wave patterns based on the dCS equations is provided. Solid-fluid non-reciprocal interactions, macroscopic solid modulus, and variations in other material parameters lead to distinct changes in wave behavior depending on the source frequency.

- Changes in wave velocity and attenuation behavior are shown to be expected above the critical frequency limit, which varies significantly depending on the solid-fluid combination.
- The wave equations written in terms of porosity and pressure variables allowed the study of temporary increase in porosity, which leads to fluid flow enhancement. At high frequency, velocity and attenuation patterns change significantly depending on the porosity effective pressure coefficient.

Fourth objective: comprised the development of a three-field dCS FE model in terms of relative fluid velocity and its application to the simulation of layered domains and high-frequency examples. This research is disseminated in:

B. Campos and R. Gracie, "Fluid velocity finite element formulation for layered porous media domain". Manuscript under preparation, September 2024.

The key contributions of this work are:

- The dCS governing equations are written in terms of solid displacement, fluid pressure, and relative fluid velocity. Verification and convergence studies are performed to ensure the robustness of the FE model.
- The application of the dCS model to sandstone-shale layered domains highlighted the wave propagation patterns, and the transmission and reflection effects happening at the material interface. Comparison with BT model led to similar results, given that simulations are below or close to the BT critical frequency limit.
- Wave transmission and reflection at the interface enhances the slow wave behavior in the pressure field, which was not noticed in infinite domains. The layered configuration also highlighted the propagation of surface waves at the shale-sandstone material interface.
- The simulation of high-frequency wave propagation in a sandstone sample showed more visible discrepancies between BT and dCS theories due to dCS fluid viscous dissipation terms. The high-frequency correction factor introduced in BT theory seems insufficient to capture fluid motion at such frequency range.

7.3 Directions for Future Study

There is still plenty to be investigated in the context of the dCS theory, which can be done based on the finite element models herein presented. Some of these possibilities include:

Wave propagation: the studies on wave patterns herein performed considered, on the plane wave assumption, that solid and fluid have the same wavenumber. The numerical examples of wave propagation, however, showed how this assumption does not necessarily hold. Hence, a possible path of study is the development of dCS wave equations in terms of different solid and fluid wavenumbers, adding some complexity to the derivation of wavenumber–frequency relations. It would be interesting to evaluate whether this change impacts the current results and to what extent.

Fracture models: the simulation of fluid flow through fractures can rely on a range of assumptions/simplifications, such as impervious rock along the fracture. Neglecting leakage of fluid into the adjacent rock could lead to incorrect predictions in flow velocity and pressure, especially if the medium is composed by highly-permeable formations. More to that, common fracture models are based on Poiseuille flow and consequent neglect inertia terms. It has been shown, however, that inertial effects have a significant role in the propagation of hydraulic fractures. In this sense, the GG22 fracture flow model was recently presented as an alternative, less restrictive option over the Poiseuille flow [69, 70, 71, 72]. The coupling of the GG22 model with a porous representation of the rock formations is, hence, an important extension of this work.

Nonlinear solid behavior: the porous media constitutive equations adopted in this thesis are based on a linear elastic behavior of the solid matrix. However, the extension to nonlinear models has been done over the years in the context of BT theory. Visco-elastic, plastic, visco-plastic, hyper-elastic models, for instance, are useful when simulating rubber materials, soil liquefaction, fibrous media, brain tissues, amongst others. To that end, the Arbitrary Lagrangian Eulerian (ALE) formulation has to be considered so that a reference frame is introduced to the porous media simulation, and large Lagrangian mesh distortions are overcome. A valuable continuation to this work, therefore, is the development of dCS models accounting for nonlinear solid matrix behavior.

Non-Darcy flow: a significant part of the dCS (and BT) theory applications is in the realm of Darcy flows, where viscous effects are dominant over inertial effects. This leads to linear theories, which are advantageous since (i) numerical implementation is more straightforward and (ii) stability and convergence are more easily achieved in comparison to the nonlinear case. The simulation of inertia-dominant effects, nevertheless, requires a more complex flow representation that includes nonlinear terms to correctly reproduce high-velocity flow. The dCS FE model written in terms of solid displacement, fluid pressure, and (relative) fluid velocity is a suitable framework for future implementation of non-Darcy flows.

References

[1] A. R. 40. Recommended Practices for Core Analysis Procedures, 1998.

[2] R. Al-Raoush and A. Papadopoulos. Representative elementary volume analysis of porous media using X-ray computed tomography. *Powder technology*, 200(1-2):69–77, 2010.

[3] T. E. G. Álvarez-Arenas, M. D. Fariñas, and A. Ginel. Fast and non-destructive ultrasonic test for face masks. *Ultrasonics*, 117:106556, 2021.

[4] G. Amadasi, A. Cerniglia, and B. Duperray. Experimental determination of poro-elastic properties of materials commonly used for noise and vibration control. In *15th International Congress on Sound and Vibration*, pages 1–8, 2008.

[5] E. Anthony and N. Vedanti. Simulation of seismic wave propagation in poroelastic media using vectorized Biot's equations: An application to a CO 2 sequestration monitoring case. *Acta Geophysica*, 68(2):435–444, 2020.

[6] G. Athanasopoulos, P. Pelekis, and G. Anagnostopoulos. Effect of soil stiffness in the attenuation of Rayleigh-wave motions from field measurements. *Soil Dynamics and Earthquake Engineering*, 19(4):277–288, 2000.

[7] J. Ba, J. Carcione, and J. Nie. Biot-Rayleigh theory of wave propagation in double-porosity media. *Journal of Geophysical Research: Solid Earth*, 116(B6), 2011.

[8] J. Ba, J. Zhao, J. M. Carcione, and X. Huang. Compressional wave dispersion due to rock matrix stiffening by clay squirt flow. *Geophysical Research Letters*, 43(12):6186–6195, 2016.

[9] Y. Bachmat and J. Bear. On the concept and size of a representative elementary volume (REV). In *Advances in transport phenomena in porous media*, pages 3–20. Springer, 1987.

[10] S. Badsar, M. Schevenels, W. Haegeman, and G. Degrande. Determination of the material damping ratio in the soil from SASW tests using the half-power bandwidth method. *Geophysical Journal International*, 182(3):1493–1508, 2010.

[11] K. Bathe. *Finite Element Procedures*. Prentice-Hall, 1996.

[12] J. Bear. *Dynamics of fluids in porous media*. American Elsevier, 1972.

[13] D. Benmorsli, Z. E. A. Fellah, D. Belgroune, N. O. Ongwen, E. Ogam, C. Depollier, and M. Fellah. Transient Propagation of Longitudinal and Transverse Waves in Cancellous Bone: Application of Biot Theory and Fractional Calculus. *Symmetry*, 14(10):1971, 2022.

[14] M. A. Biot. General Theory of Three Dimensional Consolidation. *Journal of Applied Physics*, 155(12):155–164, 1941.

[15] M. A. Biot. Theory of Propagation of Elastic Waves in a Fluid-Saturated Porous Solid - I. Low-Frequency Range. *The Journal of the Acoustical Society of America*, 28(168):168–178, 1956.

[16] M. A. Biot. Theory of Propagation of Elastic Waves in a Fluid-Saturated Porous Solid - II. Higher-Frequency Range. *The Journal of the Acoustical Society of America*, 28(168):179–191, 1956.

[17] M. A. Biot and D. G. Willis. The Elastic Coefficients of the Theory of Consolidation. *Journal of Applied Mechanics*, 24(4):594–601, 1957.

[18] M. A. Biot. Theory of elasticity and consolidation for a porous anisotropic solid. *Journal of Applied Physics*, 26(2):182–185, 1955.

[19] M. A. Biot. Theory of deformation of a porous viscoelastic anisotropic solid. *Journal of Applied Physics*, 27(5):459–467, 1956.

[20] M. A. Biot. Generalized theory of acoustic propagation in porous dissipative media. *The Journal of the Acoustical Society of America*, 34(9A):1254–1264, 1962.

[21] D. Boffi, F. Brezzi, and M. Fortin. *Mixed Finite Element Methods and Applications*. Springer-Verlag, 2013.

[22] T. J. Boone and A. R. Ingraffea. A numerical procedure for simulation of hydraulically-driven fracture propagation in poroelastic media. *Numerical and Analytical Methods in Geomechanics*, 14(1):27–47, 1990.

[23] F. Brezzi. On the existence, uniqueness and approximation of saddle-point problems arising from Lagrangian multipliers. *Publications des séminaires de mathématiques et informatique de Rennes*, 8(R2):129–151, 1974.

[24] R. J. Brown and J. Korringa. On the dependence of the elastic properties of a porous rock on the compressibility of the pore fluid. *Geophysics*, 40(4):608–616, 1975.

[25] B. Campos and R. Gracie. A FEM for three-field u–p–η poroelasticity with nonreciprocal interactions. *International Journal for Numerical and Analytical Methods in Geomechanics*, 48(1):332–355, 2023.

[26] J. M. Carcione. *Wave fields in real media: Wave propagation in anisotropic, anelastic, porous and electromagnetic media*. Elsevier, 2007.

[27] J. M. Carcione, F. Cavallini, J. E. Santos, C. L. Ravazzoli, and P. M. Gauzellino. Wave propagation in partially saturated porous media: simulation of a second slow wave. *Wave Motion*, 39(3):227–240, 2004.

[28] J. M. Carcione and B. Gurevich. Differential form and numerical implementation of Biot's poroelasticity equations with squirt dissipation. *Geophysics*, 76(6):N55–N64, 2011.

[29] N. Castelletto, S. Klevtsov, H. Hajibeygi, and H. A. Tchelepi. Multiscale two-stage solver for Biot's poroelasticity equations in subsurface media. *Computational Geosciences*, 23:207–224, 2019.

[30] A. Cesmelioglu and P. Chidyagwai. Numerical analysis of the coupling of free fluid with a poroelastic material. *Numerical Methods for Partial Differential Equations*, 36(3):463–494, 2020.

[31] L. Chen, F. Fathi, and R. de Borst. Hydraulic fracturing analysis in fluid-saturated porous medium. *International Journal for Numerical and Analytical Methods in Geomechanics*, 46(17):3200–3216, 2022.

[32] Z. Chen, H. Steeb, and S. Diebels. A time-discontinuous Galerkin method for the dynamical analysis of porous media. *International Journal for Numerical and Analytical Methods in Geomechanics*, 30(11):1113–1134, 2006.

[33] M. S. Costanza-Robinson, B. D. Estabrook, and D. F. Fouhey. Representative elementary volume estimation for porosity, moisture saturation, and air-water interfacial areas in unsaturated porous media: Data quality implications. *Water Resources Research*, 47(7), 2011.

[34] O. Coussy. *Poromechanics*. John Wiley & Sons, 2004.

[35] O. Coussy. *Mechanics and physics of porous solids*. John Wiley & Sons, 2011.

[36] O. Coussy, L. Dormieux, and E. Detournay. From mixture theory to Biot's approach for porous media. *International Journal of Solids and Structures*, 35(34-35):4619–4635, 1998.

[37] N. Dai, A. Vafidis, and E. Kanasewich. Wave propagation in heterogeneous, porous media: A velocity-stress, finite-difference method. *Geophysics*, 60(2):327–340, 1995.

[38] S. Dana and M. F. Wheeler. Convergence analysis of fixed stress split iterative scheme for anisotropic poroelasticity with tensor Biot parameter. *Computational Geosciences*, 22:1219–1230, 2018.

[39] B. C. Davidson, M. B. Dusseault, and J. Wang. Laboratory experiments on pressure pulse flow enhancement in porous media. In *Technical Meeting/Petroleum Conference of The South Saskatchewan Section, Regina*, pages 1–8, 1999.

[40] B. C. Davidson, M. B. Dusseault, and J. Wang. Pore-scale heterogeneity assessed by the Lattice-Boltzmann Method. In *Technical Meeting/Petroleum Conference of The South Saskatchewan Section, Regina*, pages 1–8, 1999.

[41] R. de Boer. *Theory of Porous Media: Highlights in Historical Development and Current State*. Springer-Verlag, 2000.

[42] R. De Boer and W. Ehlers. A historical review of the formulation of porous media theories. *Acta Mechanica*, 74(1):1–8, 1988.

[43] R. De Boer, W. Ehlers, and Z. Liu. One-dimensional transient wave propagation in fluid-saturated incompressible porous media. *Archive of applied mechanics*, 63(1):59–72, 1993.

[44] V. De La Cruz and T. J. T. Spanos. Seismic Wave Propagation in a Porous Medium. *Geophysics*, 50(10):1525–1648, 1985.

[45] V. De La Cruz and T. J. T. Spanos. Thermomechanical coupling during seismic wave propagation in a porous medium. *Journal of Geophysical Research: Solid Earth*, 94(B1):637–642, 1989.

[46] V. De La Cruz, P. Sahay, and T. Spanos. Thermodynamics of porous media. *Proceedings of the Royal Society of London. Series A: Mathematical and Physical Sciences*, 443(1917):247–255, 1993.

[47] E. Detournay and A. H.-D. Cheng. Fundamentals of poroelasticity. In *Analysis and design methods*, pages 113–171. Elsevier, 1993.

[48] M. S. Diallo and E. Appel. Acoustic wave propagation in saturated porous media: reformulation of the Biot/Squirt flow theory. *Journal of Applied Geophysics*, 44(4):313–325, 2000.

[49] M. Diallo, M. Prasad, and E. Appel. Comparison between experimental results and theoretical predictions for P-wave velocity and attenuation at ultrasonic frequency. *Wave motion*, 37(1):1–16, 2003.

[50] S. Diebels and W. Ehlers. Dynamic analysis of a fully saturated porous medium accounting for geometrical and material non-linearities. *International Journal for Numerical Methods in Engineering*, 39(1):81–97, 1996.

[51] M. Dusseault, J. Spanos, and B. Davidson. A dynamic pulsing workover technique for wells. In *Technical Meeting/Petroleum Conference of The South Saskatchewan Section, Regina*, pages 18–21, 2000.

[52] J. Dvorkin, G. Mavko, and A. Nur. Squirt flow in fully saturated rocks. *Geophysics*, 60(1):97–107, 1995.

[53] J. Dvorkin, R. Nolen-Hoeksema, and A. Nur. The squirt-flow mechanism: Macroscopic description. *Geophysics*, 59(3):428–438, 1994.

[54] J. Dvorkin and A. Nur. Dynamic poroelasticity: A unified model with the squirt and the Biot mechanisms. *Geophysics*, 58(4):524–533, 1993.

[55] I. Edelman. Bifurcation of the Biot slow wave in a porous medium. *The Journal of the Acoustical Society of America*, 114(1):90–97, 2003.

[56] H. Egger and M. Sabouri. On the structure preserving high-order approximation of quasistatic poroelasticity. *Mathematics and Computers in Simulation*, 189:237–252, 2021.

[57] M. Fellah, Z. Fellah, A. Berbiche, E. Ogam, F. Mitri, and C. Depollier. Transient ultrasonic wave propagation in porous material of non-integer space dimension. *Wave Motion*, 72:276–286, 2017.

[58] Z. E. A. Fellah, J. Y. Chapelon, S. Berger, W. Lauriks, and C. Depollier. Ultrasonic wave propagation in human cancellous bone: Application of Biot theory. *The Journal of the acoustical Society of america*, 116(1):61–73, 2004.

[59] Z. E. A. Fellah, M. Fellah, E. Ogam, A. Berbiche, and C. Depollier. Reflection and transmission of transient ultrasonic wave in fractal porous material: Application of fractional calculus. *Wave Motion*, 106:102804, 2021.

[60] M. Ferronato, N. Castelletto, and G. Gambolati. A fully coupled 3-D mixed finite element model of Biot consolidation. *Journal of Computational Physics*, 229(12):4813–4830, 2010.

[61] P. Fillunger. Der auftrieb in talsperren. *Osterr. Wochenschrift fur den offentl. Baudienst*, 19:532–556, 567–570, 1913.

[62] J. Fish and T. Belytschko. *A First Course in Finite Elements*. John Wiley & Sons, Ltd, 2007.

[63] A. Gajo and L. Mongiovi. An analytical solution for the transient response of saturated linear elastic porous media. *International Journal for Numerical and Analytical Methods in Geomechanics*, 19(6):399–413, 1995.

[64] A. Gajo, A. Saetta, and R. Vitaliani. Evaluation of three- and two-field Finite Element Methods for the dynamic response of saturated soil. *International Journal for Numerical Methods in Engineering*, 37(7):1231–1247, 1994.

[65] J. Gao, W. Han, Y. He, H. Zhao, H. Li, Y. Zhang, and Z. Xu. Seismic wave equations in tight oil/gas sandstone media. *Science China Earth Sciences*, 64:377–387, 2021.

[66] F. Gaspar, F. Lisbona, and P. Vabishchevich. Staggered grid discretizations for the quasi-static Biot's consolidation problem. *Applied numerical mathematics*, 56(6):888–898, 2006.

[67] F. Gassman. Elastic wave through a packing of spheres. *Geophysics*, 16(4):577–720, 1957.

[68] C. Gavagnin, L. Sanavia, and L. De Lorenzis. Stabilized mixed formulation for phase-field computation of deviatoric fracture in elastic and poroelastic materials. *Computational Mechanics*, 65:1447–1465, 2020.

[69] B. Gee and R. Gracie. Beyond Poiseuille flow: A transient energy-conserving model for flow through fractures of varying aperture. *Advances in Water Resources*, 164:104192, 2022.

[70] B. Gee and R. Gracie. Beyond the cubic law: A finite volume method for convective and transient fracture flow. *International journal for numerical methods in fluids*, 94(11):1841–1862, 2022.

[71] B. Gee and R. Gracie. Inertial and turbulent flow in hydro-mechanically coupled KGD-like fractures. *International Journal for Numerical and Analytical Methods in Geomechanics*, 47(16):2925–2950, 2023.

[72] B. Gee and R. Gracie. The influence of turbulence and inertia in radial fracture flow. *Journal of Fluid Mechanics*, 981:A1, 2024.

[73] J. Geertsma. The effect of fluid pressure decline on volumetric changes of porous rocks. *Transactions of the AIME*, 210(01):331–340, 1957.

[74] M. Geilikman, T. Spanos, and E. Nyland. Porosity diffusion in fluid-saturated media. *Tectonophysics*, 217(1-2):111–115, 1993.

[75] J. González, P. Sahay, and T. Müller. Acoustic signature of impermeable barriers in porous media. *Geophysical Journal International*, 234(3):2095–2113, 2023.

[76] J. G. González, P. N. Sahay, and T. M. Müller. S-wave propagation across material discontinuities in poroelasticity. *Geophysics*, 86(6):MR315–MR324, 2021.

[77] J. G. González, P. N. Sahay, and T. M. Müller. Shear wave transmissivity and wave-induced vorticity diffusion through conversion scattering to slow-shear diffusion wave. *Proceedings of the Royal Society A*, 479(2273):20230056, 2023.

[78] D. H. Green and H. F. Wang. Fluid pressure response to undrained compression in saturated sedimentary rock. *Geophysics*, 51(4):948–956, 1986.

[79] S. Ham and K. J. Bathe. A Finite Element Method enriched for wave propagation problems. *Computers & structures*, 94:1–12, 2012.

[80] J. He, Z. Rui, and K. Ling. A new method to determine Biot's coefficients of Bakken samples. *Journal of Natural Gas Science and Engineering*, 35:259–264, 2016.

[81] G. Heinrich and K. Desoyer. Hydromechanische Grundlagen für die Behandlung von stationären und instationären Grundwasserströmungen. *Ingenieur-Archiv*, 23(2):73–84, 1955.

[82] G. Heinrich and K. Desoyer. Hydromechanische Grundlagen für die Behandlung von stationären und instationären Grundwasserströmungen. *Ingenieur-Archiv*, 24(2):81–84, 1956.

[83] C. J. Hickey. *Mechanics of Porous Media*. PhD thesis, University of Alberta, Edmonton, Alberta, Canada, 1994.

[84] C. J. Hickey, J. E. Eastwood, and T. J. T. Spanos. Seismic Wave Propagation in Oil Sands. *AOSTRA Journal of Research*, 7:67–81, 1991.

[85] C. J. Hickey, T. J. T. Spanos, and V. de la Cruz. Deformation parameters of permeable media. *Geophysical Journal International*, 121(2):359—370, 1995.

[86] M. S. Hiremath, R. S. Sandhu, L. W. Morland, and W. E. Wolfe. Analysis of one-dimesional wave propagation in a fluid-saturated finite soil column. *International Journal for Numerical and Analytical Methods in Geomechanics*, 12(2):121–139, 1988.

[87] A. Hosokawa and T. Otani. Ultrasonic wave propagation in bovine cancellous bone. *The Journal of the Acoustical Society of America*, 101(1):558–562, 1997.

[88] X. Huang, S. Greenhalgh, L. Han, and X. Liu. Generalized effective Biot theory and seismic wave propagation in anisotropic, poroviscoelastic media. *Journal of Geophysical Research: Solid Earth*, 127(3):e2021JB023590, 2022.

[89] T. J. R. Hughes. *The Finite Element Method: Linear Static and Dynamic Finite Element Analysis*. Prentice-Hall, 1987.

[90] A. Jasim, B. Hemmings, K. Mayer, and B. Scheu. *Volcanic Unrest: From Science to Society*, chapter Groundwater flow and volcanic unrest. Springer International Publishing, 2019.

[91] B. Jeremić, Z. Cheng, M. Taiebat, and Y. Dafalias. Numerical simulation of fully saturated porous materials. *International Journal for Numerical and Analytical Methods in Geomechanics*, 32(13):1635–1660, 2008.

[92] D. L. Johnson, J. Koplik, and R. Dashen. Theory of dynamic permeability and tortuosity in fluid-saturated porous media. *Journal of fluid mechanics*, 176:379–402, 1987.

[93] M. Kaczmarek, J. Kubik, and M. Pakula. Short ultrasonic waves in cancellous bone. *Ultrasonics*, 40(1-8):95–100, 2002.

[94] D. M. Kahler and Z. J. Kabala. Acceleration of groundwater remediation by rapidly pulsed pumping: Laboratory column tests. *Journal of Environmental Engineering*, 145(1):06018009, 2019.

[95] D. Kalisman, A. Yakirevich, S. Sorek, and T. Kamai. Enhancing solute transport by pressure-wave driven flow in unsaturated porous media. *Journal of Hydrology*, 612:128196, 2022.

[96] Y. Kang, P. Wei, Y. Li, and P. Zhang. Elastic waves propagation through a liquid-saturated poroelastic interlayer based on the fractional viscoelastic BISQ model. *Waves in Random and Complex Media*, 34(3):2268–2296, 2024.

[97] L. Karl, W. Haegeman, G. Degrande, and D. Dooms. Determination of the material damping ratio with the bender element test. *Journal of geotechnical and geoenvironmental engineering*, 134(12):1743–1756, 2008.

[98] S. Khasi, A. Fayazi, and A. Kantzas. Break-up and mobilization of DNAPL by acoustic excitation: Experimental evidence and pore network modeling. *Chemosphere*, 325:138345, 2023.

[99] A. Khoei, O. Barani, and M. Mofid. Modeling of dynamic cohesive fracture propagation in porous saturated media. *International Journal for Numerical and Analytical Methods in Geomechanics*, 35(10):1160–1184, 2011.

[100] D.-S. Kim and J.-S. Lee. Propagation and attenuation characteristics of various ground vibrations. *Soil dynamics and Earthquake engineering*, 19(2):115–126, 2000.

[101] J. Kim. *Sequential Methods for Coupled Geomechanics and Multiphase Flow*. PhD thesis, Stanford University, 2010.

[102] J. Kim, H. A. Tchelepi, and R. Juanes. Stability and convergence of sequential methods for coupled flow and geomechanics: Drained and undrained splits. *Computer Methods in Applied Mechanics and Engineering*, 200(23-24):2094–2116, 2011.

[103] M. Kimura. Study on the Biot-Stoll model for porous marine sediments. *Acoustical science and technology*, 28(4):230–243, 2007.

[104] M. S. King. Recent developments in seismic rock physics. *International Journal of Rock Mechanics and Mining Sciences*, 46(8):1341–1348, 2009.

[105] T. Klimentos and C. McCann. Why is the Biot slow compressional wave not observed in real rocks? *Geophysics*, 53(12):1605–1609, 1988.

[106] J. Koestel, M. Larsbo, and N. Jarvis. Scale and REV analyses for porosity and pore connectivity measures in undisturbed soil. *Geoderma*, 366:114206, 2020.

[107] M. Komijani and R. Gracie. Enriched mixed finite element models for dynamic analysis of continuous and fractured porous media. *Computer Methods in Applied Mechanics and Engineering*, 343:74–99, 2019.

[108] J. Korsawe, G. Starke, W. Wang, and O. Kolditz. Finite element analysis of poroelastic consolidation in porous media: Standard and mixed approaches. *Computer Methods in Applied Mechanics and Engineering*, 195:1096–1115, 2006.

[109] M. Levenston, E. Frank, and A. Grodzinsky. Variationally derived 3-field finite element formulations for quasistatic poroelastic analysis of hydrated biological tissues. *Computer methods in applied mechanics and engineering*, 156(1-4):231–246, 1998.

[110] R. Lewis, B. Schrefler, and L. Simoni. Coupling versus uncoupling in soil consolidation. *International Journal for Numerical and Analytical Methods in Geomechanics*, 15(8):533–548, 1991.

[111] G. Li, X. Su, and H. Pu. An unconditionally stable and high-accuracy finite element scheme for dynamic analysis of saturated poroelastic media. *Soil Dynamics and Earthquake Engineering*, 136:106226, 2020.

[112] H. Li, Z. Yang, F. An, and J. Wu. Simulation of dynamic pulsing fracking in poroelastic media by a hydro-damage-mechanical coupled cohesive phase field model. *Engineering Geology*, 334:107502, 2024.

[113] J. Liang and J. Liang. A user-defined element for dynamic analysis of saturated porous media in ABAQUS. *Computers and Geotechnics*, 126:103693, 2020.

[114] L. Liang, X. Jingru, D. Xiuli, and S. Jia. A fully explicit staggered algorithm for near-field wave propagation of fluid-saturated porous media based on u-p dynamic

formulation. *International Journal for Numerical and Analytical Methods in Geomechanics*, 46(18):3283–3309, 2022.

[115] T. Liu and M. Wang. Critical REV size of multiphase flow in porous media for upscaling by pore-scale modeling. *Transport in Porous Media*, 144(1):111–132, 2022.

[116] Z. Liu, B. Lin, X. Liang, and A. Du. Inversion of surface damage and residual stress in ground silicon wafers by laser surface acoustic wave technology. *Ultrasonics*, 113:106367, 2021.

[117] W.-C. Lo, G. Sposito, and Y.-H. Huang. Modeling seismic stimulation: Enhanced non-aqueous fluid extraction from saturated porous media under pore-pressure pulsing at low frequencies. *Journal of applied geophysics*, 78:77–84, 2012.

[118] W.-C. Lo, C.-C. Yang, S.-Y. Hsu, C.-H. Chen, C.-L. Yeh, and M. Hilpert. The dynamic response of the water retention curve in unsaturated soils during drainage to acoustic excitations. *Water Resources Research*, 53(1):712–725, 2017.

[119] S. L. Lopatnikov. Dynamic equations for new materials: Porous media saturated with magnetic and electrorheological fluids. In *Doklady Physics*, volume 43, pages 378–380. Pleiades Publishing, Ltd., 1998.

[120] S. L. Lopatnikov and A. H.-D. Cheng. Variational formulation of fluid infiltrated porous material in thermal and mechanical equilibrium. *Mechanics of Materials*, 34(11):685–704, 2002.

[121] S. L. Lopatnikov and A. H.-D. Cheng. Macroscopic Lagrangian formulation of poroelasticity with porosity dynamics. *Journal of the Mechanics and Physics of Solids*, 52(12):2801–2839, 2004.

[122] S. L. Lopatnikov and J. W. Gillespie. Poroelasticity-I: governing equations of the mechanics of fluid-saturated porous materials. *Transport in porous media*, 84(2):471–492, 2010.

[123] Z. Lotfian and M. V. Sivaselvan. A topology-motivated mixed Finite Element Method for dynamic response of porous media. *International Journal for Numerical Methods in Engineering*, 00:1–35, 2014.

[124] Z. Lotfian and M. V. Sivaselvan. Mixed finite element formulation for dynamics of porous media. *International Journal for Numerical Methods in Engineering*, 115(2):141–171, 2018.

[125] R. Martin, D. Komatitsch, and A. Ezziani. An unsplit convolutional perfectly matched layer improved at grazing incidence for seismic wave propagation in poroelastic media. *Geophysics*, 73(4):T51–T61, 2008.

[126] Y. J. Masson, S. Pride, and K. Nihei. Finite difference modeling of Biot's poroelastic equations at seismic frequencies. *Journal of Geophysical Research: Solid Earth*, 111(B10), 2006.

[127] A. Mikelić, B. Wang, and M. F. Wheeler. Numerical convergence study of iterative coupling for coupled flow and geomechanics. *Computational Geosciences*, 18:325–341, 2014.

[128] A. Mikelić and M. F. Wheeler. Convergence of iterative coupling for coupled flow and geomechanics. *Computational Geosciences*, 17:455–461, 2013.

[129] S. Mochizuki. Attenuation in partially saturated rocks. *Journal of Geophysical Research: Solid Earth*, 87(B10):8598–8604, 1982.

[130] T. Mohammadnejad and A. Khoei. An extended Finite Element Method for fluid flow in partially saturated porous media with weak discontinuities; the convergence analysis of local enrichment strategies. *Computational Mechanics*, 51(3):327–345, 2013.

[131] P. Mostaghimi, M. J. Blunt, and B. Bijeljic. Computations of absolute permeability on micro-CT images. *Mathematical Geosciences*, 45:103–125, 2013.

[132] L. Mountassir, T. Bassidi, and H. Nounah. Theoretical and experimental studies of the bone damage detection by the ultrasonic method. *Russian Journal of Nondestructive Testing*, 57:525–540, 2021.

[133] T. M. Müller and P. N. Sahay. Solid-phase bulk modulus and microinhomogeneity parameter from quasistatic compression experiments. *Geophysics*, 79(6):1ND–Z201, 2014.

[134] T. M. Müller and P. N. Sahay. Elastic potential energy in linear poroelasticity. *Geophysics*, 84(4):W1–W20, 2019.

[135] T. M. Müller and P. N. Sahay. Porosity perturbations and poroelastic compressibilities. *Geophysics*, 78(1):A7–A11, 2013.

[136] T. M. Müller and P. N. Sahay. Biot coefficient is distinct from effective pressure coefficient. *Geophysics*, 81(4):L27–L33, 2016.

[137] T. M. Müller and P. N. Sahay. Generalized poroelasticity framework for micro-inhomogeneous rocks. *Geophysical Prospecting*, 64(4-Advances in Rock Physics):1122–1134, 2016.

[138] M. A. Murad and A. F. Loula. Improved accuracy in finite element analysis of Biot's consolidation problem. *Computer Methods in Applied Mechanics and Engineering*, 95(3):359–382, 1992.

[139] M. A. Murad and A. F. Loula. On stability and convergence of finite element approximations of Biot's consolidation problem. *International Journal for Numerical Methods in Engineering*, 37(4):645–667, 1994.

[140] P. Navas, M. Pastor, A. Yagüe, M. M. Stickle, D. Manzanal, and M. Molinos. Fluid stabilization of the u- w Biot's formulation at large strain. *International Journal for Numerical and Analytical Methods in Geomechanics*, 45(3):336–352, 2021.

[141] N. M. Newmark. A method of computation for structural dynamics. *Journal of the engineering mechanics division*, 85(3):67–94, 1959.

[142] L. P. S. Ortiz. Estimation of Biot's coefficient in the laboratory during porosity measurement under stress. Master's thesis, Texas A & M University, 2021.

[143] V. A. Osinov. The u-p approximation versus the exact dynamic equations for anisotropic fluid-saturated solids. II. Harmonic waves. *International Journal for Numerical and Analytical Methods in Geomechanics*, 48(2):396–418, 2024.

[144] S. Ovaysi and M. Piri. Direct pore-level modeling of incompressible fluid flow in porous media. *Journal of Computational Physics*, 229(19):7456–7476, 2010.

[145] P. J. Phillips and M. F. Wheeler. A coupling of mixed and continuous Galerkin Finite Element Methods for poroelasticity II: the discrete-in-time case. *Computational Geosciences*, 11(2):145–158, 2007.

[146] S. Picotti, J. M. Carcione, and M. Pavan. Seismic attenuation in Antarctic firn. *The Cryosphere*, 18(1):169–186, 2024.

[147] T. J. Plona. Observation of a second bulk compressional wave in a porous medium at ultrasonic frequencies. *Applied physics letters*, 36(4):259–261, 1980.

[148] M. Preisig and J. H. Prévost. Stabilization procedures in coupled poromechanics problems: A critical assessment. *International Journal for Numerical and Analytical Methods in Geomechanics*, 35(11):1207–1225, 2011.

[149] T. Pritz. Frequency power law of material damping. *Applied Acoustics*, 65(11):1027–1036, 2004.

[150] G. Quiroga-Goode, S. Jiménez-Hernández, and R. Padilla-Hernández. Numerical evidence of elliptical polarization in homogeneous fluid-saturated porous sandstone and the nexus to inhomogeneous plane waves. *Journal of Geophysical Research: Solid Earth*, 114(B5), 2009.

[151] G. Quiroga-Goode, S. Jimenez-Hernandez, M. A. Perez-Flores, and R. Padilla-Hernandez. Computational study of seismic waves in homogeneous dynamic porosity media with thermal and fluid relaxation: Gauging Biot theory. *Journal of Geophysical Research: Solid Earth*, 110(B7):B07303, 2005.

[152] G. Quiroga-Goode, R. Padilla-Hernandez, and Jimenez-Hernandez. Seismic wave properties in time-dependent porosity homogeneous media. *Geophysical Journal International*, 170(3):1227–1242, 2007.

[153] J. Réthoré, R. d. Borst, and M.-A. Abellan. A two-scale approach for fluid flow in fractured porous media. *International Journal for Numerical Methods in Engineering*, 71(7):780–800, 2007.

[154] C. Rodrigo, F. J. Gaspar, X. Hu, and L. T. Zikatanov. Stability and monotonicity for some discretizations of the Biot's consolidation model. *Computer Methods in Applied Mechanics and Engineering*, 298:183–204, 2016.

[155] E. Rohan. Homogenization of acoustic waves in strongly heterogeneous porous structures. *Wave motion*, 50(7):1073–1089, 2013.

[156] E. Saenger, S. Shapiro, and Y. Keehm. Seismic effects of viscous Biot-coupling: Finite difference simulations on micro-scale. *Geophysical Research Letters*, 32(14), 2005.

[157] P. N. Sahay. Biot constitutive relation and porosity perturbation equation. *Geophysics*, 78(5):L57–L67, 2013.

[158] P. N. Sahay, T. J. T. Spanos, and V. de la Cruz. Seismic wave propagation in inhomogeneous and anisotropic porous media. *Geophysical Journal International*, 145(1):209–222, 2001.

[159] P. N. Sahay. Elastodynamics of deformable porous media. *Proceedings of the Royal Society of London. Series A: Mathematical, Physical and Engineering Sciences*, 452(1950):1517–1529, 1996.

[160] P. N. Sahay. On the Biot slow S-wave. *Geophysics*, 73(4):N19–N33, 2008.

[161] M. Sharma. Squirt-flow in fluid-saturated porous media: propagation of Rayleigh waves. *Transport in Porous Media*, 122:25–42, 2018.

[162] D.-H. Sheen, K. Tuncay, C.-E. Baag, and P. J. Ortoleva. Parallel implementation of a velocity-stress staggered-grid finite-difference method for 2-D poroelastic wave propagation. *Computers & Geosciences*, 32(8):1182–1191, 2006.

[163] B. R. Simon, O. C. Zienkiewicz, and D. K. Paul. An analytical solution for the transient response of saturated porous elastic solids. *International Journal for Numerical and analytical methods in Geomechanics*, 8(4):381–398, 1984.

[164] B. Simon, J.-S. Wu, O. Zienkiewicz, and D. Paul. Evaluation of u–w and u–π Finite Element Methods for the dynamic response of saturated porous media using one-dimensional models. *International Journal for Numerical and analytical methods in Geomechanics*, 10(5):461–482, 1986.

[165] T. J. T. Spanos. *The Thermophysics of Porous Media*. Chapman & Hall, 2002.

[166] T. Spanos, B. Davidson, M. Dusseault, D. Shand, and M. Samaroo. Pressure pulsing at the reservoir scale: a new IOR approach. *Journal of Canadian Petroleum Technology*, 42(02), 2003.

[167] X. Sun, S. Fan, and C. Liu. Attenuation characteristics of concrete using smart aggregate transducers: Experiments and numerical simulations of P-wave propagation. *Journal of Intelligent Material Systems and Structures*, 35(5):556–572, 2024.

[168] X.-M. Tang, X.-l. Chen, and X.-k. Xu. A cracked porous medium elastic wave theory and its application to interpreting acoustic data from tight formations. *Geophysics*, 77(6):D245–D252, 2012.

[169] P. Tasiopoulou, M. Taiebat, N. Tafazzoli, and B. Jeremic. Solution verification procedures for modeling and simulation of fully coupled porous media: static and dynamic behavior. *Coupled Systems Mechanics*, 4(1):67–98, 2015.

[170] C. Taylor and P. Hood. A numerical solution of the Navier-Stokes equations using the finite element technique. *Computers & Fluids*, 1(1):73–100, 1973.

[171] Y. Tian, J. Yang, Z. Li, J. Huang, and S. Qin. Hierarchical wave-mode separation in the poroelastic medium using eigenform analysis. *Geophysics*, 88(1):T33–T44, 2023.

[172] R. Ulusay and J. Hudson. *The Complete ISRM Suggested Methods for Rock Characterization, Testing and Monitoring: 1974-2006*. ISRM Turkish National Group, 2007.

[173] K. von Terzaghi. Die Berechnung der Durchassigkeitsziffer des Tones aus dem Verlauf der hydrodynamischen Spannungs. erscheinungen. *Sitzungsber. Akad. Wiss. Math. Naturwiss. Kl. Abt. 2A*, 132:105–124, 1923.

[174] S. J. Wang and K. C. Hsu. The application of the first-order second-moment method to analyze poroelastic problems in heterogeneous porous media. *Journal of Hydrology*, 369(1-2):209–221, 2009.

[175] Z. Wang and A. Nur. Dispersion analysis of acoustic velocities in rocks. *The Journal of the Acoustical Society of America*, 87(6):2384–2395, 1990.

[176] J. Wen and Y. He. A strongly conservative Finite Element Method for the coupled Stokes–Biot model. *Computers & Mathematics with Applications*, 80(5):1421–1442, 2020.

[177] F. Wenzlau and T. M. Müller. Finite-difference modeling of wave propagation and diffusion in poroelastic media. *Geophysics*, 74(4):T55–T66, 2009.

[178] S. Whitaker. Diffusion and dispersion in porous media. *AIChE Journal*, 13(3):420–427, 1967.

[179] S. Whitaker. *The method of volume averaging*, volume 13. Springer Science & Business Media, 1998.

[180] J. A. White and R. I. Borja. Stabilized low-order finite elements for coupled solid-deformation/fluid-diffusion and their application to fault zone transients. *Computer Methods in Applied Mechanics and Engineering*, 197(49-50):4353–4366, 2008.

[181] U. Wollner, A. Kerimov, and G. Mavko. Scale and boundary effects on the effective elastic properties of 2-D and 3-D non-REV heterogeneous porous media. *Journal of Geophysical Research: Solid Earth*, 123(7):5451–5465, 2018.

[182] M. Wu, J. Wu, J. Wu, and B. X. Hu. A new criterion for determining the representative elementary volume of translucent porous media and inner contaminant. *Hydrology and Earth System Sciences*, 24(12):5903–5917, 2020.

[183] W. Wu, H. Zheng, and Y. Yang. Enriched three-field numerical manifold formulation for dynamics of fractured saturated porous media. *Computer Methods in Applied Mechanics and Engineering*, 353:217–252, 2019.

[184] W. Wu, H. Zheng, and Y. Yang. Numerical manifold method for dynamic consolidation of saturated porous media with three-field formulation. *International Journal for Numerical Methods in Engineering*, 120(6):768–802, 2019.

[185] C. Xiaolin, D. Guoliang, G. Weiming, Z. Fengxi, and X. Jiang. Resistance of saturated soil to a laterally vibrating pile. *Soil Dynamics and Earthquake Engineering*, 141:106496, 2021.

[186] F. Xiong, J. Liu, Z. Guo, and J. Liu. Deep-neural-networks-based approaches for Biot–squirt model in rock physics. *Acta Geophysica*, 70(2):593–607, 2022.

[187] F. Xiong, B. Wang, J. Liu, Z. Guo, and J. Liu. Biot's theory-based dynamic equation modeling using a machine learning auxiliary approach. *Journal of Geophysics and Engineering*, 20(6):1348–1360, 2023.

[188] C. Xu, J. Song, X. Du, and Z. Zhong. A completely explicit Finite Element Method for solving dynamic up equations of fluid-saturated porous media. *Soil Dynamics and Earthquake Engineering*, 97:364–376, 2017.

[189] D. Yang and Z. Zhang. Effects of the Biot and the squirt-flow coupling interaction on anisotropic elastic waves. *Chinese Science Bulletin*, 45:2130–2138, 2000.

[190] D. Yang and Z. Zhang. Poroelastic wave equation including the Biot/squirt mechanism and the solid/fluid coupling anisotropy. *Wave Motion*, 35(3):223–245, 2002.

[191] S.-b. Yang, C.-y. Bai, and S. Greenhalgh. Seismic wavefield modelling in two-phase media including undulating topography with the modified Biot/squirt model by a curvilinear-grid finite difference method. *Geophysical Prospecting*, 68(2):591–614, 2020.

[192] Y. Yang, G. Cascante, and M. A. Polak. New method for the evaluation of material damping using the wavelet transform. *Journal of Geotechnical and Geoenvironmental Engineering*, 137(8):798–808, 2011.

[193] C. Yew and P. Jogi. The determination of Biot's parameters for sandstones: Part 1: Static tests Experimental procedure for determining Biot's parameters for four rock specimens is presented and theoretical values of wave speeds propagating through

them are compared with experimental values. *Experimental Mechanics*, 18:167–172, 1978.

[194] S.-S. Yoo, H.-C. Kim, J. Kim, E. Kim, K. Kowsari, J. Van Reet, and K. Yoon. Enhancement of cerebrospinal fluid tracer movement by the application of pulsed transcranial focused ultrasound. *Scientific reports*, 12(1):12940, 2022.

[195] C. Yuan-Feng, Y. Ding-Hui, and Y. Hui-Zhu. Biot/squirt model in viscoelastic porous media. *Chinese Physics Letters*, 19(3):445, 2002.

[196] R. Zaccherini, A. Palermo, A. Marzani, A. Colombi, V. K. Dertimanis, and E. Chatzi. Geometric and material attenuation of surface acoustic modes in granular media. *Geophysical Journal International*, 230(1):288–297, 2022.

[197] T. Zakirov and M. Khramchenkov. Representative elementary volumes for various characteristics of two-phase flows in porous media: A statistical approach. *Geoenergy Science and Engineering*, 229:212104, 2023.

[198] J. Zapoměl, V. Dekỳš, P. Ferfecki, A. Sapietová, M. Sága, and M. Žmindák. Identification of material damping of a carbon composite bar and study of its effect on attenuation of its transient lateral vibrations. *International journal of applied mechanics*, 7(06):1550081, 2015.

[199] D. Zhang, R. Zhang, S. Chen, and W. E. Soll. Pore scale study of flow in porous media: Scale dependency, REV, and statistical REV. *Geophysical research letters*, 27(8):1195–1198, 2000.

[200] S. Zhang, F. Yang, D. Xu, and Y. Wang. Seismic wave simulation by velocity–stress wave equations in two-phase anisotropic media. *Journal of Geophysics and Engineering*, 11(1):015008, 2014.

[201] Y. Zhang, D. M. Pedroso, and W. Ehlers. One-dimensional dynamics of saturated incompressible porous media: analytical solutions and influence of inertia terms. *International Journal for Numerical and Analytical Methods in Geomechanics*, 40(18):2489–2513, 2016.

[202] H. Zhao, B. Wu, and J. Gao. Effects of petrophysical parameters on attenuation and dispersion of seismic waves in the simplified poroelastic theory: Comparison between the Biot's theory and viscosity-extended theory. *Geophysical Prospecting*, 69(1):204–219, 2021.

[203] J. Zheng, T. Li, J. Xie, and Y. Sun. Improved numerical solution of anisotropic poroelastic wave equation in microseismicity: Graphic process unit acceleration and moment tensor implementation. *Geophysical Prospecting*, 2024.

[204] Y. Zheng, R. Burridge, and D. R. Burns. Reservoir simulation with the Finite Element Method using Biot poroelastic approach. Technical report, Massachusetts Institute of Technology. Earth Resources Laboratory, 2003.

[205] O. C. Zienkiewicz. Basic Formulation of Static and Dynamic Behaviours of Soil and Other Porous Media. *Applied Mathematics and Mechanics*, 3(4):457—-468, 1982.

[206] O. C. Zienkiewicz and T. Shiomi. Dynamic behaviour of saturated porous media; The generalized Biot formulation and its numerical solution. *International Journal for Numerical and Analytical Methods in Geomechanics*, 8(1):71–96, 1984.

[207] R. W. Zimmerman, W. H. Somerton, and M. S. King. Compressibility of porous rocks. *Journal of Geophysical Research: Solid Earth*, 91(B12):12765–12777, 1986.

[208] R. Zimmerman, J. Haraden, and W. Somerton. The Effects of Pore Pressure and Confining Pressure on Pore and Bulk Volume Compressibilities of Consolidated Sandstones. In *Measurement of Rock Properties at Elevated Pressures and Temperatures*. ASTM International, 01 1985.

[209] R. P. Zschuppe. *Pulse Flow Enhancement in Two-Phase Media*. PhD thesis, University of Waterloo, 2001.

[210] A. S. Zubov, A. N. Khlyupin, M. V. Karsanina, and K. M. Gerke. In search for representative elementary volume (REV) within heterogeneous materials: A survey of scalar and vector metrics using porous media as an example. *Advances in Water Resources*, 192:104762, 2024.

APPENDICES

Appendix A

Stress Definition in BT and dCS Theories

In Biot's theory, the solid and fluid stresses can be written, in index notation, as

$$\sigma_{ik}^{s\,BT} = N(\partial_i u_k^s + \partial_k u_i^s) + \delta_{ik}\lambda\partial_j u_j^s + \delta_{ik}\frac{Q^2}{R}\partial_j u_j^s + \delta_{ik}Q\partial_j u_j^f \tag{A.1}$$

$$\sigma_{ik}^{f\,BT} = -\eta_0\delta_{ik}p \tag{A.2}$$

and summing up both equations, the total stress $\sigma_{ik}^{BT} = \sigma_{ik}^{s\,BT} + \sigma_{ik}^{f\,BT}$ is given by

$$\sigma_{ik}^{BT} = \underbrace{N(\partial_i u_k^s + \partial_k u_i^s) + \delta_{ik}\lambda\partial_j u_j^s}_{\text{effective stress}} \underbrace{+\delta_{ik}\left(\frac{Q^2}{R}\partial_j u_j^s + Q\partial_j u_j^f\right)}_{\text{solid-fluid coupling}} \underbrace{-\delta_{ik}\eta_0 p}_{\text{fluid stress}} \tag{A.3}$$

or using the pressure equation (3.7) with $\alpha = \left(\frac{Q}{R} + 1\right)\eta_0$,

$$\sigma_{ik}^{BT} = \underbrace{N(\partial_i u_k^s + \partial_k u_i^s) + \delta_{ik}\lambda\partial_j u_j^s}_{\text{effective stress}} \underbrace{-\delta_{ik}\alpha p}_{\text{fluid pressure contribution}} \tag{A.4}$$

For numerical implementation purposes, the Voigt form for a two-dimensional domain can be written as

$$\boldsymbol{\sigma}^{BT} = \begin{Bmatrix}\sigma_{xx}\\ \sigma_{yy}\\ \sigma_{xy}\end{Bmatrix} = \begin{bmatrix}2\mu+\lambda & \lambda & 0\\ \lambda & 2\mu+\lambda & 0\\ 0 & 0 & \lambda\end{bmatrix}\begin{Bmatrix}\varepsilon_{xx}\\ \varepsilon_{yy}\\ 2\varepsilon_{xy}\end{Bmatrix} - \alpha\mathbf{m}p \tag{A.5}$$

where $\mathbf{m} = [1, 1, 0]^\top$ is a mapping vector [205]. Analyzing the stress definitions in the dCS theory, the pore scale solid stress is given by

$$\sigma_{ik}^{s\,dCS} = \delta_{ik} K_s \partial_j u_j^s + \mu_s (\partial_i u_k^s + \partial_k u_i^s - \frac{2}{3}\delta_{ik}\partial_j u_j^s) \tag{A.6}$$

and, when applying the volume-averaging technique [178, 165],

$$< \sigma_{ik}^{s\,dCS} > = < \delta_{ik} K_s \partial_j u_j^s > + < \mu_s (\partial_i u_k^s + \partial_k u_i^s - \frac{2}{3}\delta_{ik}\partial_j u_j^s) > \tag{A.7}$$

$$= \delta_{ik} K_s < \partial_j u_j^s > + \mu_s < (\partial_i u_k^s + \partial_k u_i^s - \frac{2}{3}\delta_{ik}\partial_j u_j^s) > \tag{A.8}$$

$$= \delta_{ik} K_s \partial_j < u_j^s > + \delta_{ik} K_s \underbrace{\frac{1}{V}\int_{A^{sf}} \mathbf{u}_f \mathbf{n}\, dA}_{-(\eta - \eta_0)} + \tag{A.9}$$

$$\mu_s (\partial_i < u_k^s > + \partial_k < u_i^s > - \frac{2}{3}\delta_{ik}\partial_j < u_j^s >)$$

$$+ \mu_s \underbrace{\frac{1}{V}\int_{A^{sf}} (u_i^s n_k + u_k^s n_i - \frac{2}{3}\delta_{ik}\partial_j u_j^s)\, dA}_{I_{ik}^2} \tag{A.10}$$

$$= \delta_{ik} K_s \partial_j < u_j^s > - \delta_{ik} K_s (\eta - \eta_0) + \mu_s (\partial_i < u_k^s > + \partial_k < u_i^s >$$

$$- \frac{2}{3}\delta_{ik}\partial_j < u_j^s >) + \mu_s I_{ik}^2 \tag{A.11}$$

where A^{sf} is the solid-fluid interface, $\frac{1}{V}\int_{A^{sf}} \mathbf{u}_f \mathbf{n}\, dA = -(\eta - \eta_0)$ is the volume swept out at the solid-fluid boundary [134], and I_{ik}^2 represents the coupling effect of the constituents at the interface [165]. Since $< \sigma_{ik}^{s\,dCS} > = (1 - \eta_0)\bar{\sigma}_{ik}^{s\,dCS}$,

$$(1-\eta_0)\bar{\sigma}_{ik}^{s\,dCS} = \delta_{ik} K_s (1-\eta_0)\partial_j \bar{u}_j^s - \delta_{ik} K_s (\eta - \eta_0) + \mu_s (1-\eta_0)(\partial_i \bar{u}_k^s + \partial_k \bar{u}_i^s - \frac{2}{3}\delta_{ik}\partial_j \bar{u}_j^s) + \mu_s I_{ik}^2. \tag{A.12}$$

The pore scale definition of the fluid stress is

$$\sigma_{ik}^{f\,dCS} = \mu_f (\partial_i v_k^f + \partial_k v_i^f - \frac{2}{3}\delta_{ik}\partial_j v_j^f) + \delta_{ik}\xi_f \partial_j v_j^f - \delta_{ik} p; \tag{A.13}$$

applying the volume-averaging technique,

$$< \sigma_{ik}^{f\,dCS} > =< \mu_f(\partial_i v_k^f + \partial_k v_i^f - \frac{2}{3}\delta_{ik}\partial_j v_j^f) > + < \delta_{ik}\xi_f \partial_j v_j^f > - < \delta_{ik} p > \tag{A.14}$$

$$= \mu_f < (\partial_i v_k^f + \partial_k v_i^f - \frac{2}{3}\delta_{ik}\partial_j v_j^f) > + \delta_{ik}\xi_f < \partial_j v_j^f > - \delta_{ik} < p > \tag{A.15}$$

$$= \mu_f(\partial_i < v_k^f > + \partial_k < v_i^f > - \frac{2}{3}\delta_{ik}\partial_j < v_j^f >)$$
$$+ \mu_f \underbrace{\frac{1}{V}\int_{A^{sf}} (v_i^f n_k + v_k^f n_i - \frac{2}{3}\delta_{ik}\partial_j v_j^f)\, dA}_{\frac{\partial}{\partial t} I_{ik}^4} + \tag{A.16}$$

$$\delta_{ik}\xi_f \partial_j < v_j^f > + \delta_{ik}\xi_f \underbrace{\frac{1}{V}\int_{A^{sf}} \mathbf{v}_f \mathbf{n}\, dA}_{-\frac{\partial}{\partial t}(\eta - \eta_0)} - \delta_{ik} < p > \tag{A.17}$$

$$= \mu_f(\partial_i < v_k^f > + \partial_k < v_i^f > - \frac{2}{3}\delta_{ik}\partial_j < v_j^f >) + \mu_f \frac{\partial}{\partial t} I_{ik}^4$$
$$+ \delta_{ik}\xi_f \partial_j < v_j^f > - \delta_{ik}\xi_f \frac{\partial}{\partial t}(\eta - \eta_0) - \delta_{ik} < p > \tag{A.18}$$

and using $< \sigma_{ik}^{f\,dCS} >= \eta_0 \bar{\sigma}_{ik}^{f\,dCS}$, we have that

$$\eta_0 \bar{\sigma}_{ik}^{f\,dCS} = \mu_f \eta_0(\partial_i \bar{v}_k^f + \partial_k \bar{v}_i^f - \frac{2}{3}\delta_{ik}\partial_j \bar{v}_j^f) + \mu_f \frac{\partial}{\partial t} I_{ik}^4 + \delta_{ik}\xi_f \eta_0 \partial_j \bar{v}_j^f - \delta_{ik}\xi_f \frac{\partial}{\partial t}(\eta - \eta_0) - \delta_{ik}\eta_0 \bar{p}. \tag{A.19}$$

Summing up both solid and fluid stresses, the total stress $\bar{\sigma}_{ik}^{dCS} = (1-\eta_0)\bar{\sigma}_{ik}^{s\,dCS} + \eta_0 \bar{\sigma}_{ik}^{f\,dCS}$ is equal to

$$\bar{\sigma}_{ik}^{dCS} = \delta_{ik} K_s (1-\eta_0)\partial_j \bar{u}_j^s + \mu_s(1-\eta_0)(\partial_i \bar{u}_k^s + \partial_k \bar{u}_i^s - \frac{2}{3}\delta_{ik}\partial_j \bar{u}_j^s) - \delta_{ik} K_s(\eta - \eta_0)$$
$$+ \mu_f \eta_0(\partial_i \bar{v}_k^f + \partial_k \bar{v}_i^f - \frac{2}{3}\delta_{ik}\partial_j \bar{v}_j^f) + \delta_{ik}\xi_f \eta_0 \partial_j \bar{v}_j^f - \delta_{ik}\xi_f \frac{\partial}{\partial t}(\eta - \eta_0) - \delta_{ik}\eta_0 \bar{p}, \tag{A.20}$$

considering that the interface integrals I_{ik}^2, I_{ik}^4 cancel out because

$$\frac{\partial}{\partial t} I_{ik}^4 = -I_{ik}^2 \tag{A.21}$$

and

$$I^4_{ik} = \delta_\mu(1-\eta_0)(u^s_i n_k + u^s_k n_i - \frac{2}{3}\delta_{ik}\partial_j u^s_j). \tag{A.22}$$

The solid material constants can be rewritten as $(1-\eta_0)\lambda_s = (1-\eta_0)K_s - \frac{2}{3}(1-\eta_0)\mu_s$ and $\mu = (1-\eta_0)\mu_s$, and thus

$$\begin{aligned}\bar{\sigma}^{dCS}_{ik} = {} & \mu(\partial_i \bar{u}^s_k + \partial_k \bar{u}^s_i) + \delta_{ik}(1-\eta_0)\lambda_s \partial_j \bar{u}^s_j - \delta_{ik}K_s(\eta-\eta_0) - \delta_{ik}\eta_0\bar{p} \\ & + \mu_f\eta_0(\partial_i \bar{v}^f_k + \partial_k \bar{v}^f_i - \frac{2}{3}\delta_{ik}\partial_j \bar{v}^f_j) + \delta_{ik}\xi_f\eta_0\partial_j\bar{v}^f_j - \delta_{ik}\xi_f\frac{\partial}{\partial t}(\eta-\eta_0).\end{aligned} \tag{A.23}$$

Furthermore, the microscopic constant λ_s can also be related to the averaged λ by the relation $\lambda = (1-\eta_0)\lambda_s + (\alpha-\eta_0)K_s$. This comes from the fact that the averaged bulk modulus K appearing in $\lambda = K - \frac{2}{3}\mu$ is related to the pore scale solid bulk modulus by $K = (1-\alpha)K_s$. Hence,

$$\begin{aligned}\bar{\sigma}^{dCS}_{ik} = {} & \underbrace{\mu(\partial_i \bar{u}^s_k + \partial_k \bar{u}^s_i) + \delta_{ik}\lambda\partial_j\bar{u}^s_j}_{\text{averaged effective stress}} \underbrace{+\delta_{ik}(\alpha-\eta_0)K_s\partial_j\bar{u}^s_j - \delta_{ik}K_s(\eta-\eta_0)}_{\text{solid-fluid coupling}} \\ & \underbrace{+\mu_f\eta_0(\partial_i \bar{v}^f_k + \partial_k \bar{v}^f_i - \frac{2}{3}\delta_{ik}\partial_j\bar{v}^f_j) + \delta_{ik}\xi_f\eta_0\partial_j\bar{v}^f_j - \delta_{ik}\xi_f\frac{\partial}{\partial t}(\eta-\eta_0) - \delta_{ik}\eta_0\bar{p}}_{\text{fluid stress}}\end{aligned} \tag{A.24}$$

or in Voigt form

$$\begin{aligned}\bar{\boldsymbol{\sigma}}^{dCS} = \begin{Bmatrix}\bar{\sigma}_{xx}\\ \bar{\sigma}_{yy}\\ \bar{\sigma}_{xy}\end{Bmatrix} = {} & \begin{bmatrix}2\mu+\lambda & \lambda & 0\\ \lambda & 2\mu+\lambda & 0\\ 0 & 0 & \lambda\end{bmatrix}\begin{Bmatrix}\bar{\varepsilon}_{xx}\\ \bar{\varepsilon}_{yy}\\ 2\bar{\varepsilon}_{xy}\end{Bmatrix} + (\alpha-\eta_0)K_s\mathbf{m}^\top\mathbf{m}\begin{Bmatrix}\bar{\varepsilon}_{xx}\\ \bar{\varepsilon}_{yy}\\ 0\end{Bmatrix} \\ & + \begin{bmatrix}2\mu_f\eta_0 - 2\mu_f\eta_0/3 + \xi_f\eta_0 & -2\mu_f\eta_0/3 + \xi_f\eta_0 & 0\\ -2\mu_f\eta_0/3 + \xi_f\eta_0 & 2\mu_f\eta_0 - 2\mu_f\eta_0/3 + \xi_f\eta_0 & 0\\ 0 & 0 & \mu_f\eta_0\end{bmatrix}\begin{Bmatrix}\bar{v}^f_{xx}\\ \bar{v}^f_{yy}\\ 2\bar{v}^f_{xy}\end{Bmatrix} \\ & - K_s(\eta-\eta_0)\mathbf{m} - \xi_f\mathbf{m}\frac{\partial}{\partial t}(\eta-\eta_0) - \eta_0\mathbf{m}\bar{p}.\end{aligned} \tag{A.25}$$

To recover the analogy with BT theory, the fluid stress is written only in terms of the fluid pressure, and the porosity variable is replaced by equation (3.20) as in

$$\bar{\sigma}^{dCS}_{ik} = \underbrace{\mu(\partial_i \bar{u}^s_k + \partial_k \bar{u}^s_i) + \delta_{ik}\lambda\partial_j\bar{u}^s_j}_{\text{averaged effective stress}} \underbrace{+\delta_{ik}\{[(\alpha-\eta_0)K_s - K_s\delta_s]\partial_j\bar{u}^s_j + K_s\delta_f\partial_j\bar{u}^f_j - \eta_0\bar{p}\}}_{\text{fluid pressure contribution}}, \tag{A.26}$$

where $(\alpha-\eta_0)K_s-K_s\delta_s=\dfrac{Q^2}{R}$ and $K_s\delta_f=Q$, thus returning to equation (A.3). Therefore, it can be observed that the total stress from the dCS theory yields an effective stress term, a solid-fluid coupling term due to interface interaction, and a fluid stress term, similarly to the BT formulation. The dimensionless constant δ_μ in the macroscopic shear modulus appears in the definitions of the integrals I_{ik}^2, I_{ik}^4, which have counterparts in the solid and fluid stressed and hence vanish in the total stress equation.

Appendix B

Modal Analysis in Porous Media

In this appendix, the modal analysis for the $\mathbf{u}_s - p$ dCS system of equations is presented. It is noteworthy that the three-field system $\mathbf{u}_s - p - \eta$ introduced in Chapter 3 can be simplified to a two field $\mathbf{u}_s - p$ system when combining the second and third equations in (3.21). By doing that and adding inertia terms, the dynamic $\mathbf{u}_s - p$ system is given by

$$\begin{cases} \nabla \cdot \boldsymbol{\tau} - \rho \ddot{\mathbf{u}}_s = 0, \\ -\dfrac{\kappa}{\mu_f}\nabla^2 p - \dfrac{\rho_f \kappa}{\mu_f}\nabla \cdot \ddot{\mathbf{u}}_s + \eta_0 \dfrac{\eta_0 - \delta_f + \delta_s}{\eta_0 - \delta_f}\nabla \dot{\mathbf{u}}_s + \dfrac{\eta_0}{K_f(1-\delta_f/\eta_0)}\dot{p} = 0. \end{cases} \tag{B.1}$$

in which the material parameters are detailed in Section 3.2. Considering a porous media domain Ω with boundary Γ, and for weight functions $\delta\mathbf{u}_s, \delta p$ defined in appropriate function spaces, the correspondent weak form is written as

$$\int_\Omega (\delta \mathbf{u}_s)^\top \rho \ddot{\mathbf{u}}_s \, d\Omega + \int_\Omega (\nabla \delta \mathbf{u}_s)^\top \boldsymbol{\sigma} \, d\Omega - \alpha \int_\Omega (\nabla \delta \mathbf{u}_s)^\top \mathbf{m} p \, d\Omega - \int_\Gamma (\delta \mathbf{u}_s^\top) \bar{\mathbf{t}} \, d\Gamma = 0 \tag{B.2}$$

$$\begin{aligned} \frac{\kappa}{\mu_f}\int_\Omega (\nabla \delta p)\nabla p \, d\Omega + \int_\Gamma (\delta p)\bar{q} \, d\Gamma - \frac{\rho_f \kappa}{\mu_f}\int_\Omega (\delta p)\mathbf{m}^\top \nabla \cdot \ddot{\mathbf{u}}_s \, d\Omega \\ + \eta_0 \frac{\eta_0 - \delta_f + \delta_s}{\eta_0 - \delta_f}\int_\Omega (\delta p)\mathbf{m}^\top \nabla \cdot \dot{\mathbf{u}}_s \, d\Omega + \frac{\eta_0}{K_f(1-\delta_f/\eta_0)}\int_\Omega (\delta p)\, \dot{p} \, d\Omega = 0 \end{aligned} \tag{B.3}$$

where $\bar{\mathbf{t}}, \bar{q}$ are the load and flux boundary conditions, and $\mathbf{m}$ is a mapping vector [205].

B.1 Transient Case

Let us start by performing the modal analysis for the transient case, with $\ddot{\mathbf{u}}_s = 0$. The semi-discrete form of the $\mathbf{u}_s - p$ governing equations is given by

$$\mathbf{K}_{ss}\hat{\mathbf{u}}_s - \mathbf{K}_{sp}\hat{\mathbf{p}} = \mathbf{f}_s \tag{B.4}$$

$$\mathbf{C}_{ps}\dot{\hat{\mathbf{u}}}_s + \mathbf{K}_{pp}\hat{\mathbf{p}} + \mathbf{C}_{pp}\dot{\hat{\mathbf{p}}} = \mathbf{f}_p \tag{B.5}$$

in which $\hat{\mathbf{u}}_s, \hat{\mathbf{p}}$ are nodal values and the submatrices are defined as

$$\mathbf{K}_{ss} = \int_\Omega \mathbf{B}_s^\top \mathbf{D}\mathbf{B}_s \; d\Omega, \tag{B.6}$$

$$\mathbf{K}_{sp} = \alpha \int_\Omega \mathbf{B}_s^\top \mathbf{m}\mathbf{N}_p \; d\Omega, \tag{B.7}$$

$$\mathbf{K}_{pp} = \frac{\kappa}{\mu_f} \int_\Omega \mathbf{B}_p^\top \mathbf{B}_p \; d\Omega, \tag{B.8}$$

$$\mathbf{C}_{ps} = \eta_0 \frac{\eta_0 - \delta_f + \delta_s}{\eta_0 - \delta_f} \int_\Omega \mathbf{N}_p^\top \mathbf{m}^\top \mathbf{B}_s d\Omega, \tag{B.9}$$

$$\mathbf{C}_{pp} = \frac{\eta_0}{K_f(1 - \delta_f/\eta_0)} \int_\Omega \mathbf{N}_p^\top \mathbf{N}_p \; d\Omega, \tag{B.10}$$

$$\mathbf{f}_s = \int_{\Gamma_t} \mathbf{N}_s^\top \bar{\mathbf{t}} \; d\Gamma, \tag{B.11}$$

$$\mathbf{f}_p = \int_\Gamma \mathbf{N}_p^\top \bar{q} \; d\Gamma. \tag{B.12}$$

We then write the vectors of nodal variables as $\hat{\mathbf{u}}_s = \mathbf{\Phi}_s \mathbf{x}_s$ and $\hat{\mathbf{p}} = \mathbf{\Phi}_p \mathbf{x}_p$, where $\mathbf{\Phi}_s, \mathbf{\Phi}_p$ are the matrices of eigenvectors and $\mathbf{x}_s, \mathbf{x}_p$ are the generalized vectors for solid displacement and pressure, respectively. The resulting system is

$$\mathbf{K}_{ss}\mathbf{\Phi}_s\mathbf{x}_s - \mathbf{K}_{sp}\mathbf{\Phi}_p\mathbf{x}_p = \mathbf{f}_s, \tag{B.13}$$

$$\mathbf{C}_{ps}\mathbf{\Phi}_s\dot{\mathbf{x}}_s + \mathbf{K}_{pp}\mathbf{\Phi}_p\mathbf{x}_p + \mathbf{C}_{pp}\mathbf{\Phi}_p\dot{\mathbf{x}}_p = \mathbf{f}_p. \tag{B.14}$$

Pre-multiplying the equations by $\mathbf{\Phi}_s^\top, \mathbf{\Phi}_p^\top$, respectively,

$$\mathbf{\Phi}_s^\top\mathbf{K}_{ss}\mathbf{\Phi}_s\mathbf{x}_s - \mathbf{\Phi}_s^\top\mathbf{K}_{sp}\mathbf{\Phi}_p\mathbf{x}_p = \mathbf{\Phi}_s^\top\mathbf{f}_s, \tag{B.15}$$

$$\mathbf{\Phi}_p^\top\mathbf{C}_{ps}\mathbf{\Phi}_s\dot{\mathbf{x}}_s + \mathbf{\Phi}_p^\top\mathbf{K}_{pp}\mathbf{\Phi}_p\mathbf{x}_p + \mathbf{\Phi}_p^\top\mathbf{C}_{pp}\mathbf{\Phi}_p\dot{\mathbf{x}}_p = \mathbf{\Phi}_p^\top\mathbf{f}_p. \tag{B.16}$$

Employing the Backwards Euler time integration technique, at time step $n+1$ we have

$$\dot{\mathbf{x}}_s^{n+1} = \frac{\mathbf{x}_s^{n+1} - \mathbf{x}_s^n}{\Delta t}, \qquad \dot{\mathbf{x}}_p^{n+1} = \frac{\mathbf{x}_p^{n+1} - \mathbf{x}_p^n}{\Delta t}, \tag{B.17}$$

and the fully discrete system in matrix form is written as

$$\begin{bmatrix} \boldsymbol{\Phi}_s^\top \mathbf{K}_{ss} \boldsymbol{\Phi}_s & -\boldsymbol{\Phi}_s^\top \mathbf{K}_{sp} \boldsymbol{\Phi}_p \\ \boldsymbol{\Phi}_p^\top \mathbf{C}_{ps} \boldsymbol{\Phi}_s & \boldsymbol{\Phi}_p^\top \mathbf{K}_{pp} \boldsymbol{\Phi}_p \Delta t + \boldsymbol{\Phi}_p^\top \mathbf{C}_{pp} \boldsymbol{\Phi}_p \end{bmatrix} \begin{Bmatrix} \mathbf{x}_s^{n+1} \\ \mathbf{x}_p^{n+1} \end{Bmatrix} = \tag{B.18}$$

$$\begin{Bmatrix} \boldsymbol{\Phi}_s^\top \mathbf{f}_s^{n+1} \\ \boldsymbol{\Phi}_p^\top \mathbf{f}_p^{n+1} \Delta t + \boldsymbol{\Phi}_p^\top \mathbf{C}_{ps} \boldsymbol{\Phi}_s \mathbf{x}_s^n + \boldsymbol{\Phi}_p^\top \mathbf{C}_{pp} \boldsymbol{\Phi}_p \mathbf{x}_p^n \end{Bmatrix} \tag{B.19}$$

The eigenproblem is solved for the uncoupled, undamped free-response equations, as in

$$\mathbf{K}_{ss} \hat{\mathbf{u}}_s = \mathbf{0}, \qquad \mathbf{K}_{pp} \hat{\mathbf{p}} = \mathbf{0}. \tag{B.20}$$

To verify the mode superposition accuracy, we take the water-sandstone material parameters and the geometry from the consolidation example in [108]. The analytical solution for one-dimensional consolidation is taken from [138]; the numerical simulation is carried out considering a mesh of 100 elements with a linear approximation for p and a quadratic approximation for $\mathbf{u}_s$. A time step of $\Delta t = 10^{-2}$s is chosen for a final simulation time of $t_{end} = 10$s.

The first six mode shapes obtained are depicted in Figure B.1. We observe how the pressure natural frequencies are many orders lower than the solid displacement natural frequencies, and how the solid and fluid mode shapes are out-of-phase. Figure B.2 compares the results for the $\mathbf{u}_s, p$ variation over the domain length (at the final simulation time) and over time (at a point in the middle of the domain), showing how both time solution and modal analysis are in agreement with the analytical solution.

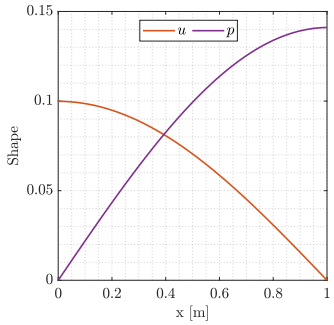
In the two-dimensional case, the modal analysis is studied for the consolidation example in [204]. The domain has dimensions 2×3m and is composed by a water-saturated sandstone material. A mesh of 171 elements is used with a bi-linear approximation for the pressure field and a bi-quadratic approximation for the solid displacement field. The final simulation time is $t_{end} = 1$s for a time step of $\Delta t = 10^{-3}$s. Figure B.3 depicts the first six mode shapes for the problem with the respective frequencies.

B.2 Dynamic Case

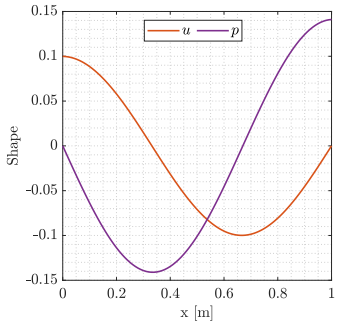
We now study the modal analysis solution for the dynamic case, thus considering the complete system in (B.1). The semi-discrete form is given by

$$\mathbf{M}_{ss} \hat{\dot{\mathbf{u}}}_s + \mathbf{K}_{ss} \hat{\mathbf{u}}_s - \mathbf{K}_{sp} \hat{\mathbf{p}} = \mathbf{f}_s \tag{B.21}$$

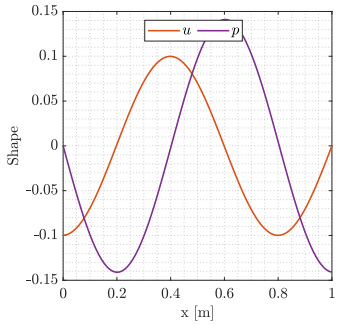
$$-\mathbf{M}_{ps} \hat{\dot{\mathbf{u}}}_s + \mathbf{C}_{ps} \hat{\mathbf{u}}_s + \mathbf{K}_{pp} \hat{\mathbf{p}} + \mathbf{C}_{pp} \hat{\dot{\mathbf{p}}} = \mathbf{f}_p \tag{B.22}$$



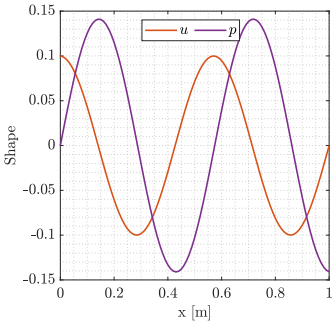
(a) Mode 1: $\omega_u = 20.23$ Hz, $\omega_p = 4.94 \times 10^{-5}$ Hz



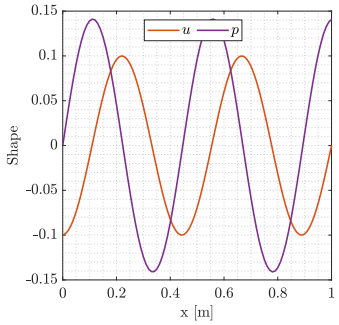
(b) Mode 2: $\omega_u = 60.68$ Hz, $\omega_p = 1.48 \times 10^{-4}$ Hz



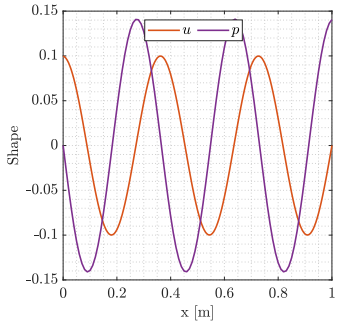
(c) Mode 3: $\omega_u = 101.14$ Hz, $\omega_p = 2.47 \times 10^{-4}$ Hz



(d) Mode 4: $\omega_u = 141.59$ Hz, $\omega_p = 3.46 \times 10^{-4}$ Hz



(e) Mode 5: $\omega_u = 182.05$ Hz, $\omega_p = 4.44 \times 10^{-4}$ Hz



(f) Mode 6: $\omega_u = 222.49$ Hz, $\omega_p = 5.43 \times 10^{-4}$ Hz

Figure B.1: First six mode shapes for one-dimensional transient consolidation problem [108].

where the matrices are the same as in (B.4)-(B.5) with the addition of the mass matrices

$$\mathbf{M}_{ss} = \rho \int_\Omega \mathbf{N}_s^\top \mathbf{N}_s \; d\Omega, \qquad \mathbf{M}_{ps} = \frac{\rho_f \kappa}{\mu_f} \int_\Omega \mathbf{N}_p^\top \mathbf{m}^\top \mathbf{B}_s \; d\Omega. \tag{B.23}$$

Rewriting the system in terms of the generalized vectors $\mathbf{x}_s, \mathbf{x}_p$ and the correspondent eigenvectors $\mathbf{\Phi}_s, \mathbf{\Phi}_p$, we have

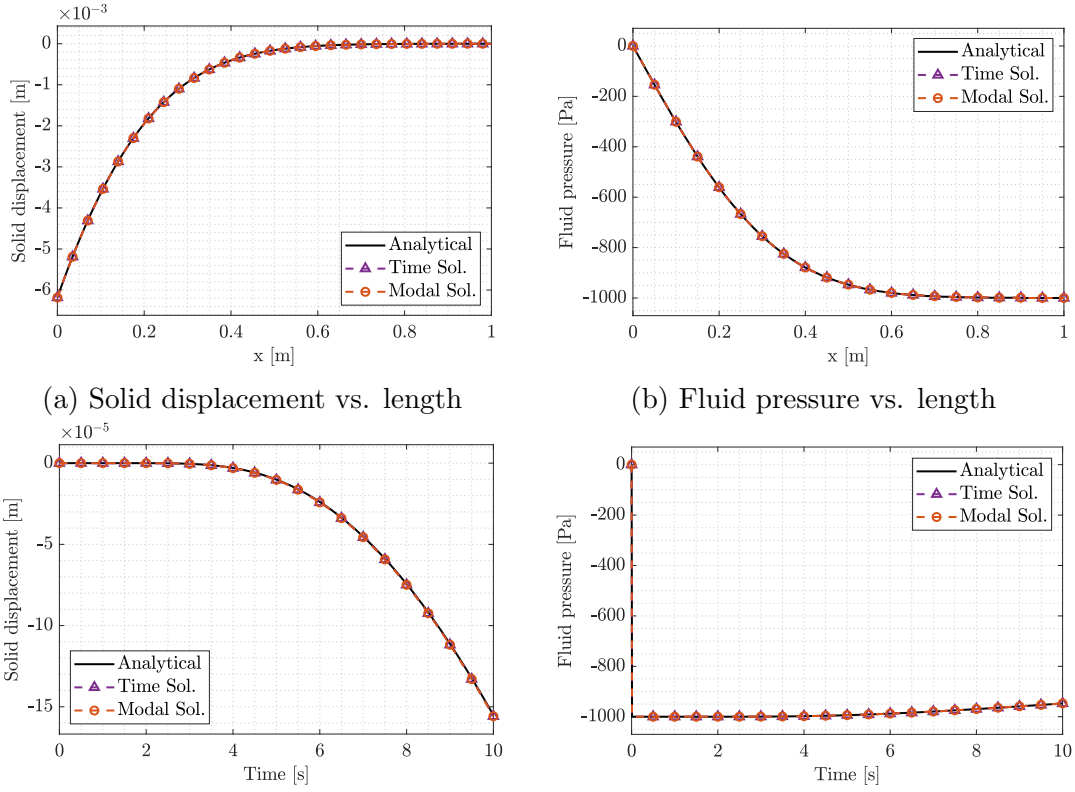
$$\mathbf{M}_{ss}\mathbf{\Phi}_s\ddot{\mathbf{x}}_s + \mathbf{K}_{ss}\mathbf{\Phi}_s\mathbf{x}_s - \mathbf{K}_{sp}\mathbf{\Phi}_p\mathbf{x}_p = \mathbf{f}_s, \tag{B.24}$$

$$-\mathbf{M}_{ps}\mathbf{\Phi}_s\ddot{\mathbf{x}}_s + \mathbf{C}_{ps}\mathbf{\Phi}_s\dot{\mathbf{x}}_s + \mathbf{K}_{pp}\mathbf{\Phi}_p\mathbf{x}_p + \mathbf{C}_{pp}\mathbf{\Phi}_p\dot{\mathbf{x}}_p = \mathbf{f}_p, \tag{B.25}$$

and pre-multiplying the equations by $\mathbf{\Phi}_s^\top, \mathbf{\Phi}_p^\top$

$$\mathbf{\Phi}_s^\top\mathbf{M}_{ss}\mathbf{\Phi}_s\ddot{\mathbf{x}}_s + \mathbf{\Phi}_s^\top\mathbf{K}_{ss}\mathbf{\Phi}_s\mathbf{x}_s - \mathbf{\Phi}_s^\top\mathbf{K}_{sp}\mathbf{\Phi}_p\mathbf{x}_p = \mathbf{\Phi}_s^\top\mathbf{f}_s, \tag{B.26}$$

$$-\mathbf{\Phi}_p^\top\mathbf{M}_{ps}\mathbf{\Phi}_s\ddot{\mathbf{x}}_s + \mathbf{\Phi}_p^\top\mathbf{C}_{ps}\mathbf{\Phi}_s\dot{\mathbf{x}}_s + \mathbf{\Phi}_p^\top\mathbf{K}_{pp}\mathbf{\Phi}_p\mathbf{x}_p + \mathbf{\Phi}_p^\top\mathbf{C}_{pp}\mathbf{\Phi}_p\dot{\mathbf{x}}_p = \mathbf{\Phi}_p^\top\mathbf{f}_p. \tag{B.27}$$



(a) Solid displacement vs. length

(b) Fluid pressure vs. length

(c) Solid displacement vs. time

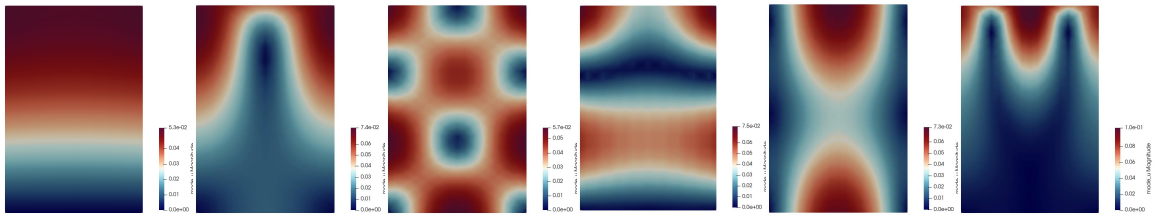
(d) Fluid pressure vs. time

Figure B.2: One-dimensional transient consolidation: comparison of solid displacement (left) and pressure (right) curves for time discretization and mode superposition solution strategies.

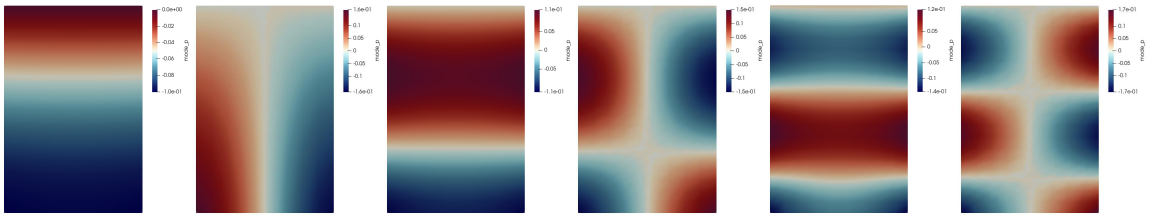
For the time-discrete system let us consider the Generalized Newmark scheme [141] with parameters $\delta = 0.5, \alpha = 0.25$, i.e. the trapezoidal rule, so that

$$\ddot{\mathbf{x}}^{n+1} = \frac{4}{\Delta t^2}(\mathbf{x}^{n+1} - \mathbf{x}^n) - \frac{4}{\Delta t}\dot{\mathbf{x}}^n - \ddot{\mathbf{x}}^n, \tag{B.28}$$

$$\dot{\mathbf{x}}^{n+1} = \frac{2}{\Delta t}(\mathbf{x}^{n+1} - \mathbf{x}^n) - \dot{\mathbf{x}}^n. \tag{B.29}$$



(a) Displacement – natural frequencies (left to right): $\omega_{1u} = 5955.93$Hz, $\omega_{2u} = 9898.80$Hz, $\omega_{3u} = 15415.34$Hz, $\omega_{4u} = 17740.18$Hz, $\omega_{5u} = 18190.85$Hz, $\omega_{6u} = 19145.33$Hz



(b) Pressure – natural frequencies (left to right): $\omega_{1p} = 1.28 \times 10^{-6}$Hz, $\omega_{2p} = 3.81 \times 10^{-6}$Hz, $\omega_{3p} = 3.82 \times 10^{-6}$Hz, $\omega_{4p} = 5.08 \times 10^{-6}$Hz, $\omega_{5p} = 6.27 \times 10^{-6}$Hz, $\omega_{6p} = 6.88 \times 10^{-6}$Hz

Figure B.3: First six mode shapes for (a) solid displacement and (b) fluid pressure in a two-dimensional transient consolidation problem [204].

The resulting fully discrete system is written as

$$\begin{bmatrix} \frac{4}{\Delta t^2}\boldsymbol{\Phi}_s^\top \mathbf{M}_{ss}\boldsymbol{\Phi}_s + \boldsymbol{\Phi}_s^\top \mathbf{K}_{ss}\boldsymbol{\Phi}_s & -\boldsymbol{\Phi}_s^\top \mathbf{K}_{sp}\boldsymbol{\Phi}_p \\ -\frac{4}{\Delta t^2}\boldsymbol{\Phi}_p^\top \mathbf{M}_{ps}\boldsymbol{\Phi}_s + \frac{2}{\Delta t}\boldsymbol{\Phi}_p^\top \mathbf{C}_{ps}\boldsymbol{\Phi}_s & \boldsymbol{\Phi}_p^\top \mathbf{K}_{pp}\boldsymbol{\Phi}_p + \frac{2}{\Delta t}\boldsymbol{\Phi}_p^\top \mathbf{C}_{pp}\boldsymbol{\Phi}_p \end{bmatrix} \begin{Bmatrix} \mathbf{x}_s^{n+1} \\ \mathbf{x}_p^{n+1} \end{Bmatrix} = \tag{B.30}$$

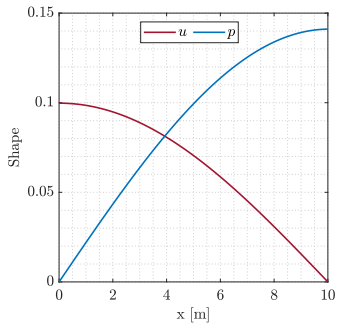
$$\begin{Bmatrix} \boldsymbol{\Phi}_s^\top \mathbf{f}_s^{n+1} + \boldsymbol{\Phi}_s^\top \mathbf{M}_{ss}\boldsymbol{\Phi}_s(\frac{4}{\Delta t^2}\mathbf{x}_s^n + \frac{4}{\Delta t}\dot{\mathbf{x}}_s^n + \ddot{\mathbf{x}}_s^n) \\ \boldsymbol{\Phi}_p^\top \mathbf{f}_p^{n+1} - \boldsymbol{\Phi}_p^\top \mathbf{M}_{ps}\boldsymbol{\Phi}_s(\frac{4}{\Delta t^2}\mathbf{x}_s^n + \frac{4}{\Delta t}\dot{\mathbf{x}}_s^n + \ddot{\mathbf{x}}_s^n) + \boldsymbol{\Phi}_p^\top \mathbf{C}_{ps}\boldsymbol{\Phi}_s(\dot{\mathbf{x}}_s^n + \frac{4}{\Delta t}\mathbf{x}_s^n) + \boldsymbol{\Phi}_p^\top \mathbf{C}_{pp}\boldsymbol{\Phi}_p(\dot{\mathbf{x}}_p^n + \frac{2}{\Delta t}\mathbf{x}_p^n) \end{Bmatrix}. \tag{B.31}$$

The eigenproblem is solved for the uncoupled, undamped free-response equations, as in

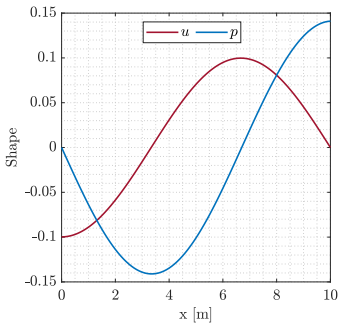
$$\mathbf{M}_{ss}\hat{\ddot{\mathbf{u}}}_s + \mathbf{K}_{ss}\hat{\mathbf{u}}_s = \mathbf{0}, \qquad \mathbf{K}_{pp}\hat{\mathbf{p}} = \mathbf{0}. \tag{B.32}$$

To verify the mode superposition in dynamic coupled systems, a one-dimensional example is performed. The domain geometry and boundary conditions, as well as material parameters

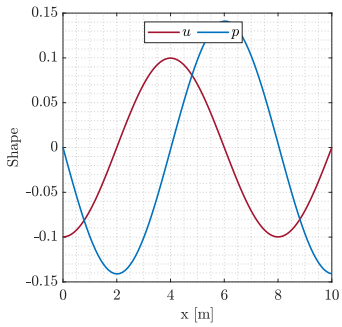
for a water-saturated sandstone, are taken from [123]. The domain is discretized into 100 elements with a linear approximation for pressure and a quadratic approximation for the solid displacement field. For the final simulation time of $t_{end} = 10$s, the chosen time step is $\Delta t = 10^{-4}$s.



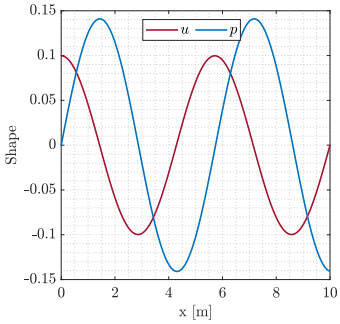
(a) Mode 1: $\omega_u = 16.84$ Hz, $\omega_p = 1.58 \times 10^{-5}$ Hz



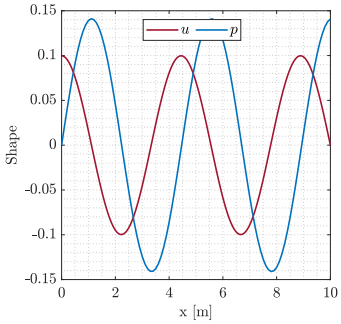
(b) Mode 2: $\omega_u = 50.52$ Hz, $\omega_p = 4.73 \times 10^{-5}$ Hz



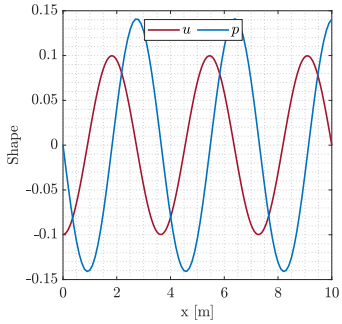
(c) Mode 3: $\omega_u = 84.20$ Hz, $\omega_p = 7.89 \times 10^{-5}$ Hz



(d) Mode 4: $\omega_u = 117.89$ Hz, $\omega_p = 1.10 \times 10^{-4}$ Hz



(e) Mode 5: $\omega_u = 151.57$ Hz, $\omega_p = 1.42 \times 10^{-4}$ Hz

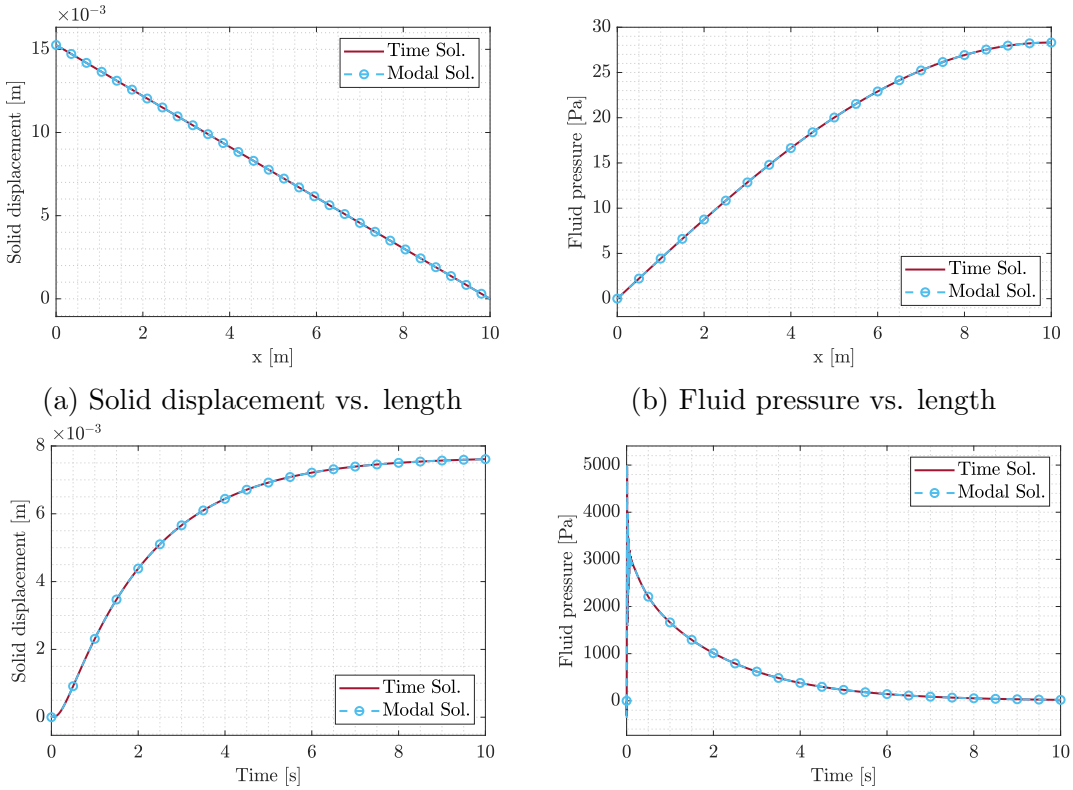


(f) Mode 6: $\omega_u = 185.25$ Hz, $\omega_p = 1.73 \times 10^{-4}$ Hz

Figure B.4: First six mode shapes for one-dimensional dynamic porous media.

Figure B.4 depicts the mode shapes for both solid displacement and pressure fields with the respective natural frequencies. We notice how both frequencies and shapes are very similar to the transient example, where solid and fluid are still in an out-of-phase pattern. Figure B.5 shows the curves for solid displacement and fluid pressure over the domain length (at the final simulation time) and over time (at a point in the middle of the domain). Both time solution and mode superposition lead to the same results; besides, there is an instability in the pressure field at the beginning of the simulation. This is due to the sudden load application at the initial time; nonetheless, we observe that the pressure distribution is smooth over the domain at the final simulation time, meaning that initial instabilities are

dissipated.



(a) Solid displacement vs. length

(b) Fluid pressure vs. length

(c) Solid displacement vs. time

(d) Fluid pressure vs. time

Figure B.5: One-dimensional dynamic consolidation: comparison of solid displacement (left) and pressure (right) curves for time discretization and mode superposition solution strategies.

Appendix C

Porosity-Pressure Coupled Waves

In this appendix, the porosity-pressure wave equations introduced in [165] are used to derive a relation between the wavenumber and the source frequency, leading to the investigation of velocity and attenuation patterns. In addition, we study the difference in wave behavior due to variations in the coefficient n, representing non-reciprocal solid-fluid interactions.

C.1 Wave Equations

To obtain the porosity-pressure equations, we make use of the storage equation (5.5) and the porosity perturbation equation (5.6) and substitute them into the momentum equations (5.8)-(5.9), yielding

$$A\ddot{\eta} + B\dot{\eta} + C\nabla^2\dot{\eta} = D\ddot{p} + E\dot{p} + \nabla^2 p + F\nabla^2\dot{p}, \tag{C.1}$$

$$G\ddot{\eta} + H\dot{\eta} + I\nabla^2\eta = J\ddot{p} + K\dot{p} + L\nabla^2 p, \tag{C.2}$$

in which

$$A = \frac{\rho_f}{\eta_0} - \frac{\rho_{12}}{\eta_0^2} - \frac{\rho_{12}}{\eta_0}\left(\frac{1}{\delta_s} - \frac{\delta_f}{\delta_s \eta_0}\right), \tag{C.3}$$

$$B = \frac{\mu_f \eta_0}{\kappa}\left(\frac{1}{\eta_0} + \frac{1}{\delta_s} - \frac{\delta_f}{\delta_s \eta_0}\right), \tag{C.4}$$

$$C = -\frac{4\mu_f}{3\eta_0} + \frac{(1-\eta_0)\mu_f}{\eta_0}\left(\frac{\mu_M}{(1-\eta_0)\mu_s} - 1\right)\frac{4}{3}\left(\frac{1}{\delta_s} - \frac{\delta_f}{\delta_s \eta_0}\right), \tag{C.5}$$

$$D = -\frac{\rho_f}{K_f} + \frac{\rho_{12}}{\eta_0 K_f} - \frac{\rho_{12}\delta_f}{\eta_0 \delta_s K_f} \tag{C.6}$$

$$E = \frac{\mu_f \eta_0}{\kappa K_f}\left(\frac{\delta_f}{\delta_s} - 1\right), \tag{C.7}$$

$$F = \left(\xi_f + \frac{4}{3}\mu_f\right)\frac{1}{K_f} + \frac{(1-\eta_0)\mu_f}{\eta_0}\left(\frac{\mu_M}{(1-\eta_0)\mu_s} - 1\right)\frac{4\delta_f}{3\delta_s K_f}, \tag{C.8}$$

$$G = -\rho_s\left(\frac{1}{\delta_s} - \frac{\delta_f}{\delta_s \eta_0}\right) + \frac{\rho_{12}}{1-\eta_0}\left(\frac{1}{\eta_0} + \frac{1}{\delta_s} - \frac{\delta_f}{\delta_s \eta_0}\right), \tag{C.9}$$

$$H = -\frac{\mu_f \eta_0^2}{\kappa(1-\eta_0)}\left(\frac{1}{\eta_0} + \frac{1}{\delta_s} - \frac{\delta_f}{\delta_s \eta_0}\right), \tag{C.10}$$

$$I = \frac{4\mu_M}{3(1-\eta_0)}\left(\frac{1}{\delta_s} - \frac{\delta_f}{\delta_s \eta_0}\right) + K_s\left(\frac{1}{\delta_s} - \frac{\delta_f}{\delta_s \eta_0}\right) - \frac{K_s}{1-\eta_0}, \tag{C.11}$$

$$J = -\frac{\rho_s \delta_f}{\delta_s K_f} + \frac{\rho_{12}}{1-\eta_0}\left(-\frac{1}{K_f} + \frac{\delta_f}{\delta_s K_f}\right), \tag{C.12}$$

$$K = -\frac{\mu_f \eta_0^2}{\kappa(1-\eta_0)}\left(-\frac{1}{K_f} + \frac{\delta_f}{\delta_s K_f}\right), \tag{C.13}$$

$$L = \frac{K_s \delta_f}{\delta_s K_f} + \frac{4\mu_M \delta_f}{3(1-\eta_0)\delta_s K_f}. \tag{C.14}$$

We then assume a plane wave solution for the porosity and pressure fields as in

$$\eta = \varepsilon_\eta \exp\left[\mathrm{i}(k_{px}x + k_{py}y) - \mathrm{i}\omega t\right], \tag{C.15}$$

$$p = \varepsilon_p \exp\left[\mathrm{i}(k_{px}x + k_{py}y) - \mathrm{i}\omega t\right], \tag{C.16}$$

where $\varepsilon_\eta, \varepsilon_p$ are the wave amplitudes, k_{px}, k_{py} are the wavenumbers in the x and y directions, and ω is the given source frequency.

Substituting these expressions into the wave equations, after computing the corresponding derivatives and rearranging the system, we have

$$(-A\omega^2 - B\mathrm{i}\omega - C\mathrm{i}\omega k_p^2)\varepsilon_\eta + (D\omega^2 + E\mathrm{i}\omega + k_p^2 - F\mathrm{i}\omega k_p^2)\varepsilon_p = 0, \tag{C.17}$$

$$(-G\omega^2 - H\mathrm{i}\omega - Ik_p^2)\varepsilon_\eta + (J\omega^2 + K\mathrm{i}\omega + Lk_p^2)\varepsilon_p = 0, \tag{C.18}$$

in which $k_p^2 = k_{px}^2 + k_{py}^2$. The polynomial to solve in terms of the wavenumber is given by

$$Mk_p^4 + Nk_p^2 + Q = 0, \tag{C.19}$$

where

$$M = C\,L\mathrm{i}\omega - F\,I\mathrm{i}\omega + I, \tag{C.20}$$

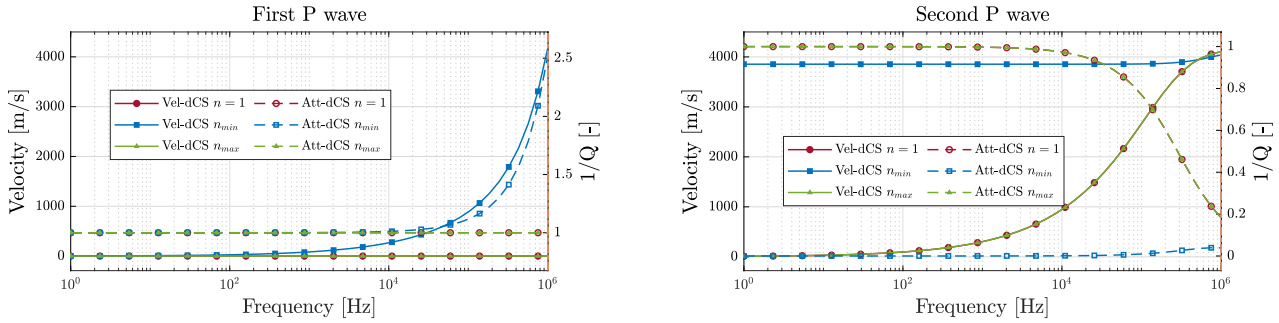
$$N = C\,J\mathrm{i}\omega^3 - C\,K\omega^2 - F\,G\mathrm{i}\omega^3 + F\,H\omega^2 - A\,L\omega^2 - B\,L\mathrm{i}\omega + D\,I\omega^2 + E\,I\mathrm{i}\omega + G\omega^2 + H\mathrm{i}\omega, \tag{C.21}$$

$$Q = -A\,J\omega^4 - A\,K\mathrm{i}\omega^3 - B\,J\mathrm{i}\omega^3 + B\,K\omega^2 + D\,G\omega^4 + D\,H\mathrm{i}\omega^3 + E\,G\mathrm{i}\omega^3 - E\,H\omega^2. \tag{C.22}$$

C.2 Velocity and Attenuation Study

We study the behavior of the porosity-pressure waves in the context of a water-saturated sandstone domain [193] and for different values of the parameter n, as depicted in Figure C.1. The vertical orange line indicates the frequency critical limit at $\omega_c = 1.01 \times 10^6$ Hz. The first P wave has a very small velocity (order of 10^{-7} m/s) for $n = 1$ and n_{max}, but it increases significantly with frequency for n_{min}. The same behavior is noticed for the attenuation of the first P wave.

The velocity of the second P wave seems constant for the frequency range considering n_{min}, but it gradually augments with frequency for $n = 1, n_{max}$. Attenuation for the second P wave has the opposite behavior of the first P wave, showing very low values for n_{min} and similar patterns for $n = 1, n_{max}$. Porosity-pressure waves behave differently in the regimes $n \geq 1$ and $n < 1$; furthermore, they are strongly dependent on the parameter n, since the first P wave velocity changes in several orders of magnitude depending on the porosity effective pressure coefficient.



(a) (b)

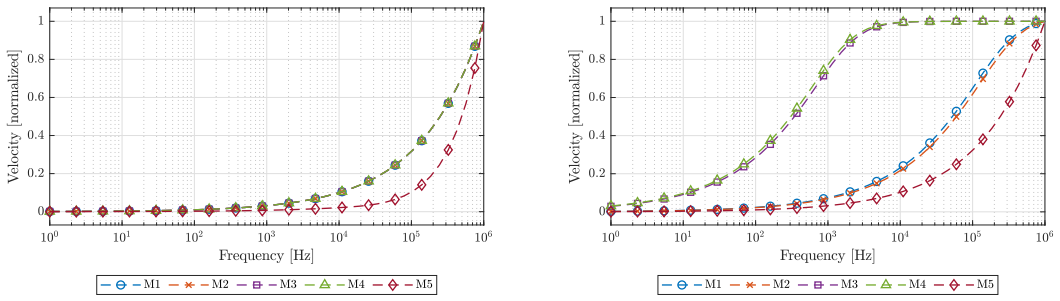
Figure C.1: Velocity and attenuation for porosity-pressure waves in water-saturated sandstone.

C.3 Variation of Solid-Fluid Constituents

Similarly to Section 5.3.6, we observe the velocity and attenuation patterns in porosity-pressure waves for various porous media constituents. For the same combinations M1–M5, Figure C.2 depicts the first and second P waves with normalized values. Velocity of first P wave has the same patterns for all materials, and the second P wave velocity for combinations M3 and M4 reach a plateau earlier than for the other combinations due to the lower critical frequency limit. Table C.1 reports the maximum wave velocity values for M1–M5 combinations, were we notice how the first P wave velocity is lower than the second P wave by several orders of magnitude. Attenuation of the first P wave for M5 decreases significantly at high frequencies, while small changes are noticed for the other material combinations. The attenuation behaviour for the second P wave changes depending on the critical frequency limits, as reported in Table C.1. The lower the critical limit ω_c, the faster the velocity and attenuation curves reach a plateau.

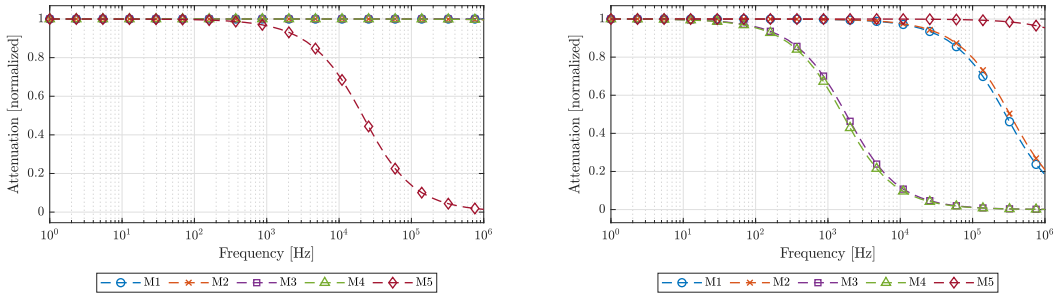
Table C.1: Peak wave velocity for porosity-pressure P waves.

Combination	ω_c [Hz]	v_{max}, first P [m/s]	v_{max}, second P [m/s]
M1	1.01×10^6	2.56×10^{-6}	4.10×10^3
M2	1.84×10^5	8.00×10^{-6}	1.30×10^3
M3	2.19×10^3	3.74×10^{-4}	2.70×10^3
M4	3.33×10^3	6.11×10^{-5}	1.48×10^1
M5	3.33×10^7	2.58×10^{-6}	4.44×10^0



(a) First P - velocity

(b) Second P - velocity



(c) First P - attenuation

(d) Second P - attenuation

Figure C.2: Porosity-pressure waves patterns for different solid-fluid combinations.